Nd:YAG Laser Welding of ZE41A-T5 Magnesium Sand Casting Alloy

Haider Al-Kazzaz

A Thesis

In

The Department

of

Mechanical and Industrial Engineering

Presented in Partial Fulfillment of the Requirements
for the Degree of Master of Applied Science (Mechanical Engineering) at
Concordia University
Montreal, Quebec, Canada

April 2006

ABSTRACT

Nd:YAG Laser Welding of ZE41A-T5 Magnesium Sand Casting alloy

Haider Al-Kazzaz
hkazzaz@yahoo.com

Butt joints of ZE41A-T5 plates with two thicknesses (2 and 6 mm) were laser welded using 1.6 mm EZ33A-T5 filler wire and a continuous wave Nd:YAG system with variable laser process parameters; power (2.5 – 4 kW), welding speed (2 – 7 m/min), joint gap (0 – 0.6 mm) and defocusing distance (0 to -4 mm). Acceptable weld geometries with smooth top and bottom profiles and minor defects were produced with the open keyhole mode. The optimum laser power was 4 kW for both thicknesses, and the welding speed was 6 and 2 m/min for thin and thick plates, respectively. The suitable gap size for the 2 mm and 6 mm plates was found to be between 0.3 and 0.4 mm. The increase in welding speed reduced the FZ defects on a condition of having an open keyhole mode. The fusion zone showed significant grain refinement due to high cooling rate. No grain coarsening was observed in the HAZ. The microhardness test showed that fusion zone hardness was recovered to the value of the base metal after natural aging of around one year. The HAZ with a typical width between 1.5 and 2 mm, showed a drop in hardness compared with the BM. Tensile test showed that the optimum parameters had a joint efficiency between 85 and 95 %. Moderate and high Weibull moduli were obtained for the mechanical properties and weld geometry indicating that the laser welding process seems to have good repeatability. Simulation of laser welding process was developed through combining different models and concepts that enabled to describe the keyhole and weld profile. This model shows good agreement with the experimental results.

بسم الله الرحمن الرحيم

{ وما بكم من نعمة فمن الله }

ACKNOWLEDGEMENTS

I would like to dedicate this work to my beloved wife Arwa and to my family; I would like to thank them for their support and encouragement. Thank you my soul mate Arwa for spending a good time reviewing my presentations and posters, and many thanks for you and my great father for encouraging me to continue my study. I would like to thank my friend Mr. Faris Jasim for informing me about the availability of this opportunity at Concordia University. I am indebted to my supervisor Dr. M. Medraj for his advices; the excellent and useful supervision through the individual and group meetings and for supporting me during my study. His ideas and suggestions were very helpful to me, and it improved my experience and skills. I would like to thank Drs. X. Cao, M. Jahazi and M. Xiao of AMTC-NRC for their advices and the useful information. Their experiences were really a good help to me in order to complete this work. Finally, I would like to thank my group members for their suggestions and support during the whole period of my project.

TABLE OF CONTENTS

LIST OF FIGURES

Literature Survey

Results and Discussion

Effect of Welding Speed on Weldability

Effect of Gap Size on Weldability

Effect of Laser Power on Weldability

Repeatability of Laser Welding Process

Laser Welding of 6 mm thick Plate

Calculating Laser Efficiencies from the Experimental FZ Geometry

Modeling of Keyhole Laser Welding

LIST OF TABLES

Literature Survey

Results and Discussion

Effect of Welding Speed on Weldability

Effect of Gap Size on Weldability

Effect of Laser Power on Weldability

Repeatability of Laser Welding Process

Laser Welding of 6 mm thick Plate

NOMENCLATURE

BM	Base metal	HAZ	Heat affected zone
PMZ	Partial melted zone	FZ	Fusion Zone
Porosity%	Porosity area percentage	T5	Artificial aging heat treatment
E	Heat input (J/m)	f	f-number = F/D
P	Total laser power (W) or (kW)	A_{wire}	Cross sectional area of filler wire (mm^2)
V	Welding speed (m/sec) or (m/min)	A_{gap}	Cross sectional area of joint gap (mm^2)
d	Focal spot diameter (mm)	Laser fluence	= E/d (J/mm^2)
λ	Wave length (mm)	HV	Vickers hardness measured with 200 g at 15 sec dwell time
F	Focal length (mm)	m	Weibull modulus
D	Beam diameter on the optic (mm)	Z_r	Rayleigh length (mm)
M	Laser beam mode	TS	Tensile strength
θ_{beam}	Beam convergence angle (radian)	El	Fracture elongation
L	Depth of focus (mm)	I_s	Threshold surface intensity (W/mm^2)
T_v	Vaporization temperature (K)	A	Absorptivity at normal incidence
P_{ref}	Reflecting power outside the keyhole due to filler wire (kW)	P_{plume}	Absorbed laser power by plasma plume (kW)
η_A	Coupling efficiency = P_{abs} / P	η_{th}	Thermal efficiency = $P_{melting}$ / P_{abs}
η_p	Process efficiency = melting efficiency = $P_{melting}$ / P	MR	Melting ration = η_p
A_w	Total FZ area (mm^2)	ρ	Density (kg/m^3)
C_p	Specific heat $(\frac{J}{kg.K})$	T_{mp}	Solidus temperature (K)

T_o	Room temperature (K)	ΔH_f	Latent heat of fusion (J/kg)
(r,φ)	Polar coordinate of the keyhole	$T(r,\varphi)$	Temperature at any location (K)
P`	Line source strength (W/m)	k	Thermal conductivity $(\frac{W}{m.K})$
P_e	Peclet number	Kd	Thermal diffusivity (m^2/s)
K_o	Modified Bessel function of second kind and zero order	Pd	Penetration depth (mm)
q	Heat flow (W/m^2)	I_{ab}	Absorbed intensity at the keyhole wall (W/mm^2)
θ	Keyhole angle with the vertical direction (radian)	K_1	Modified Bessel function of second kind and first order
I	Intensity at any location (W/mm^2)	r_f	Beam radius at any plane (mm)
I_{00}	Maximum peak intensity at the focal plane with radius zero (W/mm^2)	r_o	Focal radius (mm)
Z_o	Defocusing distance (mm)	$\alpha_{Fresnel}$	Fresnel absorption coefficient
ε	Parameter used to calculate $\alpha_{Fresnel}$	ϕ	Angle between incidence ray and normal to keyhole surface (radian)
I_{plasma}	Absorbed intensity by the plasma inside the keyhole (W/mm^2)	α_{IB}	Bremsstrahlung coefficient (1/m)
L	Path length of the ray inside the plasma	I_{Fr1}	Absorbed intensity by first Fresnel absorption(W/mm^2)
$I_{Fr\text{-}MR}$	Absorbed intensity during the multiple reflections (W/mm^2)	θ_h	Angle between the reflected ray with the horizontal (radian)
r_k	Keyhole top radius (mm)		

Chapter 1

1.1 Introduction

Magnesium alloys are becoming some of the most important alloys in the 21st century. They are interesting alloys for automobile and aerospace industries. Having specific characteristics magnesium alloys are competitive with aluminum and steel alloys. The most important characteristics of magnesium alloys can be summarized as follows: having high strength to weight ratio [1,2], low density [2,4], fatigue resistance [2], excellent damping capacity (impact resistance and noise reduction) [1,2,5], high thermal conductivity [1], high recycleability [1,5] and dimensional stability [2].

The low density of Mg alloys and thus the low total mass of the product results in a low fuel consumption in the automotive and aerospace applications (ex. for automobile industries the vehicle mass is responsible for 60% of fuel consumption, and a 10% reduction in weight can produce a drop in fuel consumption of 5% as a rough estimation [4].). For this reason and because of the high specific strength of Mg alloys, they are important alloys for lightweight structure components.

The application of magnesium alloys is increasing rapidly: for automotive in addition to the current use of Mg as a gearbox housing and in some vehicle interior parts [4], Mg is finding new applications in the automobile industry such as for engine blocks and the car body. For aerospace industries, ZE41A-T5 sand cast Mg alloy has been used in aircraft engine casings, auxiliary gearboxes, and gearbox casings [3]. Most of these applications are as-cast products but extrusion sections are also used; like the vehicle

interior design. Because of the HCP crystal structure of Mg the mechanical deformation is limited at room temperature but the extrusion sections can be produced easier at higher temperature.

This increase in Mg applications highlights the need to develop a proper joining technology [6]. Welding is considered one of the important joining technologies implemented in automotive and aerospace industries [7].

In general Magnesium alloys are difficult to weld due to the following reasons: *Inflammability* that produces oxide film during the welding process [8,9]. *Porosity formation,* that is generated during the welding process and directly affects the mechanical properties of the weld joint [8-12]. *Crack formation* especially when the Mg alloy contains more than 6 wt% Al and 1 wt% Zn elements [8-10]. A *low viscosity* of molten Mg leads to drop-through (sag) of the weld pool and this drop-through becomes significant for large pools with thick sections resulting in the notch effect [6,12]. Further, the low thermal conductivity of Mg alloys (when compared with Al alloys) combined with the low viscosity effect contribute to the formation of a large weld pool with inadmissible root drop-through, especially when the welding parts are subjected to excessive heat input [6,8,12].

The classical inert gas welding techniques are limited in the case of Mg alloys because they produce large heat affected zones [6]. Also, the high heat input involved in these process cause embrittlement due to the grain coarsening in the heat affected zone and the precipitation of brittle phases in both the heat affected zone and fusion zone.

Moreover, these factors worsen the mechanical properties [13] and thus the need for post weld heat treatment becomes essential [14].

Welding difficulties of Mg alloys can be reduced by applying low heat input with high power density and by applying shielding gas to protect the metal from being oxidized [1]. The most suitable techniques that provide these characteristics are the laser welding and electron beam welding. Nevertheless laser beam welding has the important advantage over the electron beam technique represented in the possibility of being performed under ambient pressure. Therefore a lot of attention is directed towards using laser welding for Mg alloys applications.

Focusing on laser welding technology, this process has many advantages over the conventional welding processes. This is because laser welding is a low heat input process [14-18], has high energy density [14,15], high welding speed [2,15-17] narrow heat affected zone [14,15,18], low distortion [11,15,18], ease of automation [14,15], the penetration is deeper and thus high aspect ratio is obtained [14,15], excellent focusing ability [14], well controlled and accurate process [16], and laser beam provides line heating source through the thickness (keyhole formation) rather than point heating source in conventional welding processes [2]. In addition to the ability to weld with or without filler wire, laser welding is an important tool used in tailor weld blank strategy which is widely used in auto body manufacturing [2,15,17].

Weldability of Mg alloys is affected by different types of parameters. To reach a full optimization for a certain Mg alloy, requires understanding of the influence of each parameter on the weldability and weld result. These parameters are: laser power, welding

velocity, focusing parameters and shield gas parameters. Weld defects like porosity formation and cracks formation can be minimized by selecting the proper laser parameters. This can be done by understanding the mechanisms that produce the weld defects and through experimental work. Each alloy interacts differently with the laser welding process because the alloy parameters such as: composition, physical properties, thickness, defects and mechanical properties are different for each alloy. Hence process optimization may result in different parameters for different alloys. Little information is available about utilizing filler wire in laser welding of Mg alloys.

1.2 Objective

This project is conducted to investigate the laser weldability of ZE41A-T5 (Mg-4.2Zn-1.2Ce-0.7Zr) using filler wire EZ33A-T5 (Mg-3Re-2.5Zn-0.6Zr) with the objective to develop a reliable welding process. The weldability of this alloy will be studied through analyzing the effect of laser welding process parameters on the weld geometry, microstructure, defects and mechanical properties. This study will focus on laser welding of 2 and 6 mm butt joint parts. Another important objective is to simulate the laser welding process using MATLAB software that can describe the keyhole and weld geometry profiles also to estimate the laser process, thermal and coupling efficiencies.

Chapter 2 / Literature Survey

Laser welding is in general keyhole fusion welding technique that provides line-heating source through the material thickness [2,19]. Compared with the conventional welding processes, laser welding produces higher penetration depth in a single pass, this is obtained because the heating source through the material thickness is more uniform than the heating distribution in the conventional welding processes, and thus the production rate is higher and the cost of welding is lower [19]. The keyhole can be described as a vapor capillary tube surrounded by a molten metal [8]. This keyhole occurs if the laser power absorbed by the metal is at least equal to the material specific intensity threshold [8,17], that means the critical intensity limit for keyhole formation must be overcome by the intensity of laser beam.

Hence the objective of laser welding process is to create a moving keyhole surrounded by a molten metal by absorption of incident radiation laser beam [20]. Because of the relative velocity between the keyhole and the molten metal [8], the molten metal is cooled rapidly behind the moving keyhole and gets solidified to create the joint between the welding parts (refer in Appendix A.1). The heating power is obtained by focusing the laser beam into a very small spot of the material surface, and that gives very high power density [8,18-20]. The range of power density that creates the keyhole is between 10^3 to 10^5 Watt/ mm^2, and above this range cutting and drilling are achieved [19].

2.1 Laser Welding Modes

Laser welding modes depend on the laser power absorbed by the metal, if the laser power density is less than the threshold value conduction mode is obtained. In the conduction mode the workpiece surface remains unbroken (vapor capillary tube will not form) during the welding process. If the laser density is greater than the threshold value, the keyhole mode is obtained and evaporation takes place during the welding process [20].

Zhao *et al* [10,17] reported that mixed mode could be produced during laser welding, which results in the instability in the keyhole and leads to spiky under bead and might produce porosity. They compared laser welding modes produced during the welding of Al alloys (5182 and 5754) and Mg alloy (AM60B), and found that the mixed mode is responsible for the instability observed in the Al – alloys [10,17,21]. The mixed mode was produced when the laser power density is just above the threshold value.

2.2 Keyhole Stability

The focused laser beam heats the workpiece till it creates liquid metal. When the threshold power density is overcome by the laser beam density, small amount of metal is removed by vaporization process to initiate the keyhole which penetrates through the workpiece thickness. The vapor pressure inside the keyhole is preventing the keyhole wall from collapsing [19]. The stability of the keyhole depends on the equilibrium balance between the keyhole and the molten metal around it, and this can be described by the following equation:

$$\mathbf{P_v + P_l = P_\sigma + P_g + P_h} \qquad (2.1)$$

Where P_v: vaporization pressure,

P_σ: surface tension,

P_h: hydrodynamic pressure,

P_g: hydrostatic pressure,

P_l: radiation pressure [20].

Because of small amount of (P_l, P_g, P_h) the equation can be simplified to:

$$\mathbf{Pv = P\sigma} \qquad (2.2)$$

This means the stability of the keyhole depends on the balance between the vapor pressure and the surface tension pressure; this conclusion is also reported in the experimental results of Zhao *et al.* [10,17] and Punkari *et al.* [21]. The vapor pressure tends to open the keyhole whereas the surface tension pressure tends to close it.

The collapse of the keyhole takes place when there is a sudden drop in the vapor pressure causing the molten metal to slump into the keyhole center [17]. This can be experienced when laser-welding Al alloys having high Mg contents like 5182 and 5754 alloys. The high vapor pressure produced during the welding is due to Mg [17,21], and because of the high excessive heat input, Mg may be depleted from the surface causing sudden pressure drop in the keyhole [17].

Comparing Mg – alloys with Al – alloys, Mg has lower surface tension and higher vapor pressure which gives more stability to the molten pool. Another advantage for Mg alloys is that there is no risk of collapse of the keyhole, because Mg is the major element and the vapor pressure will be high enough which provides a stable keyhole through the welding process [10, 17].

2.3 Laser Types

There are two laser types used for welding process, CO_2 and Nd:YAG lasers. The CO_2 laser is largely used in industry in which the primary laser medium is carbon dioxide. The laser is produced at (10.6 μm) wave - length [19]. The advantages of the CO_2 laser are: wide range of power (0.2 – 45 kW), high electrical efficiency and low operation cost [20].

Nd:YAG is a solid-state laser of Neodymium glass which produces laser with output wave - length equal to (1.06 μm) [20]. The characteristics of Nd:YAG laser are: average laser power between (0.3 – 4 kW), enhanced coupling to reflective metals, higher processing efficiency compared to CO_2 laser when the same power is used. The primary advantage of Nd:YAG is that the laser light can be delivered through fiber optic, this ability makes the Nd:YAG laser attractive for industries; because of the high flexibility obtained during welding process which enables automation [19,20].

The weldability of Mg – alloys have been investigated using the two laser types with continuous and pulse modes, and the researchers concluded that Nd:YAG laser is more efficient than the CO_2 laser [5,8,22,23] as indicated in Figure 2.1. This is obtained because the laser beam delivered by Nd:YAG is highly absorbed by Mg – alloy which leads to higher penetration comparing with the CO_2 laser. For instance, Haferkamp *et al.* [8] studied the weldability of Mg wrought alloys using CO_2 and Nd:YAG laser with the same welding speed V=5 m/min and laser power P=1.5 kW. They reported that Nd:YAG produced 2 mm penetration depth whereas CO_2 laser produced 0.7 mm penetration depth.

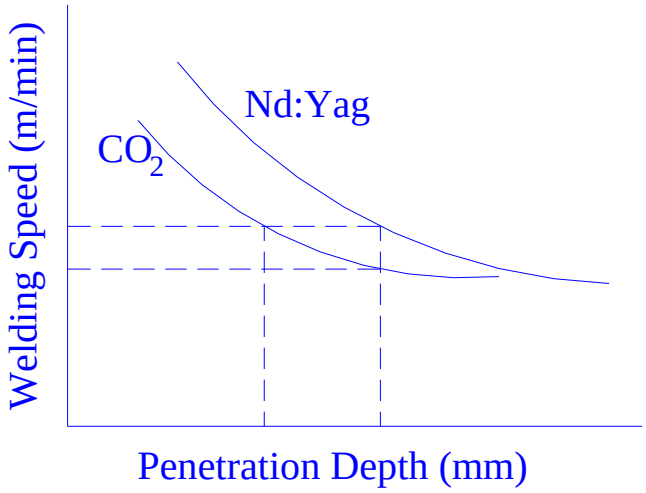

Figure 2.1 : Effect of laser type on penetration depth [20].

Also, Z. Sun *et al.* [5] investigated the weldability of Mg wrought alloy AZ31 using Nd:YAG, CO_2 and tungsten inert gas. They found that the finest weld microstructure formed when using Nd:YAG laser. This fine grain size improves the strength of the weld joint.

2.4 Effective Parameters in Laser Welding Process

Laser welding is a complex process that is affected by different types of parameters like laser parameters, alloy parameters and process parameters. The weldability of Mg alloy depends on the interaction between these parameters. Good understanding of these parameters will help find the solution for welding difficulties and defects. Some of these parameters are controllable like laser parameters and other are fixed and depend on the alloy characteristics. Optimization of laser welding process can be done by defining a set of experimental conditions that lead to acceptable, reproducible, sound weld results. The

most important laser parameters are: laser power, welding speed, focusing characteristics, and shield gas characteristics [19,20].

2.4.1 Laser Power and Welding Speed

Laser power and welding speed determine the total energy per unit length that is applied to the work piece [19]. For continuous wave operation:

$$\mathbf{E = P / V} \qquad (2.3)$$

Where:

P : laser power (watt)

V : welding velocity (m/s)

E : total energy per unit length (J/m) [1].

2.4.1.1 Effect of laser power and welding speed on the weld geometry

As described in laser welding modes, P and V values can change the welding process from keyhole mode to conduction mode and consequently from full penetration to partial penetration. The penetration, weld width, and weld area increase by increasing the total energy (E) provided by the laser beam, and this can be done by increasing laser power and / or decreasing welding speed [1,14,20].

Weishet *et al.* [14] examined the affect of laser power and welding speed on the weld geometry (Figure 2.2) for different Mg wrought and cast alloys using CO_2 laser welding. They found that to join thin plates with full penetration the welding speed range of 2.5 – 3 m/min was required at a laser power of 1.5 kW; for thick plates (5 mm

thickness) the welding speed should be reduced to 1.75 – 2 m/min and laser power must be increased to 2 kW.

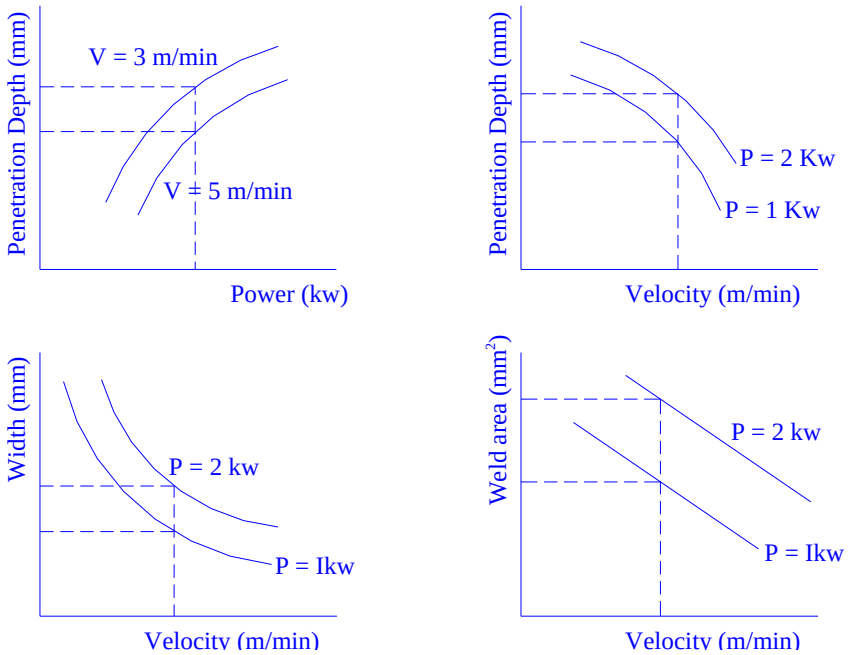

Figure 2.2 : Effects of laser power and welding speed on the weld geometry [1,14,20].

2.4.1.2 Effect of Laser Power and Welding Speed on the Microstructure, Defects and Mechanical Properties

Grain size: during the laser welding process new grains will be created. But because of the high cooling rate during laser welding process, the grain growth is minimized. The grain growth depends on the amount of heat energy supplied to the workpiece. The increase in heat energy either by increasing the laser power or decreasing the welding speed leads to increase in average grain size [10,22].

Porosity: porosity can be reduced by increasing welding speed or by decreasing the laser power as shown in Figure 2.3.

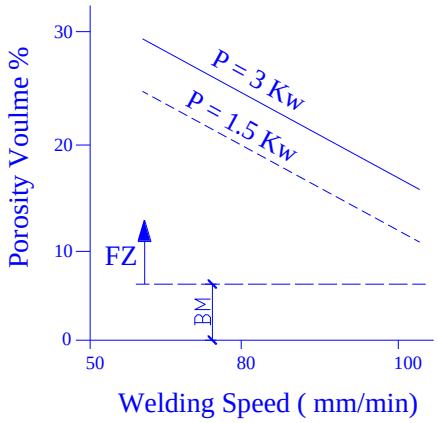

Figure 2.3 : Effects of laser power and welding speed on porosity [17].

Evaporation and alloy elemental losses: high excessive power may lead to reduction in some alloy elements that have low boiling temperature and high vapor pressure. As an Example of that, when laser welding of Mg alloy AZ31D-H24, Mg and Zn are lost during the process compared with Al, which has a lower vapor pressure [22]. Reducing the welding speed has a similar effect on the loss and evaporation of alloying elements.

Hardness: the hardness in the fusion zone and heat affected zone is affected by the grain size and the solidification of intermetallic phases during the laser welding. High speed welding may lead to an increase in hardness in the fusion zone because small grain size results in higher average hardness [10,22]. Similar effect can be obtained through reducing the laser power.

Residual stresses: high welding speed and lower heat input result in reducing residual stresses [7].

2.4.2 Focusing Parameters

The main focusing parameters are shown in Figure 2.4 and can be summarized as: focal spot, focus spot depth, f – number and focal spot location [19,20]. Optimization of these parameters means providing higher laser energy that gives higher penetration depth and an acceptable sound weld.

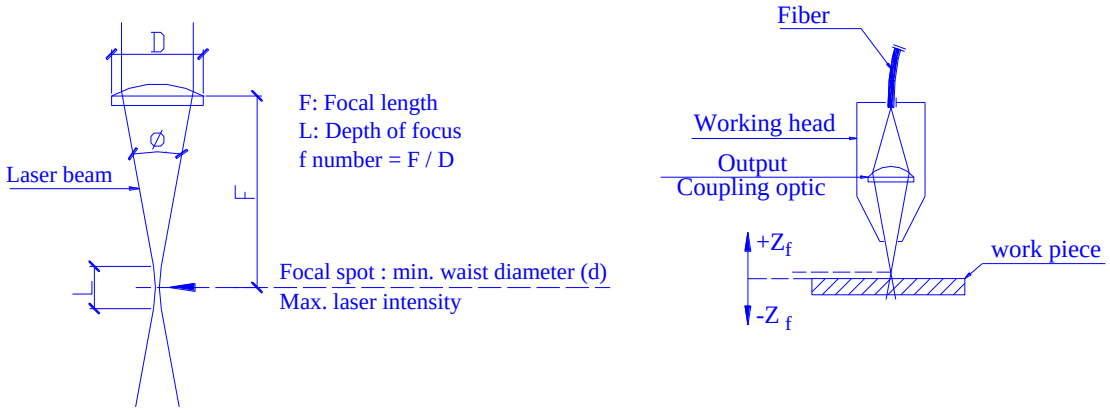

Figure 2.4 : Focusing parameters [19,20].

For a CO_2 laser, the focal spot diameter can be calculated through the following equation:

$$d = \frac{2.44 * \lambda * F * (2M + 10)}{D} \qquad (2.4)$$

Where:

λ : Wave length (mm)

F: focal length (mm)

D: beam diameter incident on optic (mm)

M: laser beam mode, which depends on the transverse electromagnetic mode (TEM) that describes- the profile of power distribution across the beam diameter. (ex. $TEM_{01} \Rightarrow M = 0.01$, $TEM_{20} \Rightarrow M = 0.2$) [19].

For Nd:YAG laser focal spot can be calculated using the following equation:

$$\mathbf{d = 2 * \theta * F} \quad (2.5)$$

Where:

θ: Beam convergence angle (radian)

F: Focal length (mm)

d: Focal spot diameter (mm) [19].

Although the highest power density is achieved by using the smallest focal spot diameter that leads to some restrictions; as the focal spot becomes too small the convergence angle becomes too large causing high variation in power density for a small change in focal spot location. In this way, the process becomes less stable and that may lead to reduction in penetration depth. Also, when the focal spot is too small it will result in very narrow weld geometry which is sensitive to the alignment accuracy of the welding pieces. Futher, significant underfill may occur due to high evaporation rate that took place in this small area causing unacceptable weld geometry [19,20].

Depth of focusing: at the focus depth region the beam diameter should not be more than 5% larger than the focal spot diameter and the corresponding laser power density should not be less than 10% of the highest power density at the focal spot location. The bigger the focus depth the more stability achieved during the welding process [19, 20].

Focus depth can be calculated by the following equation [20]:

$$L = \frac{2 * \lambda}{\pi} \left(\frac{2 * F}{D} \right)^2 \quad (2.6)$$

f – number: the ratio of focus length (F) to the beam diameter (D) is defined as f number. The optic focusing characteristic can be define by f-number as shown in Table 2.1.

Table 2.1 : Effect of f - number on focusing characteristics [19].

Higher f - Number	Lower f - Number
Higher focus length (F)	Lower focus length (F)
Higher focus depth (L)	Lower focus depth (L)
Smaller convergence angle	Larger convergence angle
Larger focal spot diameter (d)	Smaller focal spot diameter (d)
More stable welding process	Less stable welding process

Since focus depth (L) increases with increasing f-number as can seen in Table 2.1, the highest f-number is desirable in laser welding process. Common values of f – number for CO_2 laser are from 6 to 7, and for Nd:YAG near 4 [20].

Focal spot position: the focal spot should be positioned in a place relative to the work piece surface that gives the highest penetration depth. In general the work piece surface should be located within the focus depth region because after this region the variation in power density will be very high. For autogenous laser welding of Al alloys, the experiments show that when the focal spot is located below the work piece surface; more penetration was achieved than when the focal spot was on the surface [20]. For Mg alloys, however, the surface focal spot is desirable for thin plates of 2.5 to 3 mm in thickness, and for thick plates with 5 to 8 mm in thickness experimental results showed that pointing the focal spot below the work piece by 2 mm resulted in better weld quality [5,14,13]. This observation was based on weld geometry (i.e. penetration depth, aspect

ratio and underfill). On the other hand, Dhahri *et al.* [1] reported that suitable weld results were obtained for Mg alloy WE43 with 4 mm thickness plates when the focal spot position was on the surface or 1 mm under.

Laser welding modes are also affected by the degree of defocusing, Zhao *et al.* [17,10] examined the weldability of die cast Mg alloy AM60B, they reported that as the degree of defocusing increased the laser welding mode changed from keyhole to conduction mode. This is because the power density in the defocusing case was less than the threshold value of keyhole formation.

As a conclusion, for a given laser power and welding speed optimization of focusing parameters depends mainly on focal spot diameter, f-number and focal spot position. The high value of f – number yields more stable laser welding process but in the same time it results in a reduction in laser power density. Therefore larger f – number consistent with the required laser power intensity at a chosen welding speed must be used [20]. Surface focal spot position can be used when laser welding (autogenous welding) Mg alloys with thin plates (< 4 mm). For thick plates (greater than 4 mm) the focal spot must be pointed under the work piece surface to give better weld geometry.

2.4.3 Shield Gas Parameters

Shield gas is used during laser welding process for two important reasons [19,20]:

1. To protect the weld keyhole and the molten metal from oxidation and hence reduce the porosity and oxide inclusions.

2. To suppress plasma formation that is created by the ionized vapor over the weld zone which will lead to higher transmission efficiency for laser beam.

The Most important parameters in shield gas are: shield gas type, gas flow rate and nozzle geometry [19,20].

2.4.3.1 Shield Gas Types

Helium (He) is widely used with CO_2 and Nd:YAG laser because it has the highest ionization potential that gives high ability to suppress the plasma formation during the welding process. Another advantage, He is lighter than air and thus the shielding device has higher ability to remove the gases from above the welding area [19]. Nitrogen (N_2) has good ability to prevent plasma formation but it can cause embrittlement in certain alloy [19,20]. Whereas argon (Ar) has high ability to prevent oxidation, good ability to suppress plasma formation and compared with He, Argon provides substantial cost saving for large production process. One disadvantage in using Ar is that the shield gas device must provide high capability to remove the gases from above the weld area because Ar is heavier than air. If the shield device is not efficient, Ar may stagnate above the weld area causing high dense gas that reduce the transmission efficiency of the laser beam [19].

2.4.3.2 Shield Gas Flow Rate

Gas flow rate is an important factor in term of weld quality and cost. It depends on the amount of laser power, the accessibility to the joining parts, nozzle geometry and nozzle height [19,20].

2.4.3.3 Gas Shield Device

Side flow and co-axial flow are commonly used devices with CO_2 and Nd:YAG laser. Side flow device provides good visual access to the target area but its alignment with welding seam is critical. Co-axial device is more practical mechanism for robotic purposes and its alignment is not critical as in the side flow device, but the co-axial flow may produce a negative pressure be exerted along the beam axis causing drawing of some material elements from the welding area. Also, for high power laser more than 5 kW the co-axial flow may form plasma above the welding area affecting the focusing of the laser beam. In this case side flow device can be used to reduce the effect of plasma formation [19,20].

Table 2.2 lists the optimized shield gas parameters that used for different Mg alloys during laser welding process:

Table 2.2: Optimization of shield gas parameters

Ref #	Mg alloy	Laser Power (KW)	Shield gases	Optimum gas flow rate	Shield gas device
14	cast & wrought	2.5KW CO_2	He , Ar , N_2	He @ 12 l/min	co-axial
9, 17	AM60B	3KW Nd: Yag	He	He @ 94 l/min	side flow Ø8mm
22, 23	AZ31B-H24	2KW Nd: Yag	Ar	Ar @ 40 l/min	side flow: Ø8mm @ 1cm
		6KW CO_2	He	He @ 25 l/min	side flow: Ø5mm @ 1cm
12	AZ91HP	3KW Nd: Yag	He	He @ 12 l/min	co-axial
	AM50HP	6KW CO_2			
24	cast & wrought	2.5KW CO_2	He , Ar , N_2	He @ 10 l/min	----------
25	WE43 RZ5	5KW CO_2	He	He @ 50 l/min	----------

2.5 Weldability of Magnesium Alloys

The weldability of alloy can be defined as the ability to produce sound and acceptable weld joints using a certain set of laser parameters. In addition to laser welding and process parameters, the weldability of magnesium alloys are affected by alloy composition, the metallurgical properties, mechanical properties and the physical properties of the base metal. The criterion of sound weld area can be described by producing full penetration weld with no significant weld defects (i.e. cracks or porosity), good weld surface quality, and acceptable metallurgical and mechanical properties [13, 19,20,23].

2.5.1 Microstructure

The welded area is divided through microstructure analysis into two regions, the fusion zone (FZ) and heat affected zone (HAZ). The fusion zone is the main region of the weld joint where melting takes place due to absorption of laser power. Adjacent to the FZ is the heat affected zone, which separates the FZ from the base metal. The laser welding process as described before has an important advantage in that it produces a small HAZ. The HAZ is a result of the heat transfer from the FZ to the base metal. The heat induced during the laser welding process may cause unacceptable metallurgical changes in the microstructure like cracking, grains coarsening, brittleness and pore formation.

2.5.2 Fusion Zone (FZ)

Weisheit *et al.* [14,13] examined the weldability of different Mg alloys. They observed that most Mg alloys formed cellular structure in the FZ and this was attributed to the

increased segregation effect of the melt caused by the high cooling rate during the welding process. This observation was not for all Mg alloys used in their study, for instance; alloy WE54 showed more globular grain shape, alloys AZ61 and AZ91 showed more dendritic fine grained and alloy AZ31 showed grain coarsening in the FZ and HAZ as a result of low alloy content. On the other hand, Weisheit *et al.* [14,13] reported that the investigated Mg alloys except AZ31 showed grain refinement in the fusion zone as a result of high cooling rate. The grain growth in alloy AZ31 was also reported by Sanders *et al.* [22], they mentioned that using higher welding speed could reduce the grain growth effect. Haferkamp *et al.* [8] examined the effect of welding speed on the grain refinement for alloy AZ91D. They observed that high speed welding caused a significant grain refinement whereas low welding speed yielded microstructure nearly the same as in the base metal. Pastor *et al.* [10] studied the microstructure of AM60B alloy, they observed that both FZ and base metal consist of cored grains of Mg – rich solid solution surrounding by $Mg_{17}Al_{12}$ intermetallic phase. They also found that the intermetallic phase in the FZ was greater than that in the base metal caused by non-equilibrium solidification during the welding process. The morphology in the FZ changed from equiaxed to dendritic when welding speed was increased.

2.5.3 Heat Affected Zone (HAZ)

Weisheit *et al.* [14,13] reported that no grain coarsening was observed in cast and wrought alloys except wrought alloy AZ31 that showed significant grain coarsening in the HAZ. The grain size was increased about 10 times in the direction of the heat flow and 3 times in the direction perpendicular to the heal flow. They also reported that in the

investigated casting alloys, except alloy WE54, change in the microstructure of the HAZ occurred through a liquation of the grain boundaries eutectics and intermetallics that have low melting temperatures.

Many researchers [14,15,18] reported that one of the important characteristics of laser welding process is the small HAZ compared with the conventional welding processes and consequently lower possibility for metallurgical damages in this region.

2.5.4 Porosity Formation

Porosity occurred when bubbles of gas are trapped during weld solidification. The presence of porosity in the weld pool may lead to reduction in weld cross-section area resulting in a bad effect on the mechanical properties of the joint. Some of the process conditions may lead to porosity formation like unsuitable shield gas device which may cause air or moisture to be trapped in the weld pool. Another source of porosity formation is the surface contamination in the plate edges (e.g. grease, moisture and paint). Non-optimum laser parameters in addition to alloy parameter may result in porosity formation in the weld area (FZ and HAZ). Weisheit *et al.* [13,14] reported that the porosity formation in the sand cast and extruded Mg alloys were very low, whereas a few large pores were formed with Mg alloys having high contents of Zn or Al elements (e.g. alloy AZ91 and alloy ZC63). They also reported that, the porosity formation was affected by the type and condition of the alloy. For example, AZ91 and AM60 alloys that were high pressure die casted (HPDC) under non vacuum process, formed extremely high area percentage of porosity and this was attributed to the trapped gaseous elements during the manufacturing of these alloys. Haferkamp *et al.* [8] compared the porosity formation

between Mg alloy AM60B (non vacuum HPDC) and alloy AZ91 (vacuum die cast). They found that alloy AM60B has more pre-existing pores in the base metal because it was not produced under vacuum causing high concentration of gases in the base metal. The high content of the pre-existing pores in the base metal was the reason for the high porosity formation during the welding process.

Zhao *et al*. [10, 17] examined the weldability and porosity formation of Mg alloy AM60B (HPDC). They observed that the porosity content in the FZ was greater than the porosity content in the base metal. The increase in the porosity content in FZ was attributed to one or more of the following reasons: first - the keyhole stability was responsible for the porosity formation, second - the coalescence and expansion of pre-existing pores in the base metal, third - the rejection of hydrogen from the intermetallic compounds during the welding process. They concluded that the keyhole stability was not responsible for the porosity formation during the process because changing the laser-welding mode from keyhole to conduction mode by defocusing the laser beam did not eliminate the porosities. The mixed unstable mode between the keyhole and conduction mode was not found in Mg alloy AM60B comparing with Al alloys that showed unstable mixed mode when the laser power density is just above the threshold value. The coalescence and the expansion of the small pre-existing pores (also reported by [8,12]) in the base metal was the main mechanism of porosity formation and they compared the experimental results with the mathematical model, which showed good agreement. The remedy for the porosity formation was by reducing the heat input (reduce the laser power or increase the welding speed) and also the porosity can be reduced more by re-melting the welded joint using second run keyhole mode laser welding.

Mikucki *et al.* [24] reported that the porosity formation in AZ91 Mg alloy was dependent on the amount of dissolved hydrogen in the alloy. They also found that the rejection of hydrogen from intermetallic compounds such as $Mg_{17}Al_{12}$ assisted in the nucleation and growth of micro porosity during the last stage of solidification during the process.

2.5.5 Cracks formation

There are three basic types of cracks that form in the fusion or heat affected zones [19]:

A. Solidification cracking (hot cracking): happens in the liquid films which surround the solidifying grains. These films have low melting temperature and have brittle characteristic (after solidification) causing cracking when subjected to high transverse contracting stresses induced during the rapid solidification process.
B. Heat affected zone liquation cracking: the low melting films which surround the grain boundaries may also present in the HAZ causing cracking due to thermal stresses induced during the welding process.
C. Heat affected zone cold cracking: this type of cracking can occur after or during the welding process and it is caused by the dissolved hydrogen in the alloy, the brittle intermetallic phases and the residual stresses.

Weisheit *et al.* [13,14] reported that most of Mg alloys could produce crack-free weld area by applying the optimum laser parameters except QE22 alloy that showed high sensitivity to solidification cracking. On the other hand, Baeslack *et al.* [25] observed that fine cracks formed in the grain boundaries in the HAZ for Mg alloy WE54, and was

caused by the liquation of the intermetallic phases. Whereas Weisheit *et al.* [13,14] reported that no cracking caused by liquation of the grain boundaries for the same alloy.

Sun *et al.* [5] reported that the solidification crack sensitivity was high for Mg alloy AZ31. They observed that the solidification crack formation was reduced when applying high welding speed to reduce the laser heat input, which may cause simultaneous solidification of the low melting phases with the other alloy phases. On the other hand, Lathabai *et al.* [3] reported that solidification crack formation does not appear to be a problem during laser welding of Mg alloy AZ31. Further, Haferkamp *et al.* [8] reported that micro cracks may occur in weld area when laser welding Mg alloys which have high Al (more than 6% wt.) alloy elements or Zn (more than 1% wt) alloy elements.

2.5.6 Mechanical properties

Heat treatment induced during the laser welding process in the FZ and HAZ may cause a change in the mechanical properties of the weld area such as hardness, toughness, tensile strength, yield stress, fatigue strength and formability. Many researchers examined the changes in hardness in the weld area for the Mg alloys but very few studies were directed subjected towards the other mentioned mechanical properties.

2.5.6.1 Hardness

Weisheit *et al.* [13,14] investigated the effect of laser welding on the hardness of Mg cast alloys, wrought alloys and age hardened alloys. For the as – cast alloys the hardness was increased in the FZ due to the fine grain structure produced by the rapid cooling during the process. However, in the HAZ there was no change in hardness because there was no

change in the microstructure. For the wrought alloys the hardness was in the same range for the base metal, HAZ and FZ. They attributed the absence of any changes in hardness for the wrought alloys to the complete compensation of the loss in work hardening effect by grain refinement effect. For the age – hardened Mg alloys, the hardness in the FZ remained at the same level as the base metal for AZ91, ZC63 and WE54 alloys, but it decreased in alloy QE22. In the HAZ there was no change in hardness for alloys (ZC63 and WE54) whereas it decreased for alloys (AZ91 and QE22). Weisheit *et al.* did not explain the inconsistent behaviors for Mg age – hardened alloys.

Similar conclusion was reached by Pastor *et al.* [10] for high pressure die cast alloy AM60B which showed an increase in hardness in the FZ and that was attributed to grain refinement and the presence of intermetallic phase $Mg_{17}Al_{12}$. Also, Haferkamp *et al.* [8] examined the change in hardness for different cast alloys. They reported that high welding speed has a significant effect on grain refinement and thus increase in hardness occurred in the FZ whereas at low welding speed the hardness in the FZ was in the same level as the base metal. On the other hand, Dhahri *et al.* [9] reported that there was no significant change in micro hardness in the FZ for Mg cast alloys WE43 and ZE41.

For AZ31 wrought alloy, which showed grain growth in FZ and HAZ, Weisheit *et al.* [13,14] and Haferkamp *et al.* [8] reported that there was no change in hardness in FZ and HAZ, whereas Sanders *et al.* [22] and Sun *et al.* [5] reported that the hardness decreased in FZ and HAZ due to the grain growth effect.

2.5.6.2 Tensile Mechanical Properties

Lehner *et al.* [12] reported that the mechanical properties of the weld area for Mg alloys AZ91 and AM50 (HPDC under vacuum) were in the same range as the base metal. Although the weld area had an underfill which reduced the weld area, the tensile strength was in the same level as the base metal which proved that the weld area had better mechanical properties than the base metal. The tensile strength was mainly affected by the gaps between the parts. Significant decrease in the tensile strength occurred when the gap becomes relatively large compared with the plate thickness.

Haferkamp *et al.* [8] examined the mechanical properties of the welded area for different types of cast and wrought Mg alloys. For autogenous laser welding the fracture location was in the FZ. At high welding speeds of 8 m/min the fracture strain of the welded area was reduced by 64% compared with the base metal. They also reported that small volume pores with uniform distribution through the weld cross-section showed higher strength than those with few large pores. Fracture occurred in the plane, which had maximum area percentage of porosity.

2.5.7 Oxide Inclusion

Weisheit *et al.* [13,14] reported that although Mg alloy has a high affinity for oxygen, the oxidation in the welded area for most Mg alloys was not severe. The only exception was alloy WE54 that showed increase in oxide inclusion in the FZ, which was attributed to the high content of yttrium element in this alloy. Sanders *et al.* [22], also, reported that there was no increase in the oxide inclusion when laser welding Mg alloy AZ31B which indicated that the shielding device was effective.

2.5.8 Weld Geometry

Full penetration autogenous laser welding of Mg alloys leads to underfill in the weld pool which is small for the thin plates and significant for the thick ones. Also, the underfill depends on the alloying elements. The underfill is small for Mg alloys that have high amounts of Zn and tangible for Mg alloys that have high amount of Al element [13,14]. The underfill becomes significant when a large gap between the welding parts is used. If the overfill is present during full penetration autogenous laser welding, the FZ has a large amount of area percent of porosity that forces the melt to perform the overfill shape. Overfill can be reduced using higher welding speed [10].

As discussed in the keyhole stability, Mg alloys produced stable keyhole during the welding process because of high vapor pressure and low surface tension of Mg element. The low thermal conductivity of Mg alloy comparing with Al alloy, leads to larger weld area and more penetration through the thickness [8,17,21]. The effect of thermal conductivity, surface tension and vapor pressure is represented schematically in Figure 2.5.

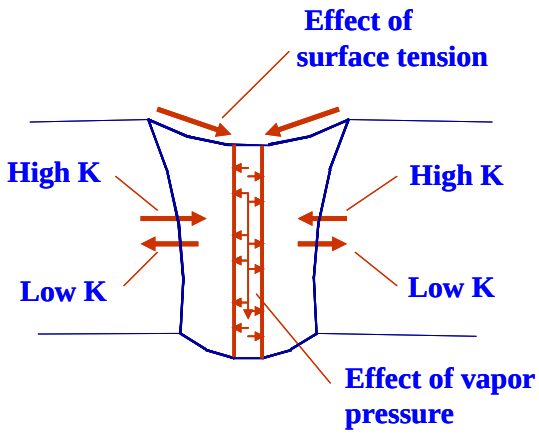

Figure 2.5: Schematic diagram for the effect of physical properties on weld geometry

2.6 Laser welding with filler wire

The development of using filler wire in laser welding process is still in its infancy, but it is getting more attention since it might solve many of the problems facing autogenous welding. The most important advantages of using filler material are: to improve weld properties [6,15,19], to increase the gap between the welding parts [6,15,19], and to weld thick sections using a multi-pass technique [15,19]. Compared with other welding techniques laser welding requires less filler wire per meter of welded seam [6], underfill and notching effect can be overcome by using filler wire [6], and finally the porosity of the welded joint can be reduced using filler metal [8].

2.6.1 Continuous wire feed system

The most important method of applying the filler wire is the use of continuous wire feed system. In this process, part of the laser beam will be reflected by the wire [15] and the interaction between laser beam, filler wire, welding parts become a complicated process. Non –optimum feeding rate may cause an increase in side wall porosity and it tends to increase with increasing the gap size. Root porosity may also result when using multi pass welding. Wire feed rate is dependent on the welding speed (V), gap cross section area (A_{gap}) and cross section area of the filler wire (A_{wire}) as can be seen through the volumetric flow rate constancy and as shown by the following equation [19]:

$$\text{Wire feed rate} = \frac{V_{welding} \times A_{gap}}{A_{wire}} \qquad (2.7)$$

2.6.2 Filler Wire and Gap Size

When laser welding of the butt joints, it is recommended to use a joint gap slightly wider than the diameter of the filler wire. If the gap was narrower than the wire diameter the following problems may be encountered:

- The need for precise control to place the wire right on the gap edges and that yields small positioning tolerance between the filler wire and the gap edges.
- Any change in the wire's location relative to the gap edges may cause an excessive spatter and vaporization of the weld pool. In autogenous laser welding, the maximum gap size that can be used is roughly 10% of the plate thickness whereas the gap size can be equal to the filler size when using filler wire [15].

2.6.3 Wire Feed Delivery Angle

The recommended angle between filler wire and laser axis is between ($30 - 60^{o}$) and according to [15,14] 45^{o} is preferable. A smaller angle causes the wire to intersect with a large area of the laser beam, which may lead to high reflection in the laser beam causing melting and vaporization of the wire without interaction with the weld pool [19].

2.6.4 Feeding Direction

The recommended feeding direction is the front edge of the leading laser side. The trailing edge may cause incomplete mixing of the wire into the pool [15,19].

2.6.5 Filler Wire Position

The position of the filler wire in respect to the focal spot and weld pool surface is an important parameter in the process. Intersection of the filler wire with the laser beam above the weld pool surface must be avoided because it might cause an excessive spatter of the filler martial and reduce the penetration ability of the laser beam, also it may cause tooling damage [19].

Jokinen and Kujanpaa [16] and Dawes [19] reported that for thick section plate of stainless steel, wire position should be below the focal spot. Positioning the filler wire above the focal spot may cause poor penetration, material spattering and weld defects [16,19].

2.6.6 Laser Welding With Filler Wire for Mg Alloys

Regarding Mg alloys, the minimum available diameter of the filler wire is 1.6 mm (because of the poor formability of Mg alloys) which allows very small positioning tolerance leading to difficult welding process [6]. Haferkamp *et al.* [6] reported that a 1.2 mm diameter of filler wire has been developed in Germany. This might lead to a significant development in Mg laser welding with filler wire. Haferkamp *et al.* [8] observed that the fracture strain of the weld joint of AZ31B Mg alloy which was welded using filler wire increased two times compared with autogenous laser welding. This was attributed to the absence of the notching effect and the fracture took place in the HAZ rather than the FZ.

The summary of this literature survey can be seen in Appendix (A.1).

Chapter 3 / Experimental Procedure

3.1 Material and Equipments

The experimental material was sand cast ZE41A-T5 (Mg-4.2Zn-1.2Ce-0.7Zr) magnesium alloy used generally for engine casings. The cast plates had sizes of approximately 300 x 150 x 3 to 4 or 6 mm. The plates with original thickness of 3 to 4 mm were cut into four small pieces for laser welding, each with approximate sizes of 150 x 75 x 3-4 mm. The magnesium castings were machined to 2 mm and 6mm thickness. The joint faces were also machined along the length for all the specimens. Prior to laser welding the joint faces and their surroundings were carefully cleaned by acetone to remove any contaminations. The plates were laser welded at Aerospace Manufacturing Technology Center (AMTC – NRC) Located in Montreal – Quebec.

The laser welding machine used in this study is a continuous wave (CW) 4 kW HL4006 Nd:YAG (neodymium-doped yttrium aluminum garnet) laser system equipped with an ABB robotic and magnetic fixture system. A focal length of 150 mm and a fiber diameter of 0.6 mm were employed. Helium was used to shield the top surface and argon was used for the bottom surface of the workpieces. The flow rates were 18.9 and 21.2 l/min (40 and 45 cubic feet per hour) for the top and bottom surfaces respectively. The shielding gas was directed to the top surface of the workpiece at an angle of 30^{o} (with the horizontal) and was vertically and uniformly directed to the bottom surface. The workpieces were positioned and clamped in a fixture and the butt joint with a different

gap size between 0 to 0.6 mm. Defocusing range was between 0 and -4 mm with 0.45 mm focal spot diameter.

A filler wire of EZ33A-T5 (Mg-3Re-2.5Zn-0.6Zr) Mg alloy with 1.6 mm diameter and 990 mm length was used through a continuous feeding mechanism. The position of the filler wire was just above the surface of the workpiece. A delivering angle of 60^{o} was used between the filler with and the laser beam axis to reduce the contact area between the filler and laser beam. During laser welding, the workpieces were stationary while the laser beam scanned at a various power between 2.5 to 4 kW and different speed (2 - 7 m/min). Wire feeding rate was calculated using volume flow rate constancy equation (3.1):

$$\text{Wire feed rate} = \frac{\textit{welding speed x gap area}}{\textit{filler wire area}} \qquad (3.1)$$

The laser weldability of sand cast ZE41A-T5 magnesium alloy was examined through microstructure and mechanical tests. A length of approximately 20-30 mm was cut from both ends of each joint to exclude the unstable segments at the start and end of laser welding. Cross-sectional samples for metallurgical examination were cut from the weld joints at three locations (start, middle and end). These cut specimens were mounted using hot and cold-setting resin and polished to a mirror-like finish. The polished samples were then etched in Nital solution. The microstructure details were examined using an Olympus optical microscope equipped with Discover Essential image analyzer software. The average values were calculated from the quantitive measurements of the three specimens (start, middle and end). One of these specimens was also used for the Vickers

microindentation hardness test performed by Duramin A-300 hardness Tester, under a test force of 200 g and dwell period of 15 seconds. Several tensile-specimens cut from weld joint were prepared according to ASTM standards (B557M-02A). The samples were examined for the tensile test at constant displacement rate (0.01 mm/sec) using an MTS-100 KN tensile test machine.

3.2 Key Experiments

The weldability investigation of the 2 mm butt joint plates using filler wire was divided into the following stages:

- **Effect of welding speed on weldability**

  The objective of this stage was to investigate the weldability for high welding speed; therefore the laser power was fixed at the maximum value (4 kW). The gap size was 0.4 mm which is quarter the size of the filler wire. Variable welding speed between 4 to 7 m/min was used in the process.

- **Effect of gap size on weldability**

  The optimized welding speed found in first stage was used to investigate the effect of variable gap size (between 0.1 to 0.6 mm) on the weldability. The laser power was fixed at the maximum value (4 kW).

- **Effect of laser power on weldability**

  Variable laser power between 2.5 to 4 kW was used in this stage. The optimized welding speed and gap size found in the first and second stages, respectively, were used. The literature survey showed that the optimized defocusing used for

thin plate was zero for autogenous welding; therefore this was used in laser welding of the 2 mm plates.

- **Repeatability of laser welding process**

  The reliability of laser welding process was assessed by producing repeatable welded joints utilizing the optimized parameters in the above mentioned stages. Better quality of casting was used for this purpose.

- **Laser welding of 6 mm plate**

  Due to the limited laser power this stage was challenging to produce full penetration sound weld by single pass. Because of the thick plate, the laser power was kept at 4 kW. Bead-on-plate welding was used to optimize the defocusing parameter. Autogenous laser welding was used to weld 6 mm butt joint plates to optimize the welding speed since it is easier in preparation and optimization. The starting welding speed was chosen to be one degree lower than the optimized welding speed for 2 mm plate. After producing a full penetration welding in autogenous process, the welding speed was adjusted to weld with filler wire using the optimized gap size found in the welding of 2 mm plate. The objective of welding the 6 mm plate was not limited to produce sound weld, but also to give better understanding of laser welding of thick plates.

Chapter 4 / Results and Discussions

4.1 Effect of welding speed on the weldability of 2 mm plates

The plates were laser welded at 4 kW laser power, 0.4 mm gap size, surface defocusing and with various welding speeds as shown in Table 4.1.1

Table – 4.1.1: Key experiments : effect of welding speed on the weldability

Sample #	Gap Size mm	Laser Power kW	Welding Speed m/min	Wire feeding rate m/min	Defocusing mm
1	0.4	4	4	2	0
2	0.4	4	5	2.5	0
3	0.4	4	6	3	0
4	0.4	4	7	3.5	0

4.1.1 Weld Geometry

To analyze the weld geometry of the tested samples, the average weld width (average of top and root bead width), penetration depth, crown height, root height, crown area, root area, and total weld area were measured. The effect of welding speed on the width, height and weld area are shown in Figures 4.1.1 and 4.1.2. As expected, the weld dimensions decreased with increasing welding speed. As the welding speed increases the laser fluence (eq. 4.1) decreases implying that less heat was delivered to the workpiece resulting in smaller melted weld area and joint size. The sample tested at 7 m/min shows slight deviations due to the large misalignment of the work-pieces. At high welding speed, it was found that the 1.6 mm filler wire was difficult to melt due to the small diameter of beam laser. The aspect ratios (penetration depth / top width) for all sections

were greater than 1.2 indicating that the keyholes were established during the welding [26].

$$Laser\ \ Fluence\ \ = \frac{Laser\ Power}{Focal\ \ Spot\ Diam.\ x\ Welding\ \ Speed} \tag{4.1}$$

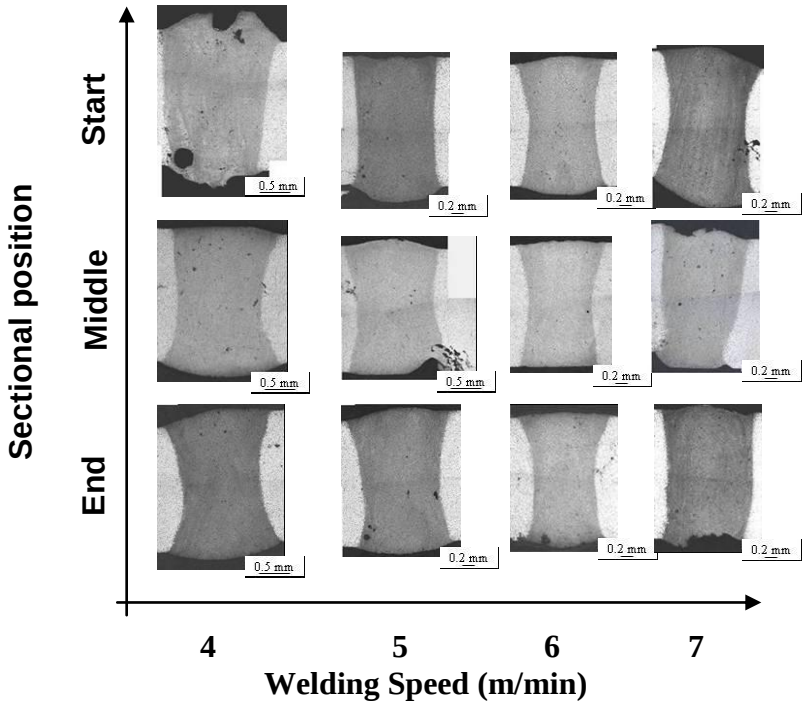

Figure 4.1.1 – Effect of Welding Speed on Weld Geometry.

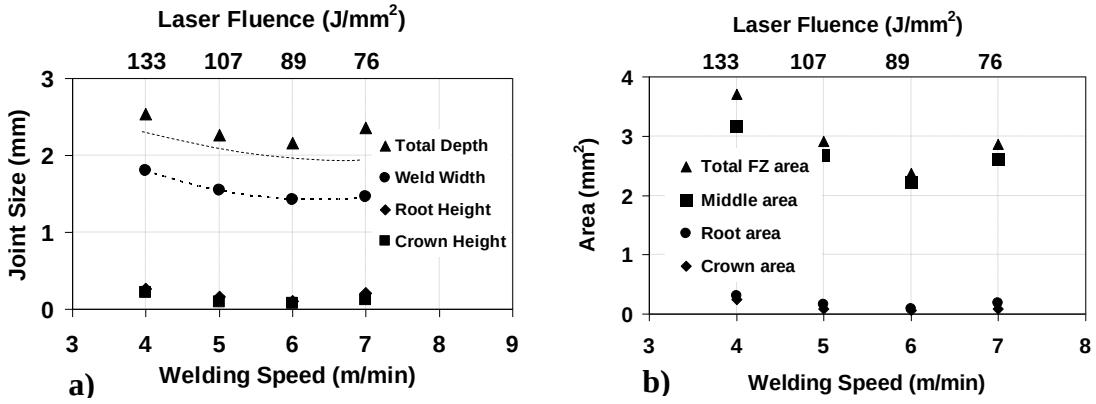

Figure 4.1.2 – Effect of Welding Speed on (a) joint size and (b) weld area.

Higher crown and root heights were observed in the starting section of the sample welded at 4 m/min as shown in Figure 4.1.1. The excessive crown and root heights might

increase the stress concentration in these areas [27]. The large crown obtained in this sample is probably due to the expansion and flotation of the gas pores [5] as demonstrated in Figure 4.1.1 where gas porosity has longer time to form and grow at lower welding speed. As well known, the use of filler wire might reduce the tendency to form underfill. The sample welded at 5 m/min (middle section as shown in Figure 4.1.1) showed a root underfill near the base metal (BM), probably due to a BM defect. The sample welded at 7 m/min (ending section as shown in Figure 4.1.1) showed a shrinkage groove at the root. The sample welded at 6 m/min showed smooth top and root bead surface with narrow and uniform weld width, which was the optimum weld geometry obtained among the tested samples.

4.1.2 Microstructure

Figure 4.1.3 shows that laser welding also produces three distinct regions: fusion zone (FZ), partially melted zone (PMZ) and heat-affected zone (HAZ). It was observed that the grains in the FZ were significantly finer than those in the BM and HAZ, which can be attributed to the high cooling rate (10^5 – 10^6 $^oC/s$) obtained in laser welding process compared with the low cooling rate (10^2 – 10^3 $^oC/s$) obtained in arc welding [28].

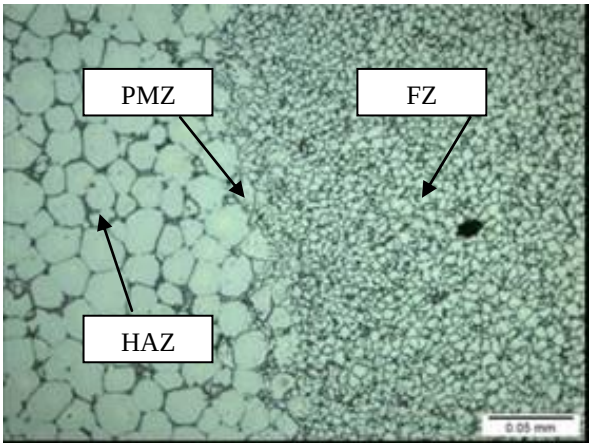

Figure 4.1.3 – Micrograph Showing the FZ, PMZ and HAZ.

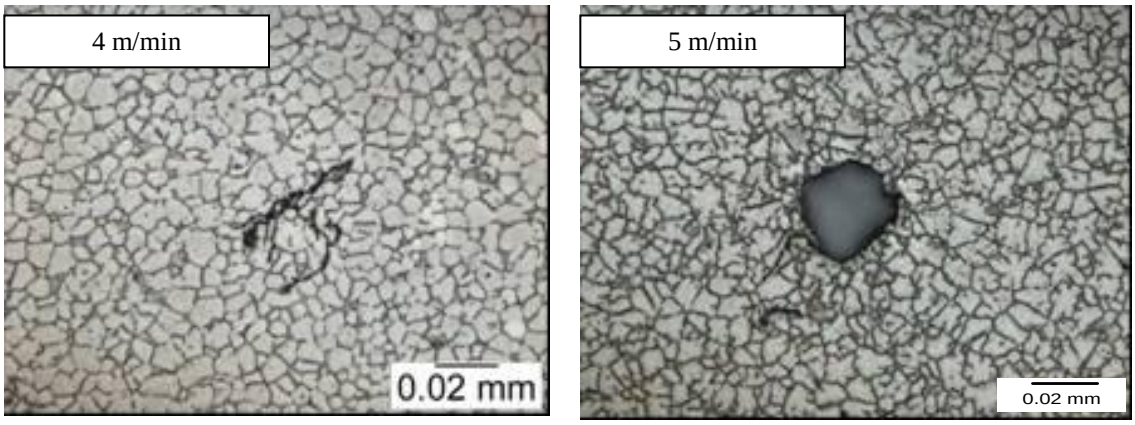

Figure 4.1.4 – Effect of Welding Speed on FZ Grain Morphology

The fusion zone microstructure was found to be fine equiaxed or rosette grains as shown in Figure 4.1.4. Although the welding speed increased from 4 to 7 m/min, no significant change in grain size in the FZ was observed. The fine equiaxed grains obtained in the laser process can also be attributed to Zr in the ZE41A-T5 alloy. It was reported that grain refining of magnesium alloys seems to be based on a peritectic reaction on Zr nuclei [28]. Originally, the grains nucleate as small spheres around the initiating Zr particles. Because the nucleation is so prolific, many grains are nucleated at once (simultaneously) and the grains cannot grow far before they mutually impinge. Figure 4.1.3 shows that the partial melting zone (PMZ) is rather narrow; only one or two grains wide. This figure also shows the cellular growth from the large grains in the PMZ. The length of the cellular growth is approximately similar to the grain size in the FZ. This limited cellular growth can be attributed to the high cooling rate and the presence of prolific Zr nuclei. It was difficult to distinguish the difference in microstructure between the HAZ and BM indicating the absence of any grain coarsening in the HAZ. For this

reason the HAZ was identified by the microindentation hardness as will be discussed later.

4.1.3 Porosity

The relation of porosity area percentage and number with welding speed is shown in Figure 4.1.5. The porosity area percentage decreased from 1.26% to 0.57% as the welding speed increased from 4 to 7 m/min. Although it was difficult to find the trend between welding speed and number of pores, in general increasing the welding speed reduces the number of pores. Figure 4.1.6 shows the average pore size distribution for all samples. It was observed that the majority of pores were smaller than 75 µm, with typical size about 20 µm.

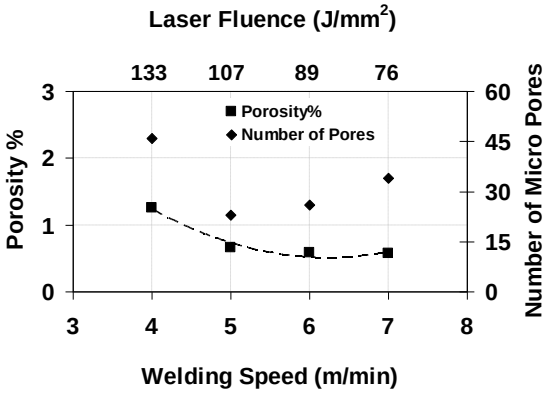

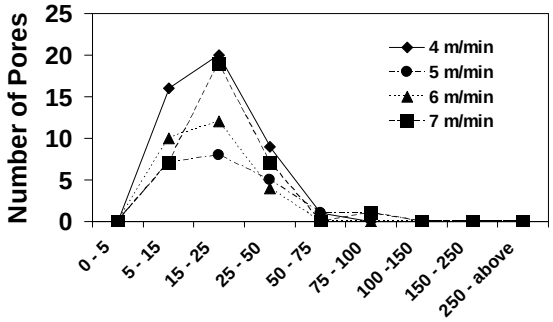

Figure 4.1.5 – Effect of Welding Speed on Porosity.

Figure 4.1.6 – Porosity Distribution

Keyhole instability is considered to be one of the most important reasons for porosity formation in Al alloys. The stability of the keyhole depends on the balance between the vapor pressure and the surface tension [20]. The vapor pressure tends to open the keyhole whereas the surface tension tends to close it. The collapse of the keyhole takes place when there is a sudden drop in vapor pressure, causing the molten

metal to slump into the keyhole. Compared with Al-alloys, Mg alloys have low surface tension and high vapor pressure (due to evaporative elements such as Zn, Mg, etc.) leading to the formation of a more stable keyhole [17].

In addition, Mikucki et al. [24] reported that the porosity in AZ91 Mg alloy was dependent on the amount of dissolved hydrogen in the alloy. The rejection of hydrogen from the solid-liquid interface assisted in the nucleation and growth of micro porosity during solidification. Regarding ZE41A-T5 Mg alloy (which contains Zr element) hydrogen reacts with zirconium to form ZrH_2. Hence, hydrogen should not be the main source for the formation of porosity in the experimental alloy ZE41A-T5 [28].

Zhao et al. [10, 17], Haferkamp et al. [8] and Lenhner et al. [12] reported that the coalescence and expansion of pre-existing pores in the BM are responsible for the porosity formation. The applied heat by the laser beam may increase the pressure inside the pores, causing the expansion and coalescence to form bigger pores especially at lower welding speed as shown in Figure 4.1.1. The maximum porosity percentage measured was 1.26% at 4 m/min but it is considered to be low compared with the published data for other Mg alloys [10]. The main reason may be due to the use of filler wire, which has low pre-existing pores since it was produced by extrusion process.

4.1.4 Crack Formation

Weld cracks were observed for ZE41A-T5 alloy. For all tested samples the area of solidification cracks was less than 1 mm^2, thus these cracks are micro-cracks [30]. The maximum total crack length in the fusion zone was 1.47 mm, and the maximum average

width was 2 μm for the sample welded at 4 m/min. It was observed that increasing the welding speed from 4 to 7 m/min reduced the total crack length from 1.47 to 0.68 mm and reduced number of cracks from 9 to 5, as shown in Figure 4.1.7. The higher welding speed reduces solidification cracks, which seems to agree with the published results of AZ31 Mg alloy [5]. Increasing the welding speed reduces laser heat input, which may cause simultaneous solidification of the low melting phases of the grain boundary with the primary solidifying phase (alloy matrix phase) because of the increase in cooling rate. The low crack formation experienced here may be attributed to the followings: (i) formation of fine microstructure in the FZ (which reduces the susceptibility for cracking), (ii) using the filler wire EZ33A-T5, since the filler wire helps to reduce evaporative losses of alloying elements and reduce the porosity formation, and (iii) rare earth elements in the experimental alloy and the filler wire, which beneficially narrow the freezing range and thus reduce the tendency of crack formation.

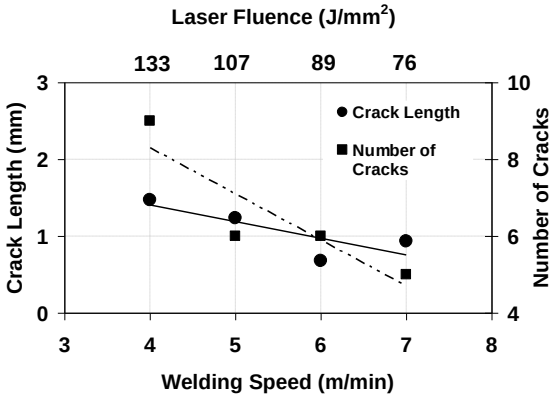

Figure 4.1.7 – Effect of Welding Speed on Crack Length and Number of Solidification Cracks in the FZ.

Solidification crack occurs in the liquid films which surround the solidifying grains. These films have low melting temperature and appear to be brittle after solidification [19], causing cracking when subjected to high transverse contracting

stresses induced during the rapid solidification process (Figure 4.1.8a). According to Borland's theory [31,32], alloying elements with high solubility and low partitioning coefficients (e.g. Zn in Mg alloys) can increase solidification cracking susceptibility by promoting a large freezing temperature range [33]. The ZE41A-T5 alloy has a wide solidification temperature range (120 ^{o}C) [28]. Thus, the occurrence of a solidification crack is possible during the laser welding. Weld cracks may start from the area of high tensile stresses or stress raisers. Therefore, the cracks may initiate from oxide film, gas and shrinkage porosity and defects from the base metal as can be seen in Figure 4.1.8.

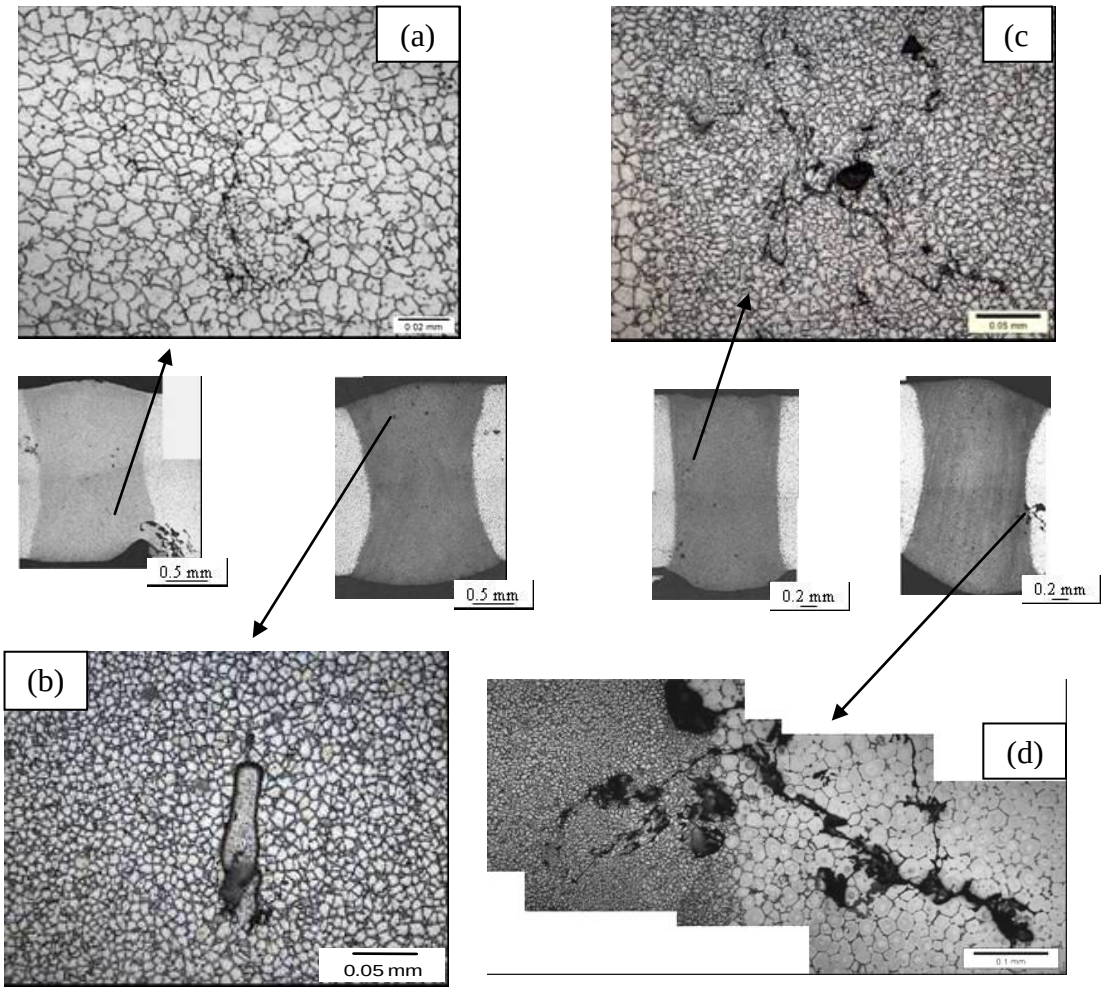

Figure 4.1.8 – Solidification Cracks in the FZ initiated by Various Sources Observed in Laser Welding of ZE41A-T5 Mg alloy.

The liquation cracks were observed in the HAZ due to the liquation of some low melting intermetallics in the grain boundaries. Figure 4.1.9 shows a HAZ liquation crack observed in a sample welded at welding speed of 5 m/min

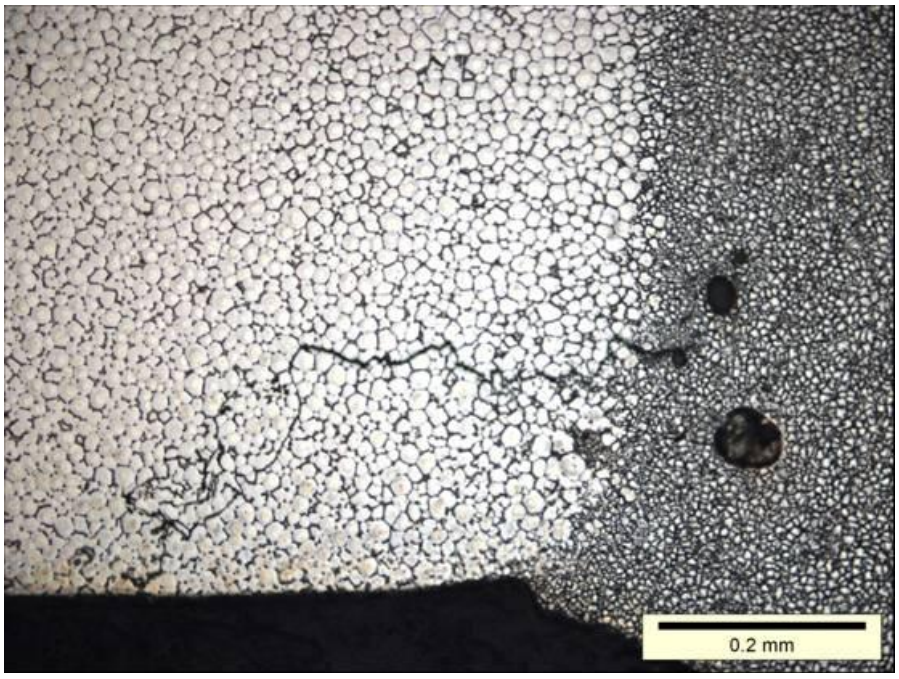

Figure 4.1.9 – HAZ Liquation Cracks Observed in Laser Welding of ZE41A-T5 Mg alloy.

4.1.5 Micro-Indentation Hardness

Vickers microindentation hardness was measured across the weld joints as shown in Figure 4.1.10. These samples have had a natural aging over a period of approximately 12 months after the welding. The hardness values in the fusion zone have recovered to or even been higher than those in the base metal, probably due to the grain refinement in the FZ. However, there was a drop in the hardness in the heat affected zone. The width of the heat affected zone as indicated in Figure 4.1.10 varies from 2 to 0.5 mm as the welding speed increased from 4 to 7 m/min. As the welding speed increased the total heat input

decreased and thus the heat transferred from FZ to the base metal was reduced resulting in smaller HAZ. The softening of the HAZ in the precipitate-hardenable alloys probably involves the dissolution of the strengthening phase Mg_9Ce and the formation and growth of nonstrengthening phases [28]. The scattered data of the hardness in the base metal are probably due to the low load used in the test (200 g), cast micro-defects, and non-uniform cooling rate during casting.

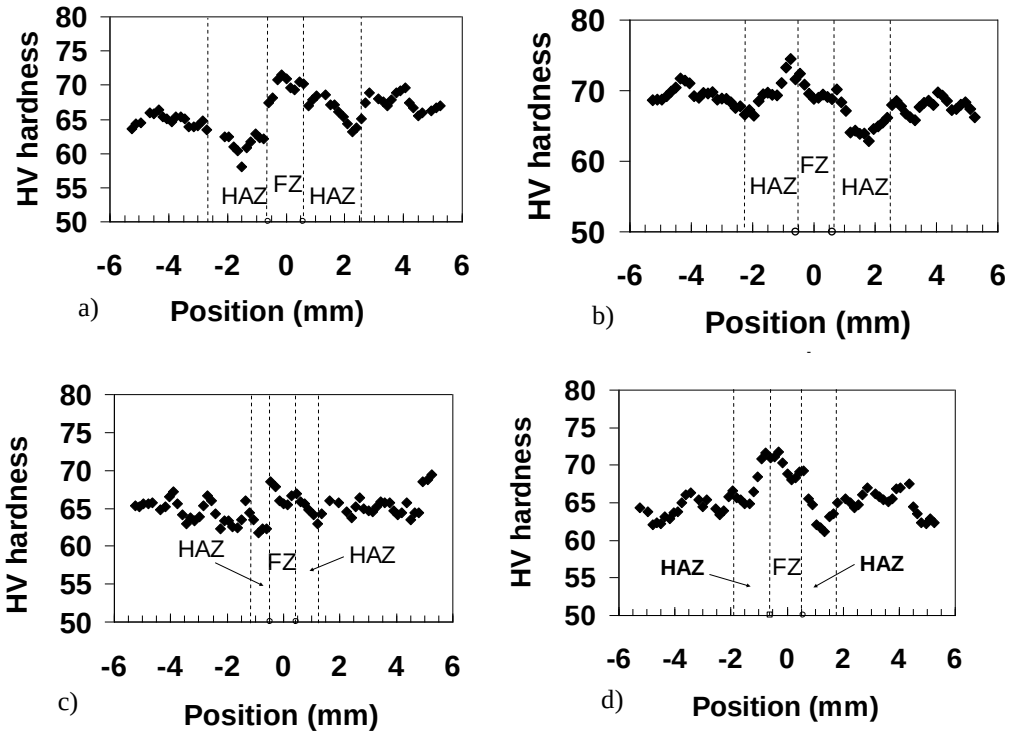

Figure 4.1.10 – Vickers Microindentation Hardness for Welding Speed at (a) 4, (b) 5, (c) 6, and (d) 7 m/min.

4.1.6 Tensile Strength

Four tensile specimens were prepared from each joint except the one welded at 7 m/min because of the large misalignment. The joint efficiency and the tensile strength property of the test samples are shown in Figure 4.1.11 and Table 4.1.2, respectively. The joint

efficiency is defined as the ratio of the tensile strength of the weld joint to that of the base metal (here 179 MPa according to AMS – 4439). It is found that the weld joints have a joint efficiency of approximately 75-90%. Only two specimens out of 12 failed in the FZ, whereas all the other fractured in the base metal at a distance of 4 to 22 mm from the PMZ. Most of the samples were fractured in the base metal indicating that the FZ is stronger than the BM. One of the samples failed in the FZ shows low tensile property due to a visible big defect in the FZ.

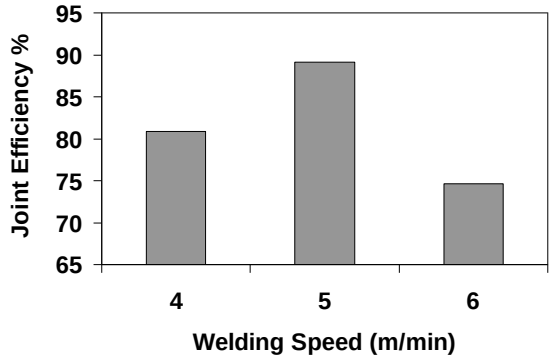

Figure 4.1.11 – Joint Efficiency of Laser Welded ZE41A-T5 Mg Alloy Using Filler Wire.

Table 4.1.2 – Tensile Strength Property for the 2-mm Plates Laser Welded at Variable Welding Speeds.

Experimental Sample	Tensile Specimen	TS Mpa	Faliure location
4 m/min	T1	164	BM
	T2	82	FZ
	T3	157	BM
	T4	176	BM
5 m/min	T1	164	BM
	T2	171	BM
	T3	157	BM
	T4	146	BM
6 m/min	T1	92	BM
	T2	------	FZ
	T3	143	BM
	T4	166	BM

4.2 Effect of joint gap on the weldability of 2 mm plates

The plates were laser welded using 4 kW laser power, 6 m/min (based on the results presented in section 4.1), surface defocusing and with variable gap sizes as shown in Table 4.2.1

Sample #	Gap Size mm	Laser Power kW	Welding Speed m/min	Wire feeding rate m/min	Defocusing mm
5	0.1	4	6	0.75	0
6	0.2	4	6	1.4	0
7	0.3	4	6	2.1	0
8	0.4	4	6	3	0
9	0.5	4	6	3.5	0
10	0.6	4	6	4.2	0

Table – 4.2.1: Key experiments / effect of gap size on the weldability

4.2.1 Weld Geometry

The effects of gap size on the width, height and weld area are shown in Figures 4.2.1 and 4.2.2. As indicated in Figure 4.2.1, there was a tendency to form irregular FZ geometry as the gap size became smaller than 0.3 mm and larger than 0.4 mm. Excessive crown height was observed in the sample welded with 0.2 mm gap, and large shrinkage groove and underfill were observed when the gap was larger than 0.4 mm. Gap size smaller than 0.3 mm may cause difficulties in mixing of the melted filler wire with the melted sides of the BM. On the other hand, when the gap size was larger than 0.4 mm, there was a tendency to form large drop – through (root height) because of the high fluidity (low surface tension) and low viscosity of the Mg alloys [2]. The hourglass weld geometry was not found when the gap size was larger than 0.4 mm. Although there was a slight deviation in the average weld width and total area, it is noticed from the joint size charts

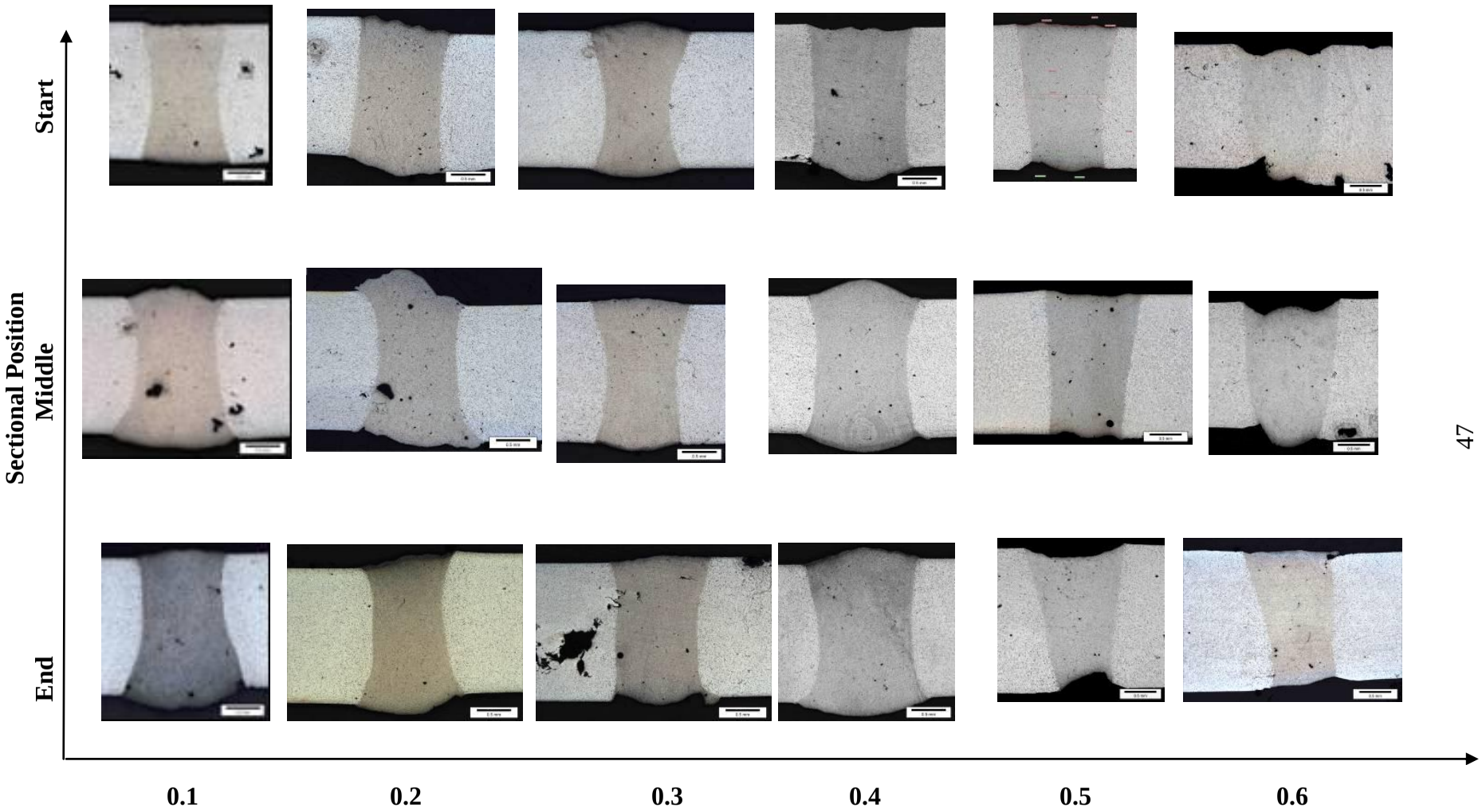

Figure 4.2.1 – Effect of Gap Size on Weld Geometry

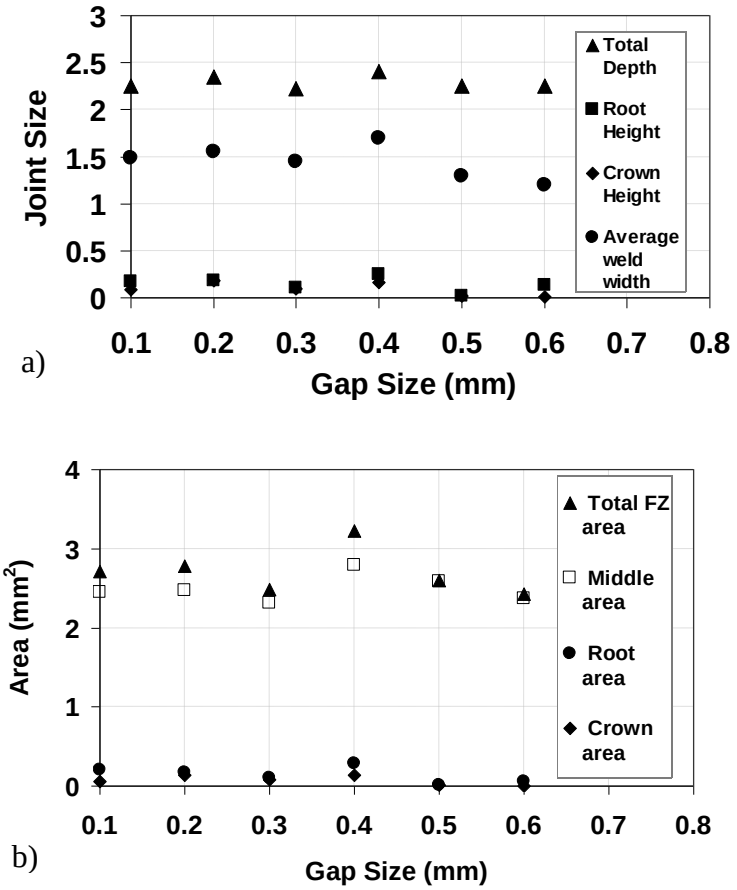

Figure 4.2.2 – Effect of Gap Size on (a) joint size and (b) weld area.

(Figure 4.2.2-a) and the corresponding cross sections (Figure 4.2.1) that increasing the gap size more than 0.4 mm may cause a slight decrease in the FZ area due to the loss of molten drops through defects. The contribution of the filler wire in the FZ area was increased from 7% to 50% as the gap size increased from 0.1 to 0.6 mm. The operational range of the gap size can be increased using a smaller filler wire (here smaller than 1.6 mm) [6,34] since the wire for conventional arc welding was relatively big for laser application. Haferkamp *et al.* [6] reported that a 0.2 mm gap size can be used in butt joint laser welding of Mg plates using experimental filler wire with 1.2 mm diameter. In this

work, good joint quality (refer to section 4.4) was obtained at 0.4 mm gap size during laser welding with 1.6 mm filler wire.

4.2.2 Microstructure

The fusion zone microstructure was observed to be fine equiaxed grains, Figures 4.2.3 and 4.2.4, but there was a tendency to form a rosette grains as the gap size increased greater than 0.4 mm as shown in Figure 4.2.4. The grain refinement in the FZ has been discussed earlier in section 4.1. Figure 4.2.3 shows that the PMZ was very narrow, and there was no grain coarsening observed in the HAZ when compared to with the BM.

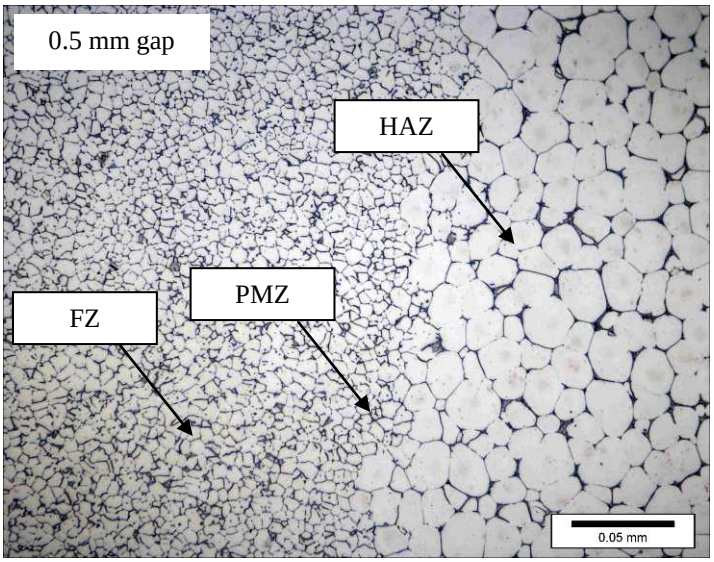

Figure 4.2.3 – Micrograph Showing the FZ, PMZ and HAZ.

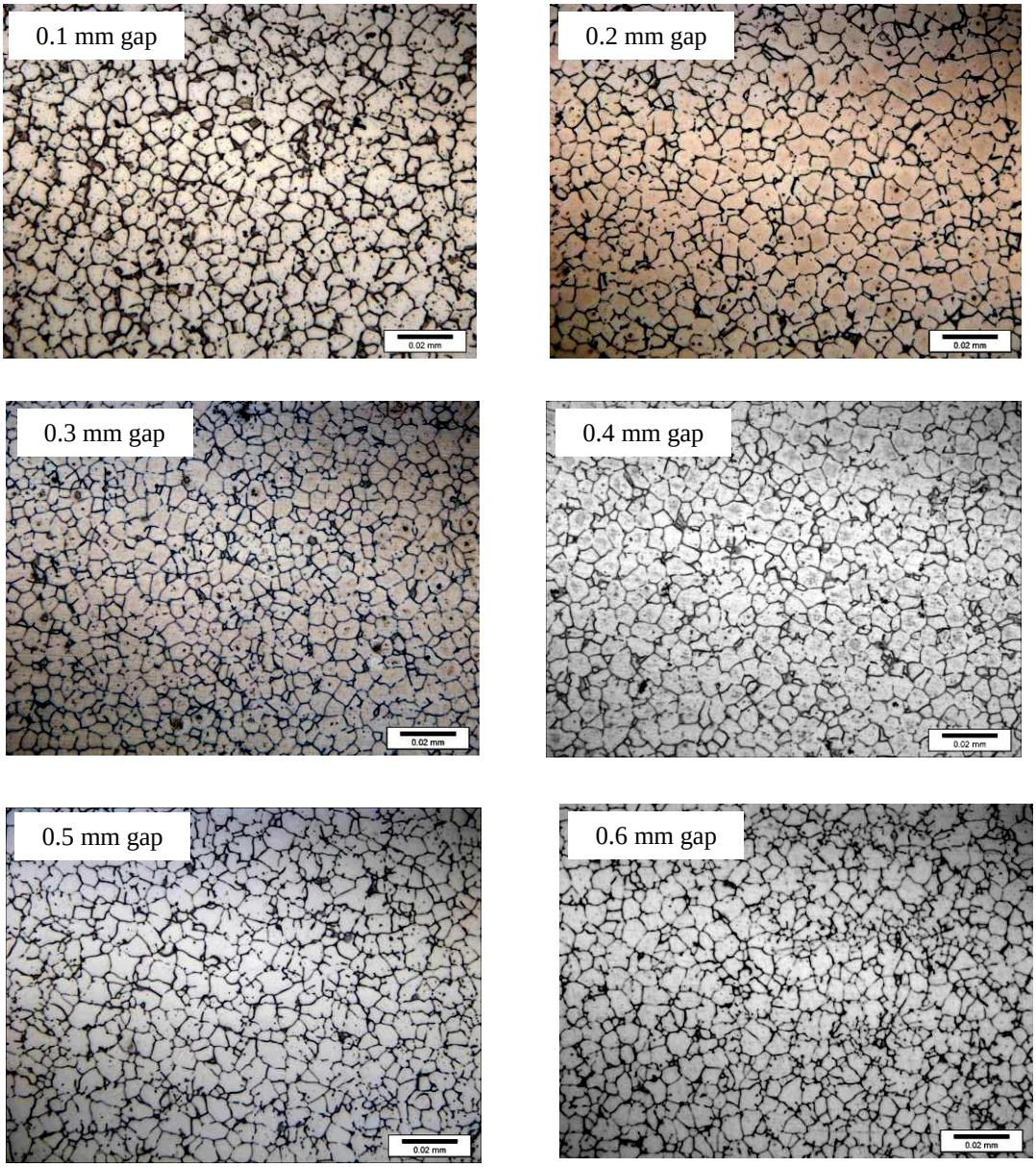

Figure 4.2.4 – Effect of gap size on the FZ microstructure

4.2.3 Porosity

The relationship of porosity area percentage and number of pores with the gap size is shown in Figures 4.2.5 and 4.2.6. The porosity area percentage decreased from 0.75% to 0.27% as the gap size increased from 0.1 to 0.4 mm, but almost remained constant above 0.4 mm. Gap size smaller than 0.3 mm may cause difficulties in mixing of the melted filler wire with the melted sides of the BM; which might have resulted in entrapment and expansion of large pores. Another possible reason is that using smaller gap size means an increase in the contribution of the BM to the FZ which may have pre-existing pores more than the filler wire. It was reported that FZ weld quality depends directly on the cast quality [35]. Figure 4.2.7 shows a large pore near the PMZ for the sample welded at small gap size. It was observed that the majority of pores were smaller than 75 µm, with typical size about 15 µm as shown in Figure 4.2.6.

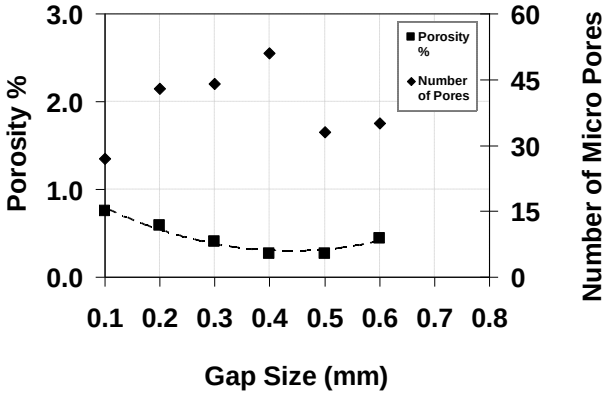

Figure 4.2.5 – Effect of gap size on Porosity.

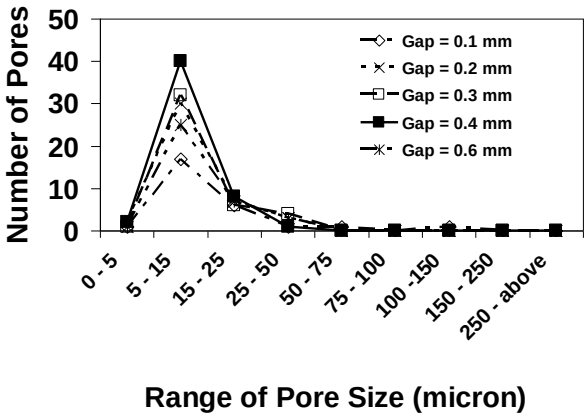

Figure 4.2.6 – Porosity distribution.

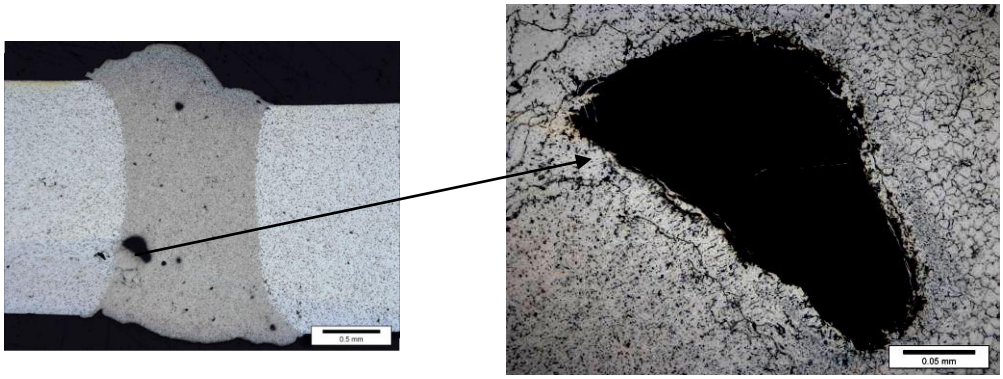

Figure 4.2.7 – Large porosity near the PMZ for the sample welded at 0.2 mm gap

4.2.4 Cracks

Weld cracks were observed in laser welded ZE41A-T5 alloy. In all samples the area of solidification cracks was less than 1 mm^2, thus these cracks are micro-cracks [30]. The maximum total crack length in the fusion zone was 1.41 mm (for the sample welded with 0.2 mm gap), and the maximum average width was 1.6 μm (for the sample welded with 0.5 mm gap). It was observed that the increase in the gap size slightly reduced the total crack length in the FZ as shown in Figure 4.2.8.

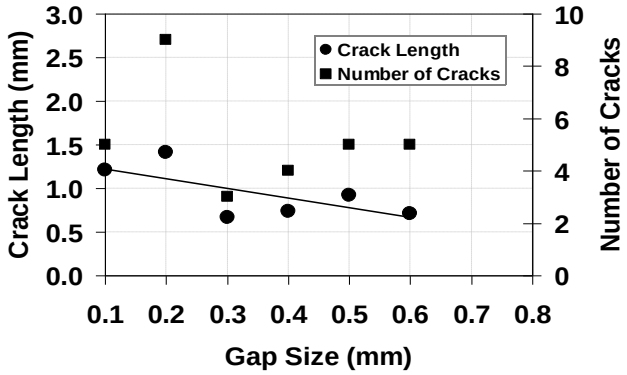

Figure 4.2.8 – Effect of Gap Size on Crack Length and Number of Solidification Cracks in the FZ.

Figures 4.2.9 – 4.2.14 show the microstructures for some of the specimens welded with various gap size. It was found that there are four major groups of cracks: (i) the first group that initiated from or around large pore (Figures 4.2.9-B, 4.2.10-A, 4.2.11-C and 4.2.14-C), (ii) second group cracks initiated from the casting defects in the BM and grew to reach the FZ (Figures 4.2.11-B, 4.2.14-B), (iii) third group cracks initiated from high stress zones at crown and root (Figures 4.2.10-B, 4.2.12-B), (iv) last group includes cracks initiated near the PMZ (Figures 4.2.9-A, 4.2.10-A, 4.2.12-A, 4.2.13-A,B,C,D,E). Therefore the solidification cracks in these groups were mainly initialed due to irregular weld geometry, pores and BM defects since the laser heat input were constant [36]. At 0.3 and 0.4 mm gap size the crack length was reduced significantly since they had less porosity and defects in the crown and root areas.

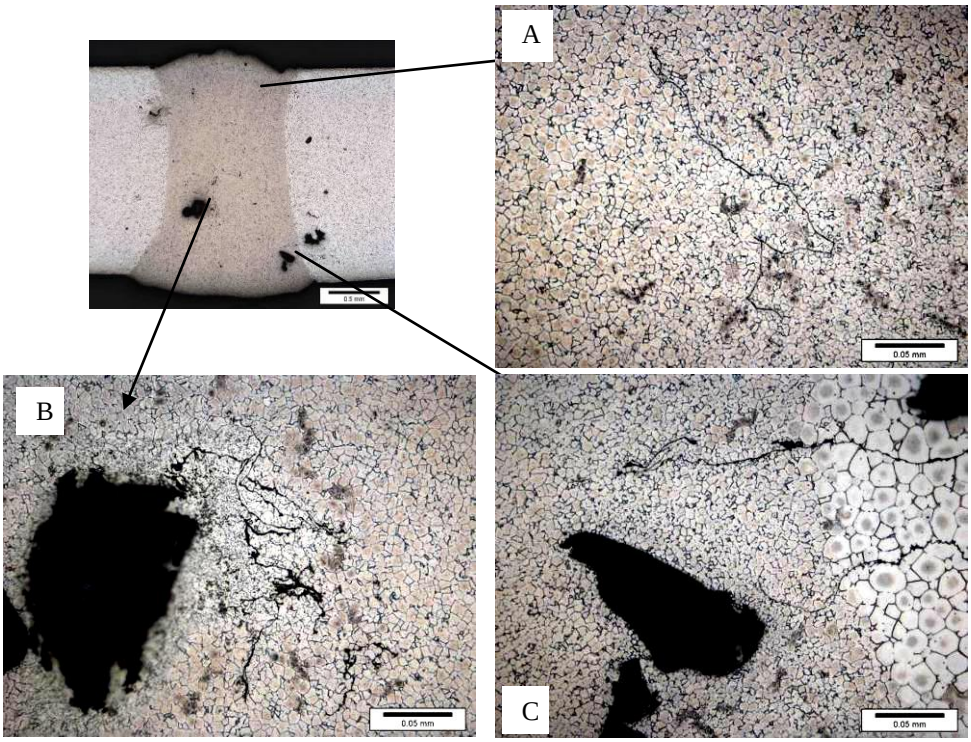

Figure 4.2.9 – Solidification Cracks in The Sample Welded at 0.1 mm gap – Middle Section

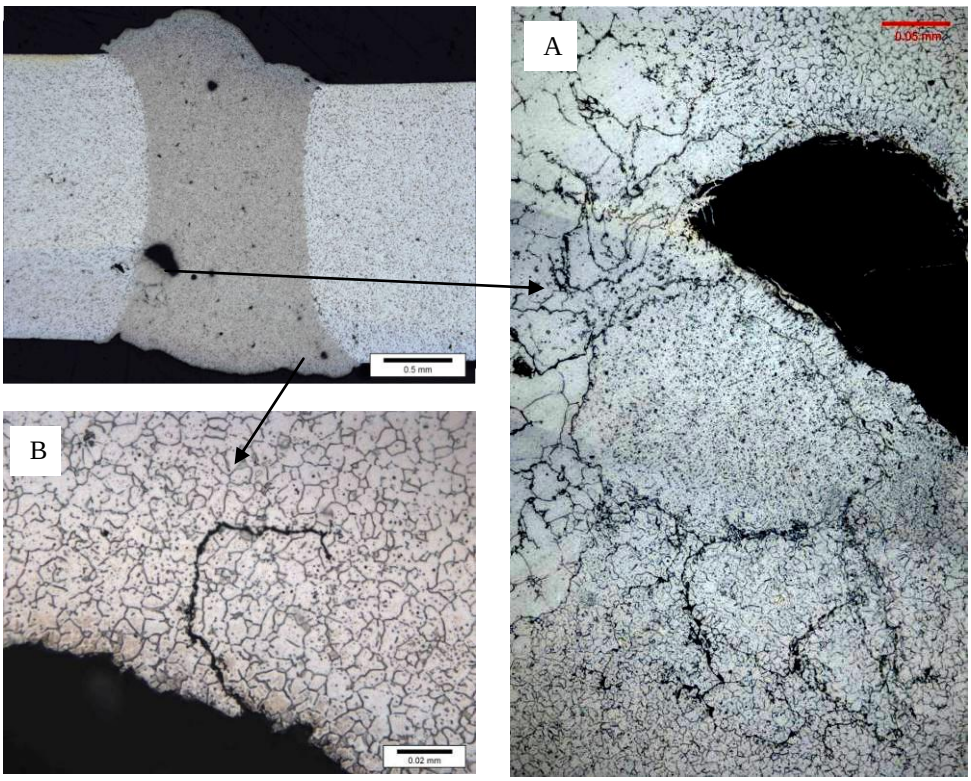

Figure 4.2.10 – Solidification Cracks in The Sample Welded at 0.2 mm gap – Middle Section

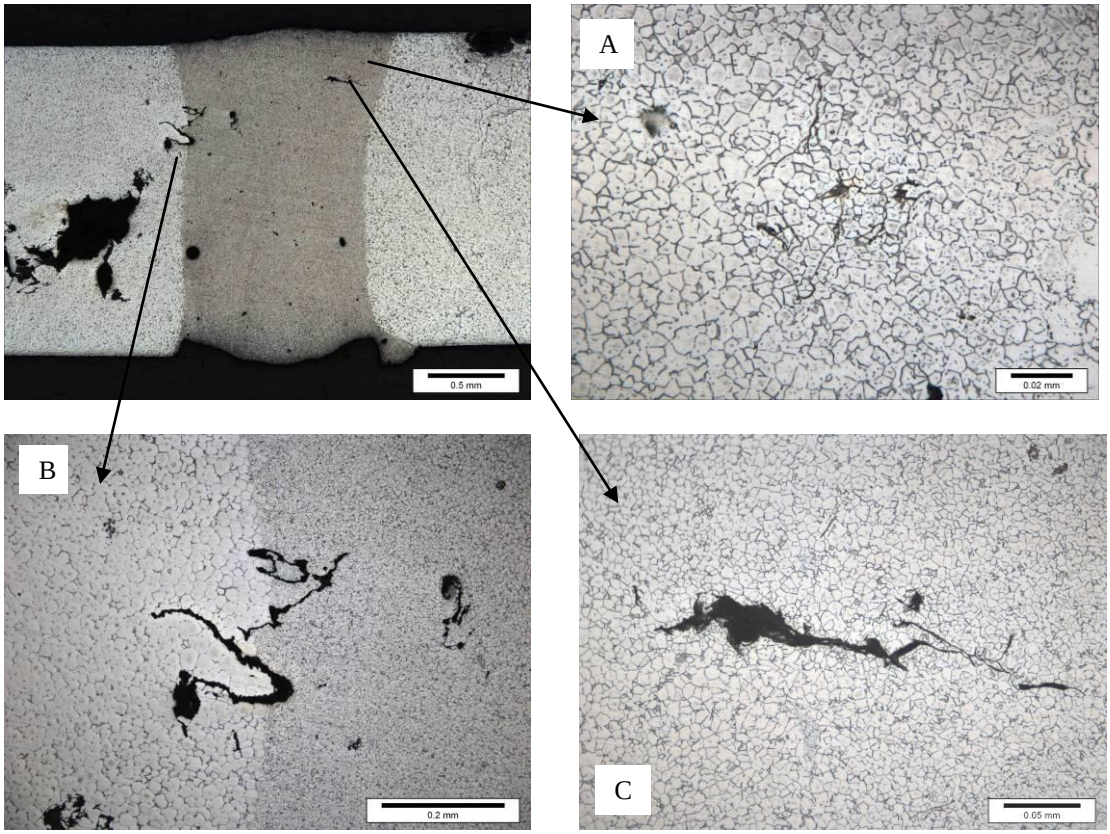

Figure 4.2.11 – Solidification Cracks in the Sample Welded at 0.3 mm gap – End Section

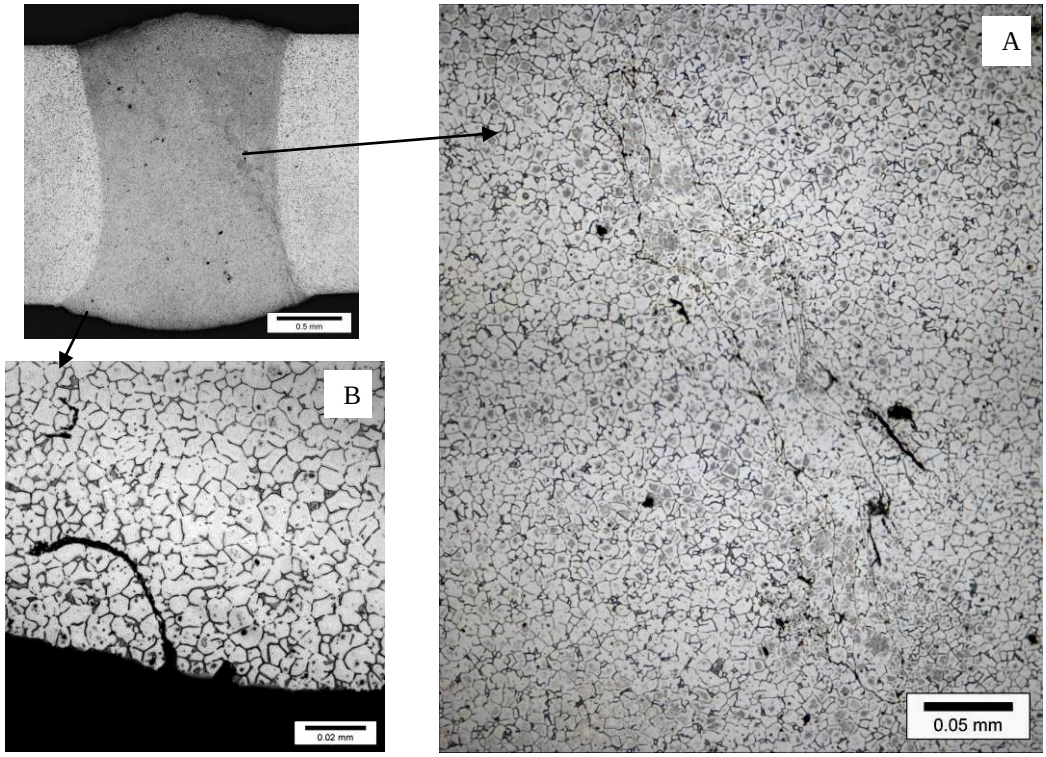

Figure 4.2.12 – Solidification Cracks in the Sample Welded at 0.4 mm gap – End Section

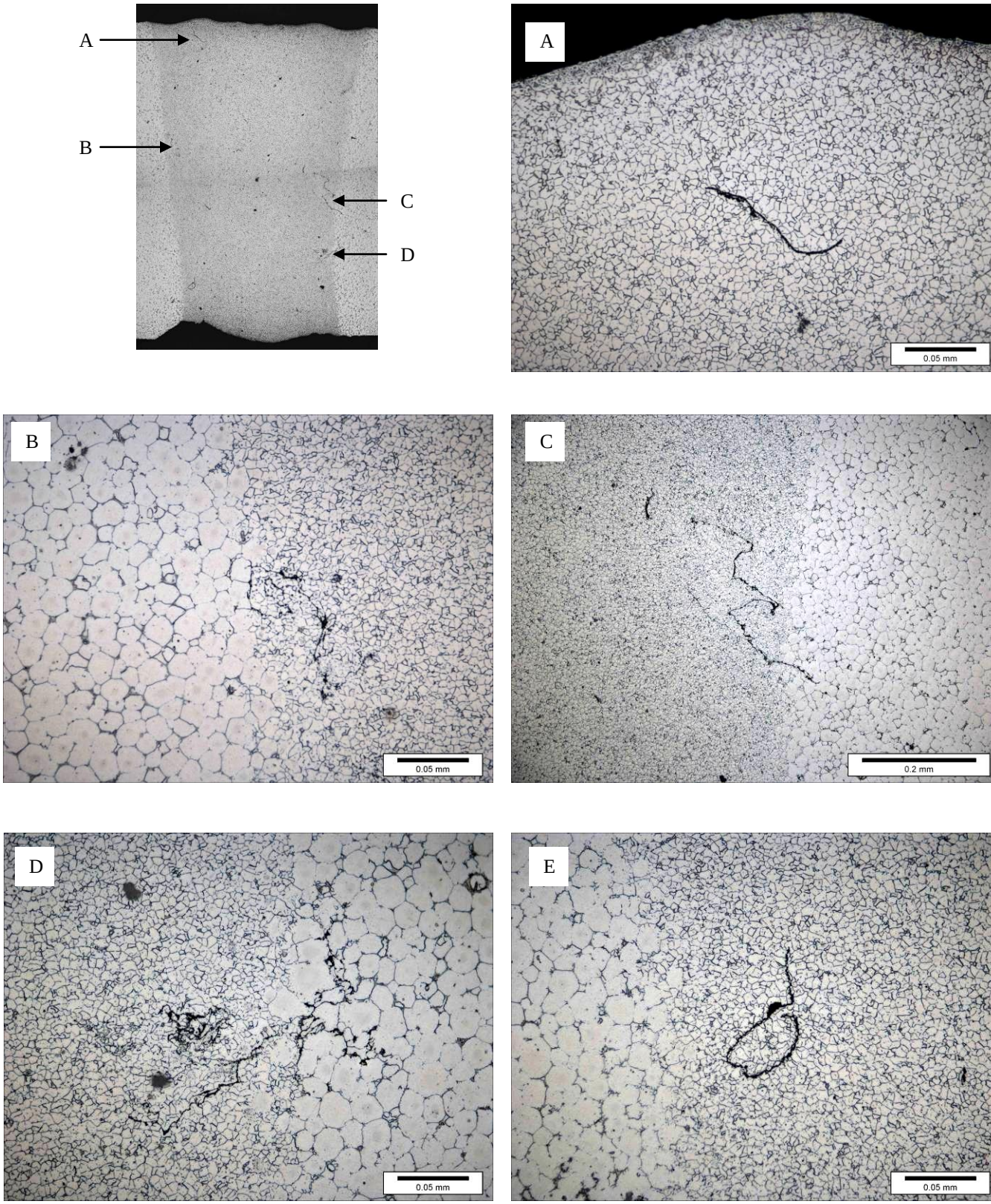

Figure 4.2.13 – Solidification Cracks in the Sample Welded at 0.5 mm gap – Start Section

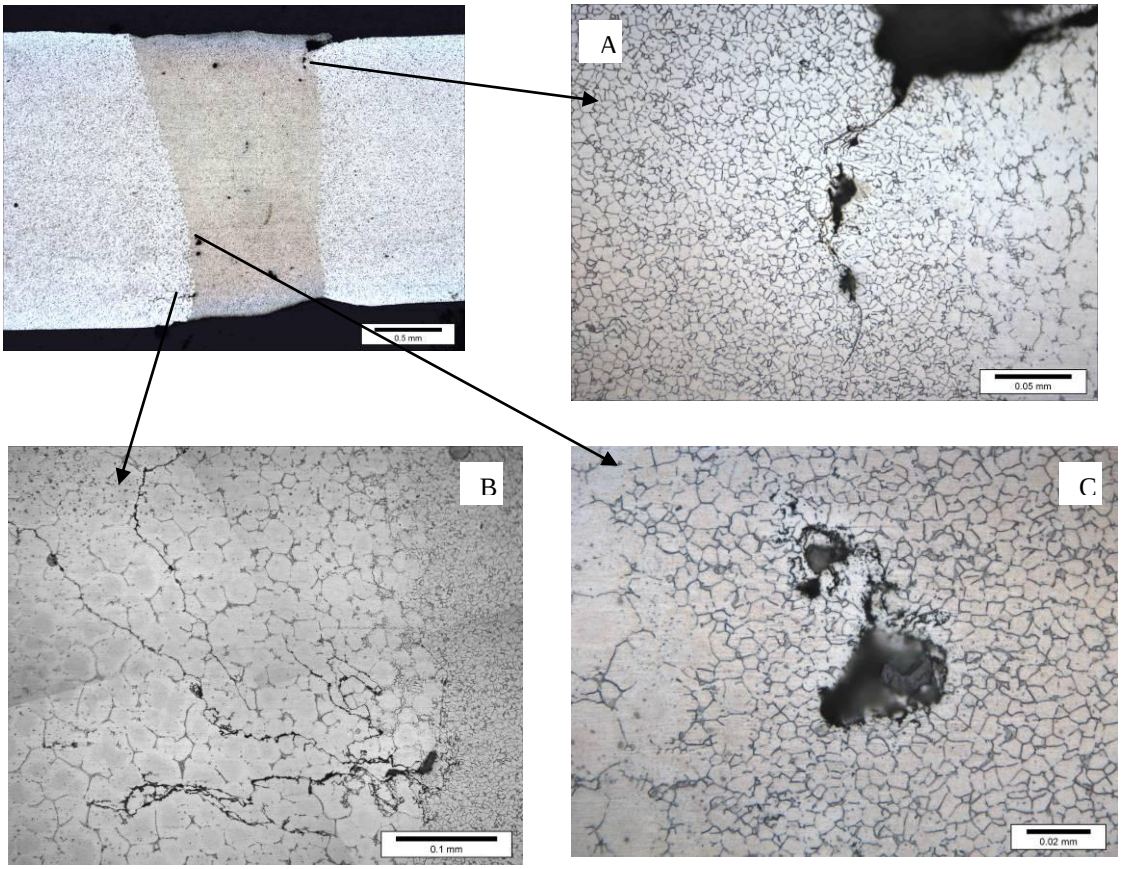

Figure 4.2.14 – Solidification Cracks in the Sample Welded at 0.6 mm gap – End Section

4.2.5 Micro-Indentation Hardness

The hardness profiles for different gap sizes are shown in Figure 4.2.15. These samples were tested after a natural aging of 18 months, therefore the FZ hardness was recovered to the BM values [37] except the one welded with 0.6 mm gap which showed higher hardness at the FZ. There was no significant change in the FZ hardness due the variation in the gap sizes as shown in Table 4.2.2. The HAZ shows a decrease in the hardness by 3 to 5 HV compared with BM, with a typical width between 1.5 and 2 mm for all gap sizes.

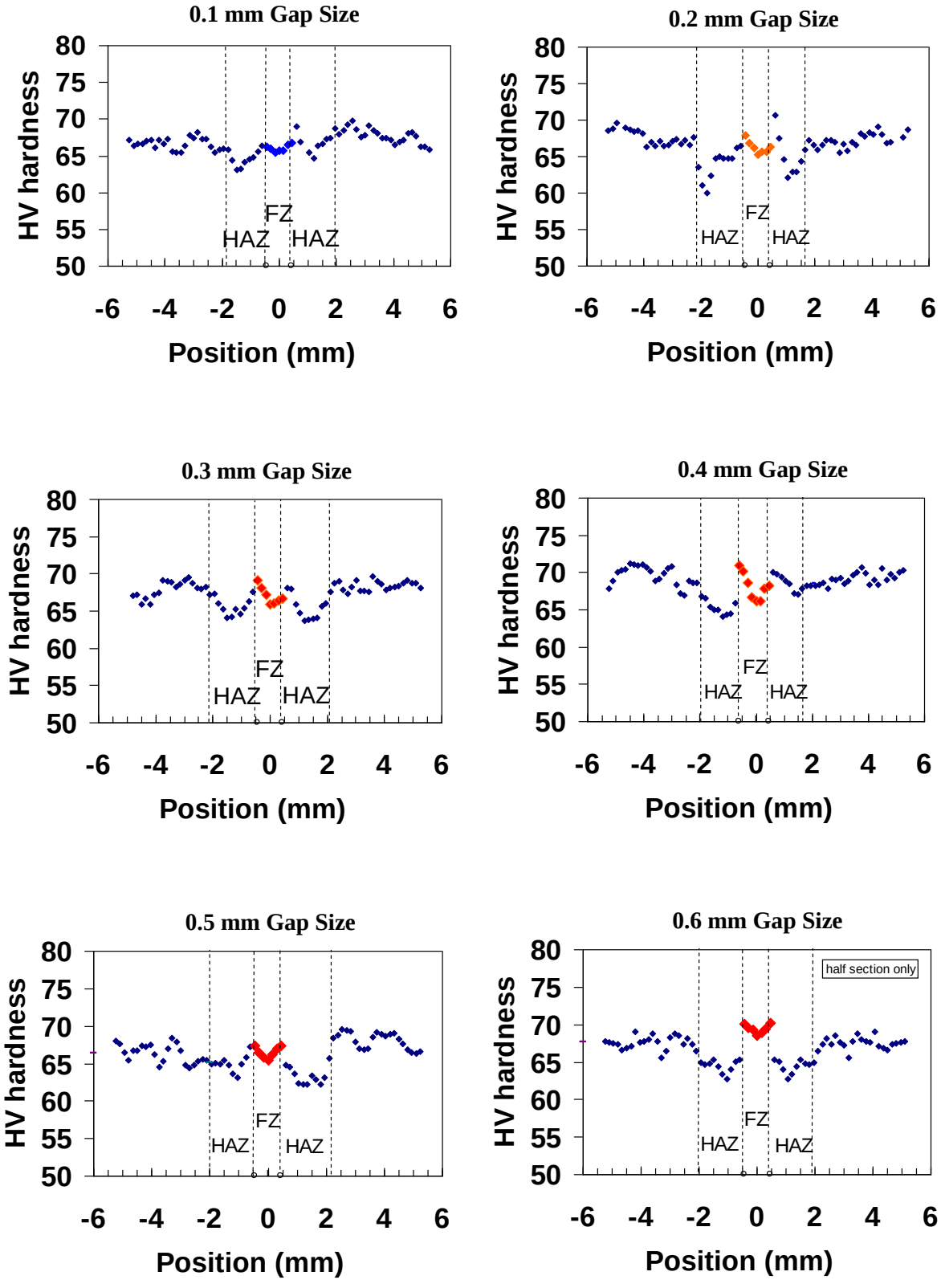

Figure 4.2.15 – Effect of Gap size on Hardness Profile

Gap Size	Average Hardness in the FZ
0.1	66.1
0.2	66.3
0.3	67.1
0.4	68.1
0.5	66.6
0.6	69.4

Table 4.2.2 – Effect of Gap Size on the Average Hardness Measured in the Center Line of the FZ

4.3 Effect of laser power on weldability of 2 mm plates

The plates were laser welded using a welding speed of 6 m/min (section 4.1), 0.4 mm gap size (section 4.2), surface defocusing and with varying laser power as shown in Table 4.3.1.

Sample #	Gap Size mm	Laser Power kW	Welding Speed m/min	Wire feeding rate m/min	Defocusing mm
11	0.4	2.5	6	3	0
12	0.4	2.75	6	3	0
13	0.4	3	6	3	0
14	0.4	3.5	6	3	0
15	0.4	3.75	6	3	0
16	0.4	4	6	3	0

Table – 4.3.1 : Key experiments / effect of laser power on the weldability

4.3.1 Weld Geometry

The effect of laser power on joint width, height and weld area are shown in Figure 4.3.1 and 4.3.2. The FZ geometry changed from partial to full penetration also the keyhole changed from closed (blind) to open profile at root when the laser power increased from 2.5 to 4 kW. The sample welded at 2.5 kW showed a partial penetration FZ as a result of partial closed keyhole, and the width of the root was smaller than the top weld width. As the power increased to 2.75 kW, full penetrated joints were obtained but the keyhole was unstable because of the fluctuation between open (start and middle section) and close (end section) at the root. The increase in penetration depth in the sample welded at 2.75 kW caused the increase in the FZ area. At 3 kW laser power there was a drop in FZ area as a consequence of the change in the keyhole profile from closed to open mode. This change from closed to open keyhole caused to reduce the energy coupling efficiency

between the laser beam and Mg plate because of the increase in laser losses at the keyhole root and the reduction in the multiple reflections inside the keyhole. The hourglass FZ profile started to form at 3.5 kW but with underfill and shrinkage groove at the root. The increase in laser power to 3.5 kW caused an increase in the root width and as a consequence of that it caused an increase in the laser beam losses at the root which caused more decrease in the FZ area. For the samples welded at 3.75 and 4 kW, the FZ area increased proportionally with the increase in laser power since the heat gain was larger than the loss of laser power at the root. This variation in melting efficiency of laser welding process and the corresponding variation in weld geometry during the change from partial to full penetration passing through the transitional region from blind to open keyhole was also reported by Krasnoperov *et al.* [38]. Smooth profiles at the top and root, with uniform hourglass shapes were observed as the laser power was higher than 3.5 kW.

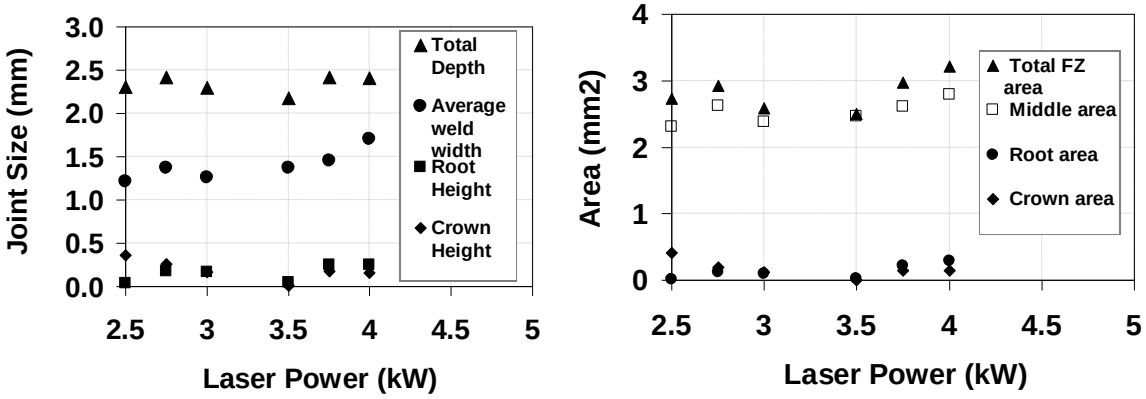

Figure 4.3.1 – Effect of Laser power on (a) joint size and (b) weld area.

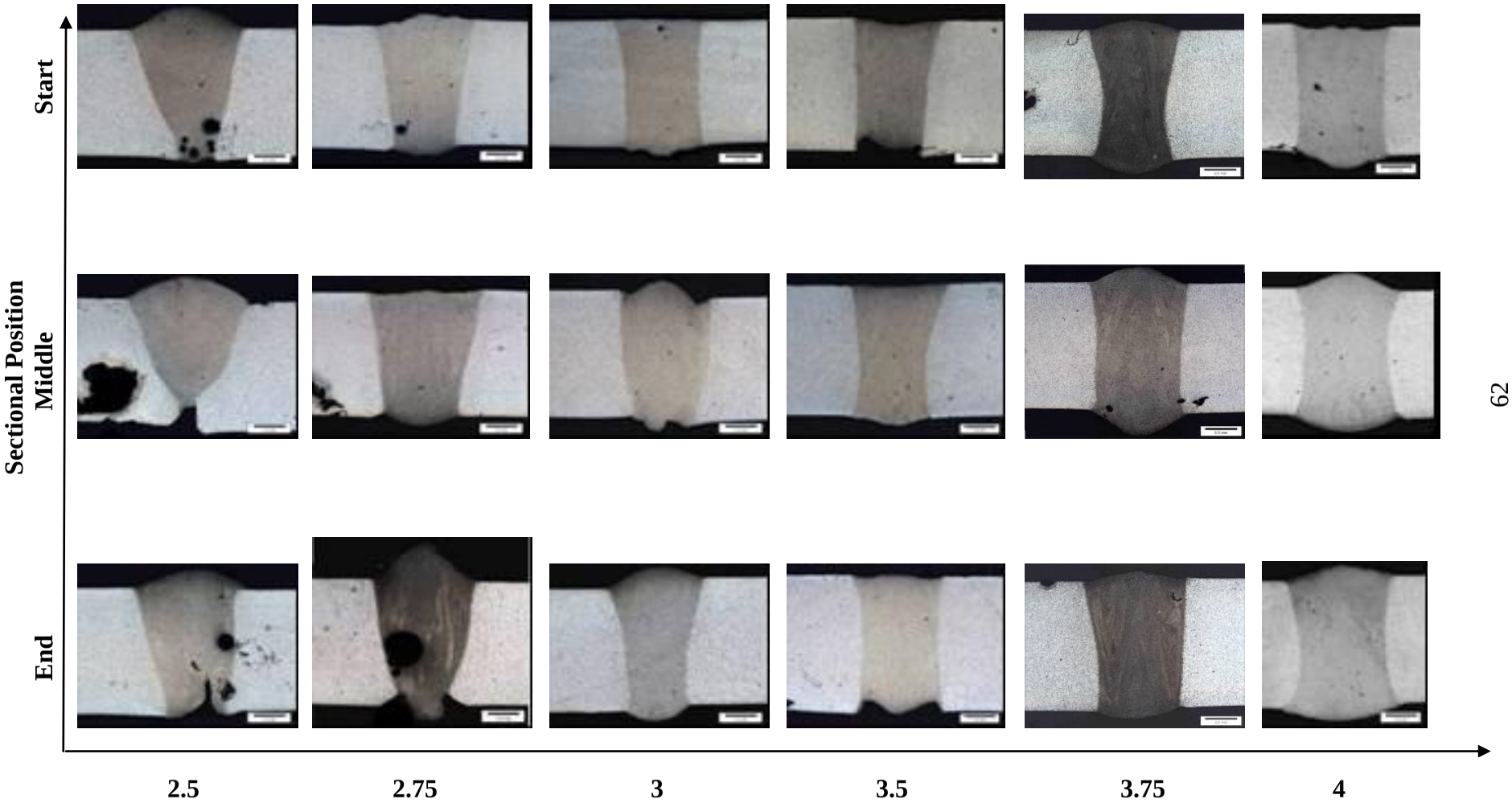

Figure 4.3.2 – Effect of Laser Power on Weld Geometry

4.3.2 Microstructure

The fusion zone microstructure was observed to be fine equiaxed grains as shown in Figures 4.3.3 and 4.3.4. The partial melting zone (PMZ) was narrow for all samples. It was difficult to distinguish the difference in microstructure between the HAZ and base metal because grain coarsening was not observed in the HAZ.

Figure 4.3.4 shows that the FZ grain size varies as a result varying the laser power. As discussed earlier, different laser power values result in different laser coupling efficiencies which, according to [39], affect the amount of heat available for the work piece. However, not all the absorbed heat by the keyhole will be available for melting since portion of the absorbed heat will be lost through the BM. In this case, the weld pool size will mainly depend on the process efficiency (melting efficiency); the higher the melting power the larger the weld pool will be. Due to this variation in coupling efficiency, the cooling rates were different in these samples. The sample which exhibited higher absorbed melting power or larger FZ area would have lower cooling rate due to the increase in the mass of the molten metal (larger weld pool). The lower cooling rate would have caused longer time for the grains to grow. This behavior can be seen in Figure 4.3.4, the grain size increased as the laser power increased from 2.5 to 2.75 kW because of the increase in laser coupling efficiency and melting efficiency, whereas the sample welded at 3.5 kW showed a decrease in the grain size although there was an increase in laser heat input. This is attributed to the decrease in the coupling and the corresponding melting efficiencies due to laser beam losses at the root and to the reduction in the multiple reflections of the laser beam inside the keyhole.

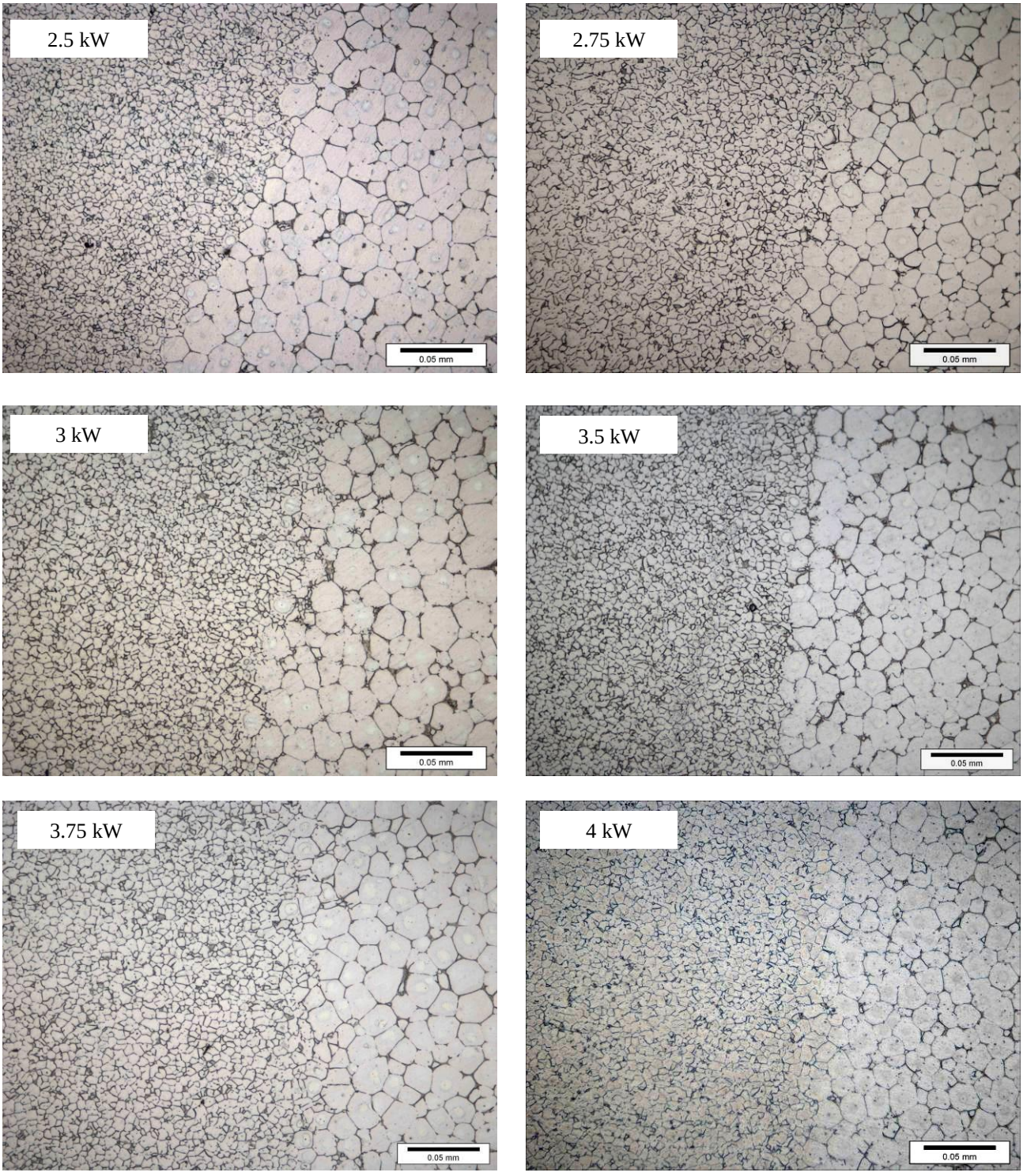

Figure 4.3.3 – Micrographs Showing the FZ, PMZ and HAZ.

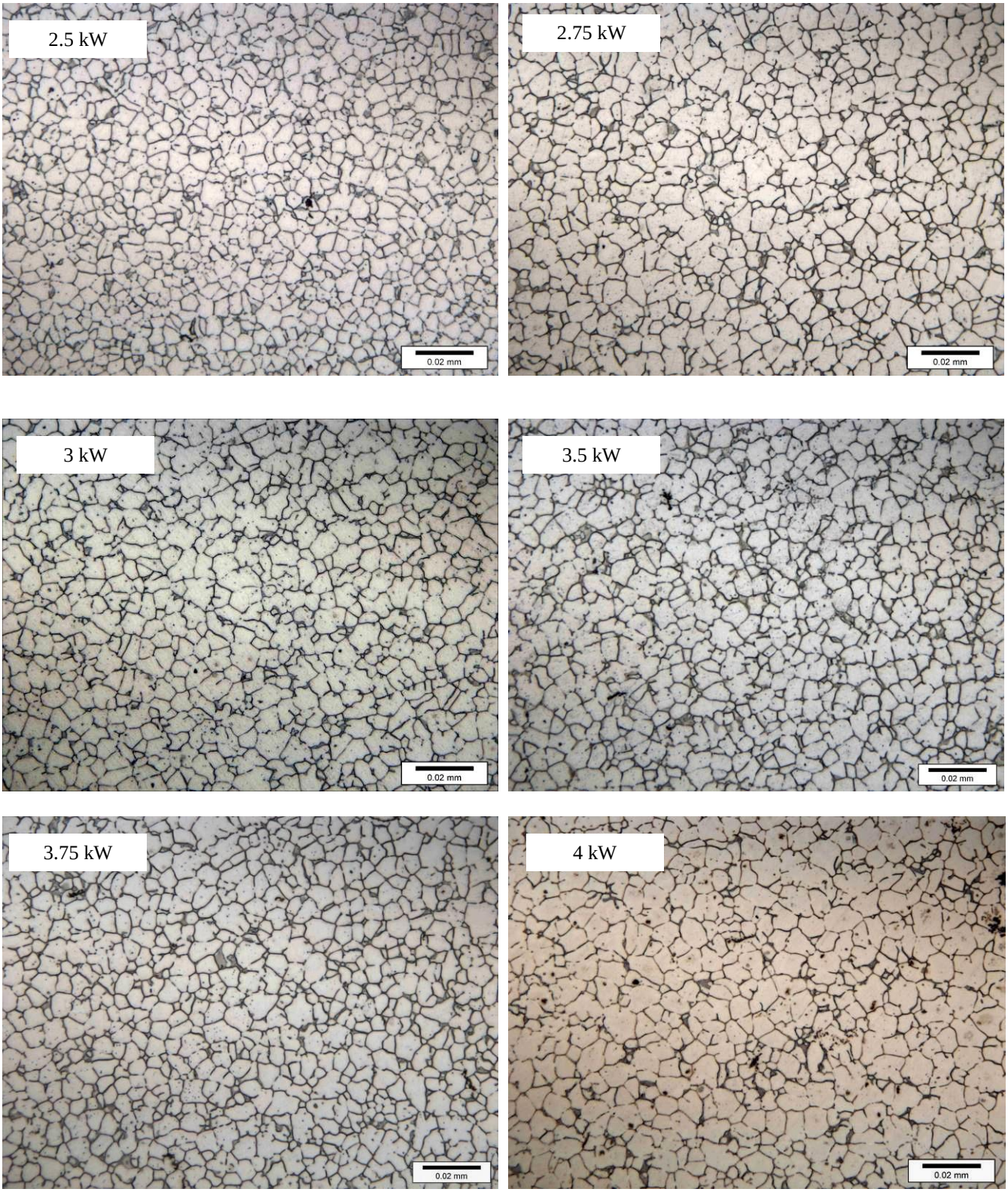

Figure 4.3.4 – Effect of laser power on the FZ microstructure

4.3.3 Porosity

The relationship between porosity area percentage and number of pores with the laser power is shown in Figure 4.3.5. The porosity area percentage decreased from 3.4% to 0.27% as laser power reached 3 kW. Large pores were observed in the samples welded at 2.5 and 2.75 kW as shown in Figure 4.3.2. As described earlier these two samples had a fluctuation between full and partial penetration as a consequence of low laser power density. When close keyhole mode occurs, the vapor had only one way to escape from the FZ which was the top keyhole opening [38], and because of that the expanded pores had to travel all the way to the top. The high welding speed caused an entrapment of the pores during this floating time. When the power reached to 3 kW, the keyhole became open at the root which resulted in having another escaping way for the vapor, and that significantly reduced the porosity. Figures 4.3.6 shows the average pores size distribution for all samples. It can be seen that the majority of pores were smaller than 75 µm, with typical size about 15 µm.

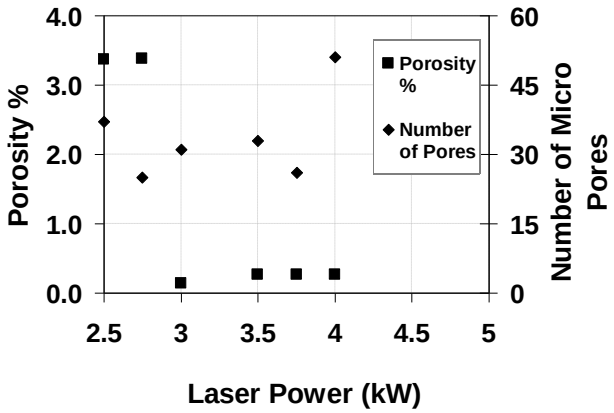

Figure 4.3.5 – Effect of power on Porosity.

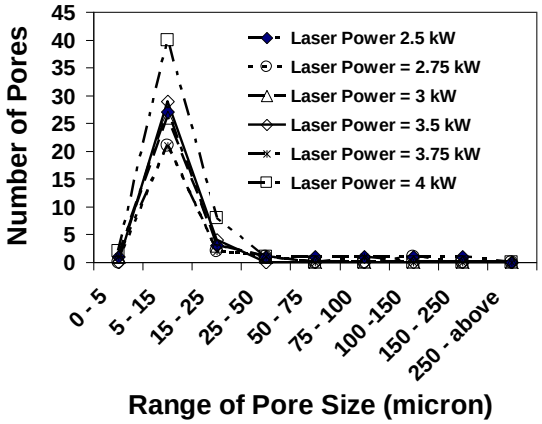

Figure 4.3.6 – Porosity Distribution

4.2.4 Crack Formation

The maximum total crack length in the fusion zone was 2.17 mm (for the sample welded at 3.75 kW power), and the maximum average width was 1.4 µm (for the sample welded at 2.5 kW). The minimum solidification crack was observed for the sample welded at 4 kW as shown in Figure 4.3.7. In general, the solidification cracks can be reduced by applying less heat input as observed earlier when discussing the effect of welding speed. It is known that, the laser heat input or laser fluence can be reduced either by increasing the welding speed or decreasing the laser power. The general observation from Figure 4.3.7 is that the crack length increased by increasing the laser power and the peak crack length was reached at laser power equal to 3.75 kW. Laser fluence of 89 J/mm^2 seems to be suitable to weld the 2 mm plate at 6 m/min which produced the minimum crack length. Abbaschian and Lima [36] reported that cracking susceptibility of Al alloys was mainly affected by the welding speed; the higher the welding speed the lower susceptibility for cracking. Whereas the effect of laser power showed different behavior than the welding speed; at low welding speed, the decrease in laser power led to decrease in cracking susceptibility, but at high welding speed the laser power showed opposite behavior. The crack defects for selective samples are shown in Figures 4.3.8 to 4.3.13. It is noticed in Figure 4.3.8 (B and D) that the microstructure around the crack was different than the regular grain morphology in the FZ.

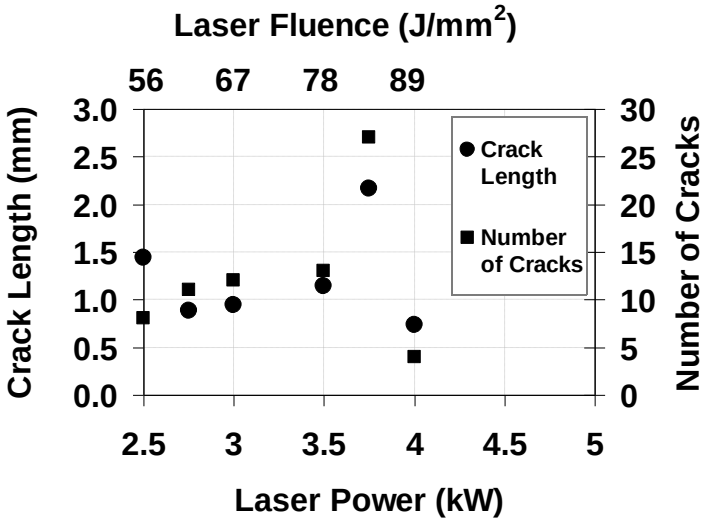

Figure 4.3.7 – Effect of Laser Power on Crack Length and Number of Solidification Cracks in the FZ.

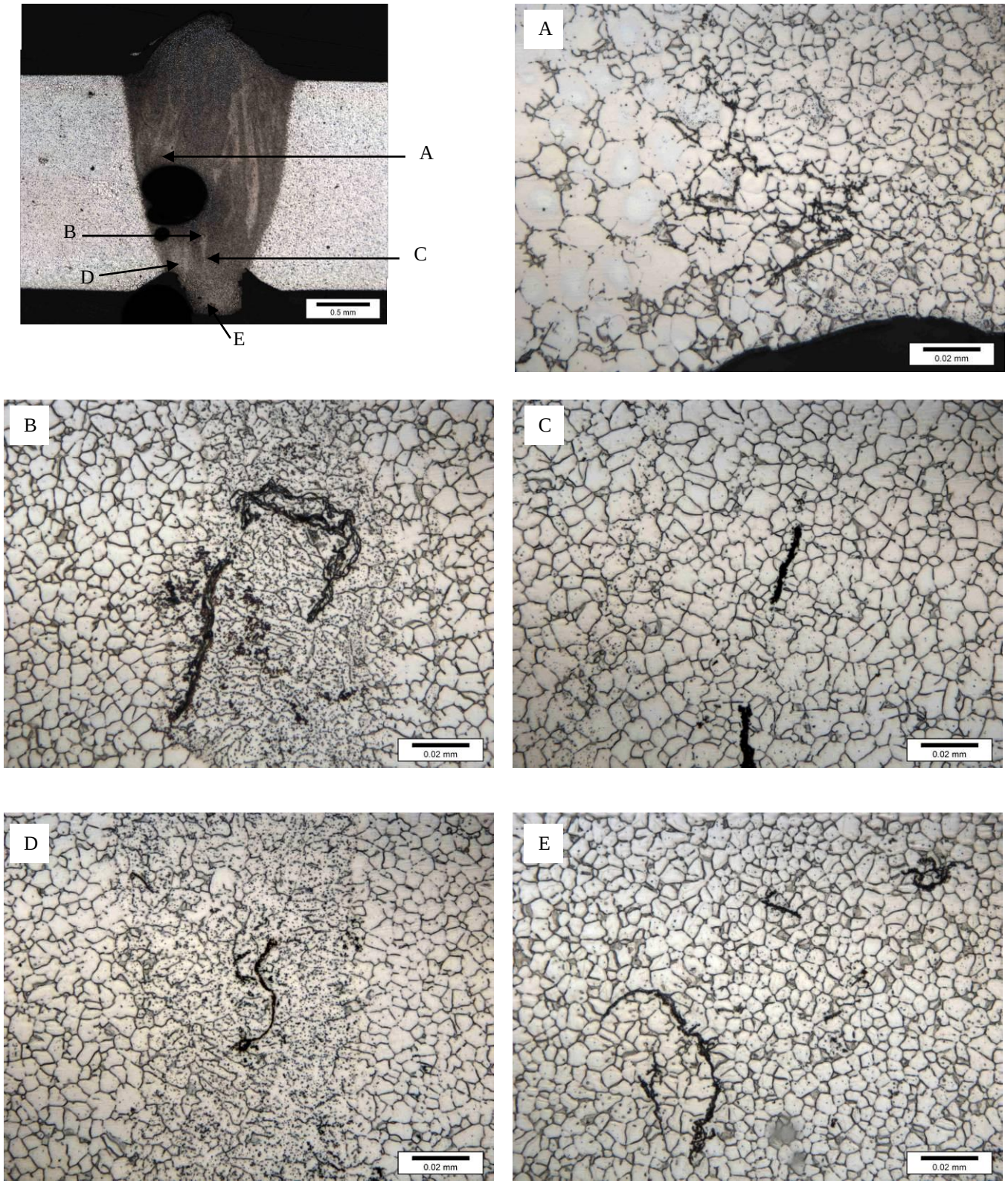

Figure 4.3.8 – Solidification Cracks in The Sample Welded at 2.75 kW – Ending Section

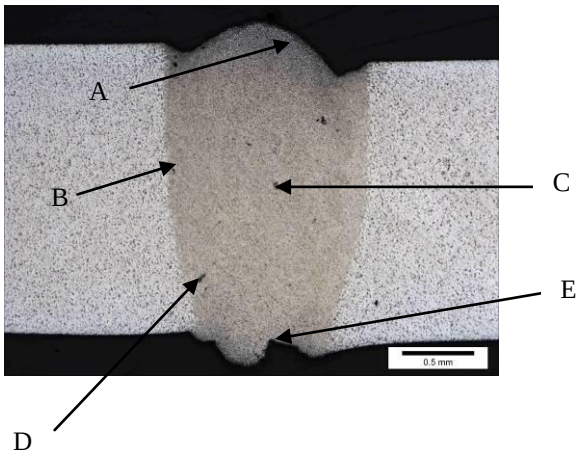

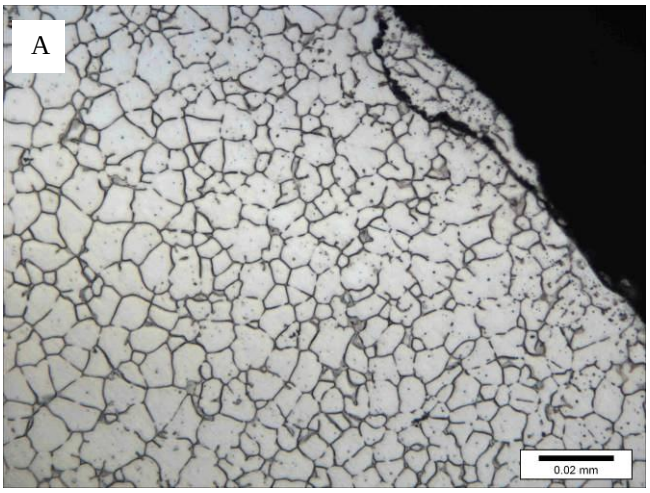

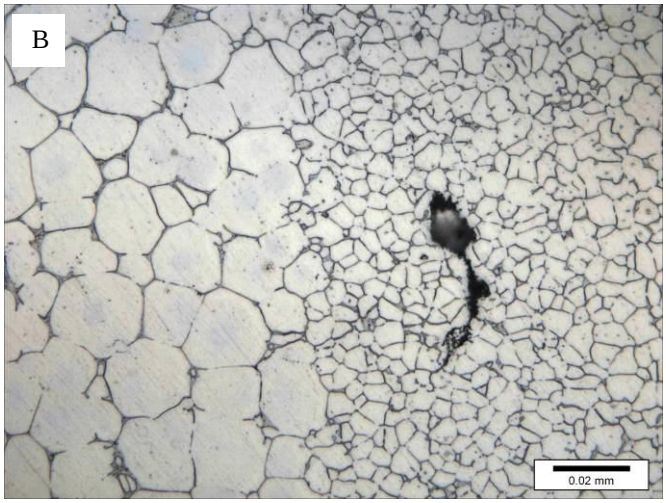

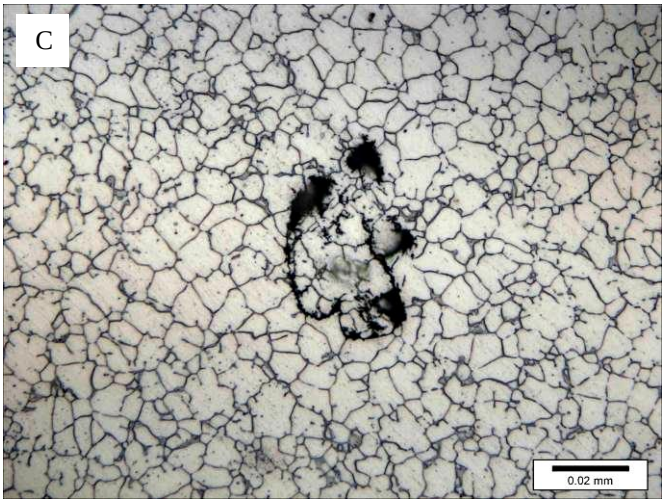

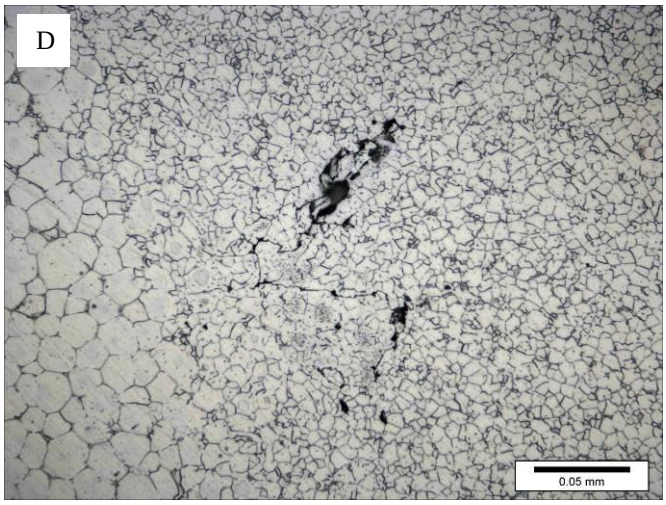

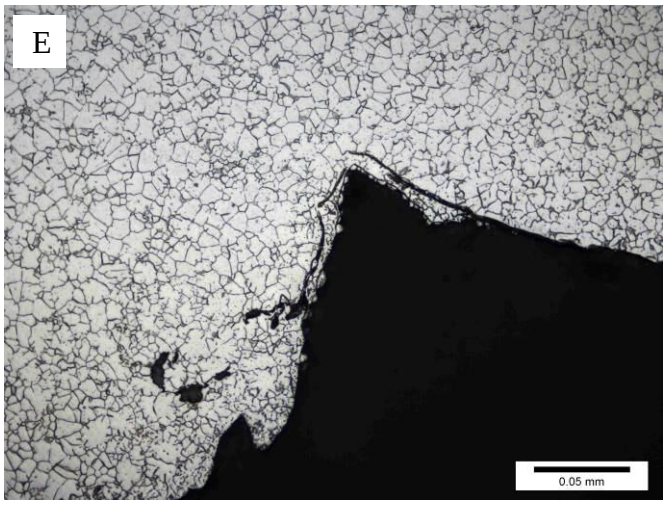

Figure 4.3.9 – Solidification Cracks in the Sample Welded at 3 kW – Middle Section

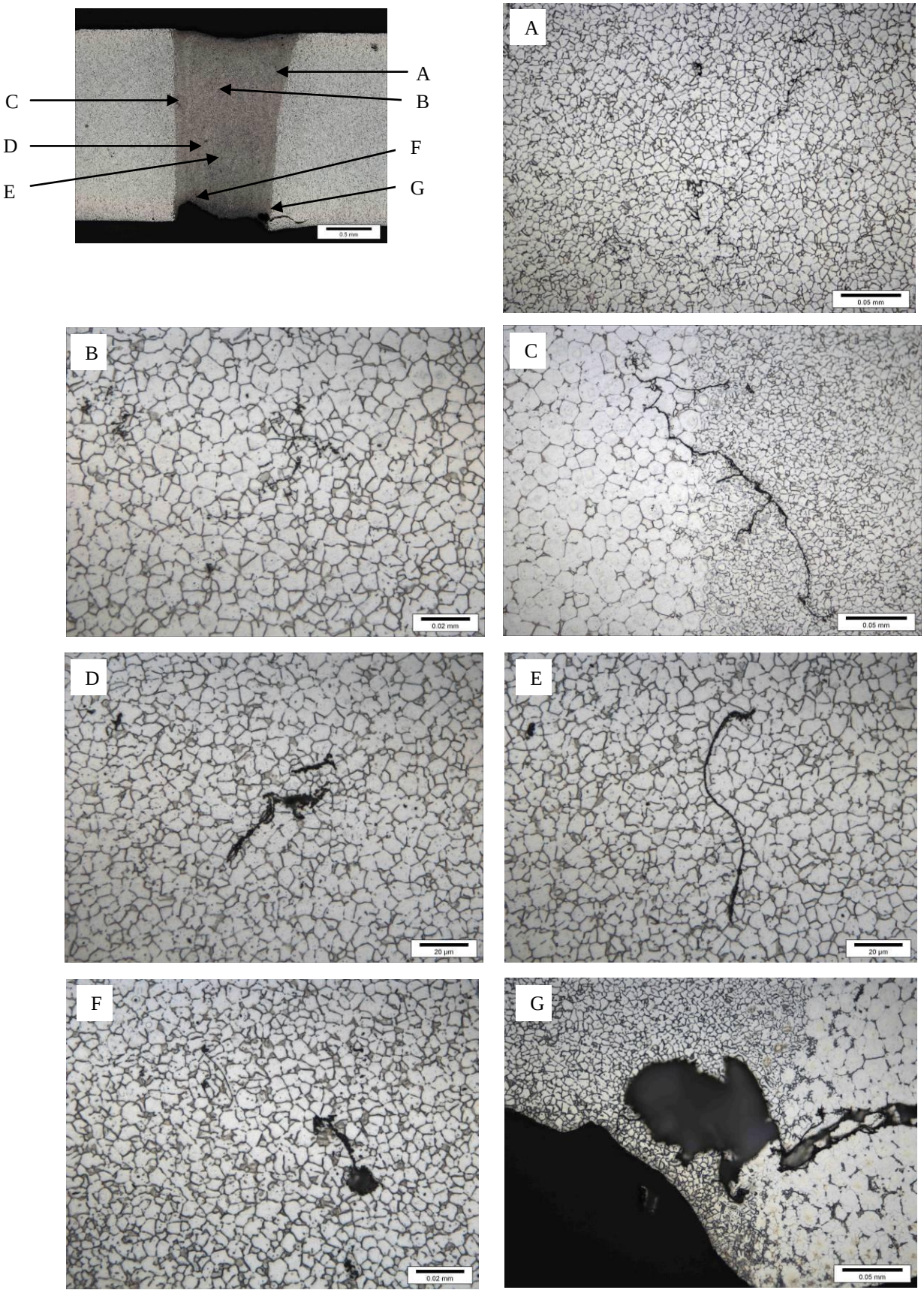

Figure 4.3.10 – Solidification Cracks in the Sample Welded at 3.5 kW – Start Section

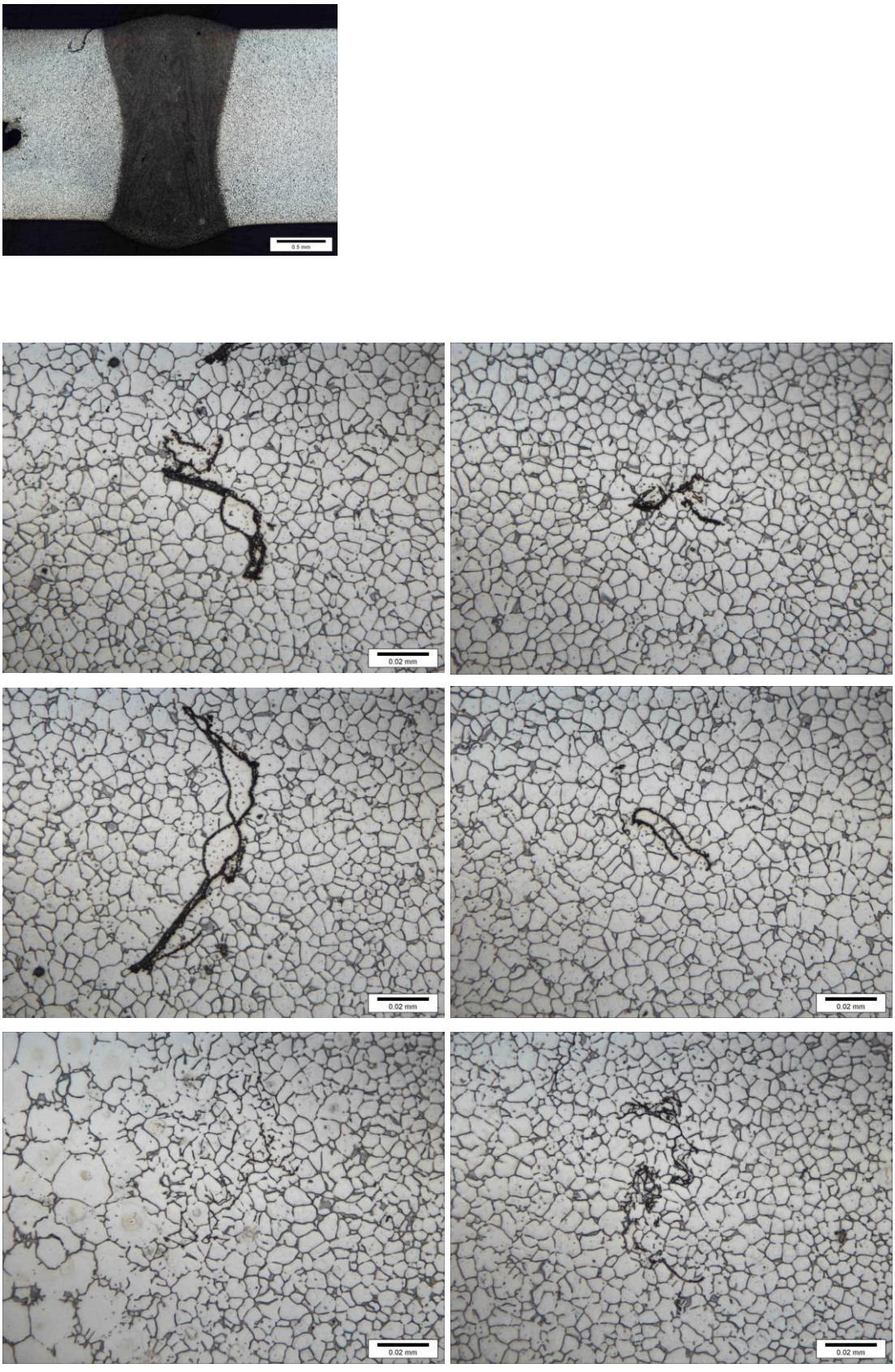

Figure 4.3.11 – Solidification Cracks in the Sample Welded at 3.75 kW – Start Section / Part -1

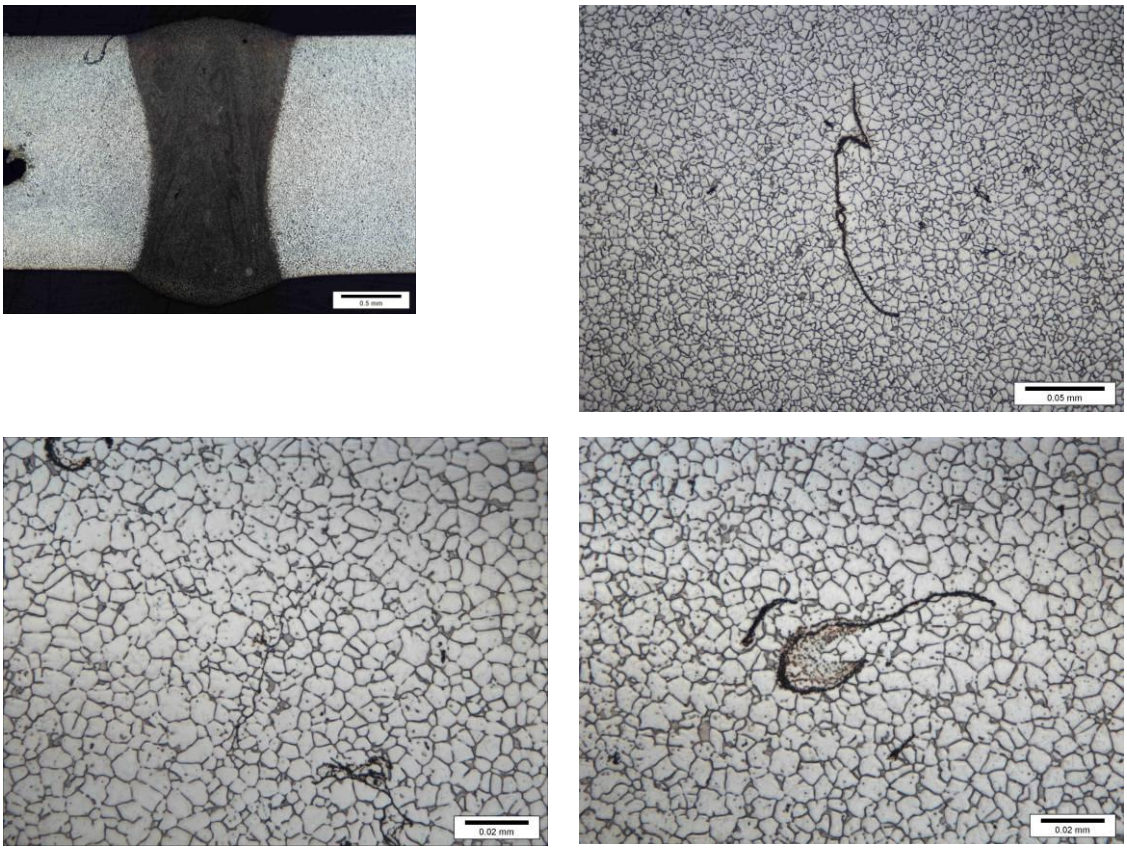

Figure 4.3.12 – Solidification Cracks in the Sample Welded at 3.75 kW – Start Section / Part -2

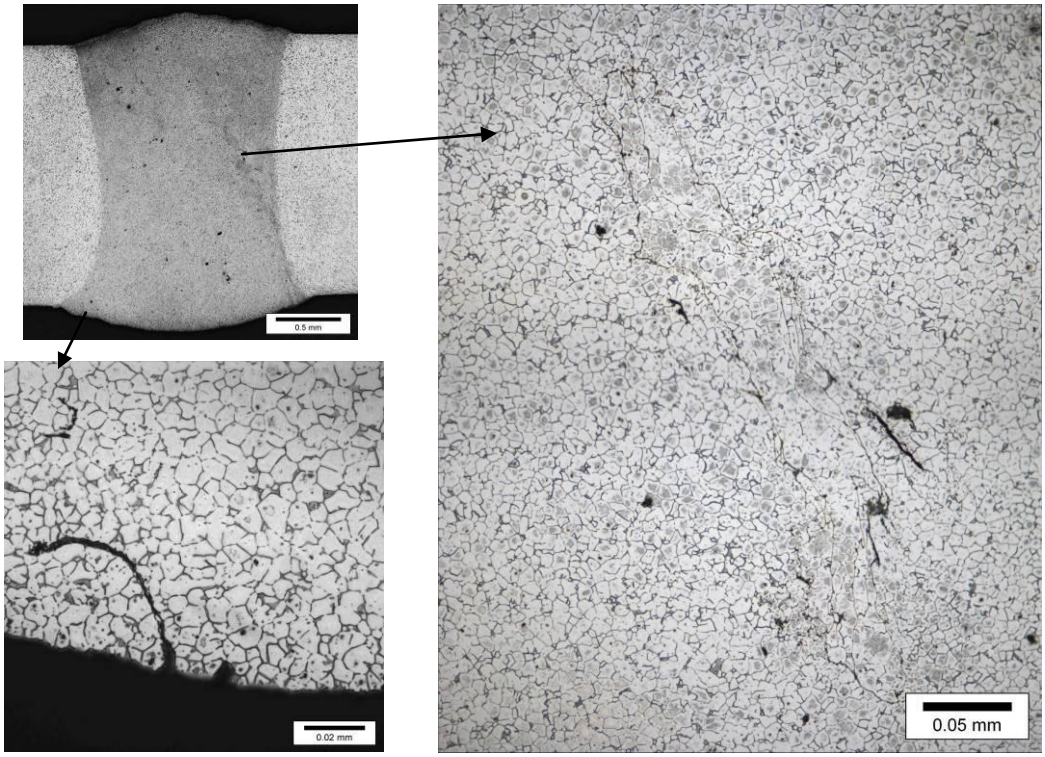

Figure 4.3.13 – Solidification Cracks in the Sample Welded at 4 kW – Ending Section

4.3.5 Micro-Indentation Hardness

Figure 4.3.14 shows the effect of laser power on hardness profile for the welded joints. Vickers microindentation hardness was measured after a natural aging over a period of approximately 18 months after the welding. Most of the samples showed a recovery in the hardness values in the fusion zone which became comparable with those in the base metal. However, there was a drop in the hardness in the heat affected zone. The width of the heat affected zone as indicated in Figure 4.3.14 was between 1.5 and 2 mm. As the laser power increased from 2.5 to 4 kW the average hardness value in the FZ fluctuated within 6 HV as indicated in Table 4.3.2 and Figure 4.3.15. The purpose of showing the middle FZ area in Figure 4.3.15 is to locate the transition zone between blind to open keyhole and also to give an indication of the weld pool size. The hardness decreased as the profile of the keyhole was changing from blind to open keyhole, whereas the hardness increased as the keyhole became open at the root. The hardness variation depends on the variation in the grain size which is function of the cooling rate inside the weld pool as discussed in section 4.3.2.

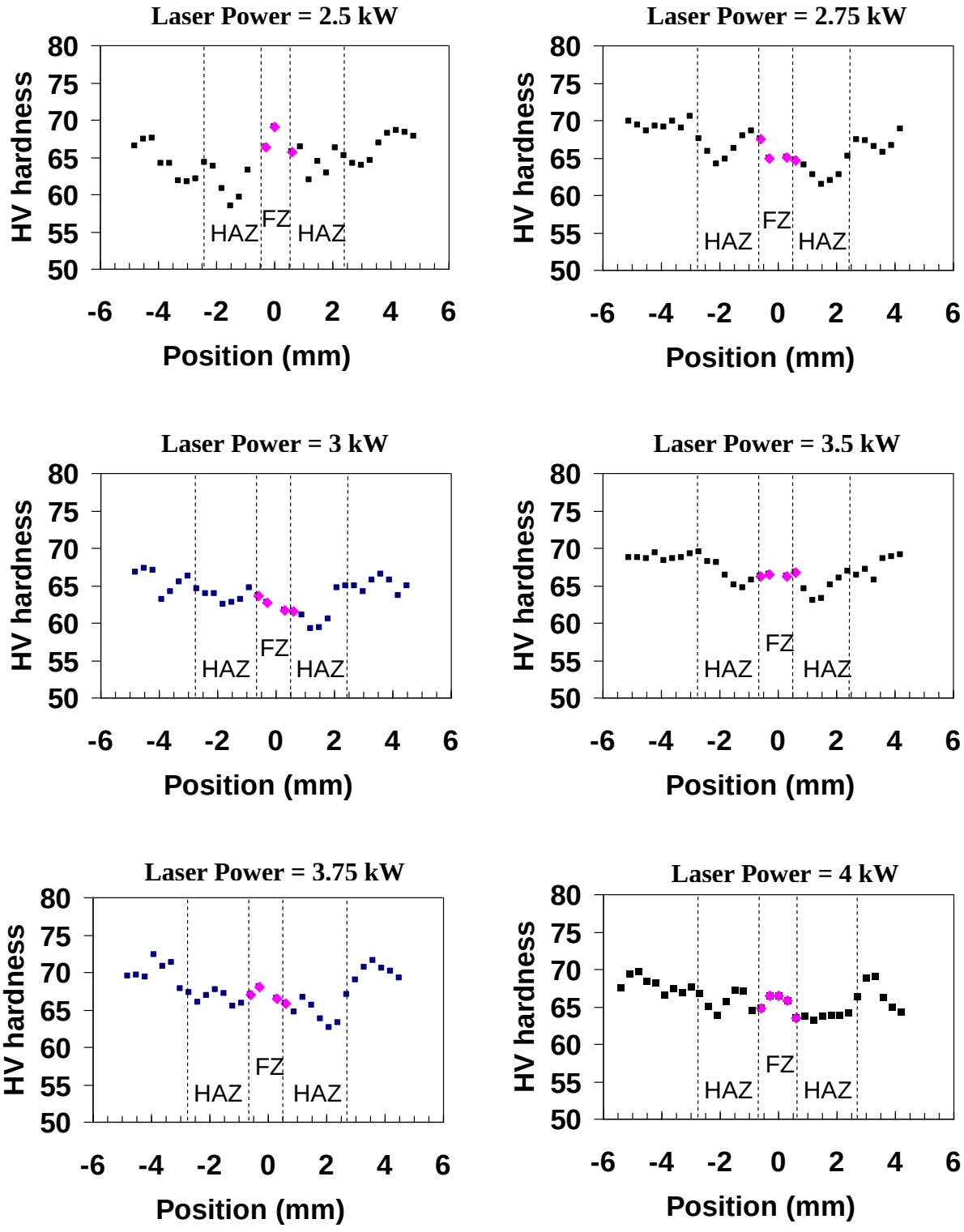

Figure 4.3.14 – Effect of Laser Power on Hardness Profile

Table 4.3.2 – Effect of Laser Power on the Average Hardness Measured on the Center Line of the FZ

Laser Power (kW)	Average Hardness in the FZ
2.5	67.1
2.75	65.5
3	62.4
3.5	66.5
3.75	66.8
4	68.2

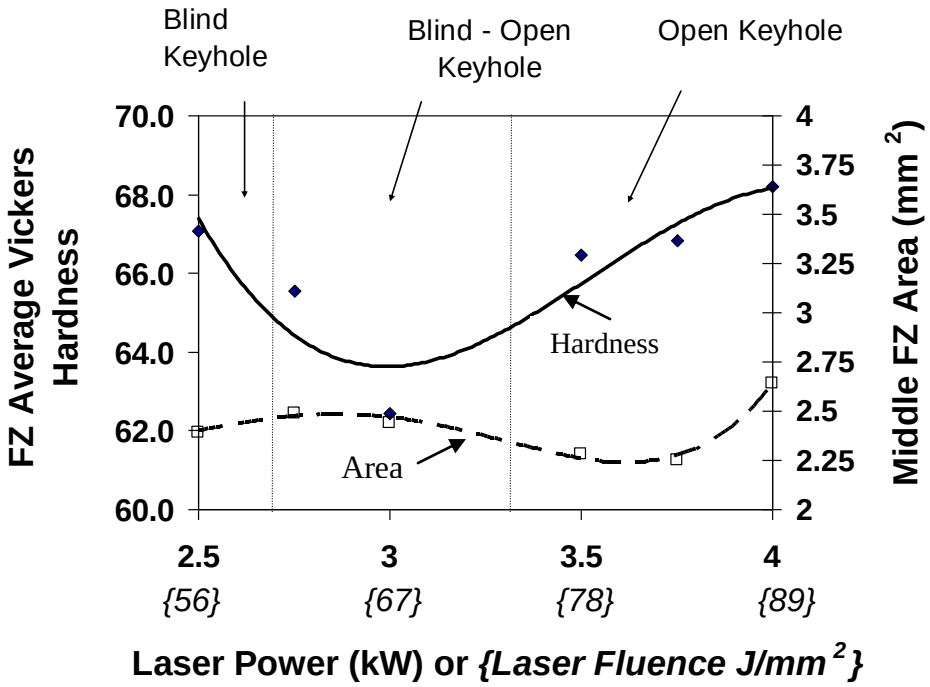

Figure 4.3.15 – Effect of Laser Power on the Average Hardness Measured on the Center Line of the FZ

4.4 Repeatability of Laser Welding Process

From the previous sections (4.1, 4.2, and 4.3), it was found that the laser parameters that produced sound welds for the 2 mm ZE41A-T5 butt joints using EZ33A-T5 filler wire are as follows:

1. Laser Power = 4 kW
2. Welding Speed = 6 m/min
3. Gap Size = 0.4 mm
4. Defocusing = 0 mm

These optimized parameters were used to check the repeatability of laser welding process using the same alloy and filler wire but with better BM quality that has less casting defects in comparison with the BM plates used for samples 1 to 16. The use of better quality BM reduces the influence of BM defects on the quality of welded joints.

4.4.1 Weld Geometry

Eight 2 mm plates were welded using the optimized process parameters, and the three cross sectional specimens (start, middle and end) for each joint are shown in Figure 4.4.1. Most of the samples showed smooth profile on the top and root. Little porosity was observed for all the samples. However, misalignments defects occurred in some joints such as sample 22 and 23. Sag (drop through) defects were observed in joints 17 and 18 due to the inaccurate feed rate which was calculated based on the nominal filler diameter. Actual filler diameter was measured to recalculate the wire feed rate which led to reduced or eliminated sag defects for the rest of the samples. In this aspect, butt joint

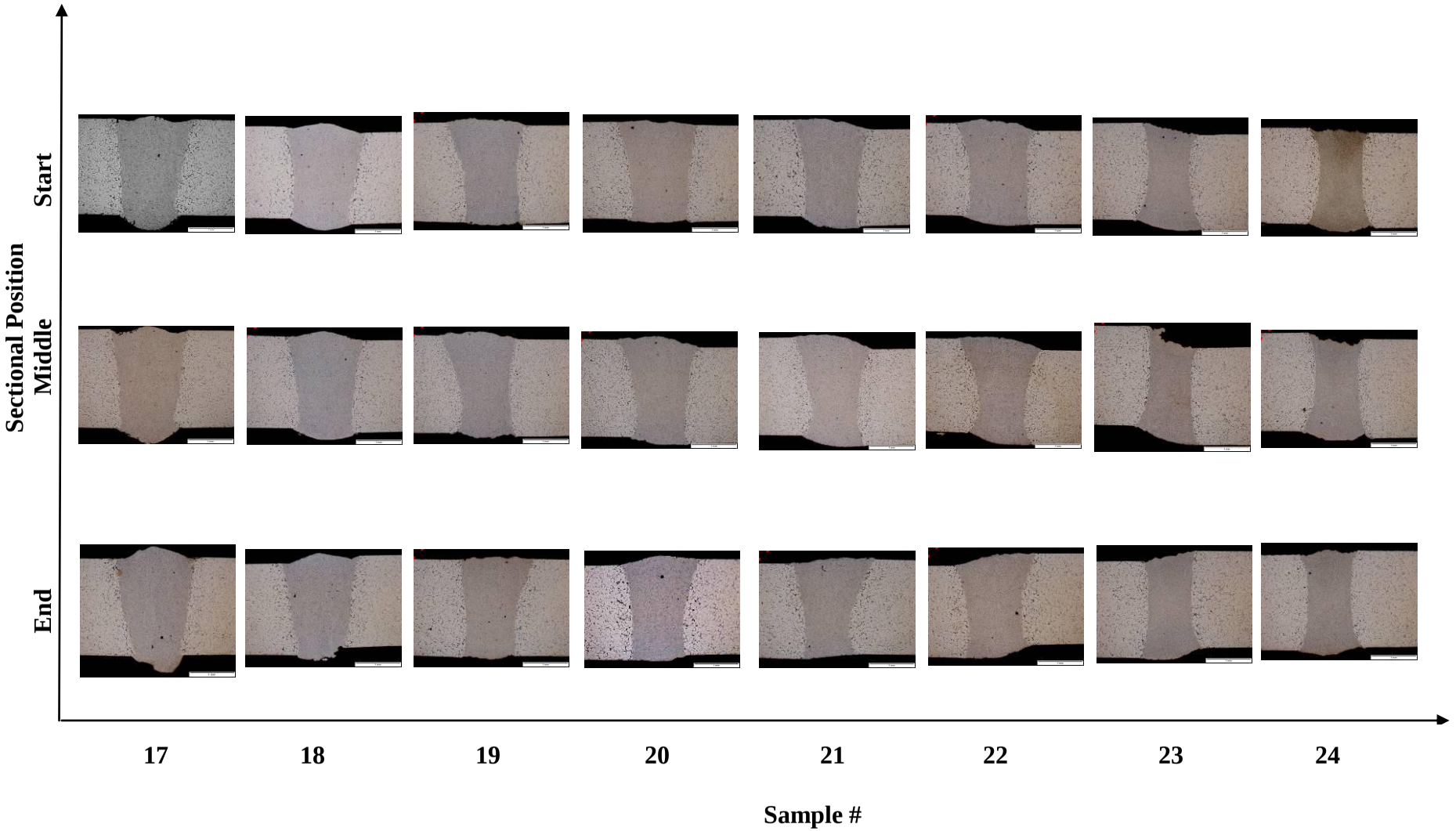

Figure 4.4.1 - repeatability of Laser Welding Process for 2 mm Plate

configuration filler feed rate and accurate position of the filler wire were very important parameters to obtain repeatable weld geometry.

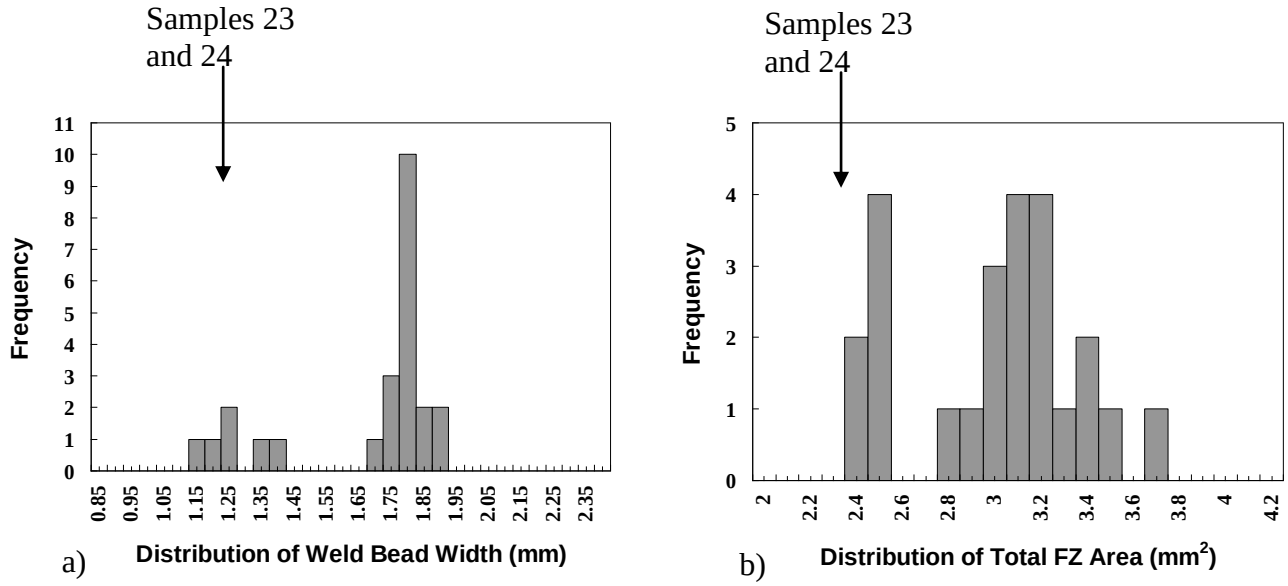

Figure 4.4.2 – Repeatability of FZ Weld Geometry (a) Distribution of Weld Bead Width (b) Distribution of Total FZ Area

Figure 4.4.2 shows the distribution of the weld bead width and total FZ area for samples 17 – 24. It is found that that samples 23 and 24 have significant deviations from other joints, probably as a result of misalignments defects and also due to the inaccurate sample preparation prior to laser welding process. The bead weld width and the total FZ area for the rest of the samples varies from 1.68 to 1.90 mm, and 2.74 to 3.66 mm^2, respectively. Weibull distribution (for more information refer to appendix A.2) was used to describe the degree of the scatter represented by Weibull modulus (m) and to determine the characteristic weld bead width and FZ area, which approximately 63.2% of the population (examined sections) can record this value.

The cumulative plots of weld bead width and total FZ area are shown in Figure 4.4.3. Samples 23 and 24 were excluded from this evaluation since they showed

deviations from all other sections. The corresponding Weibull plots for the weld bead width and total FZ area are shown in Figure 4.4.4.

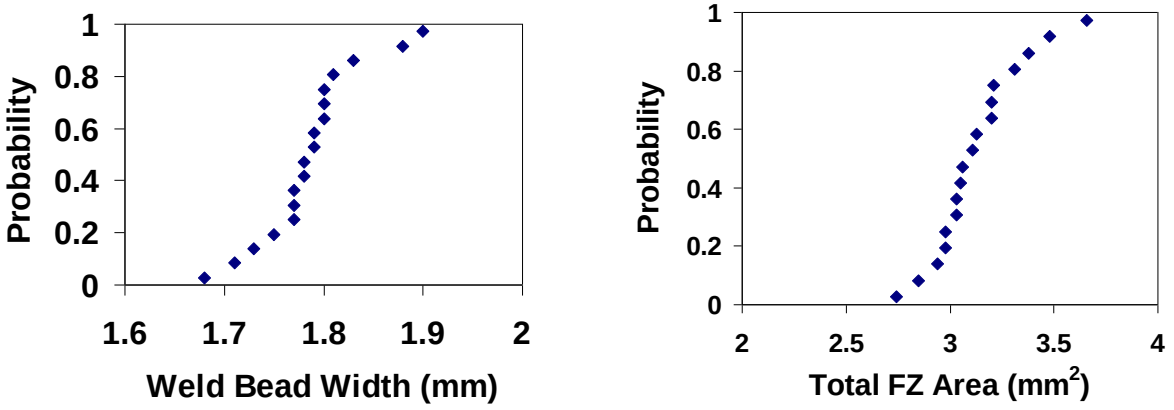

a) b)

Figure 4.4.3 – Cumulative Probability Plots for (a) Weld Bead Width (b) Total FZ Area

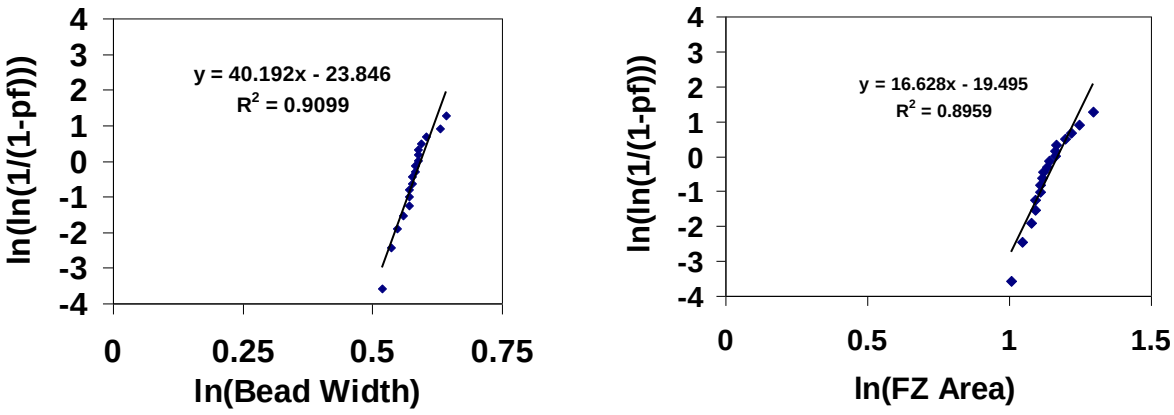

a) b)

Figure 4.4.4 – Weibull Plots for (a) Weld Bead Width (b) Total FZ Area

From Figure 4.4.4 the Weibull modulus for the weld bead width (top width) and total FZ area are 40.19 and 16.63, respectively. The characteristic weld bead width and FZ area that 63.2 % of the examined sectioned were recorded values of 1.81 mm and 3.23 mm^2 respectively. The Weibeull modulus (m) for the weld bead width was higher than

that for the total FZ area, which means the scattering in the FZ area values was higher than in the bead width. The high m value for the bead width shows that weld bead width has good repeatability. The profile of the FZ geometry was affected by the interaction between the laser beam and the vapor – liquid interface and the variation in the thermo physical properties of the BM like thermal conductivity, thermocapillary flow of the molten metal [40].

4.4.2 Microstructure

The fine equiaxed grains were observed in the FZ for samples 17 – 24 as shown in Figure 4.4.5. This Figure also shows that the microstructure appears to be slightly different for the last two samples 23 and 24 which had similar discrepancies in weld geometry compared with all other samples. The change in the microstructure in these two samples again may be correlated to the errors in sample preparation such as the gap size or filler positioning which may have affected the cooling rate and the temperature distribution inside the FZ.

The PMZ and the HAZ for the repeated samples can be seen in Figure 4.4.6. It is clear that the HAZ exhibited a significant liquation of some grain boundary near the PMZ which was not found during the laser welding of the casting used in the first round of experiments (refer to Figures 4.1.3, 4.2.3, 4.3.3).

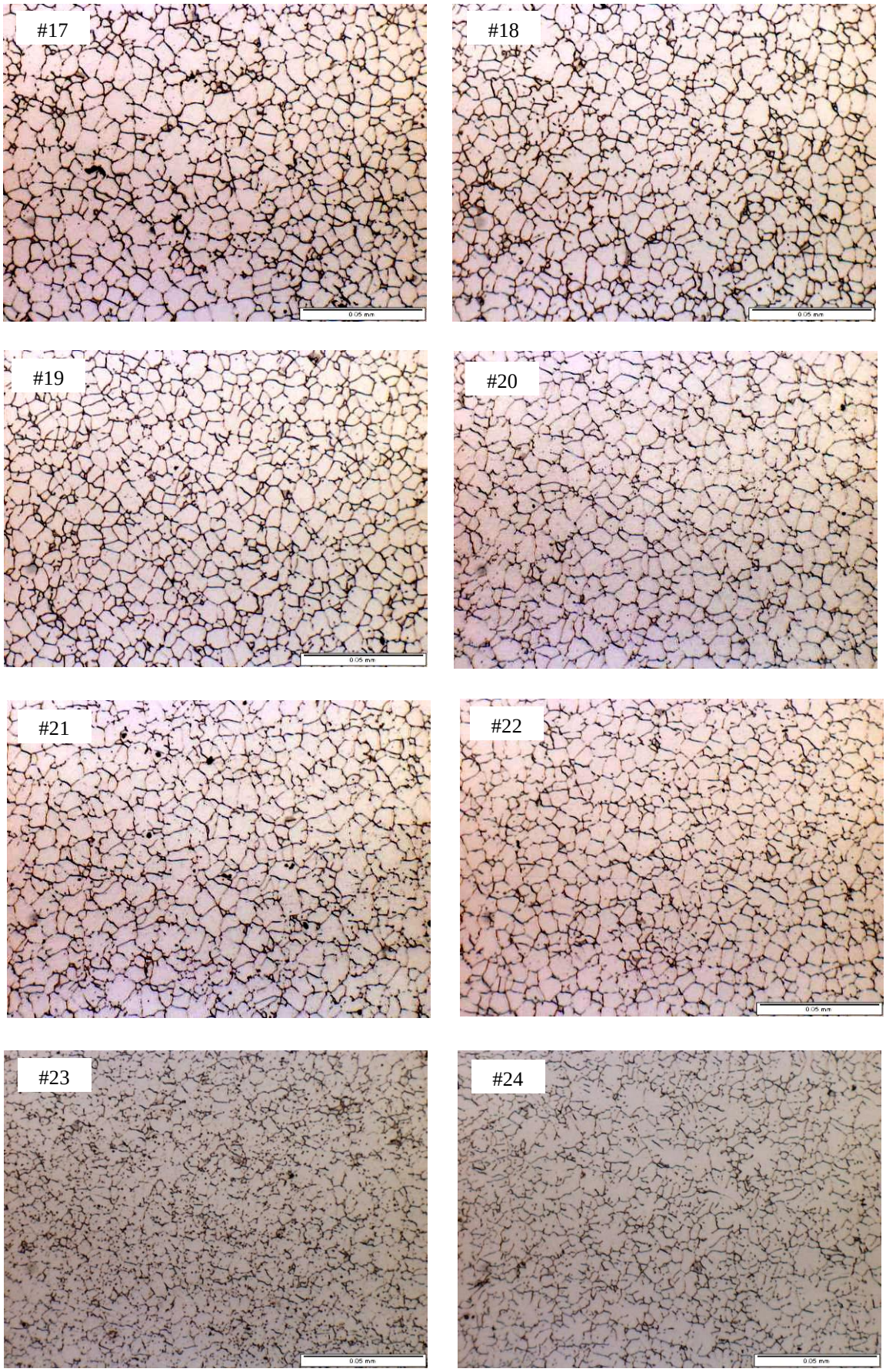

Figure 4.4.5 – FZ Microstructure for the Repeated Samples

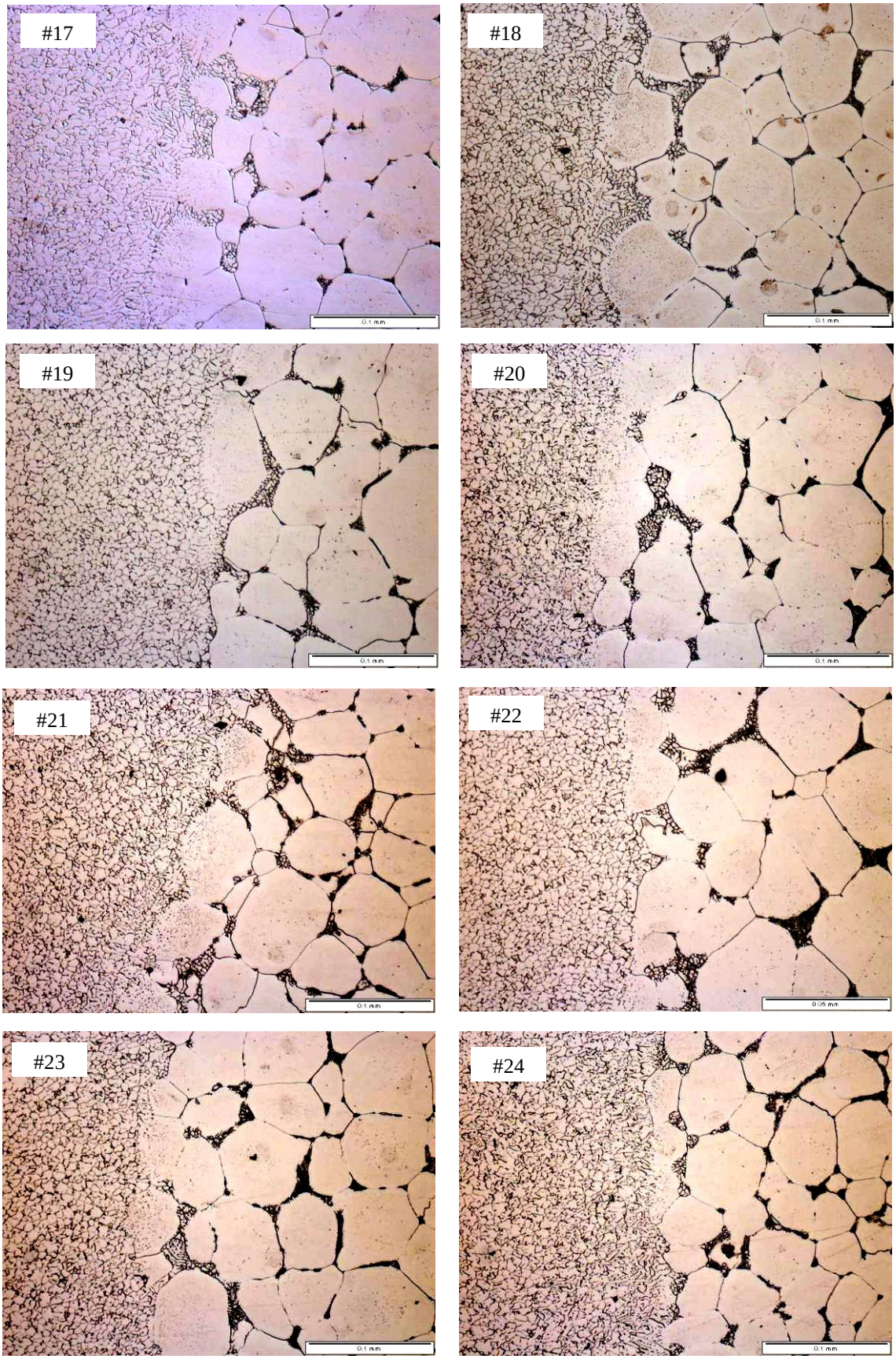

Figure 4.4.6 – Micrographs Showing the PMZ for the Repeated Laser Welded Samples.

4.4.3 Defects

The distribution of porosity area percentage and FZ solidification cracks for samples 17 – 24 are shown in Figure 4.4.7. From this Figure it is obvious that the crack is neither Weibull nor normal distribution which may affect this assessment. The maximum porosity area percentage and the maximum solidification cracks observed among the 24 tested samples were 0.27 % and 0.41 mm, respectively. To evaluate the degree of scattering in the defects, Weibull distribution was used to calculate the Weibull modulus

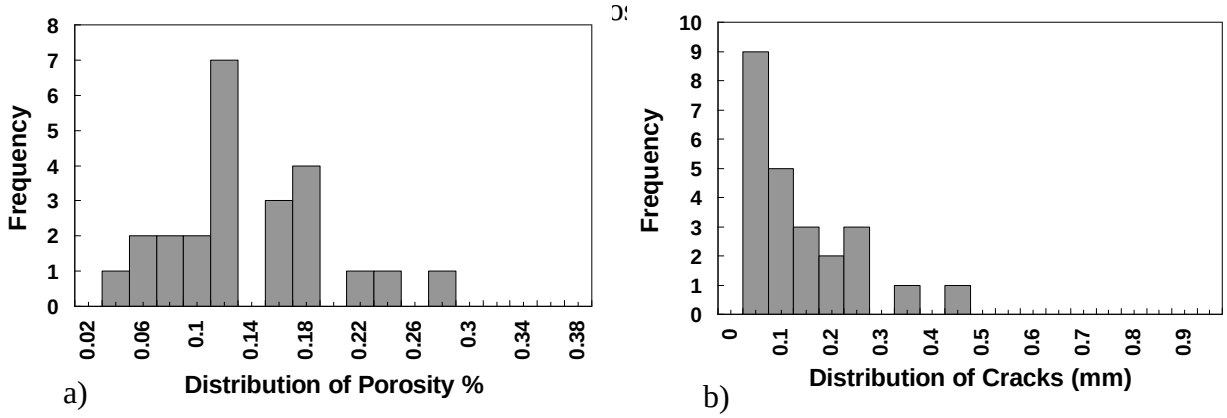

Figure 4.4.7 – Defects Distribution for the Repeated Laser Welded Samples a) Porosity Area Percentage b) Solidification Cracks Length

The cumulative plot and the corresponding Weibull plots for the porosity area percentage and solidification crack length are shown Figures 4.4.8 and 4.4.9, respectively. Referring to Figure 4.4.8 the maximum porosity area percentage and crack length were very low. From Figure 4.4.9 the Weibull modulus for the porosity area percentage and FZ solidification crack length area are 2.81 and 1.9 respectively. The characteristic porosity % and solidification crack length are 0.15% and 0.18 mm, respectively. Both types of defects showed lower m values than that for the weld

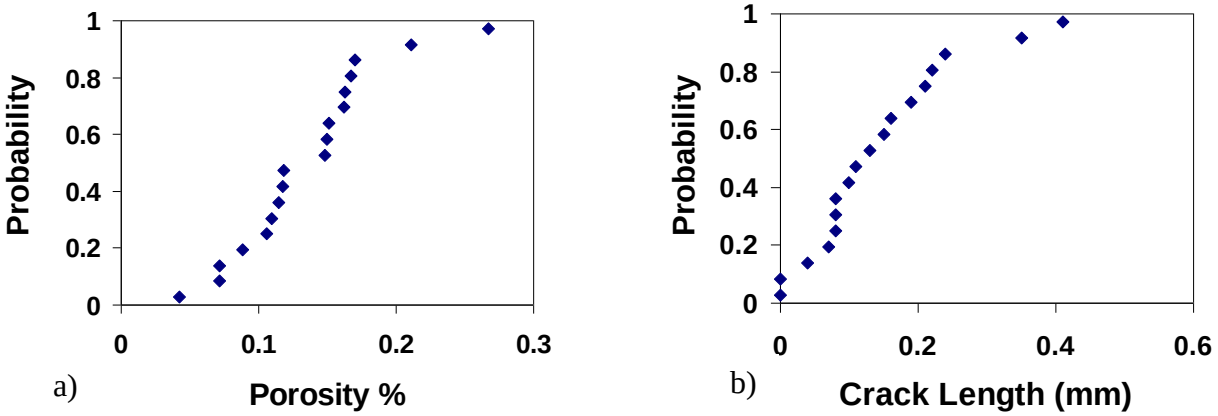

Figure 4.4.8 – Cumulative Plot of (a) Porosity Area Percentage (b) FZ Solidification Crack Length

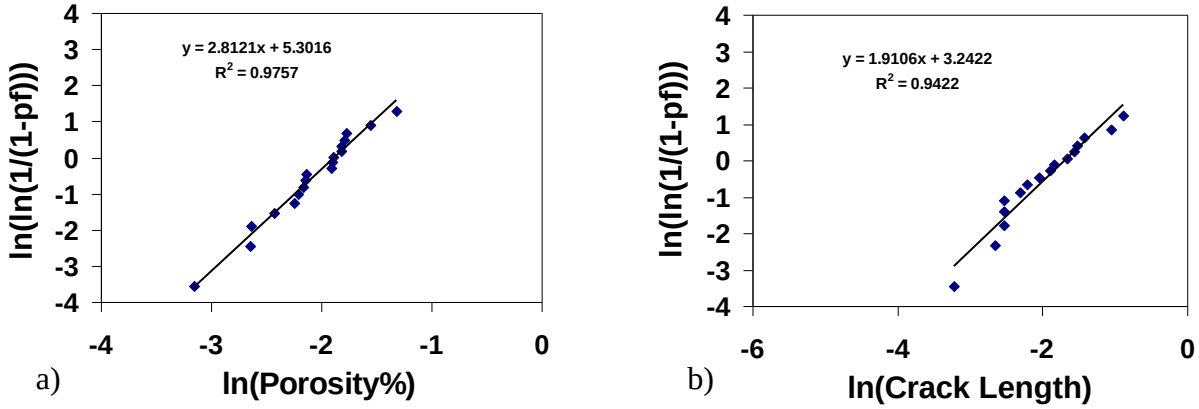

Figure 4.4.9 – Weibull Plots Obtained From (a) Porosity Area Percentage (b) FZ Solidification Crack Length

geometry, indicating more scattering in the defects measurements may be caused by many factors. Furthermore, the effect of the scattering in the defects measurements on the repeatability of the tensile properties measurements will be verified in the next section.

4.4.4 Mechanical Properties

To study the mechanical properties of the repeated samples, the specimens were divided into two groups: the first group was tested in the as-welded condition and the other was tested after T5 heat treatment (at 329 ^{o}C for 2 hr) which is an artificial aging heat treatment used for alloy ZE41A-T5 to produce a precipitating hardening phase Mg_9Ce. The microhardness profiles for the welded samples in the as – welded and heat treated conditions are shown in Figure 4.4.10 and 4.4.11, respectively. In both cases the FZ showed a drop in hardness by 5 Hv and the effect of heat treatment on the hardness profile was insignificant. The HAZ width was in the range between 1.5 and 2 mm, with a variation in hardness between 65 and 70 Hv. Table 4.4.1 shows the average hardness in the center line of the FZ. The Weibull distribution was used to evaluate the repeatability of the hardness in the FZ for as – welded and heat – treated conditions as shown in Figure 4.4.12. Both cases show a high Weibull modulus, 39 for as – welded condition and 67.8 for heat – treated conditions. The high m values mean that the hardness results are not very scattered. The heat – treated samples show higher m value compared with the as - welded samples. Table 4.4.1 shows that the heat treatment resulted in slight increase in the hardness measurements of some samples which resulted in less scattering as can be seen in Figure 4.4.12 (a). That means the post – weld aging can improve the distribution of the hardness, i.e. more uniform hardness values can be obtained in the FZ.

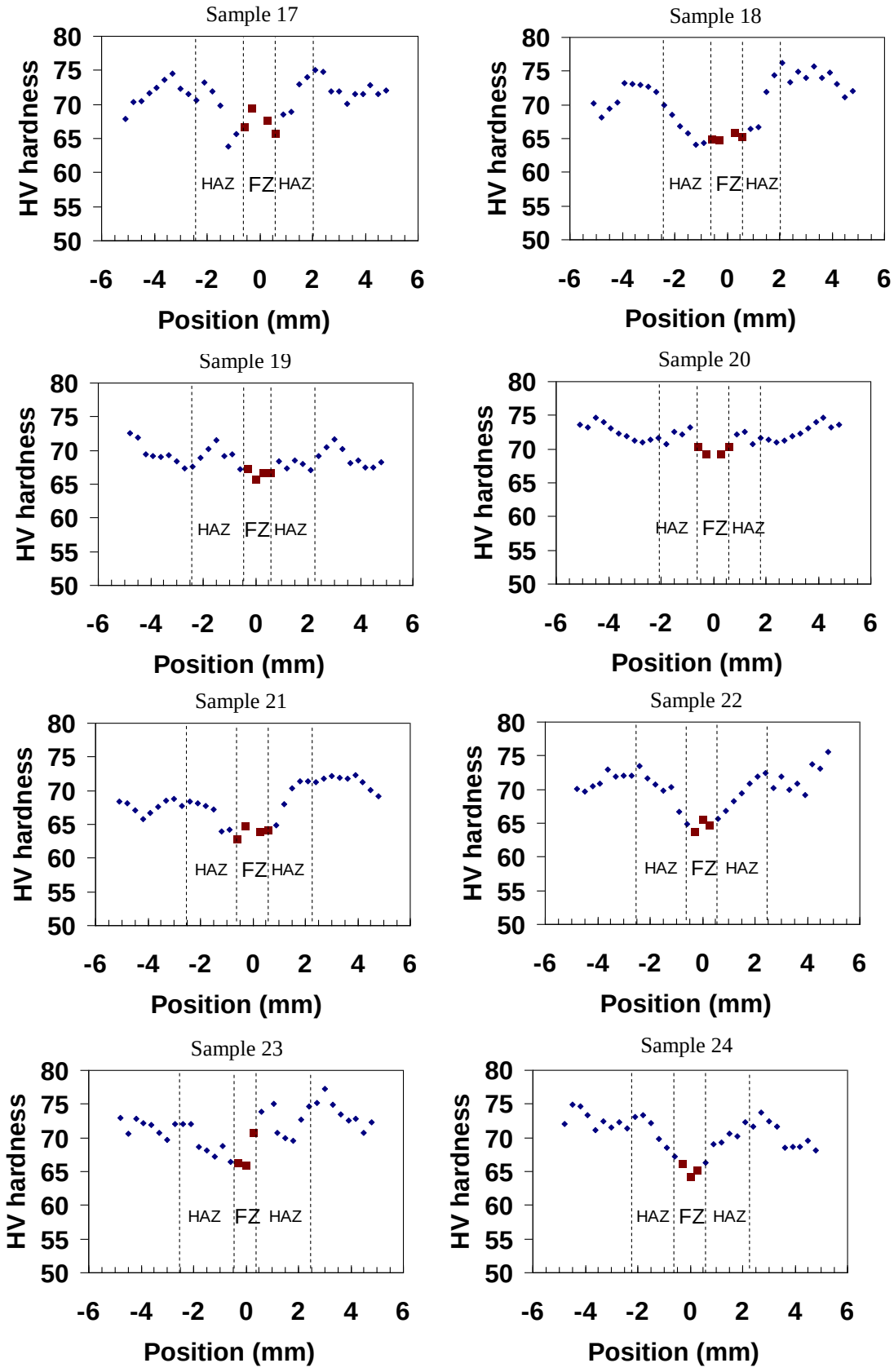

Figure 4.4.10 – Microindentation Hardness Test for the Repeated Welded Samples (as -Welded Condition)

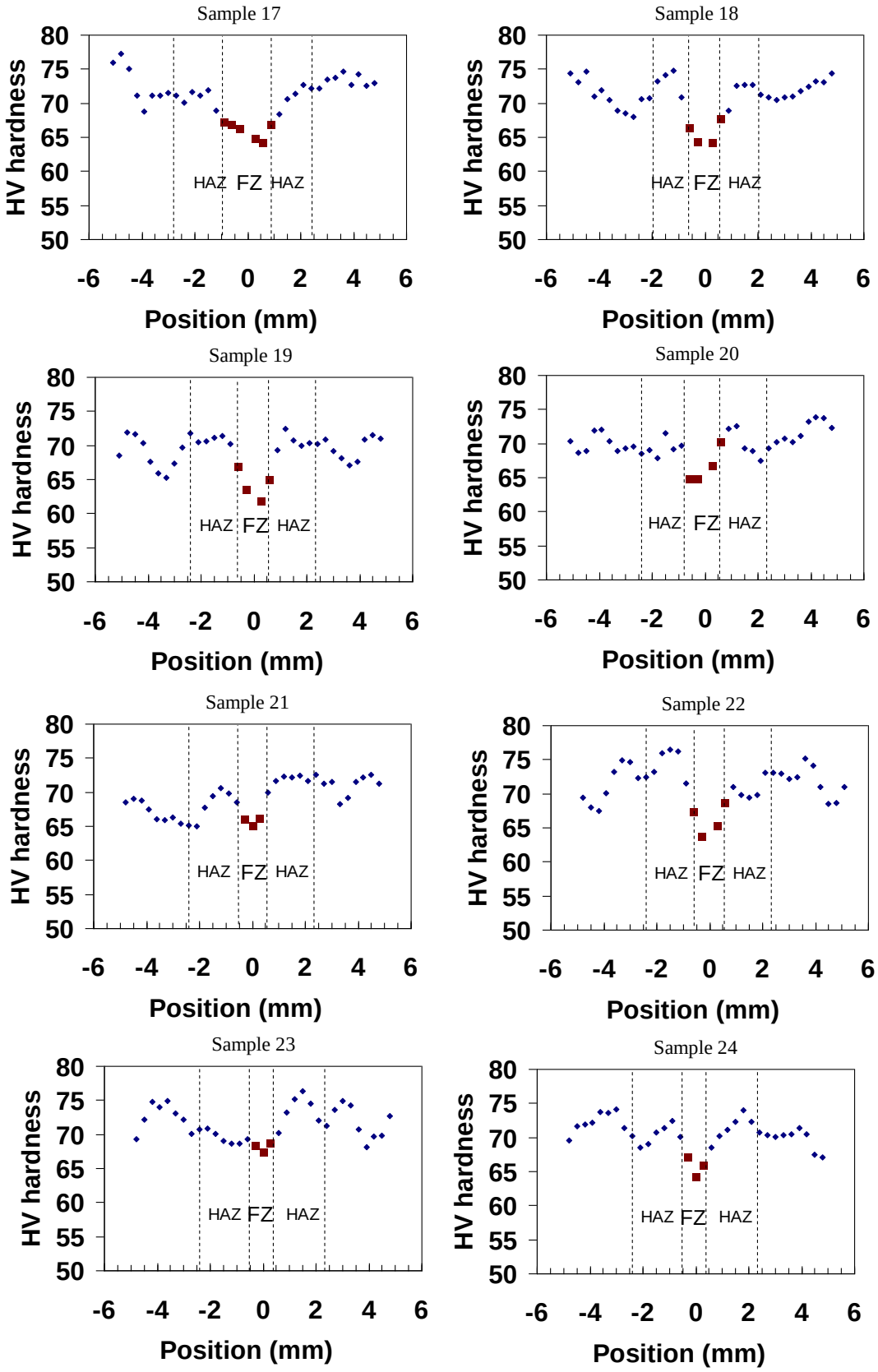

Figure 4.4.11 – Microindentation Hardness Test for the Repeated Welded Samples (Heat Treated Condition).

Table 4.4.1 – Average Vickers Hardness in the Center Line of the FZ for the Repeated Welded Samples

Sample #	Vickers Hardness as welded condition	Vickers Hardness heat treated
17	67.3	66.0
18	65.2	65.6
19	66.6	64.2
20	69.7	66.6
21	63.9	65.7
22	64.6	66.2
23	67.6	68.1
24	65.2	65.8

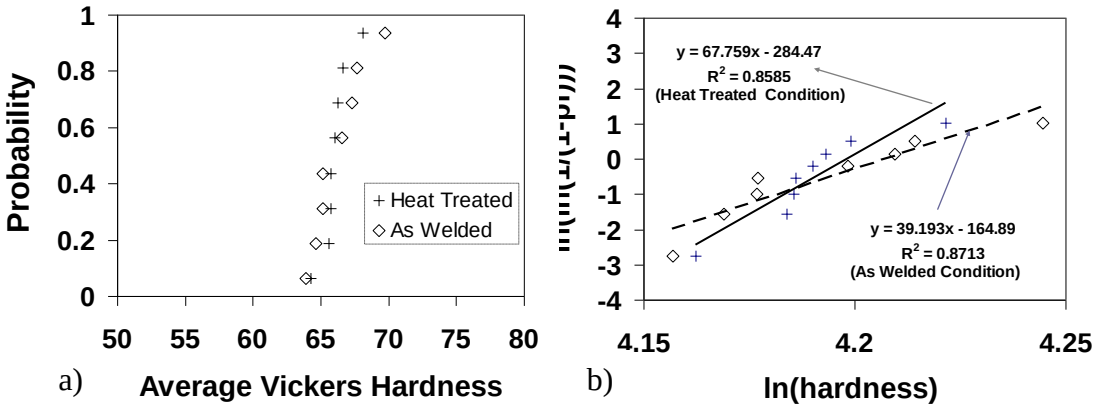

Figure 4.4.12 – Weibull Statistical Analysis for the Average Vickers Hardness Measured in the Center Line of the FZ in the as Welded and Heat Treated Conditions a) Cumulative Plots of Vickers Hardness b) Weibull Plots of Vickers Hardness

For tensile tests, maximum numbers of tensile specimens were extracted from the repeated welded samples (17 to 24), which were also divided into two groups: as – welded and heat – treated conditions. The tensile properties obtained for the two groups are shown in Tables 4.4.2 and 4.4.3. It was noticed that, the heat treatment caused to have larger number of specimens that fractured in the HAZ – PMZ (in the HAZ but near the PMZ) rather than the BM comparing with the as welded condition. The tensile strength distributions are shown Figure 4.4.13 which indicates that the trailing profile was longer

in the heat treated condition since more samples failed at lower tensile strength end than in the as welded condition.

Rank	TS (Mpa)	El%	Failure location
1	207.5	6.72	BM
2	224.1	6.74	BM
3	222.8	6.71	BM
4	214.9	5.93	BM
5	214.4	6.48	BM
6	209.9	5.74	BM
7	207.5	4.97	PMZ - HAZ
8	214.8	7.46	BM
9	217.3	--	BM
10	221.3	6.11	PMZ - HAZ
11	207.0	4.06	BM
12	231.2	5.83	BM
13	214.3	3.71	PMZ - HAZ
14	220.8	5.86	PMZ - HAZ
15	212.1	3.91	PMZ - HAZ
16	215.8	4.92	BM
17	222.9	6.43	BM
18	206.3	2.39	PMZ - HAZ
19	211.1	4.15	PMZ - HAZ
20	195.6	1.83	PMZ - HAZ
21	225.2	5.96	BM
22	227.8	5.23	PMZ - HAZ

Table 4.4.2 – Tensile properties of the repeated welded samples in the as – welded condition

Rank	TS (Mpa)	El%	Failure location
1	186.9	2.25	FZ
2	191.3	3.31	FZ
3	200.7	4.82	BM
4	209.5	6.31	BM
5	215.8	7.50	BM
6	207.8	6.43	BM
7	215.0	7.08	BM
8	223.8	8.25	FZ
9	217.4	7.92	BM
10	223.4	7.00	PMZ - HAZ
11	191.7	3.62	PMZ - HAZ
12	223.2	7.99	PMZ - HAZ
13	199.7	3.24	PMZ - HAZ
14	220.6	5.92	PMZ - HAZ
15	213.2	5.64	PMZ - HAZ
16	224.4	7.16	BM
17	216.3	5.78	PMZ - HAZ
18	208.0	8.95	HAZ
19	210.9	4.97	PMZ - HAZ
20	222.4	7.30	PMZ - HAZ
21	232.4	9.61	PMZ - HAZ
22	221.9	6.44	PMZ - HAZ

Table 4.4.3 – Tensile properties of the repeated welded samples in the heat treated condition

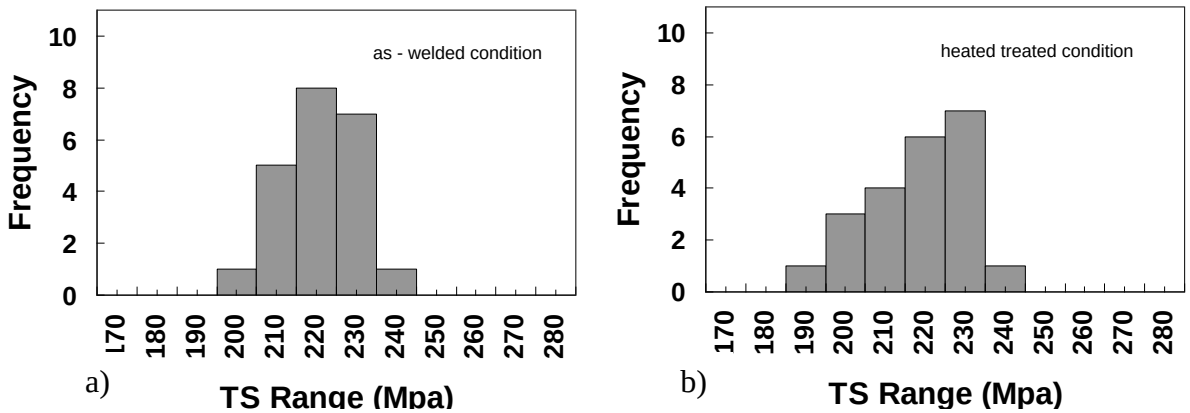

Figure 4.4.13 – Tensile Strength Distribution for a) as Welded Condition b) Heat Treated Condition.

The distribution profiles of TS results show asymmetry around the mean value. Figure 4.4.14 shows the cumulative plot and the Weibull plot for the TS property. The

modulus values are 31.1 for the as – welded condition and 20.97 for heat treated condition with corresponding characteristic TS of 219 MPa and 218 MPa, respectively. The heat treatment resulted in more scattered TS values, whereas post – weld heat treatment improved the uniform distribution of the hardness in the FZ. For ceramics the range of Weibull modulus varies from 5 to 20 reflecting the brittleness of the material [42]. In general the range of Weibull modulus for the TS property for casting alloys is between 10 and 40 [56]. For example, it was reported that the TS property for Mg alloy AZ91E has a Weibull modulus of 29.3 and 44, respectively for the alloy produced by low pressure lost foam and sand casting methods which both confirmed a narrow distribution [41]. Here, the welded specimens with m values of 31.1 and 20.97 for as – welded and heat – treated conditions, respectively show similar repeatability and reliability with good casting quality. The Weibull modulus for elongation can be inferred from Figure 4.4.15(b). The m value is 3.4 for the as welded condition with characteristic elongation of 5.93%, and 3.3 for the heat treated condition with characteristic elongation of 6.99%. The characteristic elongation and cumulative chart (Figure 4.4.15 – a) show that heat treated specimens exhibited more ductility than those tested in the as – welded condition.

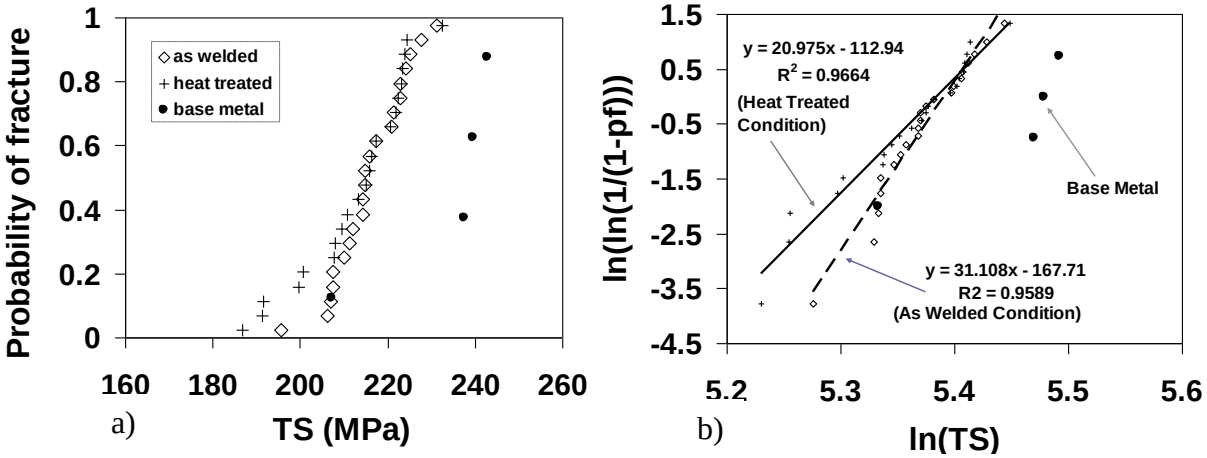

Figure 4.4.14 – Weibull Statistical Analysis for Tensile Strength
a) Cumulative Plots of Tensile Strength b) Weibull Plots of Tensile Strength

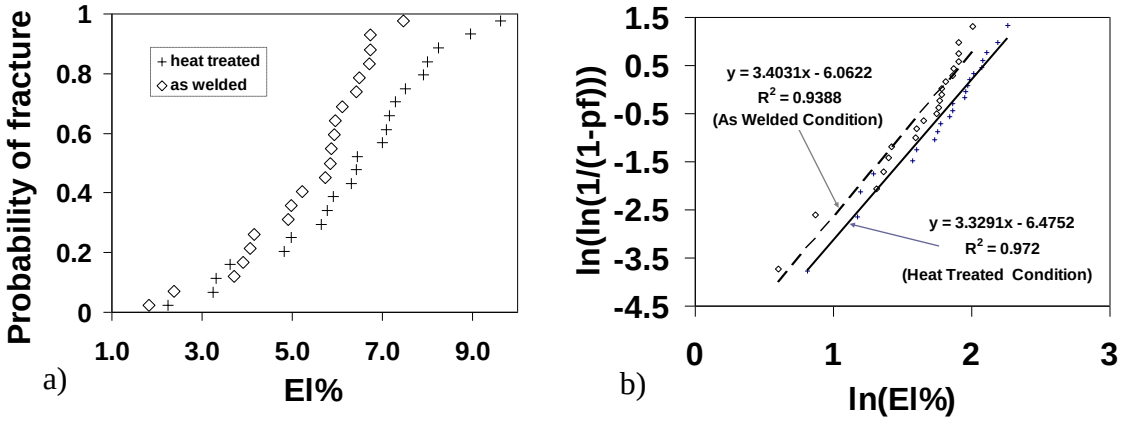

Figure 4.4.15 – Weibull Statistical Analysis for Elongation
a) Cumulative Plots of Elongation b) Weibull Plots of Elongation

4.4.5 Summary of Repeatability

Table 4.4.4 summarizes the repeatability of laser welding process. As mentioned earlier a Weibull modulus between 10 and 40 is usually considered a reliable mechanical properties of castings. Therefore, TS, hardness, weld width and FZ area are considered to have good repeatability in laser welding process. The defects data show less repeatability as indicated by the low m value which may be attributed to the high sensitivity of the porosity and crack formation to the process variables and the formation of these defects are dominated by many factors. However, the high value of m for tensile strength property shows that the defects in the tested samples were in the same level [41,42]. The elongation also shows less reliability since a small deviation in the fracture or tensile strength leads to large change in fracture elongation due to small strain harndening coefficient of the investigated alloy as indicated in Figure 4.4.16.

The calculated joint efficiencies for 2 mm laser welded plates using the optimized parameters are 93 and 91.7 % for as – welded and heat – treated conditions, respectively. The joint efficiency for each condition was calculated by taking the average TS of the

welded specimens divided by the TS of the BM (for this good quality of casting, 232 MPa. Refer to Table 4.5.5).

Table 4.4.4 – Reliability Assessment for the Repeatability of Laser Welding Process

Investigating Parameters for Laser Welding Process	Weibull Modulus - m	
	as welded	heat treated
Weld geometry / bead weld width	40.2	---
Weld geometry / total FZ area	16.6	---
Defects / porosity area percentage	2.8	---
Defects / solidification crack length	1.9	---
Mechanical properties / FZ hardness	39.2	67.7
Mechanical properties / Tensile strength	31.1	20.9
Mechanical properties / Fracture Elongation	3.4	3.3

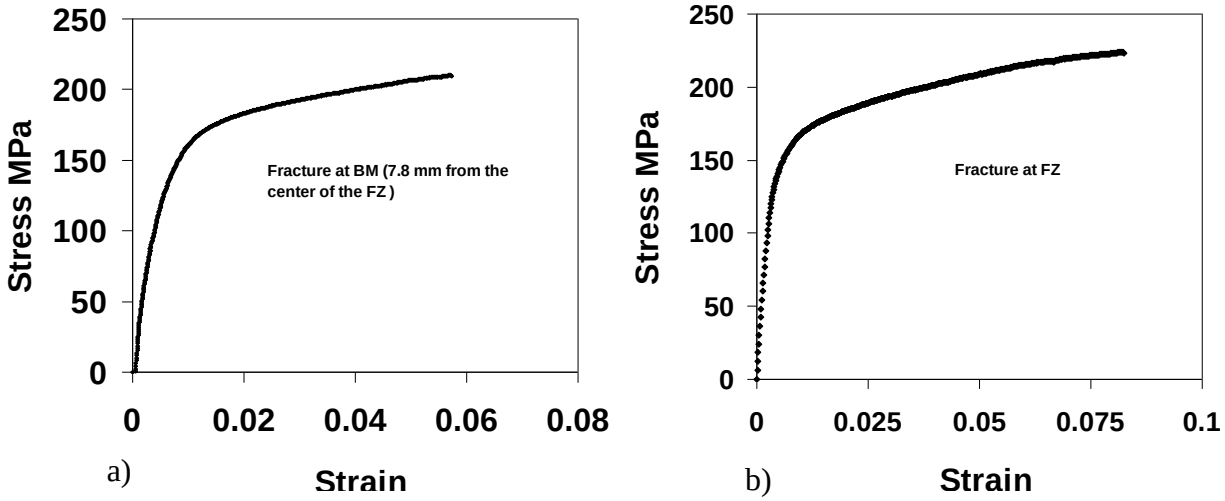

Figure 4.4.16 – Mechanical Tensile Properties / Stress – Strain Curve for sample # 19 a) as Welded Condition b) Heat Treated Condition.

4.5 Laser Welding of Thick Plates (6 mm thickness)

Table 4.5.1 lists the parameters used in laser welding of 6 mm thick plates. The procedure was divided into three main steps:

1. Optimizing the defocusing distance to get a good surface morphology (samples 25, 26, and 27). Bead-on-plate laser welding has been used for this purpose and the surface morphology was examined using stereoscope.
2. Optimizing the welding speed to get full penetrated autogenous (without filler wire) laser welded joints, samples 28 and 29.
3. Optimizing the welding speed and gap size to get full penetration laser welded 6 mm thick plates using filler wire (samples 30, 31, 32, 33).

The corresponding FZ geometries for 6 mm laser welded samples are shown in Figure 4.5.1.

Table 4.5.1 – Parameters Used in the Laser Welding of 6 mm Thick Plates

Sample #	Gap Size mm	Laser Power kW	Welding Speed m/min	Wire feeding rate m/min	Defocusing mm
25	--	4	5	--	0
26	--	4	5	--	-2
27	--	4	5	--	-4
28	0	4	5	0	-4
29	0	4	3	0	-4
30	0.2	4	3	2	-4
31	0.2	4	2	1.35	-4
32	0.4	4	3	4	-4
33	0.4	4	2	2.7	-4

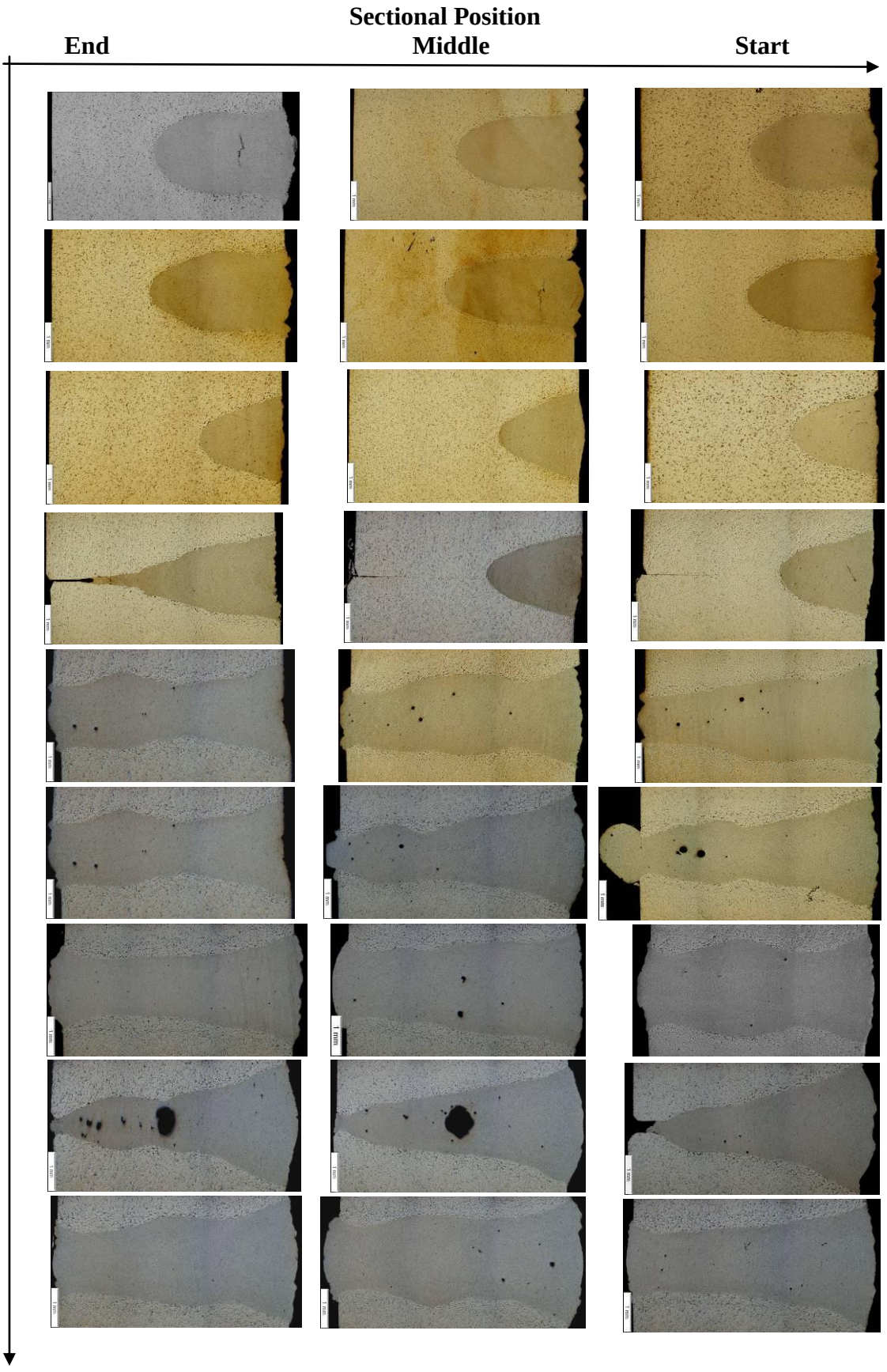

Figure 4.5.1 – Laser Welding of 6 mm Thick Plate.

4.5.1 Weld Geometry

The bead-on-plate welded samples 25 – 27 were used to optimize the defocusing of the laser beam from 0 to -4 mm based on surface quality (the minus sign means the focal point of the laser beam was below the plate surface). The effect of defocusing distance on the joint size is shown in Figure 4.5.2. The surface morphologies for samples 25 – 33 are shown in Figure 4.5.3 (A, B).

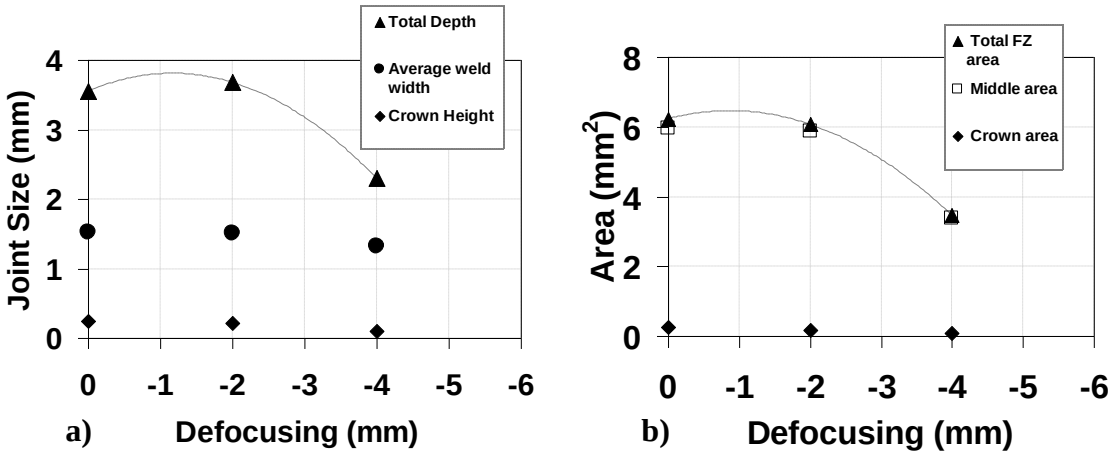

Figure 4.5.2 – Effect of Defocusing on Weld Geometry a) Joint size b) FZ Area. The welding Parameters are 4 kW Power and 5 m/min Welding Speed.

Poor top weld surface was obtained for 0 and -2 mm defocusing (samples 25 and 26) as shown in Figure 4.5.3(A). The high power density obtained at 0 and -2 mm defocusing caused high vaporization and turbulent flow of the metal in weld pool which worsened the quality of weld surface. At -4 mm defocusing (sample 27 – 33), a smooth crown profile without major defects was obtained. Figures 4.5.1 and 4.5.2 indicate that the penetration depth increased slightly as the defocusing increased from 0 to -2 mm. When the defocusing reached to -4 mm, the penetration depth was decreased significantly to 2.2 mm. Similar behavior were also observed for the total FZ area. This observation can be

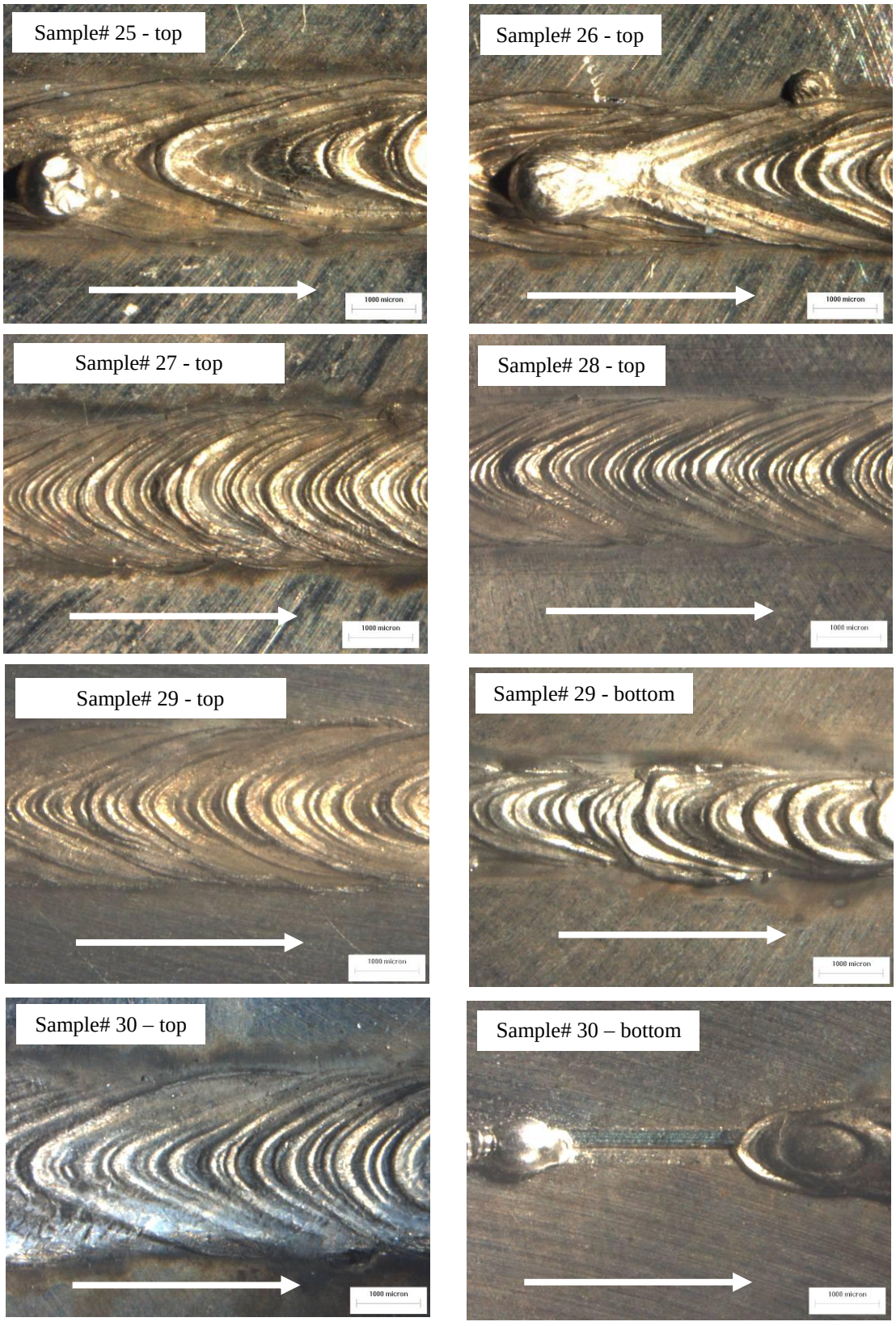

Figure 4.5.3 (A) – Top and Bottom Surface Morphology for Laser Welded 6 mm Plates.

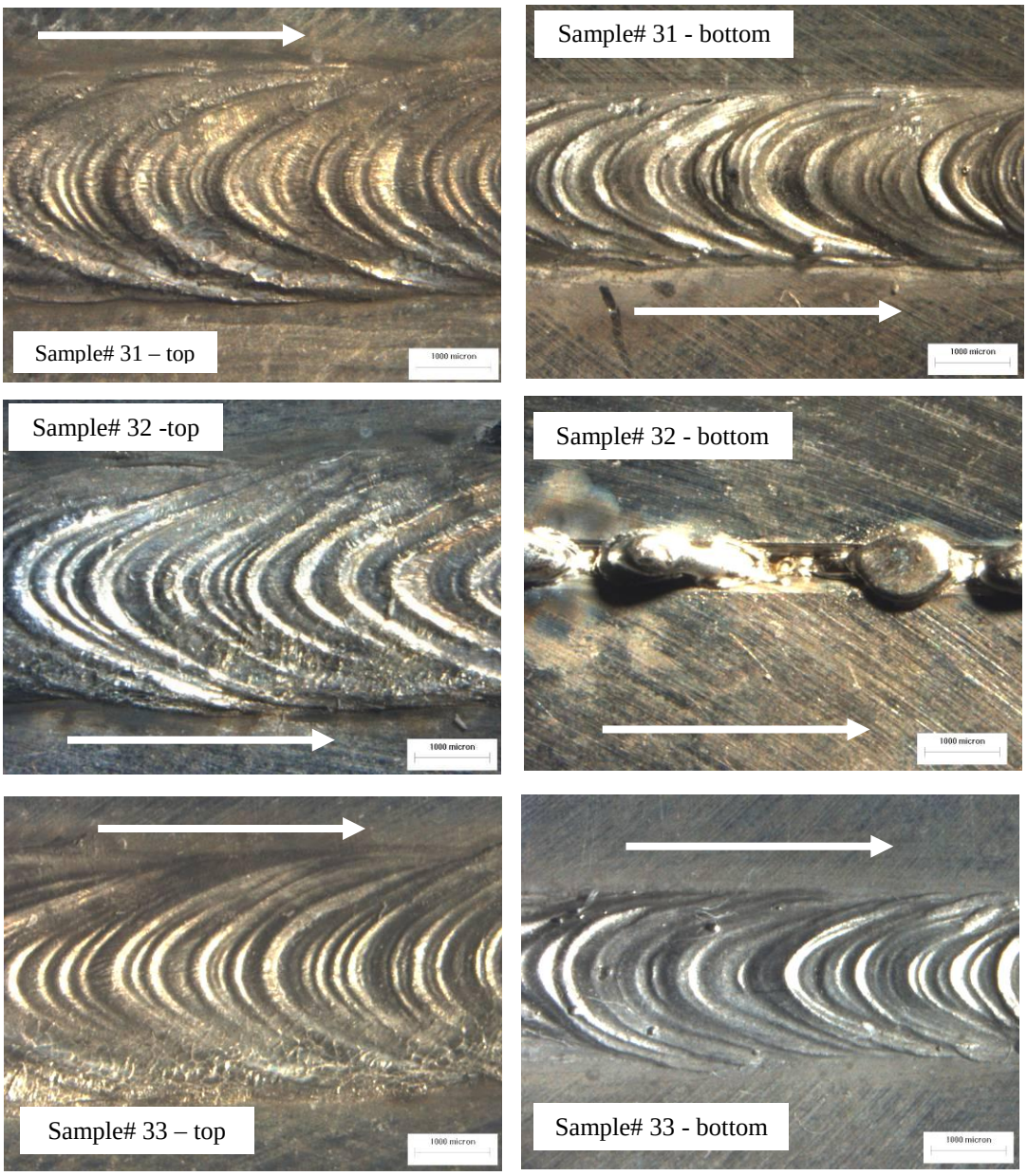

Figure 4.5.3 (B) – Top and Bottom Surface Morphology for Laser Welded 6 mm Plates.

explained as follows: the maximum intensity of laser beam is located in the focal point, and the peak intensity falls down as moving below or above the focal point. The effective intensities of the laser beam are located within +/- Rayleigh length (here in this setup it is equal to 2.34 mm); at a distance equal to +/- one Rayleigh length from the focal plane,

the peak intensity drops to one – half the peak intensity at the focal plane [43]. Therefore when the defocusing distance increased from 0 to -2 mm, the effective intensities were located inside the material (plate) which increased the coupling efficiency between the laser beam and the plate, but in the same time the laser intensity available on the top surface was reduced because of the increase in laser beam diameter. The further increase in defocusing distance to -4 mm led to have the available surface intensity below or equal to the threshold value which was required to produce the keyhole [39,43]. Therefore the laser welding process changed from the keyhole mode (samples 25, 26) to the conduction mode (sample 27) since the aspect ratio (depth / top width) for keyhole mode should be greater than 1.2 [26, 44]. At -4 defocusing the calculated surface power density was 1.6 x 10^6 W/cm^2 which is slightly higher than the published value for the keyhole threshold irradiance (1.5 x 10^6 W/cm^2) for the same alloy with machined surface condition [26]. At -4 mm defocusing distance the power density was near the threshold value but good surface quality was obtained. Thus this value (-4 mm defocusing) was used for follows tests.

The defocusing distance of -4 mm for sample 27 has been used to weld the butt joint autogenously (without filler wire). The autogenous welding was conducted to compare the effect of filler wire on the laser coupling efficiency and weld quality. Figure 4.5.1 shows that sample 28 (butt joint at zero gap) and 27 (Bead-on-plate) had almost the same FZ geometry in the start and middle sections; the start and middle sections exhibited a conduction mode welding whereas the ending section showed a keyhole mode welding. This confirms that the surface laser intensity was near the keyhole threshold value as mentioned earlier. To change the welding mode from conduction to keyhole and

to increase the penetration depth, it was required to decrease the welding speed below 5 m/min since the Nd:YAG laser power was limited up to 4 kW power and the defocusing was fixed at -4 mm as described above. It was found that 3 m/min welding speed was suitable to get a full penetrated joint (sample 29) and good surface morphology for top and under bead was obtained as shown in Figure 4.5.3 (A). It is interesting to find that in the middle of the FZ geometry tends to be widened probably due to the multiple reflections and plasma absorption inside the keyhole. The multiple reflections can increase the coupling efficiency and increase the amount of molten material [38]. The optimum gap size found in section (4.2) was 0.4 mm to weld 2 mm thin plate using 1.6 mm filler wire. Here 0.2 and 0.4 mm gap sizes were used to weld the 6 mm plates with the same filler wire. Sample 30 was welded by applying a filler wire with 0.2 mm gap, other laser parameters except the feeding rate were the same as sample 29. Sample 30 encountered a fluctuation between full penetration and partial penetration welding as shown in the surface morphology of the bottom surface (Figure 4.5.3 (A)). Although the laser fluence or laser heat input for the two samples 29 and 30 were the same, sample 30 showed a decrease in the FZ middle area from 11.4 to 10.83 mm^2. Choosing the middle area for comparison rather than the total FZ area was due to the excessive root height which might lead to wrong conclusion. Applying the filler wire caused an increase in the reflection losses of the laser beam outside the keyhole because of the interaction between the laser beam and the filler wire above the plate surface [34]. Therefore it was necessary to decrease the welding speed to 2 m/min to increase the heat input. The corrected welding speed applied for sample 31 resulted in having full penetration welding as shown in Figures 4.5.1 and 4.5.3 (B). The same procedure was used to weld the plate with 0.4

mm gap (samples 32 and 33). In this case the full penetration welding was obtained by autogenous welding (sample 29) as well as by welding with filler wire (samples 31 and 33). Table 4.5.2 summarizes the effect of the laser parameters on the weld geometry. It can be seen from this table that full penetration was obtained for both gap sizes of 0.2 and 0.4 mm only when the welding speed was reduced to 2 m/min.

Sample #	Average Weld Width mm2	FZ middle Area mm2	Total FZ Area mm2	Total Penetration mm	Notes
25	1.52	5.97	6.23	3.55	Bead on plate (0 Defocusing) unstable surface and crown
26	1.51	5.89	6.07	3.68	Bead on plate (-2 Defocusing) unstable surface and crown
27	1.33	3.38	3.46	2.30	Bead on plate (-4 Defocusing) good surface morphology
28	1.32	4.55	4.64	3.36	Autogenous butt joint (welding speed = 5 m/min) partial penetration
29	2.07	11.40	11.74	6.46	Autogenous butt joint (welding speed = 3 m/min), full penetration
30	1.74	10.83	12.02	7.05	Applying filler wire (welding speed = 3 m/min, gap = 0.2 mm) lack of penetration
31	2.34	13.05	14.16	6.74	Applying filler wire (welding speed = 2 m/min, gap = 0.2 mm) full penetration
32	1.65	9.97	10.74	6.42	Applying filler wire (welding speed = 3 m/min, gap = 0.4 mm) lack of penetration
33	2.35	13.36	14.39	6.70	Applying filler wire (welding speed = 2 m/min, gap = 0.4 mm) full penetration

Table 4.5.2 – Weld Geometry Profile for 6 mm Laser Welded Plates

4.5.2 Microstructure

The microstructures were analyzed for the 6 mm welded samples as shown in Figures 4.5.4 to 4.5.9. It was noticed that sample 28 has a rosette grains (Figure 4.5.4 - A, B, C) and there was a tendency to form a dendritic grains rather than equiaxed grains. The variation in the microstructure of the three regions inside the FZ (top, middle and bottom) was minor. Figures 4.5.4 also shows the microstructure of the partially melted zone. Sample 29 which has a full penetration as shown in Figure 4.5.5, showed the microstructures of the three regions (A,B,C) as equiaxed rosette grains. Decreasing the speed from 5 m/min (sample 28) to 3 m/min (sample 29) changed the microstructure from dendritic like to equiaxed rosette morphology. Also, it is evidence that the cooling rate was almost uniform across the thickness since the three regions in this sample have similar grain size. Sample 30, however, exhibited a slight variation in the grain size between the three regions; the bottom region shows smaller grain size than the top and middle one. The further decrease in the welding speed to 2 m/min for sample 31 which had a full penetration welding formed a uniform equiaxed grains globular like rather than the rosette morphology as can be seen in Figure 4.5.7. The grain size was also similar for the three regions because of the full penetration opened keyhole welding. The variation in the grain size in sample 32 was more obvious as can be seen in Figure 4.5.8, since it showed a partial penetration (Figure 4.5.3 (A)) blind keyhole welding. The microstructure morphology was equiaxed globular grains. The variation in the grain size at different depth in the fusion zone wad not found as the welding speed decreased from 3 to 2 m/min as can be seen in Figure 4.5.9. The overall all behavior can be summarized to the following: the variation in the grain size across the FZ depth depends on the keyhole

shape which in turn affects the cooling rates across the plate thickness. The heat transfer between the keyhole wall and the base metal is carried out by thermal conduction and by the thermocapillary flow effect [40]. The Marangoni (thermocapillary flow) is induced by the surface tension gradient and the friction force between the vapor jet and the molten metal which caused the widening of weld geometry at the top and at the bottom in the case of open keyhole condition [38,40]. The thermocapillary flow accelerates the heat transfer between the keyhole and the base metal causing larger amount of molten metal near the keyhole opening. Hence the amount of heat transferred in the top region is higher than the heat transferred by conduction only in the bottom of the closed keyhole [40]. In case of open keyhole at root the amount of heat transfer in the lower region will be increased due to existence of both heat transfer mechanisms. Behind the moving keyhole the weld pool will start to lose effectively the gained heat by conduction to the BM. For the blind keyhole the upper region will have lower average cooling rate than the lower one because of the excessive molten material. For the open keyhole the variation in the cooling rate will be less due to the fact that the mass distribution of the weld pool is more uniform across the thickness which will result in more uniform grain size. The lower cooling rate will give the grains more time to grow. The second issue is the change in the microstructure morphology due to varying the laser parameters. Increasing in welding speed (or reducing the laser heat input) has the effect of changing the morphology from equiaxed globular shape to equiaxed rosette grains. Farther increase in welding speed may result in dendritic like morphology rather than equiaxed grains.

The HAZ exhibited a liquation between some grains near the PMZ which wasn’t observed while welding with original casting that used in the first round.

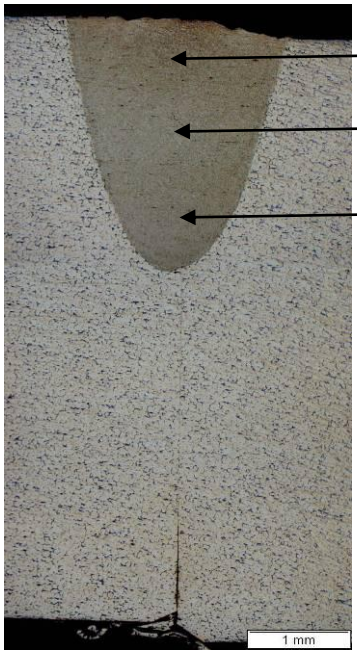

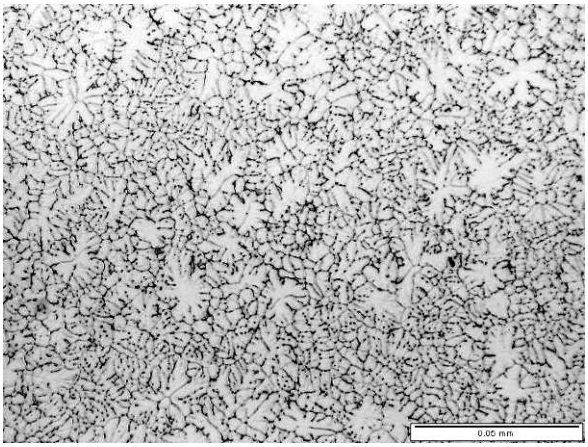

FZ Microstructure - A

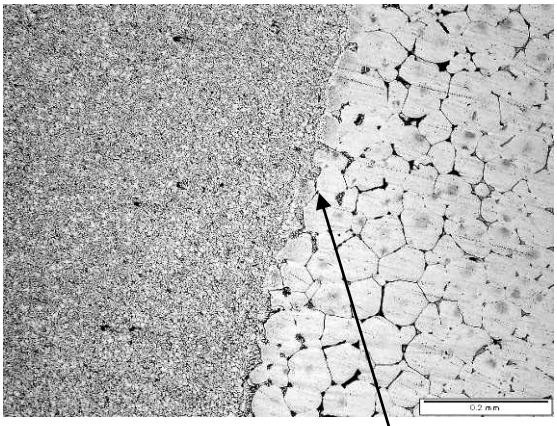

PMZ Microstructure

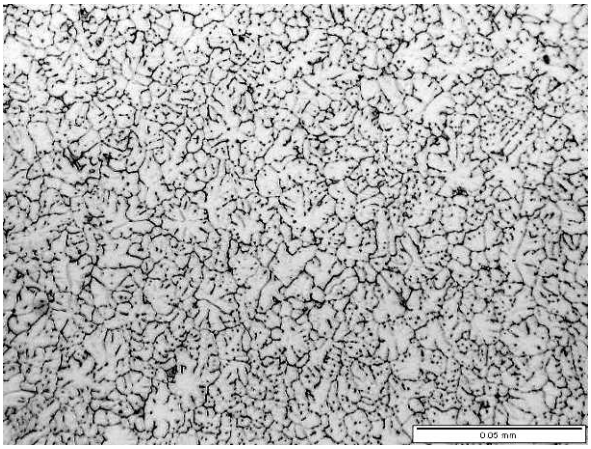

FZ Microstructure - B

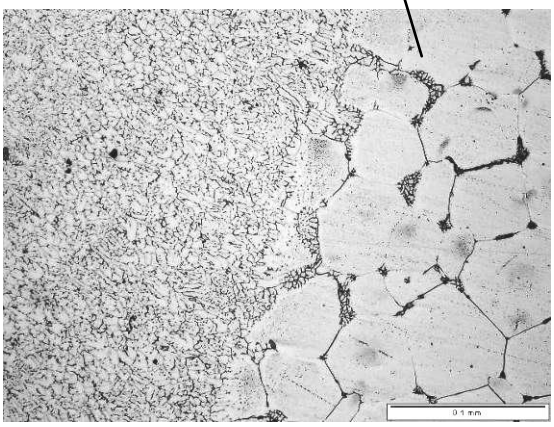

PMZ Microstructure

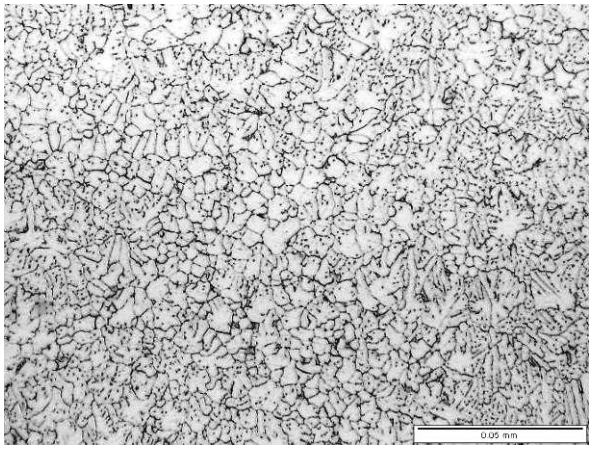

FZ Microstructure - C

Figure 4.5.4 – Microstructure for Sample 28

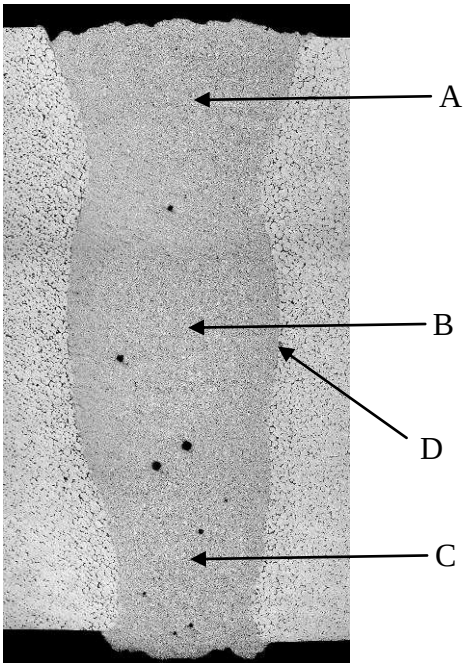

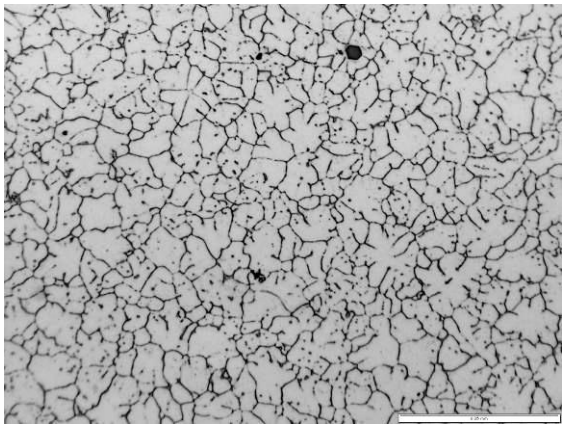

FZ Microstructure - A

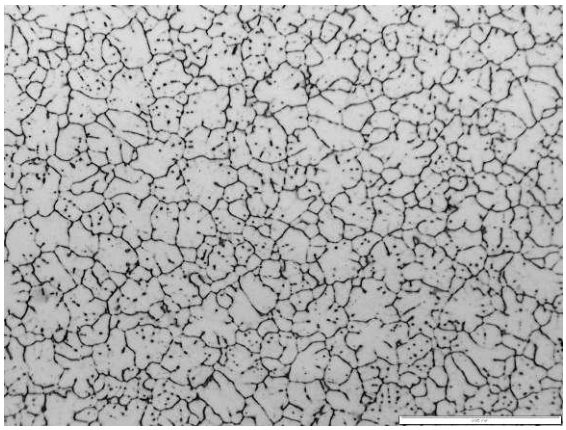

FZ Microstructure - B

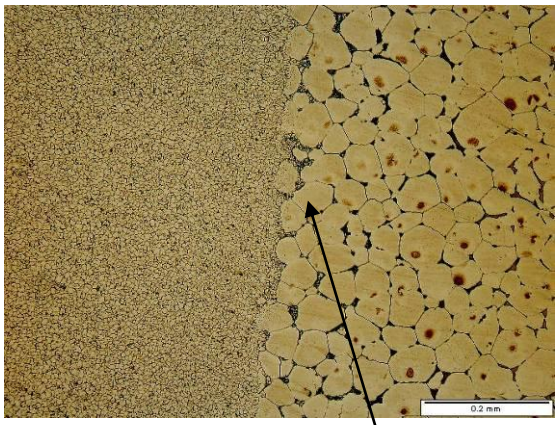

PMZ Microstructure - D

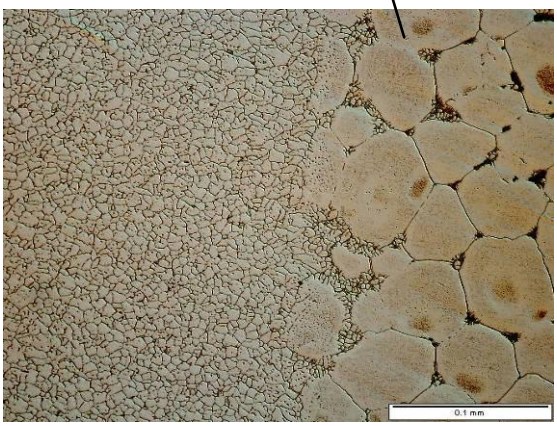

PMZ Microstructure - D

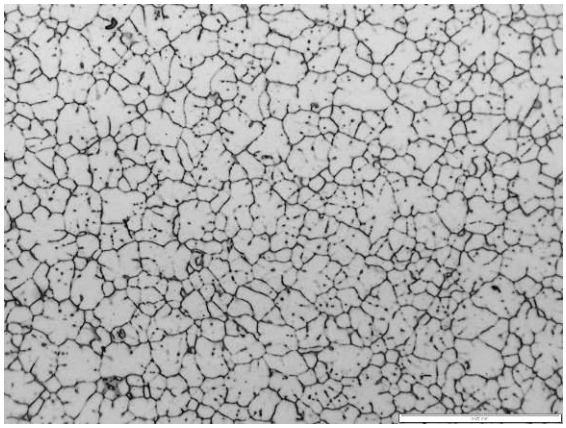

FZ Microstructure - C

Figure 4.5.5 – Microstructure for Sample 29

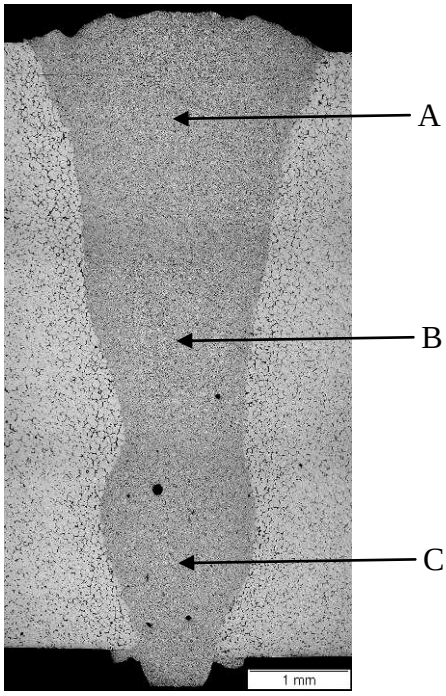

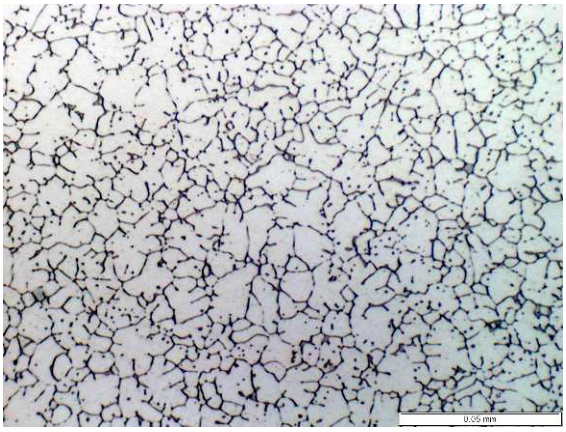

FZ Microstructure - A

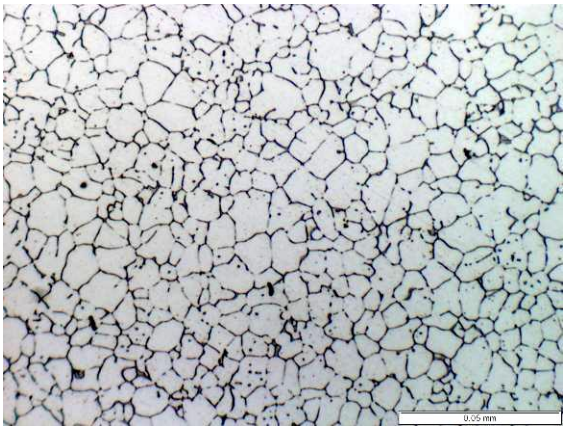

FZ Microstructure - B

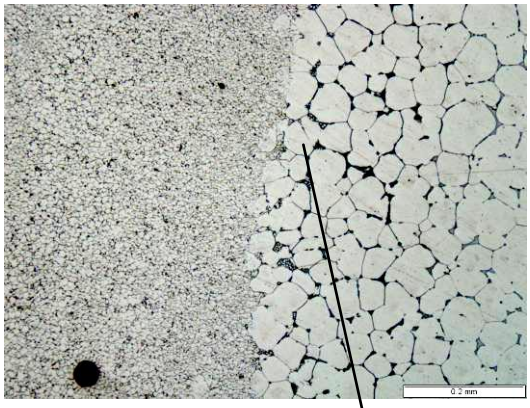

PMZ Microstructure

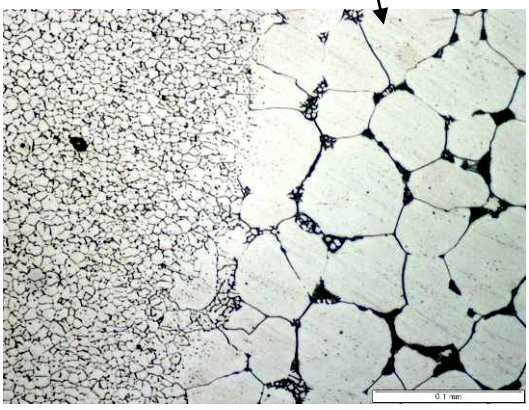

PMZ Microstructure

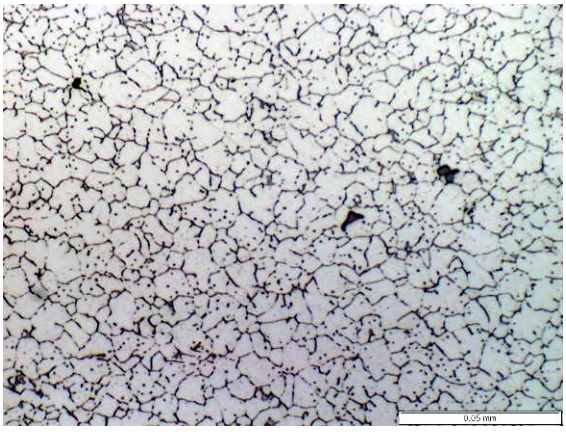

FZ Microstructure - C

Figure 4.5.6 – Microstructure for Sample 30

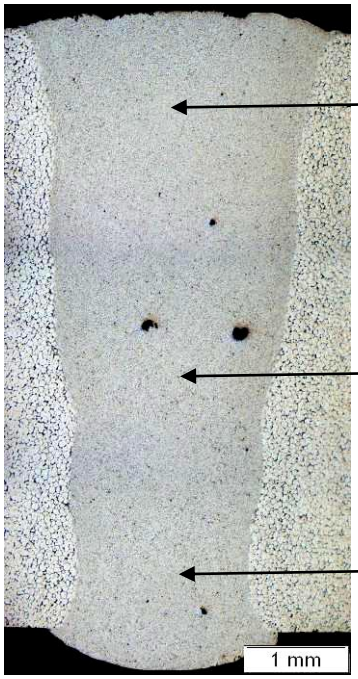

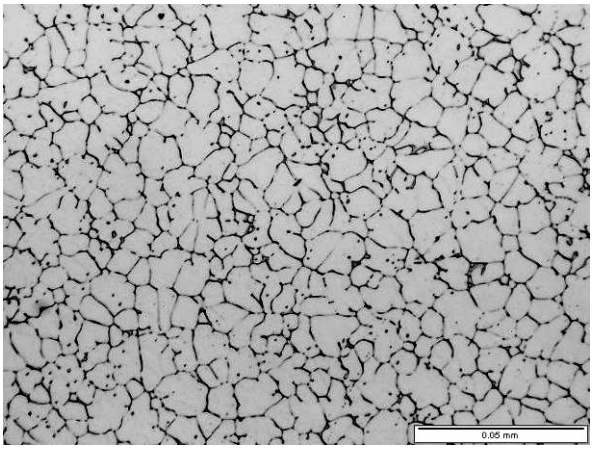

FZ Microstructure - A

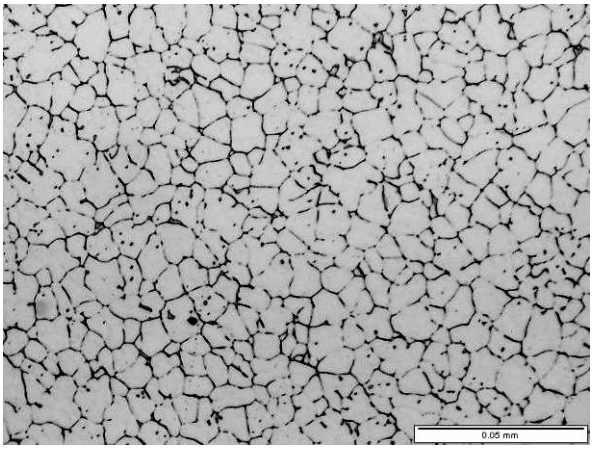

FZ Microstructure - B

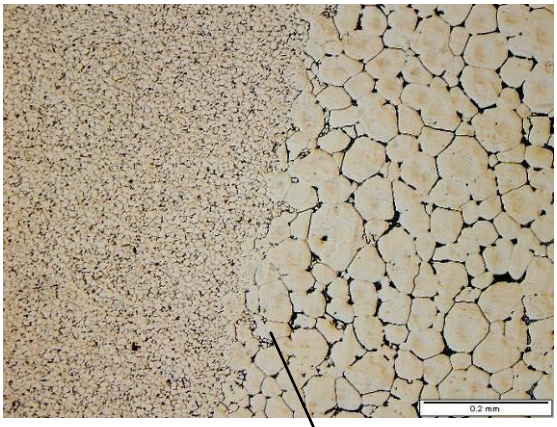

PMZ Microstructure

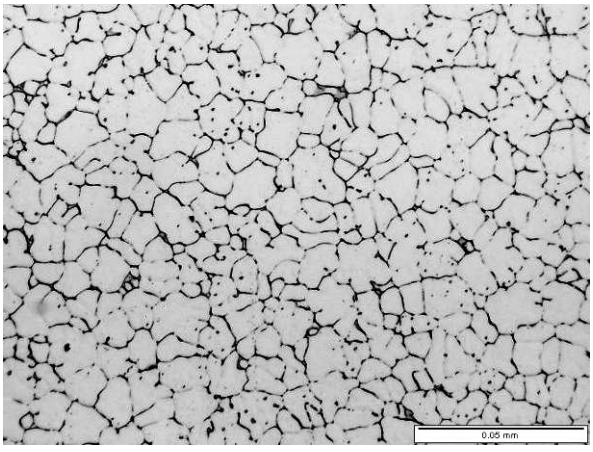

FZ Microstructure - C

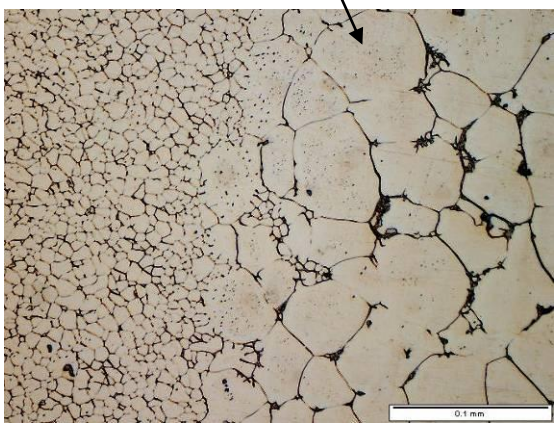

PMZ Microstructure

Figure 4.5.7 – Microstructure for Sample 31

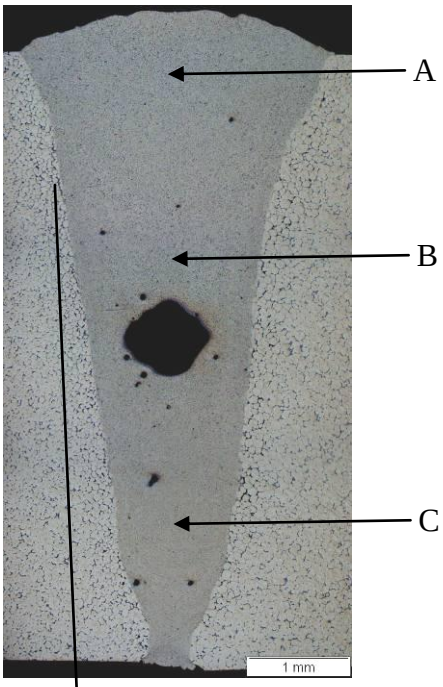

PMZ Microstructure

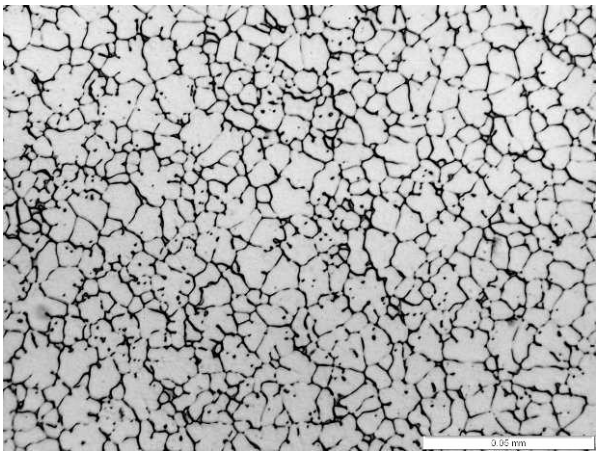

FZ Microstructure - A

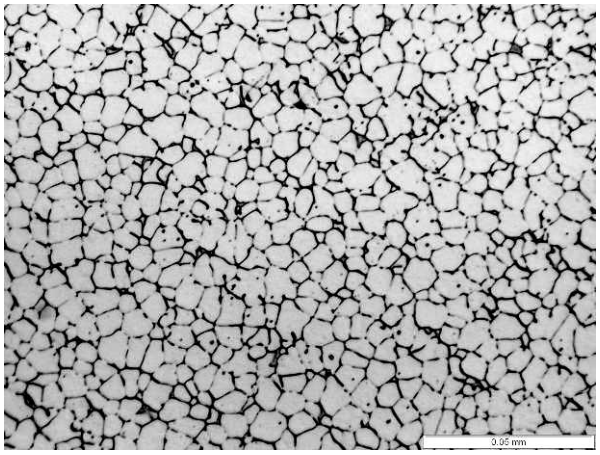

FZ Microstructure - B

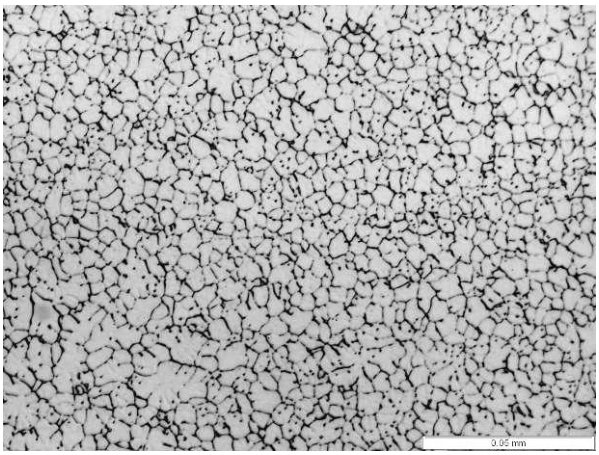

FZ Microstructure - C

Figure 4.5.8 – Microstructure for Sample 32

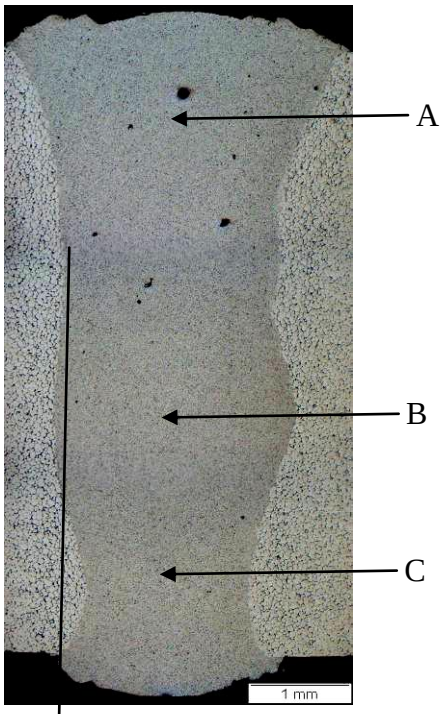

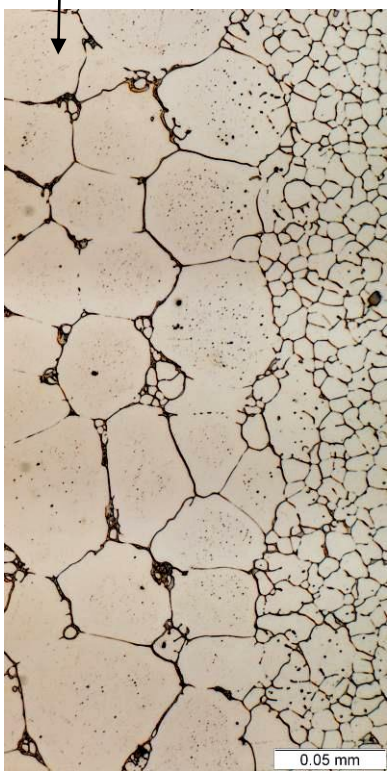

PMZ Microstructure

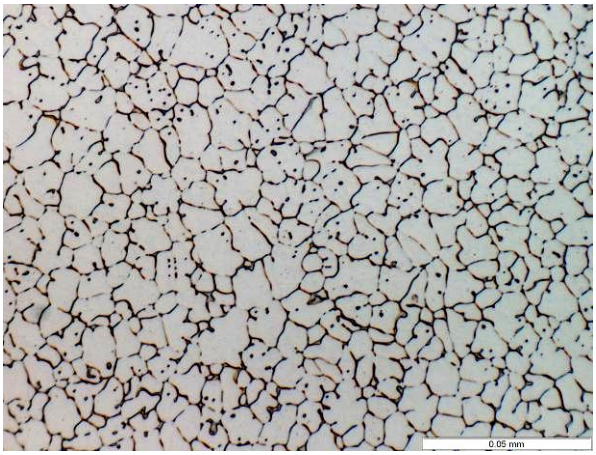

FZ Microstructure - A

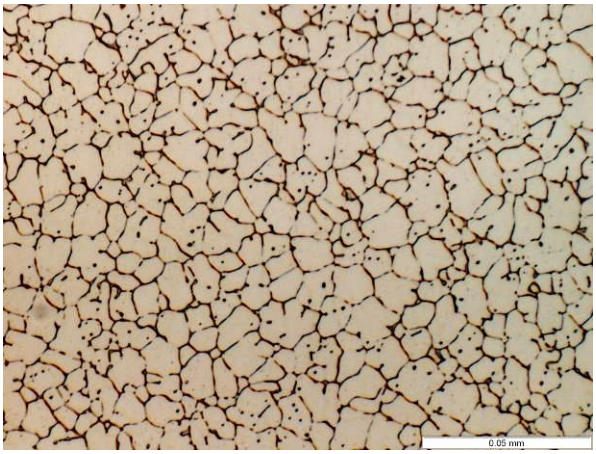

FZ Microstructure - B

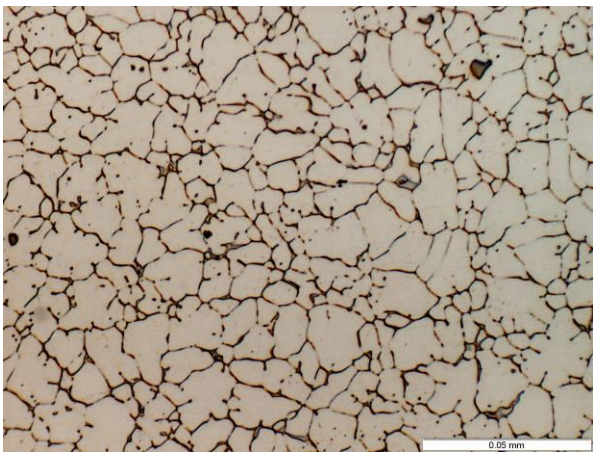

FZ Microstructure - C

Figure 4.5.9 – Microstructure for Sample 33

4.5.3 Porosity

Figure 4.5.10 shows the porosity measurements in the FZ of the 6 mm laser welded pates. Samples 30 and 32 showed the formation of large pores in the middle and lower region of the FZ as shown in Figure 4.5.1. The maximum porosity area percentage was 2.45 % (sample 32), whereas the minimum was 0.11 % (sample 28). The low heat input used to weld sample 28 resulted in having very low porosity area percentage in the FZ. As the welding speed decreased to 3 m/min (sample 29), it caused a slight increase in the porosity % due to increase in the laser heat input (refer to section – 4.1.3). Changing the keyhole mode from open to blind in sample 30 and 32 forced the vapor to escape only from the top opening of the keyhole, and due to excessive heat input, some of the pores coalesced and formed large pores which were entrapped in the molten pool during their floating time. This is supported by comparing the porosity % of samples 32 and 30. Sample 30 showed fluctuation between close and open keyhole whereas sample 32 had only a blind keyhole and that caused to have a higher porosity % in sample 32. The pores distribution for the samples shows that the typical pore diameter was between 15 – 25 micron and majority was less than 100 micron. Figure 4.5.11 shows an example of pore with a diameter of around 50 micron near the PMZ. Comparing the three fully penetrated samples (29, 31, and 33), the porosity area % was in the same level which is below 0.25%.

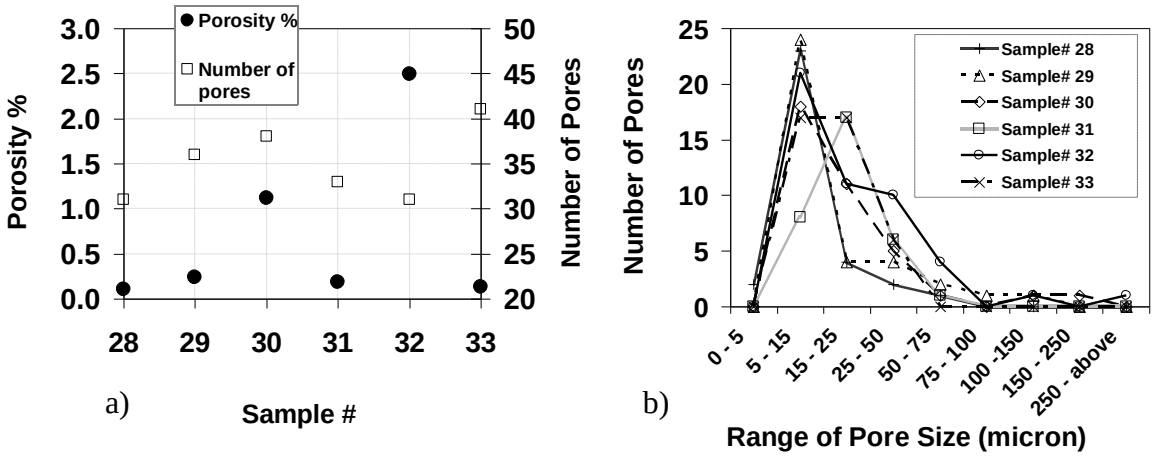

Figure 4.5.10 – Porosity Formation during Laser Welding of 6 mm Plates a) Porosity Area Percentage b) Pores Distribution

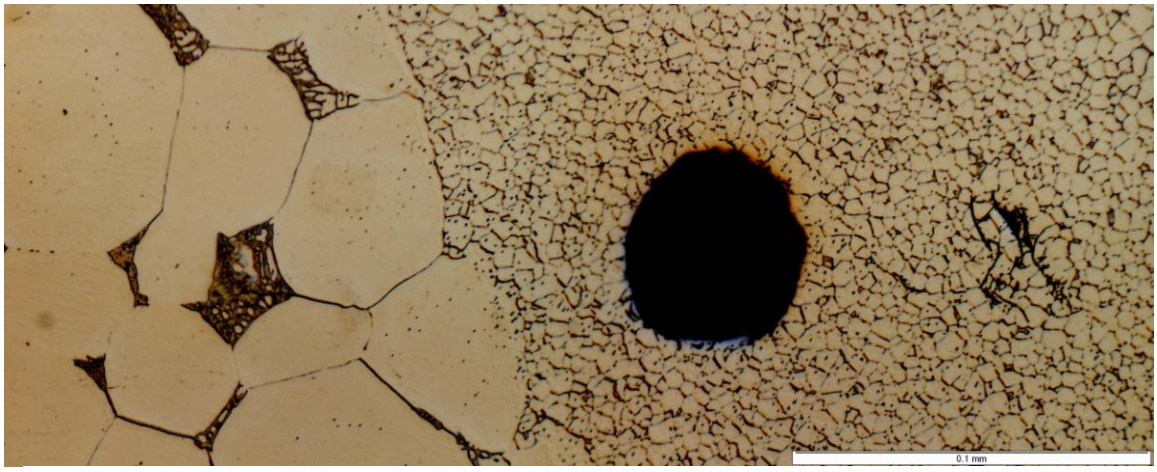

Figure 4.5.11 – Pore with a diameter 50 µm formed near the PMZ for sample# 32

4.5.4 Cracks

Solidification cracks for the 6 mm welded plates are measured as shown in Figure 4.5.12. The maximum crack length observed was 0.8 mm (sample 32). Comparing the crack lengths of the good – quality casting with samples (1 – 16) which have lower quality, the good quality casting resulted in the reduction of the solidification crack length from 2.5 mm to 0.8 mm. The geometrical defects and the high porosity % in sample 32 were the main reason for the initiation and propagation of the cracks as shown in Figure 4.5.13. It is interesting to view the cracks in sample 28 (Figure 4.5.14), it had a low porosity % and

no geometrical defects, but the crack lengths were high compared with full penetrated samples. Because this sample was near the conduction welding mode, the temperature gradient in the weld pool was high which caused the increase in the mechanical restraint and therefore the increase in the crack susceptibility [45]. This temperature gradient could activate the micro segregation of the low melting elements and caused cracks due to the imbalance between the shrinkage of the primary solidified phase and the feeding liquid [36].

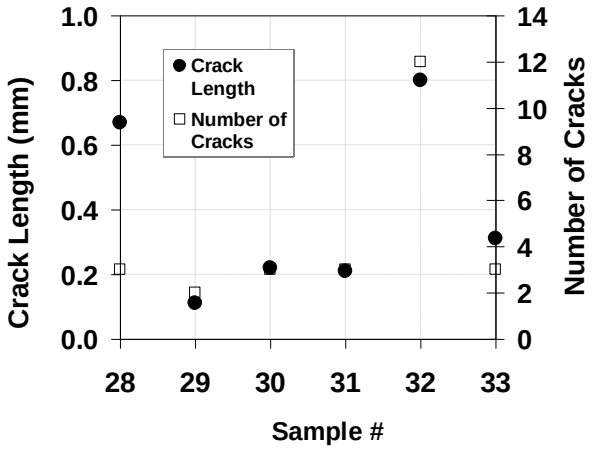

Figure 4.5.12 – Solidification Crack length for the 6 mm

The rest of the samples exhibited solidification cracks less than 0.4 mm. The main source of the cracks was the porosity and the propagation between the pores. Samples 29, for instance, showed a minimum solidification crack length of 0.11 mm. As noted from the previous porosity distribution chart (Figure 4.5.10), the majority of the pores were small due to the welding at open keyhole mode and higher speed (3 m/min) compared with samples 31 and 33 which were welded at open keyhole mode but at lower welding speed (2 m/min). Distribution of small pores in the FZ would decrease the probability that the pores will be linked together through a crack [36].

The micrographs for other samples can be seen in the appendix (A.3).

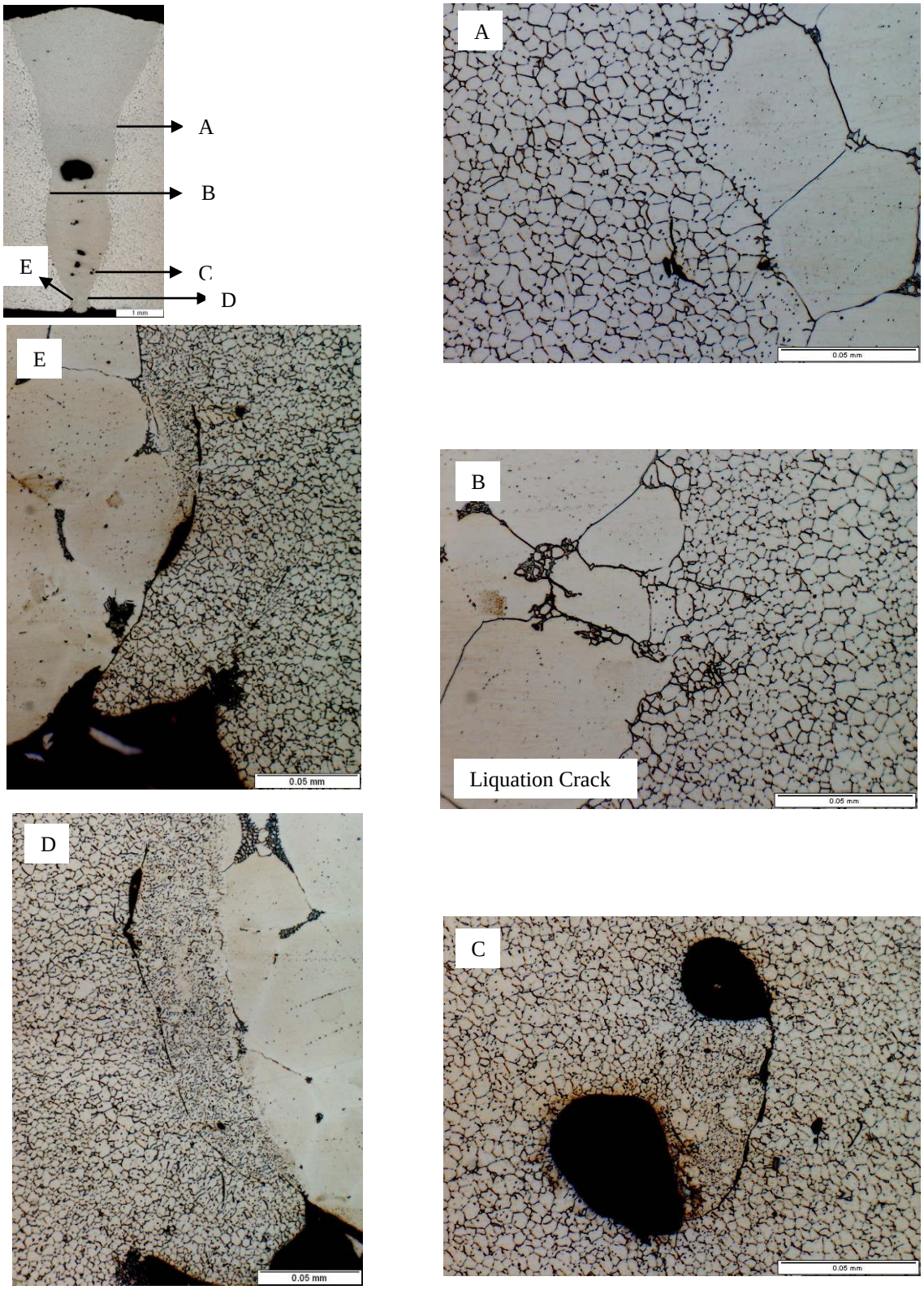

Figure 4.5.13 – Solidification and Liquation Cracks for Sample 32

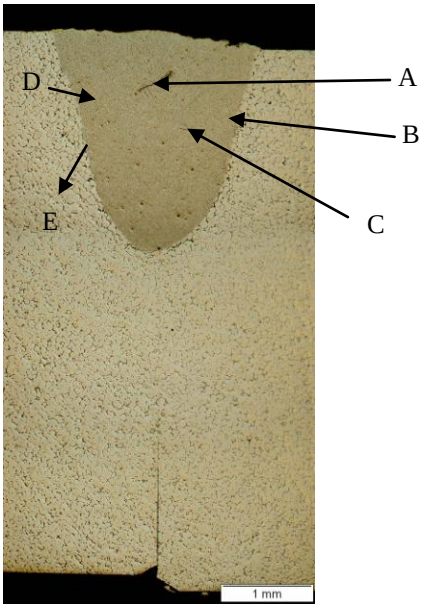

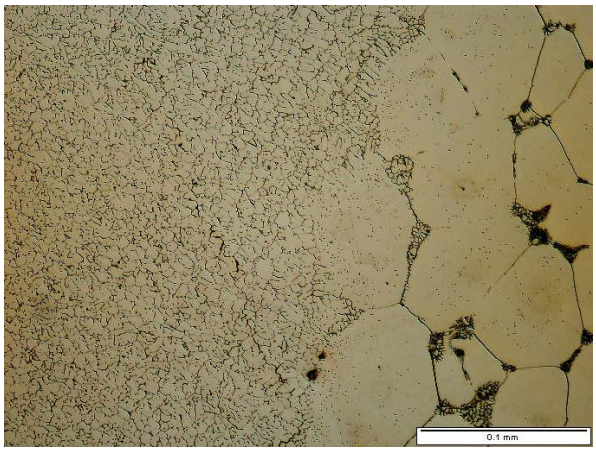

Crack - B

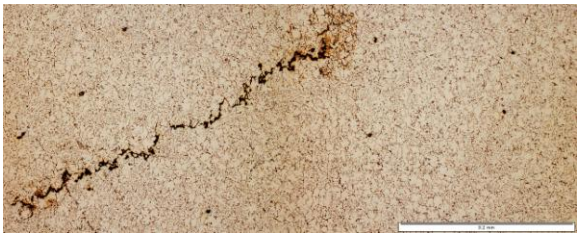

Crack - A

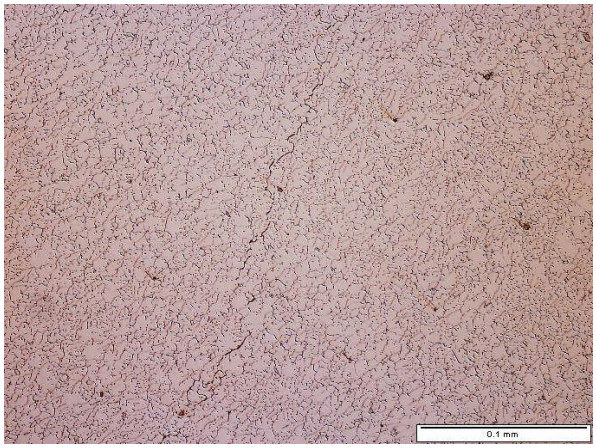

Crack - C

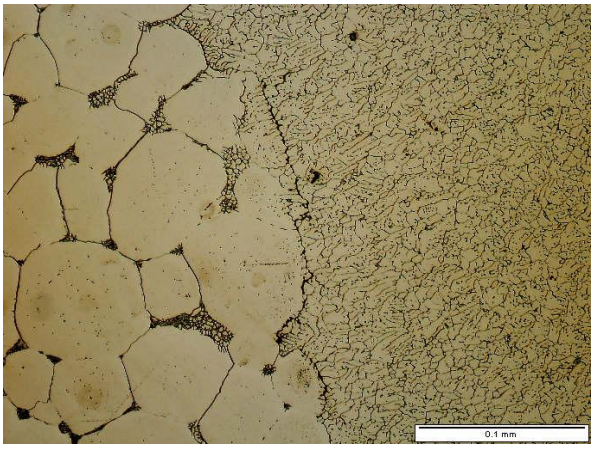

Crack - E

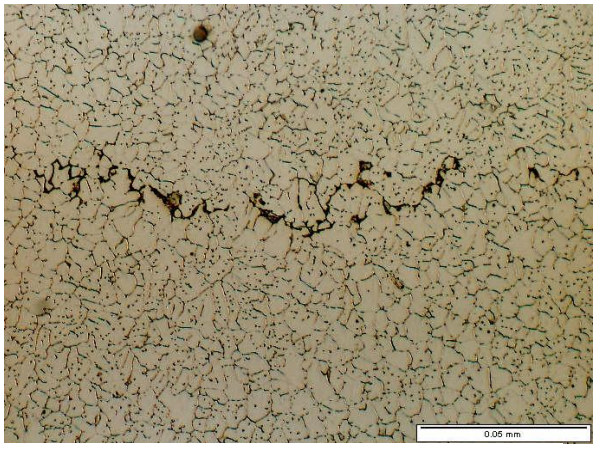

Crack - D

Figure 4.5.14 – Solidification Cracks for Sample 28

4.5.5 Mechanical Properties

Only the welded plates with full penetration (samples 29, 31 and 33) were used to investigate the mechanical properties of the 6 mm plates thickness. These samples were studied in both conditions as welded and the heat treated conditions. The microhardness profiles for the two groups are shown in Figure 4.5.19. On average there was a drop of 10 HV in the FZ hardness for the as welded condition samples whereas the heat treated samples had a drop of 5 HV. The average hardness in the center line of the FZ was calculated for both groups as shown in Table 4.5.3.

The heat treatment caused 3 to 7 HV increase in the hardness of the FZ, but it is still lower than that of the BM. Although the heat input used to weld the 6 mm plates was much higher than the heat input used to weld the 2 mm plates, the HAZ width was similar for both (around 2 mm). This is one important characteristic in laser welding; that is the increase in heat input will have less effect on the FZ and HAZ width compared with the conventional welding. The main reason is that in laser welding, the power is distributed through the keyhole wall all over the plate thickness, whereas in the convectional welding the power is concentrated on the top surface and is transferred by across material thickness.

Table 4.5.3 – Average Vickers Hardness in the Center Line of the FZ for the full penetrated 6 mm laser welded plate

Sample #	Vickers Hardness as welded condition	Vickers Hardness heat treated
29	64.3	67.3
31	61.8	68.3
33	62.3	65.2

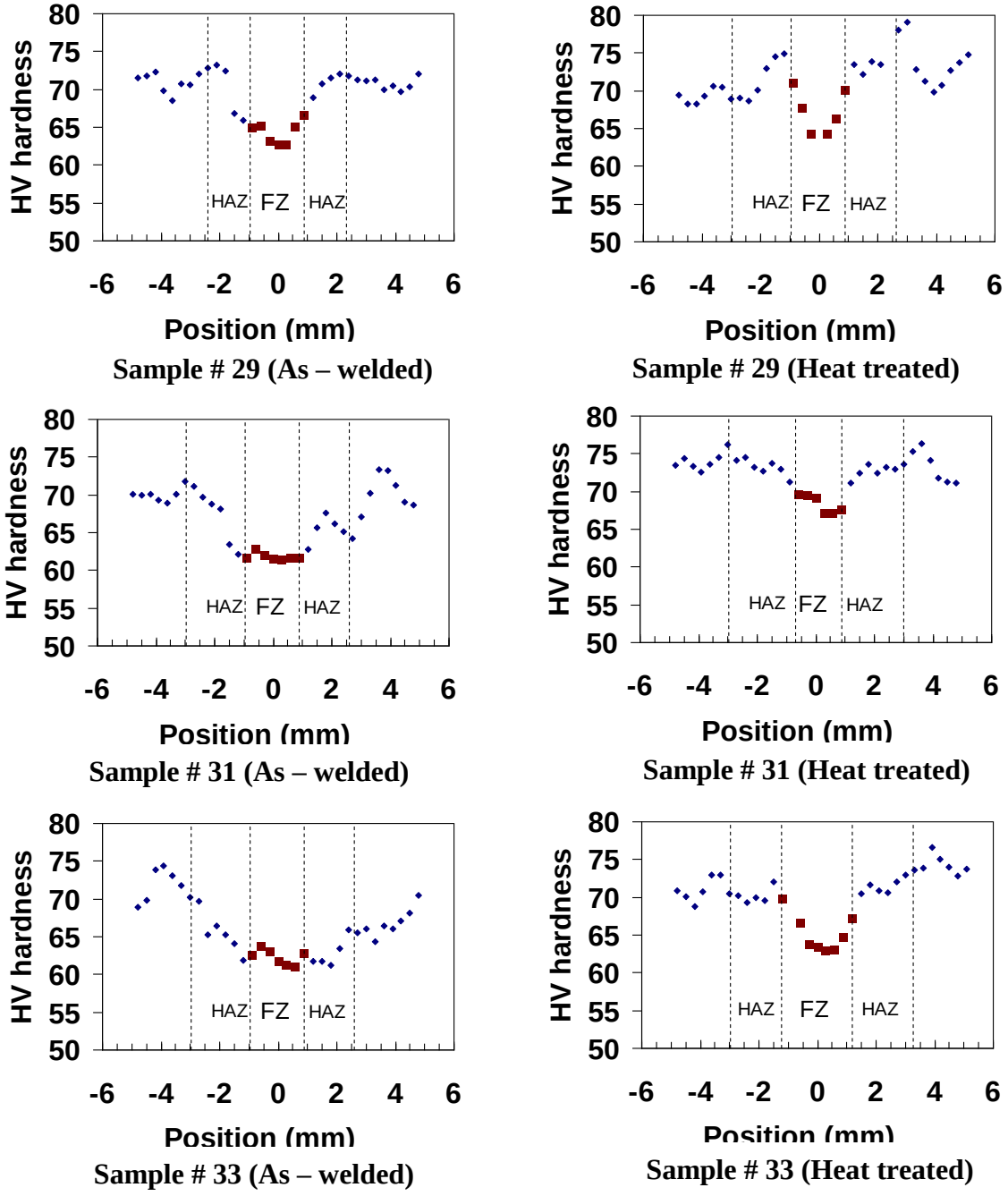

Figure 4.5.19 – Microhardness Profiles for the Full Penetrated 6 mm Laser Welded Plates in a) as – Welded Condition b) Heat Treated

Table 4.5.4 shows the tensile properties of samples 29, 31, and 33 for the as welded and heat treated conditions. As indicated in the table, all the samples fractured in the HAZ – PMZ interface except two. The microstructure which was discussed in section 4.5.2 showed that the HAZ – PMZ interface exhibited a liquation of some grains boundaries near the PMZ. In general, adding filler wire (samples 31 and 33) improved the tensile strength of the joint compared with the autogenous welding (sample 29). The joint efficiency was calculated for the three samples as shown in Figure 4.5.20. The tensile properties of the BM are shown in Table 4.5.5. The joint efficiency was increased by 3 to 5% by adding the filler wire since it reduced the effect of underfill and notching in the FZ. The joint efficiency was reduced by 5% after heat treatment compared with as welded condition.

The high joint efficiency between 85 – 95 % indicated that the defect levels for the three samples (29, 31 and 33) were similar. This also can be confirmed using Weibull analysis for the tensile strength for the three samples. The three samples had different process parameters but the comparison is taken from the joint quality point of view. Figure 4.5.21 shows that the three samples have a high Weibull modulus 35.12 (as welded condition) and 25.59 (heat treated). This high m value reflects the consistency of the tensile strength of these samples and suggests that there is no significant variation in the defect levels for the three samples.

Table 4.5.4 – Tensile properties of the Full Penetrated 6 mm Laser Welded Plates

Sample #	As Welded Condition			Heat Treated		
	TS (Mpa)	El%	Failure location	TS (Mpa)	El%	Failure location
29 - 1	202.4	4.6	PMZ - HAZ	187.4	2.9	PMZ - HAZ
29 - 2	210.4	4.7	HAZ	212.7	6.0	PMZ - HAZ
29 - 3	219.5	6.6	PMZ - HAZ	193.6	3.7	PMZ - HAZ
31 - 1	220.1	6.2	PMZ - HAZ	203.5	4.5	PMZ - HAZ
31 - 2	220.2	6.4	PMZ - HAZ	201.3	4.1	PMZ - HAZ
31 - 3	------	------	------	211.6	5.9	PMZ - HAZ
33 - 1	207.8	4.2	PMZ - HAZ	197.4	3.5	PMZ - HAZ
33 - 2	214.4	5.2	BM	217.7	5.8	PMZ - HAZ
33 - 3	222.3	5.9	PMZ - HAZ	207.1	4.0	PMZ - HAZ

Table 4.5.5 – Tensile Properties of ZE41A-T5 BM

Rank #	TS (Mpa)	El%
1	242.9	8.9
2	239.6	--
3	237.4	8.2
4	207.1	4.5

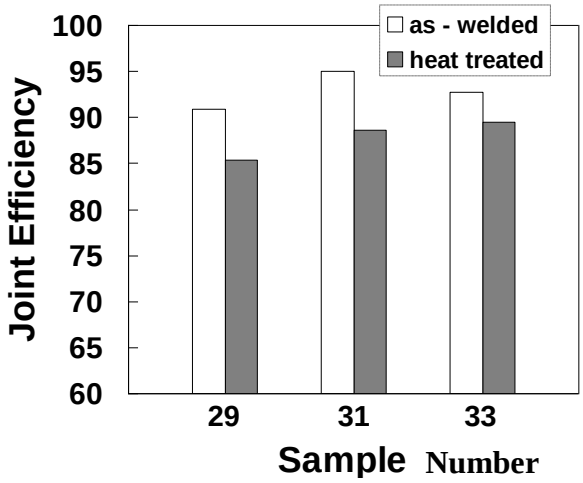

Figure 4.5.20 – Joint Efficiency of the full Penetrated 6 mm laser Welded Plates

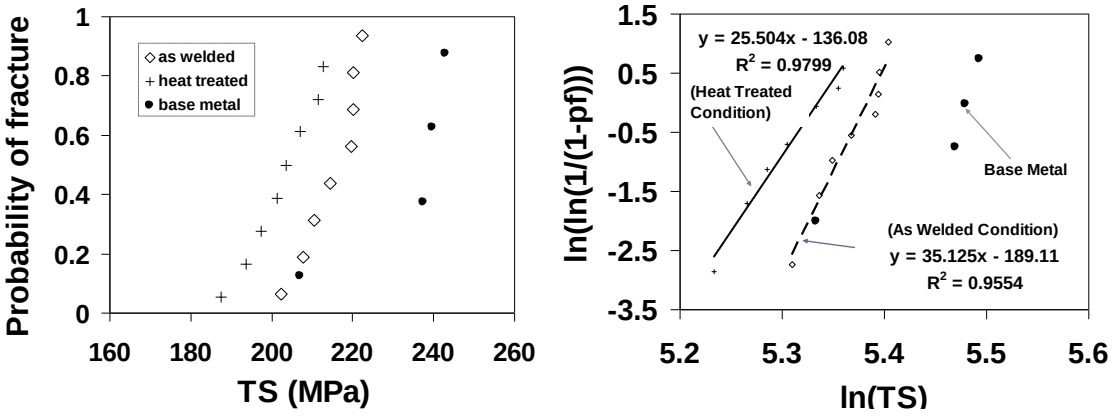

Figure 4.5.21 – Weibull Statistical Analysis of the Tensile Strength of Samples 29, 31 and 33 a) Cumulative Plots of Tensile Strength b) Weibull Plots of Tensile Strength

4.6 Calculation of Laser Efficiencies from the Experimental FZ Geometry

4.6.1 Method

During keyhole laser welding process, the delivered laser beam by the laser head will pass through multiple stages till it is converted to effective power that melts the BM and produces the weld seam as shown in Figure 4.6.1 [48,49]. The keyhole will be created after overcoming the threshold surface intensity (I_s) which is determined by the material vaporization temperature (T_v), the thermal conductively (k) and the absoptivity at normal incidence (A) [39]:

$$I_s \propto \frac{T_v \cdot k}{A} \tag{4.6.1}$$

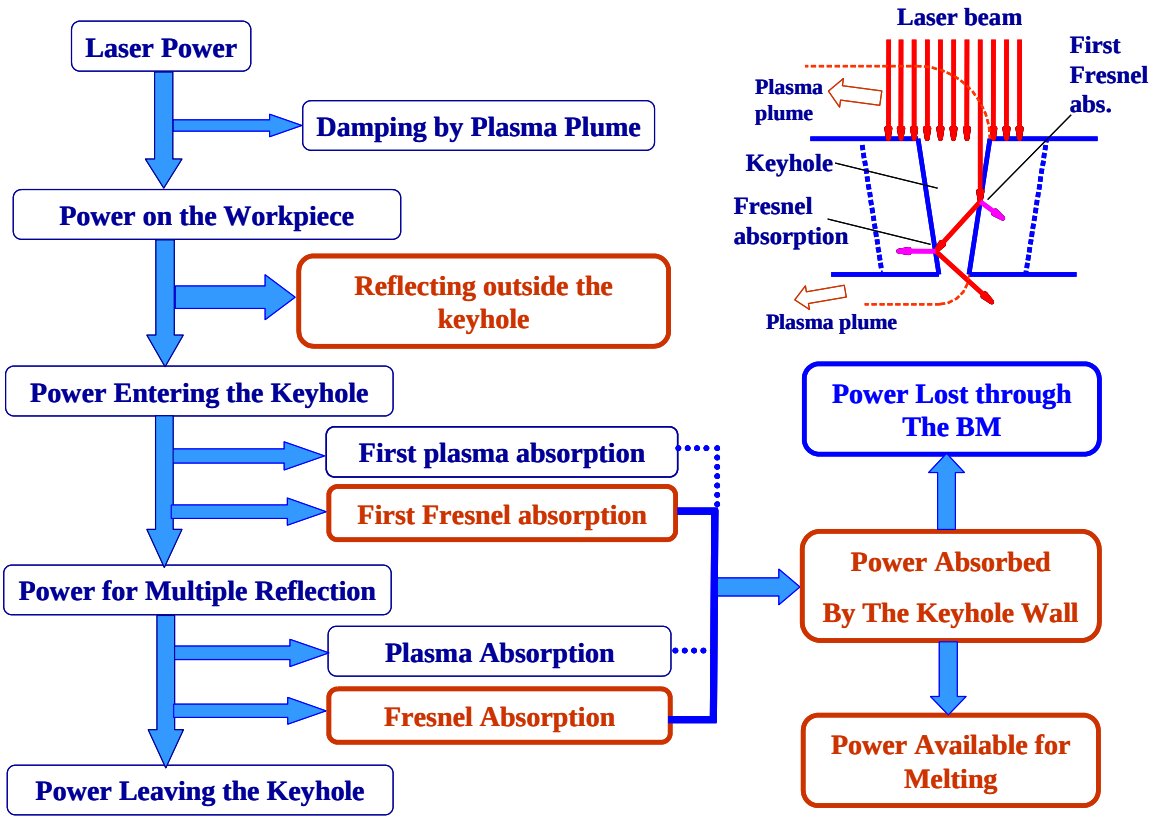

Figure 4.6.1 Schematic Diagram Showing the Power Balancing during Keyhole Laser Welding

At steady state and before the laser beam enters the keyhole, part of the laser power (P) will be lost due to reflection (P_{ref}) and the absorption by plasma plume (P_{plume}) [40]:

$$P_{\text{entering the keyhole}} = P - P_{\text{ref}} - P_{\text{plume}} \quad (4.6.2)$$

Before the laser ray reaches the keyhole wall, part of the ray intensity will be absorbed by the plasma inside the keyhole. When the laser ray reaches the keyhole wall it will be absorbed partially, depending on the wall angle and material properties. The reflected intensity will pass through multiple reflections inside the keyhole. In each reflection the laser ray will lose some intensity by plasma absorption. After the multiple reflection the laser ray will leave the keyhole from the top for blind keyhole or from bottom and top for open keyhole.

The coupling efficiency (η_A) is defined as the portion of the laser power available to the workpiece, in other words it is equal to the ratio of the absorbed power (P_{abs}) by the keyhole wall to the total laser power (P):

$$\eta_A = \frac{P_{abs}}{P} \quad (4.6.3)$$

It is worth noting that not all the absorbed laser power will be consumed for the melting but part of it will be lost by conduction through the BM. The thermal efficiency (η_{th}) is defined as the portion of the absorbed laser power that produced the weld seam [39], or it is the ratio of the heat of melting ($P_{melting}$) divided by the absorbed laser power (P_{abs}):

$$\eta_{th} = \frac{P_{melting}}{P_{abs}} \quad (4.6.4)$$

The laser process efficiency (η_P) is composed of a coupling efficiency (η_A) and a thermal efficiency (η_{th}) [39]:

$$\eta_P = \eta_A . \eta_{th} \tag{4.6.5}$$

By substituting equations 4.6.3 and 4.6.4 in equation 4.6.5, the laser process efficiency (η_P) will be defined as the ratio of the melting power divided by the total laser power:

$$\eta_P = \frac{P_{melting}}{P} \tag{4.6.6}$$

Swift-Hook and Grik [6,46] defined the melting ratio (MR) as the fraction of total incident laser power that is used to melt the weld metal:

$$MR = \frac{V.\ A_w . \rho [\, C_p (T_{mp} - T_o) + \Delta H_f \,]}{P} \tag{4.6.7}$$

Where A_w is the melted base metal area (FZ area), ρ is density, C_p is the specific heat, Δ H_f is the latent heat of fusion, V is welding speed, T_{mp} is the solidus temperature, T_o is room temperature and P is the incident laser power. Hence based on this definition the melting ratio (MR) is equal to the laser process efficiency (η_P):

$$\eta_p = \frac{V.\ A_w . \rho [\, C_p (T_{mp} - T_o) + \Delta H_f \,]}{P} \tag{4.6.8}$$

To calculate the coupling efficiency (η_A) the absorbed laser power by the keyhole must be estimated from the given FZ geometry. Rosenthal [47] derived the temperature distribution in the work piece induced by the moving line heat source as:

$$T(r,\varphi) = T_o + \frac{P'}{2\pi k} K_o(Pe) e^{-Pe.\cos(\varphi)} \tag{4.6.9}$$

Where P` is the line source strength (W / m), T (r, φ) is the temperature field in the workpiece (K), T_o is the ambient temperature (K), k is thermal conductivity , K_0 is the modified Bessel function of second kind and zero order, Pe is Peclet number, V is welding speed, and kd is the thermal diffusivity (m^2/s) [40,48].

$$Pe\,(Peclet\ number) = \frac{Converction\ heat}{Conduction\ heat} = \frac{r.V}{2.kd} \tag{4.6.10}$$

The thermal diffusivity is equal to the ratio of thermal conductivity divided by heat capacity:

$$Kd = \frac{k}{\rho.C_p} \tag{4.6.11}$$

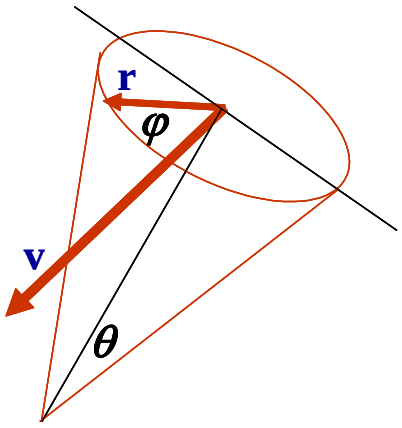

Figure 4.6.2 – Polar coordinate for the Keyhole and the Moving Line Source

The coordinates (r and φ) is measured from the beam axis which is assumed to be in the center of a conical keyhole shape [40] as shown in Figure 4.6.2. For a given FZ geometry the average line source strength can be calculated from equation 4.6.9, by applying the boundary condition at the PMZ; T is equal to $T_{melting}$, r is half the average width of the FZ and φ is taken to be $\pm\pi/2$ since it can locate the PMZ. After calculating the average source strength, the power absorbed by the keyhole can be calculated by multiplying the average source strength ($P'_{average}$) by the penetration depth (Pd) [40]:

$$P_{abs} = P'_{average} . Pd \qquad (4.6.12)$$

4.6.2 Results

The calculated coupling, thermal and process efficiencies for all tested samples are shown in Table 4.6.1. The physical properties for pure Mg at melting point (refer to appendix) were used for this purpose because the properties of the ZE41A-T5 alloy at the melting point are not available. Figure 4.6.3 shows the effect of welding speed on the coupling, thermal and process efficiencies. As the welding speed increased from 4 to 7 m/min, the coupling efficiency was increased from 25 to 42 %. In Figure 4.6.4, the effect of the welding speed on the keyhole shape and on the multiple reflections inside it was simulated using a laser keyhole welding model as will be described in the next section. As shown in Figure 4.6.4, the keyhole angle with y-axis was increased from 3.9 to 4.5 degree as the welding speed was increased from 4 to 6 m/min. This increase in speed caused to decrease the root keyhole width and caused the increase in the number of the multiple reflections. The increase in the coupling efficiency supported by the hourglass

Table 4.6.1 - Laser Efficiencies for the Experimental Tested Samples

Sample #	Effective Parameters	Coupling Efficiency % Pabs / Ptotal	Thermal Efficiency % Pmelting / Pabs	Process (Melting) Efficiency % Pmelting / Ptotal
	Effect of Welding Speed on Efficiencies - 2 mm plates			
1	welding speed = 4 m/min	25.5	40.7	10.4
2	welding speed = 5 m/min	28.2	36.1	10.2
3	welding speed = 6 m/min	30.4	32.7	9.9
4	welding speed = 7 m/min	42.7	32.7	14
	Effect of Gap Size on Efficiencies - 2 mm plates			
5	gap size = 0.1 mm	33	34.4	11.4
6	gap size = 0.2 mm	34.8	33.5	11.6
7	gap size = 0.3 mm	31.4	33.2	10.4
8	gap size = 0.4 mm	40.5	33.3	13.52
9	gap size = 0.5 mm	29.76	36.7	10.9
10	gap size = 0.6 mm	28.2	36.1	10.2
	Effect of Laser Power on Efficiencies - 2mm plates			
11	laser power = 2.5 kW	45.7	40.16	18.35
12	laser power = 2.75 kW	47.9	37.35	17.9
13	laser power = 3 kW	38.8	37.3	14.5
14	laser power = 3.5 kW	35.4	33.8	12
15	laser power = 3.75 kW	35.61	37.37	13.3
16	laser power = 4 kW	40.73	33.2	13.5
	Effect of Defocusing on Efficiencies - 6 mm plates			
25	Defocusing = 0 mm	53.2	41	21.8
26	Defocusing = -2 mm	54.6	38.868	21.24
27	Defocusing = -4 mm	29.2	41.48	12.1
	Comparison of Efficiencies between Laser Welding of 6 mm plate with and Without Filler Wire			
29	6 mm thickness (Autogenous)	70.35	35.05	24.65
30	6 mm thickness (Applying Filler Wire)	58.3	43.3	25.2
	Efficiencies for Successful Full penetrated Samples (2 and 6 mm plates)			
17 - 22	2 mm thickness (filler wire)	36.76	36.103	13.27
29	6 mm thickness (Autogenous)	70.35	35.05	24.65
31	6 mm thickness (filler wire @ 0.2 mm gap)	52.4	37.8	19.8
33	6 mm thickness (filler wire @ 0.4 mm gap)	52.75	38.19	20.15

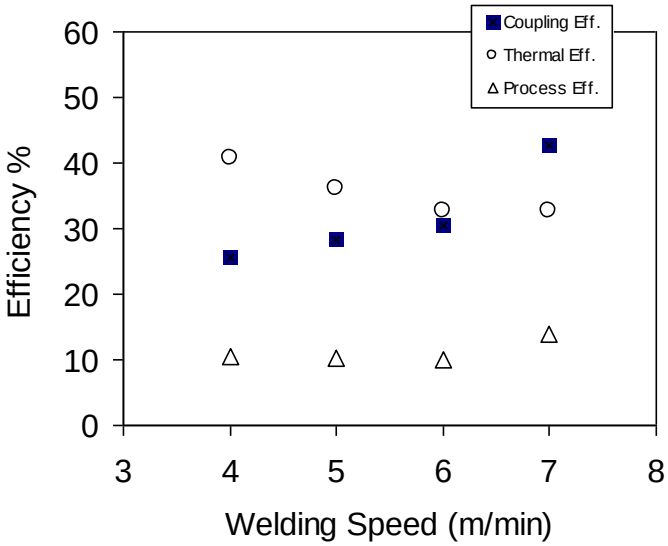

Figure 4.6.3 – Effect of Welding Speed on Coupling, Thermal and Process Efficiencies.

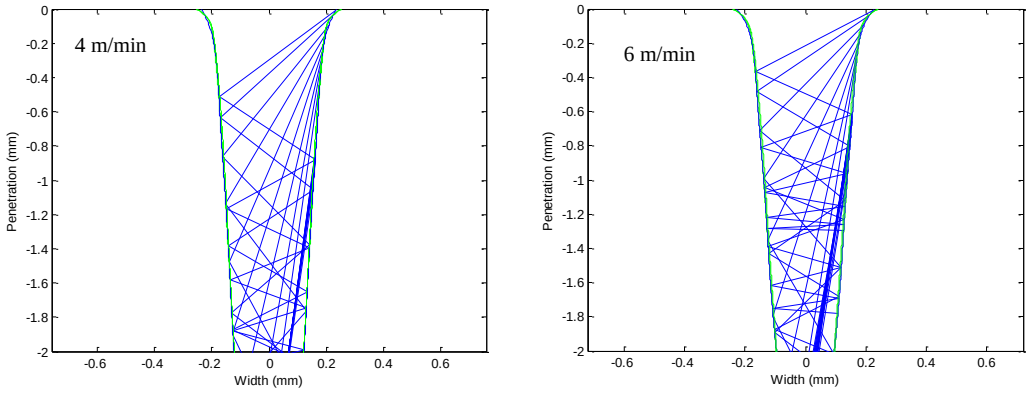

Figure 4.6.4 – Simulation Showing the Effect of Welding Speed on the Keyhole Shape and the Multiple Reflections

geometry for these samples proves that the keyhole was open at the root. If the keyhole was partially penetrated and blind at the root, the effect of increasing the welding speed on the coupling efficiency will be reversed. On the other hand Figure 4.6.3 shows that the thermal efficiency was reduced by increasing the welding speed. This reduction in thermal efficiency balanced the increase in the coupling efficiency and thus there was no significant decrease in the melting or process efficiency.

The effect of gap size on the efficiencies is shown in Figure 4.6.5. The increase in feed rate of the filler wire for the gap size from 0.1 to 0.6 mm did not cause a significant change in the process efficiency which means that the reflection losses due to interaction of the laser beam with filler wire were almost constant for different feed rate. The coupling efficiency was at maximum value at 0.4 mm gap size, which seems to be a suitable size for molten flow and formation of the keyhole.

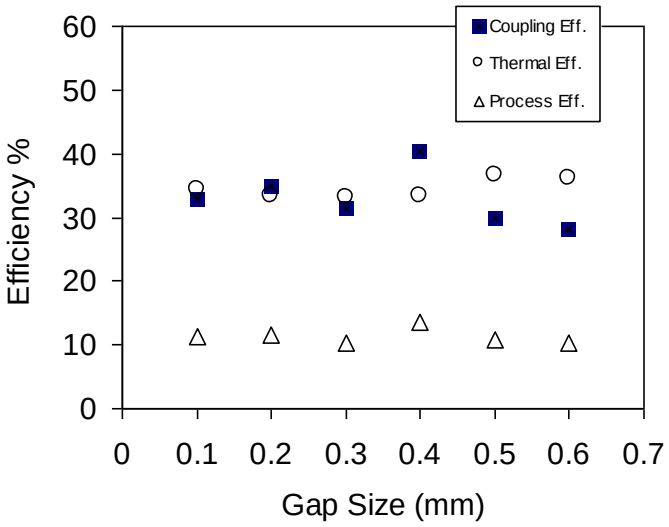

Figure 4.6.5 – Effect of gap size on Coupling, Thermal and Process Efficiencies.

Figure 4.6.6 shows the effect of laser power on coupling, thermal and process efficiencies. The partial penetration welding for laser power below 3.5 kW showed higher process and coupling efficiencies than those for the open keyhole mode. At partial penetration welding the beam will be trapped inside the keyhole and the only way to escape is through the top keyhole opening, whereas the open allows more waste of the laser beam because of the open keyhole root as indicated in Figure 4.6.7.

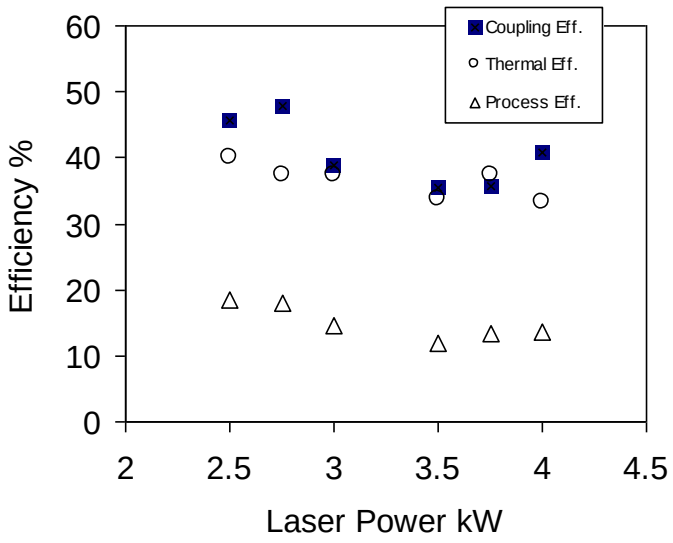

Figure 4.6.6 – Effect of Laser Power on Coupling, Thermal and Process Efficiencies

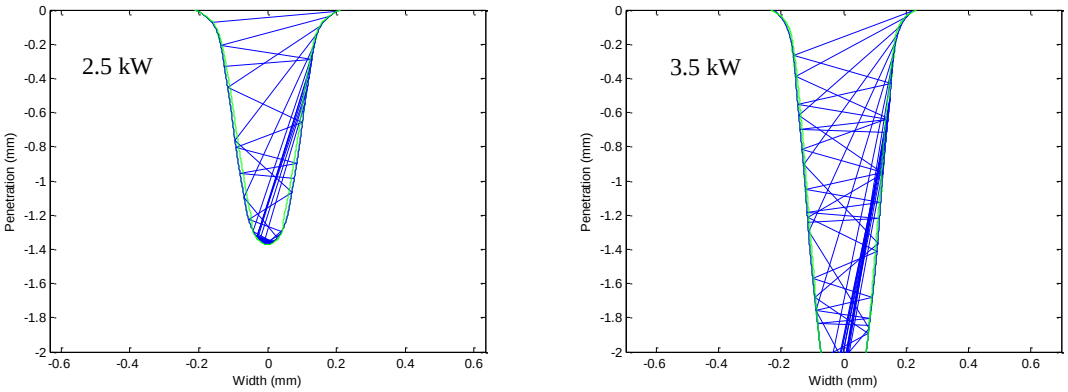

Figure 4.6.7 – Simulation Showing the Effect of Laser Power on Keyhole Shape and the Multiple Reflection

The effect of defocusing on the three efficiencies can be seen in Figure 4.6.8. The Bead-on-plate sample welded with -4 mm defocusing faced a fluctuation between keyhole and conduction welding mode since the surface intensity was near the threshold intensity as discussed in section 4.5. This conduction mode or the shallow keyhole caused a reduction in the coupling efficiencies because the laser beam had less interaction with molten metals.

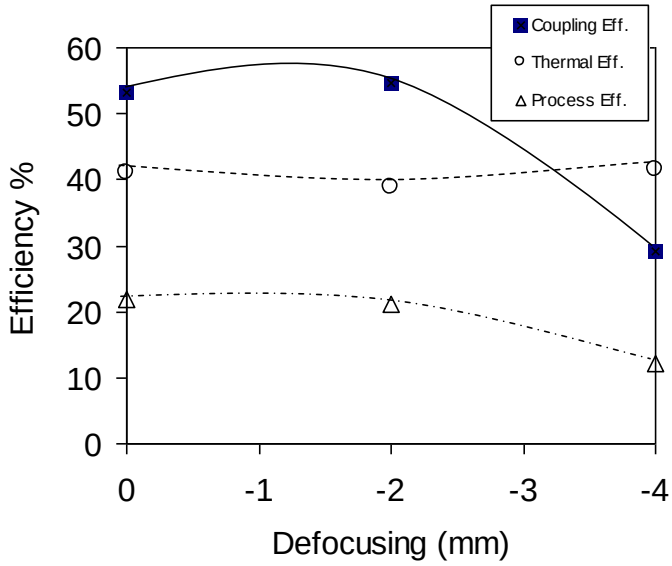

Figure 4.6.8 – Effect of Defocusing on Coupling, Thermal and Process Efficiencies

Table 4.6.1 shows that applying filler wire (sample 30) resulted in a reduction in the coupling efficiency by 12% from the autogenous welding (sample 29) due to the reflection of laser rays outside the keyhole. Figure 4.6.9 shows a comparison between the coupling, thermal and melting efficiencies of the successfully welded 2 and 6 mm plates. The coupling efficiency increased for the 6 mm plates due to the multiple reflection of the laser beam inside the keyhole. The increase in penetration will increase the chance of the multiple reflection and plasma absorption inside the keyhole. Figure 4.6.9 also shows the comparisons of the efficiencies for the 6 mm laser welded plates at 0.2 and 0.4 mm gap size, which indicates that the feed rate had no influence on the variation of the coupling, thermal and process efficiency.

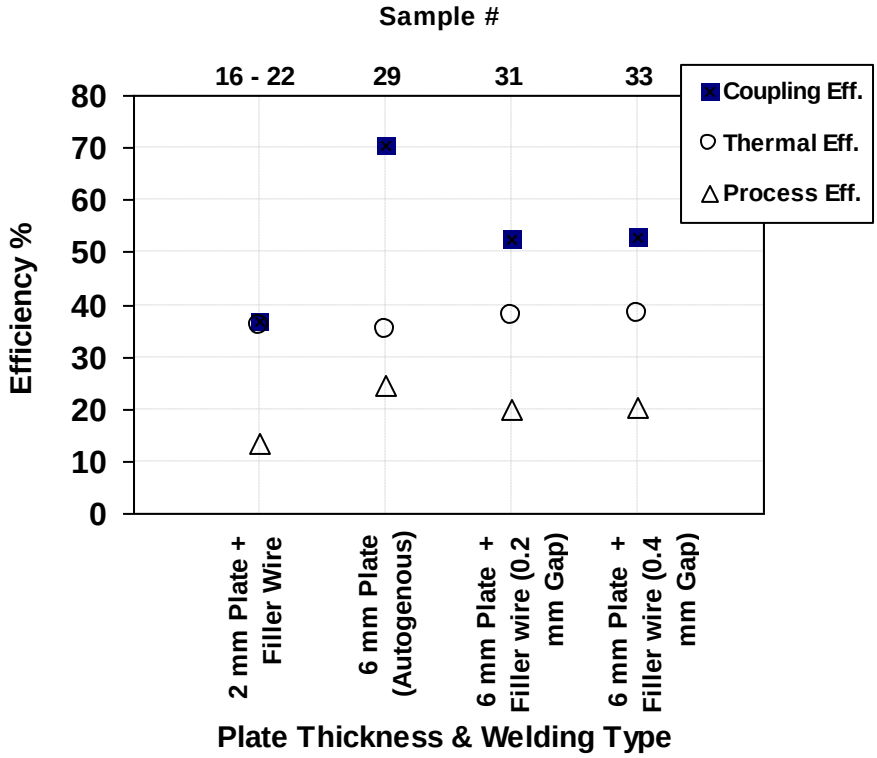

Figure 4.6.9 – Effect of Penetration Depth and Welding Type on the Coupling, thermal and Process Efficiencies

4.7 Modeling of Keyhole Laser Welding

The objective of this section is to simulate the laser welding process through combining different models and concepts used to describe the keyhole and fusion zone generated during the keyhole laser welding. The Model will help to develop better understanding of the laser welding process and the effect of different parameters on the keyhole and fusion zone profiles. Also the model can reduce the time necessary to find the suitable parameters to produce full penetration successful weld joints. In this model the following consideration and assumption were implemented:

- The keyhole profile is symmetrical in the plane perpendicular to the welding direction.
- The laser heat source is assumed to be a line heating source acting along the center of the keyhole.
- The energy balance between the heat loss at the keyhole wall and the absorbed intensity was solved in the plane perpendicular to welding direction which is the plane of interest that enables the calculation the melting temperature isothermal profile.
- The intensity of the laser beam is taken to be a Gaussian – like distribution [40, 48].
- Reflection of laser ray from the keyhole wall follows the Fresnel formulation which assumes that the angle of incidence equals to the angle of reflection [49].

4.7.1 Energy Balance at the Keyhole Wall for First Fresnel Absorption

The heat loss from the keyhole wall depends on the absorbed laser intensity which is described by the following equation [48]:

$$q_v = I_{ab} \cdot \tan(\theta) \qquad (4.7.1)$$

Where q_v is heat flow in a particular keyhole layer (w/m^2), θ is the angle of the keyhole at the particular layer, and I_{ab} is the absorbed intensity at the keyhole wall (Figures 4.7.1 and 4.7.2). The direct absorption of the incoming ray incidence through the keyhole wall called the first Fresnel absorption.

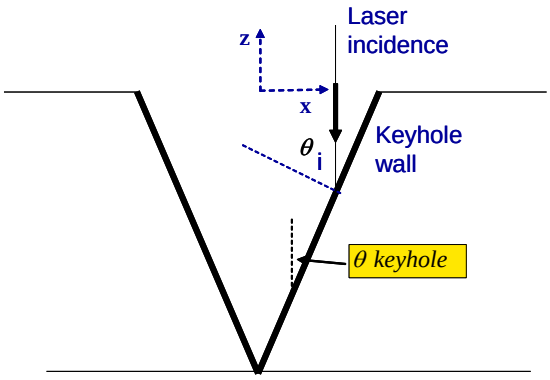

Figure 4.7.1 – the coordinate system for the Keyhole Layers

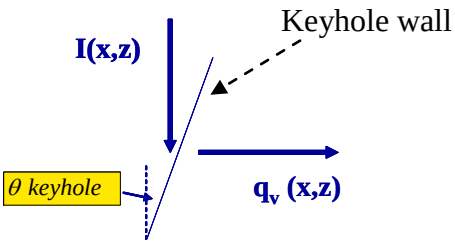

Figure 4.7.2 – Energy Balance for First Fresnel Absorption.

4.7.2 Heat Flow Equation at the Keyhole Wall

The heat absorbed through the keyhole wall is equal to the heat loss by the keyhole as derived by Kaplan [48]. The heat flow can be determined by applying Fourier's law of heat conduction that can be simplified as:

$$q = -k \frac{\partial T}{\partial r} \qquad (4.7.2)$$

By substituting the moving line source temperature field equation (4.6.9) into equation 4.7.2, the following heat flow equation was derived [40,48]:

$$q(r,\varphi) = \frac{1}{r}(T - T_o).k.Pe.(Cos\,\varphi + \frac{K_1(Pe)}{K_0(Pe)}) \qquad (4.7.3)$$

Where q is the heat flow (w/m^2) and K_1 ( ) is the modified Bessel function of second kind and first order. The polar coordinates (r,φ) are shown in Figure 4.6.2. As mention before the plane of interest is perpendicular to welding direction therefore r is equal to $\pm x$, and φ is equal to $\pm\frac{\pi}{2}$.

4.7.3 Intensity Distribution for the Laser Beam

The intensity distribution of the laser beam is assumed to follow the Gaussian – like distribution. The maximum peak intensity (I_{oo}) is located in the focal plane at zero radius, and the intensity starts to fall as moving away from the focal point in x and/or z direction as shown in Figure 4.7.4. The intensity of the laser beam at any point can be calculated by the following equation [43,48]:

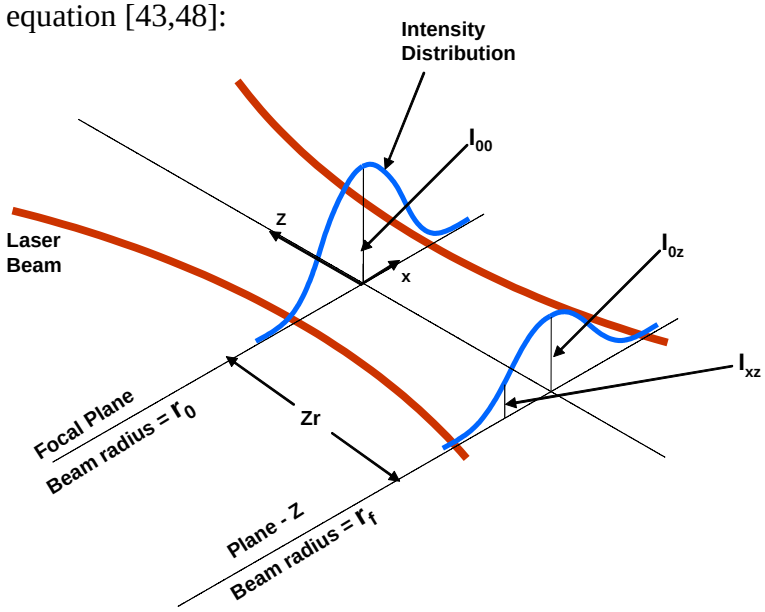

Figure 4.7.4 – Intensity Distribution for the Laser Beam [43]

$$I(x,z) = I_{0z} \cdot e^{-2x^2/r_f^2} \tag{4.7.4}$$

Where I_{oz} is the peak intensity at any z – plane and r_f is the beam radius at any z – plane and can be calculated by the following equations [43,48]:

$$I_{oz} = I_{00} \cdot \left(\frac{r_o}{r_f}\right)^2 \tag{4.7.5}$$

And,

$$r_f = r_o \cdot \left[1 + \left(\frac{z - z_0}{z_r}\right)^2\right]^{1/2} \tag{4.7.6}$$

Where Z_0 is the location of the focal plane relative to the plate top surface (defocusing distance), and Z_r is the Rayleigh length where the peak intensity at Z_r – plane equals to half the maximum intensity (I_{oo}), and can be calculated by the following equation:

$$Z_r = \pm 2\, r_o (f - number) \tag{4.7.7}$$

The maximum intensity can be computing using the following equation:

$$I_{oo} = \frac{2P}{r_0^2 \cdot \pi} \tag{4.7.8}$$

Where P is the laser power and r_o is the beam focal radius.

4.7.4 Fresnel Absorption Coefficient

The laser ray will experience a reflection and absorption by the keyhole wall, in this case the molten – vapor surface is considered to be specular which lead to have the angle of

incidence equal to the angle of reflection. The absorption coefficient of the laser ray can be calculated using Fresnel formula for circular or random polarized light as follows [49,51,52]:

$$\alpha_{Fresnel} = 1 - \frac{1}{2}\left(\frac{1+(1-\varepsilon\cos\phi)^2}{1+(1+\varepsilon\cos\phi)^2} + \frac{\varepsilon^2 - 2\varepsilon\cos\phi + 2\cos^2\phi}{\varepsilon^2 + 2\varepsilon\cos\phi + 2\cos^2\phi}\right) \quad (4.7.9)$$

Where ϕ is the angle between the incidence ray and normal to surface of the keyhole wall (Figure 4.7.5), and ε is material – dependant quantity. The absorptivity of Mg at perpendicular incidence for Nd:YAG laser is unknown. Therefore, a value for Al element 4% at 1.06 μm wavelength [39] was used. The value of ε was estimated by substituting $(\phi = 0, \alpha_{Fresnel}^{perpendicular} = 0.04)$ in equation (4.7.9) which was found to be 0.03. This value needs to be verified by testing the reflectivity of Mg at 1.06 μm wavelength for perpendicular incidence or at different angles. The calculated absorptivity of Mg at different angles is shown in Figure 4.7.5.

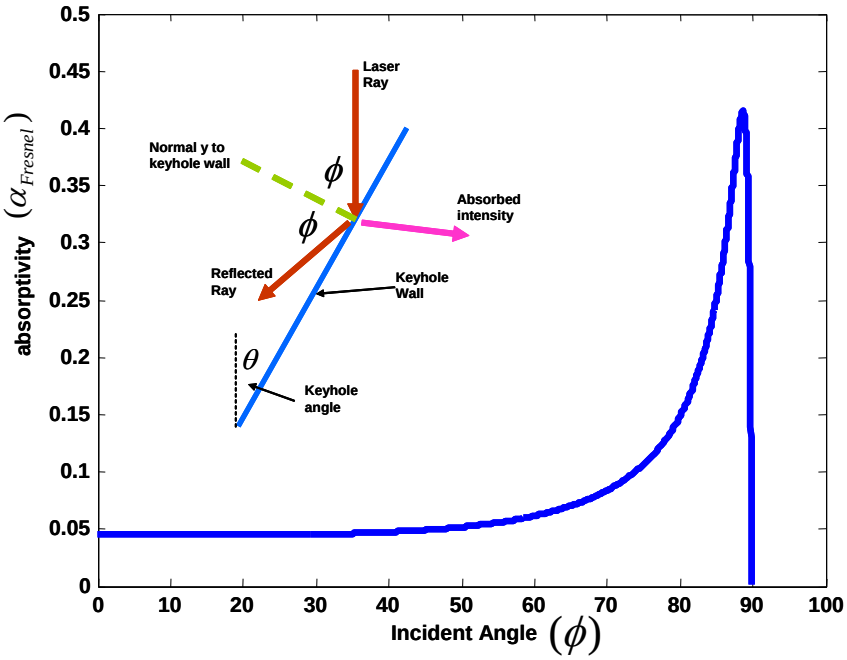

Figure 4.7.5 – Calculated Absorptivity of Al to Nd:YAG Laser Beam at Different Incident Angles at Room Temperature.

The absorbed intensity can be calculated by the following equation:

$$I_{ab} = I_{x,z} \cdot \alpha_{Fresnel} \tag{4.7.10}$$

4.7.5 Plasma Absorption

The effect of plasma absorption in the keyhole laser welding is a wider and less penetrating keyhole [49]. The absorbed intensity in the keyhole by the inverse Bremsstrahlung action will be deposited back to the keyhole wall by radiation [53]. The absorbed intensity by plasma can be calculated by the following equation [48,49]:

$$I_{Plasma} = I_{incident} - I_{incident} \cdot e^{-\alpha_{IB} L} \tag{4.7.11}$$

Where L is the path length of the ray inside the plasma, and α_{IB} is the inverse Bremsstrahlung coefficient, which is function of the density of the electrons, degree of ionization and temperature in the keyhole. The literature review showed that α_{IB} ranges from 100 to 200 m^{-1}. In this work an average value of 150 m^{-1} was used. The plasma absorption coefficient ($1 - e^{-\alpha_{IB} L}$) is proportional to the square of the wavelength. Therefore the plasma absorption in Nd:YAG laser is 1% of the plasma absorption in CO_2 Laser. Kaplan [48] reported that the plasma plume absorption outside the keyhole was in the range of 1% for different welding speed using CO_2 laser system. Therefore, the plasma plume was neglected here because of the short wavelength of the Nd:YAG laser, whereas the plasma absorption between the multiple reflection inside the keyhole were calculated while considering their deposit location.

4.7.6 Multiple Reflection of the Laser Ray

After calculating the keyhole profile by considering only the first Fresnel absorption, the keyhole profile was converted to polynomial equation using the least squares method in order, to calculate the slope and the Fresnel absorption coefficient at any location. Between two reflections the laser ray loses intensity because of the plasma absorption as mentioned above. The geometrical and intensity calculation between two reflections is demonstrated in Figure 4.7.6. The absorbed intensity from multiple reflections will work together with the direct Fresnel intensity to produce the total absorbed intensity in the particular layer [49], whereas the plasma plume will try to widen the keyhole. Therefore, the energy balance at the keyhole wall will be as follows [48,49,50]:

$$\tan(\theta_{keyhole}^{layer}) = \frac{q^{layer} - I_{plasma}^{layer}}{I_{Fr1}^{layer} + I_{Fr-Mr}^{layer}} \qquad (4.7.12)$$

$$\theta_{keyhole} = \tan^{-1}\left(\frac{dx}{dz}\right)$$

$$\phi_1 = \frac{\pi}{2} - \theta_{keyhole-1}$$

$$\theta_{h-1} = \phi_1 - \theta_{keyhole-1}$$

$$\phi_2 = \theta_{h-1} - \theta_{keyhole-2}$$

$$\alpha_{Fresnel} = f(\phi)$$

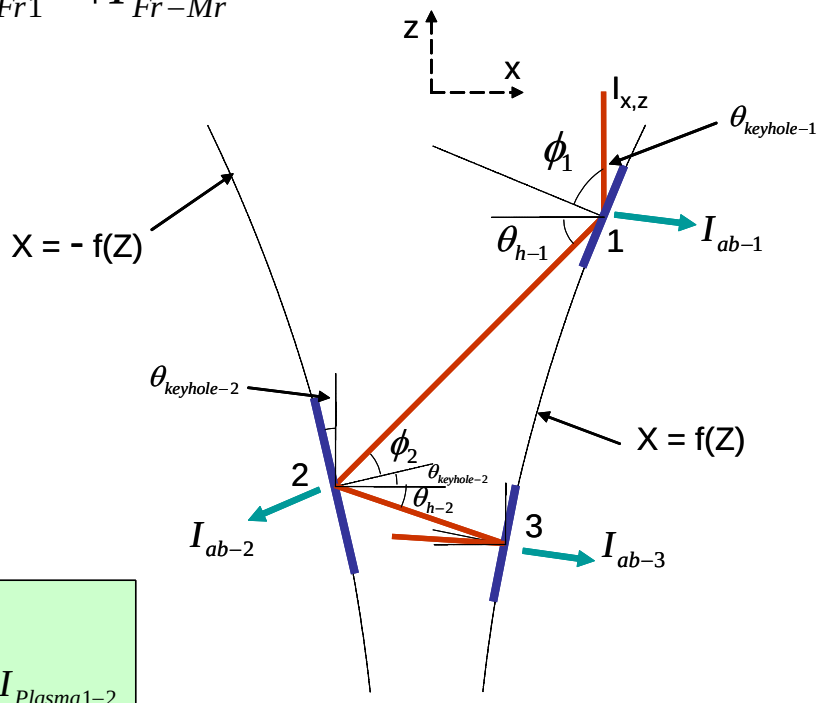

$$I_{ab-1} = I_1 . \alpha_{Fresnel}(\phi_1)$$

$$I_2 = I_1 . (1 - \alpha_{Fresnel}(\phi_1)) - I_{Plasma1-2}$$

$$I_{ab-2} = I_2 . \alpha_{Fresnel}(\phi_2)$$

Figure 4.7.6 – Geometrical Analysis for Multiple Reflections inside the Keyhole

4.7.7 Method of Calculation

MATLAB software and GUI applications was used to simulate the keyhole laser welding process the program code can be found in Appendix (A.5). The first step is to determine the keyhole radius and the keyhole profile by considering only direct Fresnel absorption. To calculate the multiple reflections and plasma absorption, the keyhole obtained from the first Fresnel absorption was converted to two mirror polynomial equations to determine the slops and intersection at any layer. The result of the multiple reflections and plasma was used to recalculate the keyhole profile and to calculate the source strengths for each layer. The last block of calculation was to generate the FZ geometry which will be parallel to final keyhole profile. Equation (4.6.9) was used to determine the radius of the melting isotherm at each layer since the source strength is unique and it is the same when the boundary condition was applied at keyhole wall ($T = T_v$, $r = r_k$), or at PMZ ($T = T_{melting,}$ $r = \frac{FZ\ width}{2}$). The effect of the thermocapillary flow on the FZ width was taken into account by correcting the source strengths [40] obtained from the keyhole profile, and sample 29 was used for this purpose. The previous section showed that there was no significant variation in the coupling efficiency due to change in filler wire feed rate. Adding filler caused to reduce the coupling efficiency by 10 to 14 %. Therefore, a value of 10 % was considered to be losses of power and intensity before entering the keyhole. Figure 4.7.7 describes the calculation procedure with related references.

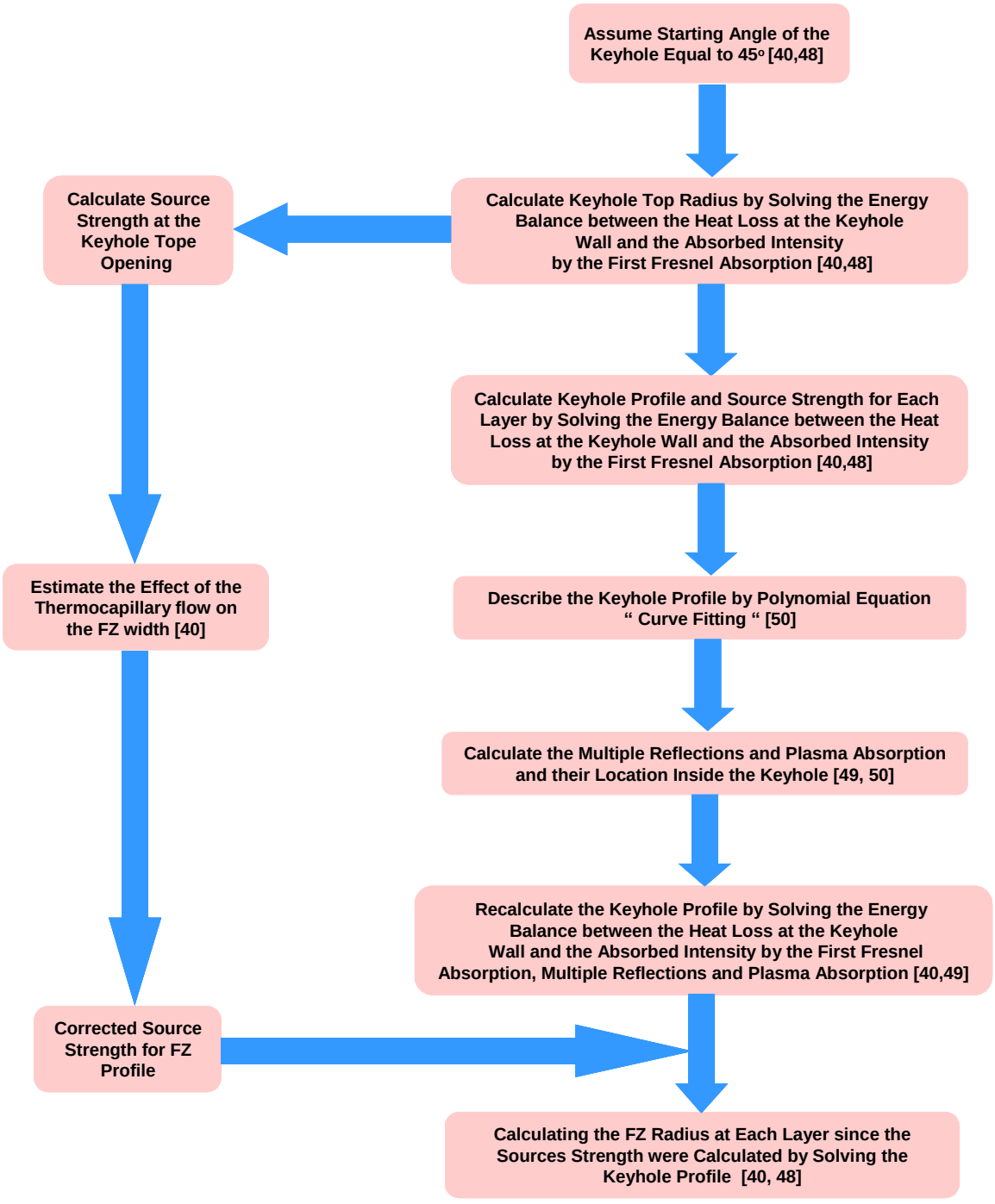

Figure 4.7.7 – Model Flow Chart for Keyhole Laser Welding

4.7.8 Comparison between the Model and the Experimental Results

Figures 4.7.8 to 4.7.12 show the comparison between the model and the experimental results. The model shows acceptable results for laser welding of the 2 mm and 6 mm butt joints plates. The Bead-on-plate laser welding shows some discrepancies between the model and the experiments especially for sample 26 (-2 mm defocusing) which may be due to the variation in the surface condition or variation in physical properties between pure Mg and ZE41A-T5.

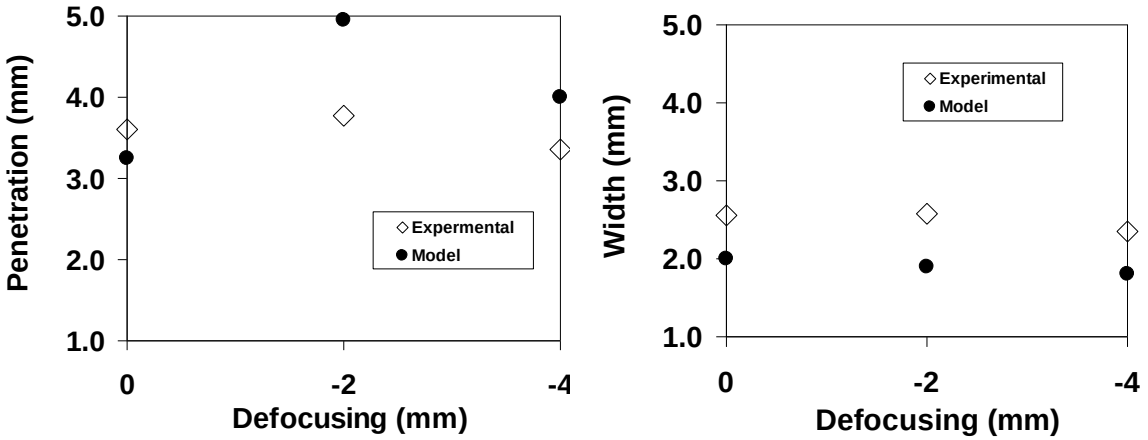

a) Bead-on-plate Laser Welding

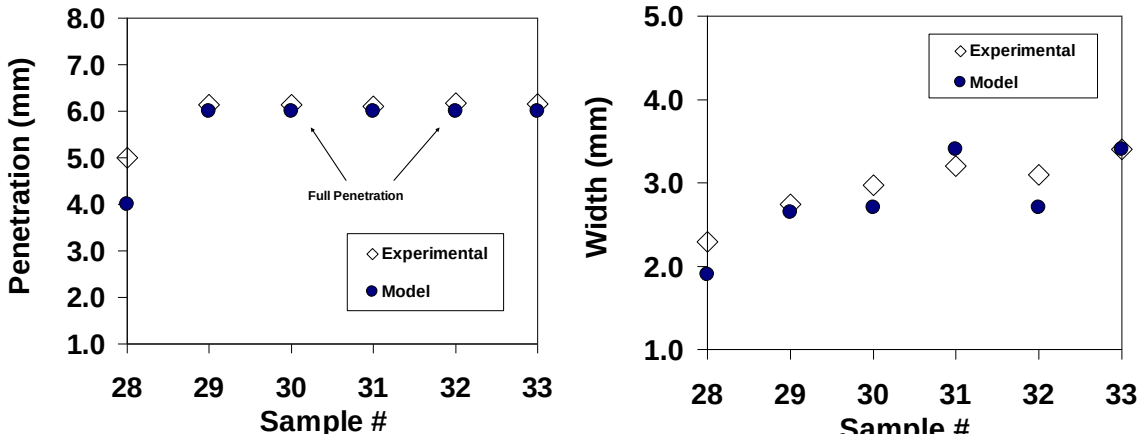

b) Laser Welding of 6 mm butt joints plates with and Without Filler Wire

Figure 4.7.8 – Comparison between the Experimental results and the Model for Laser Welding of 6 mm Plates

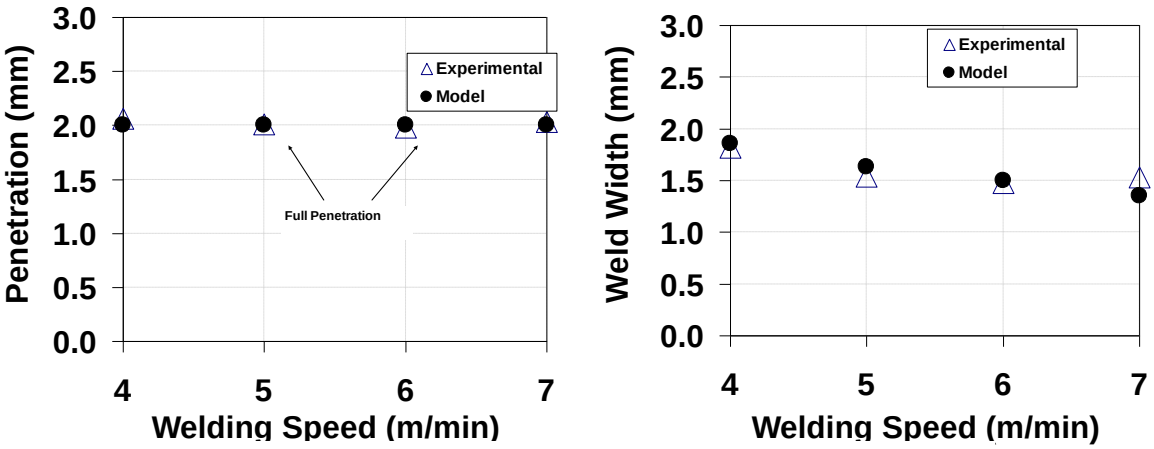

a) Effect of Welding Speed on Laser Weldability of 2 mm Plates

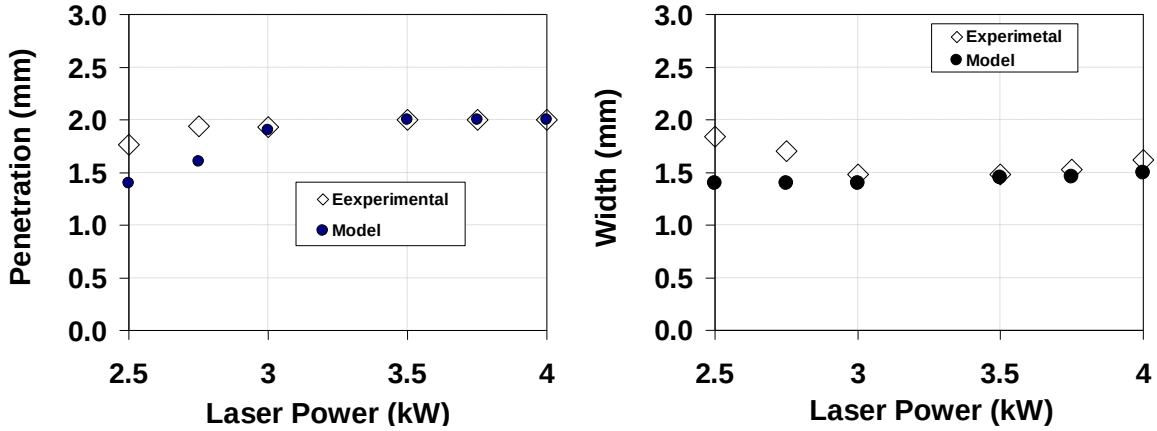

b) Effect of Laser Power on Laser Weldability of 2 mm Plates

Figure 4.7.9 - Comparison between the Experimental results and the Model for Laser Welding of 2 mm Plates

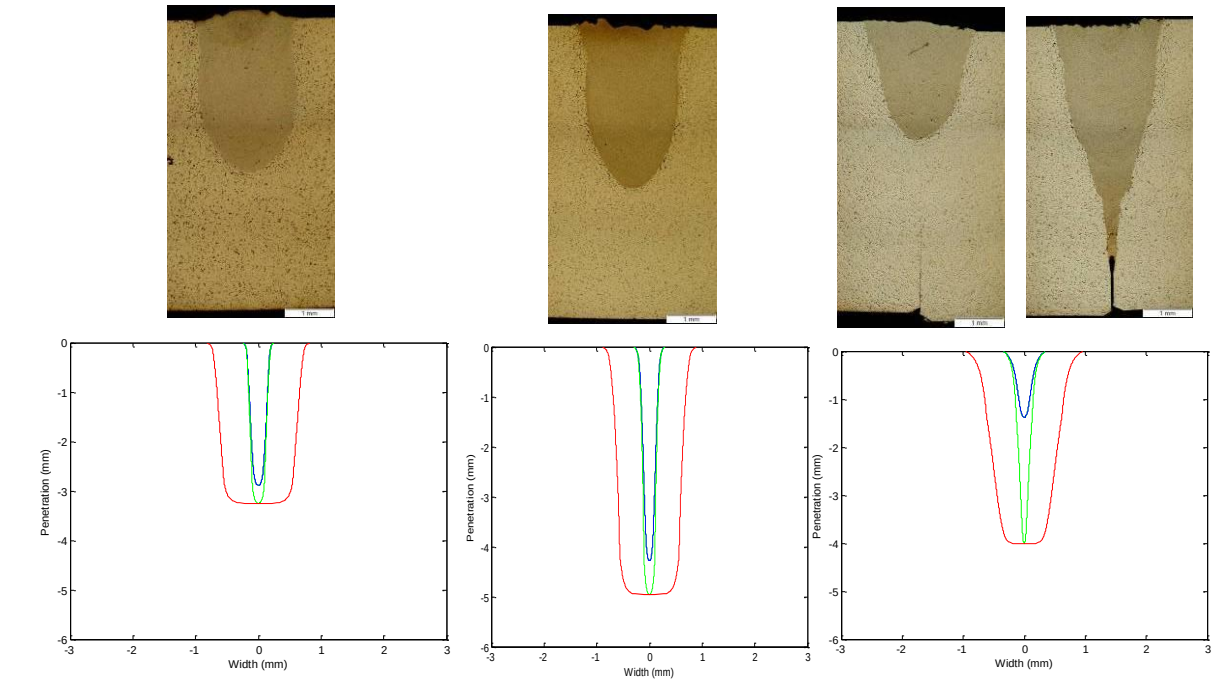

Sample 25 **Sample 26** **Sample 27,28**

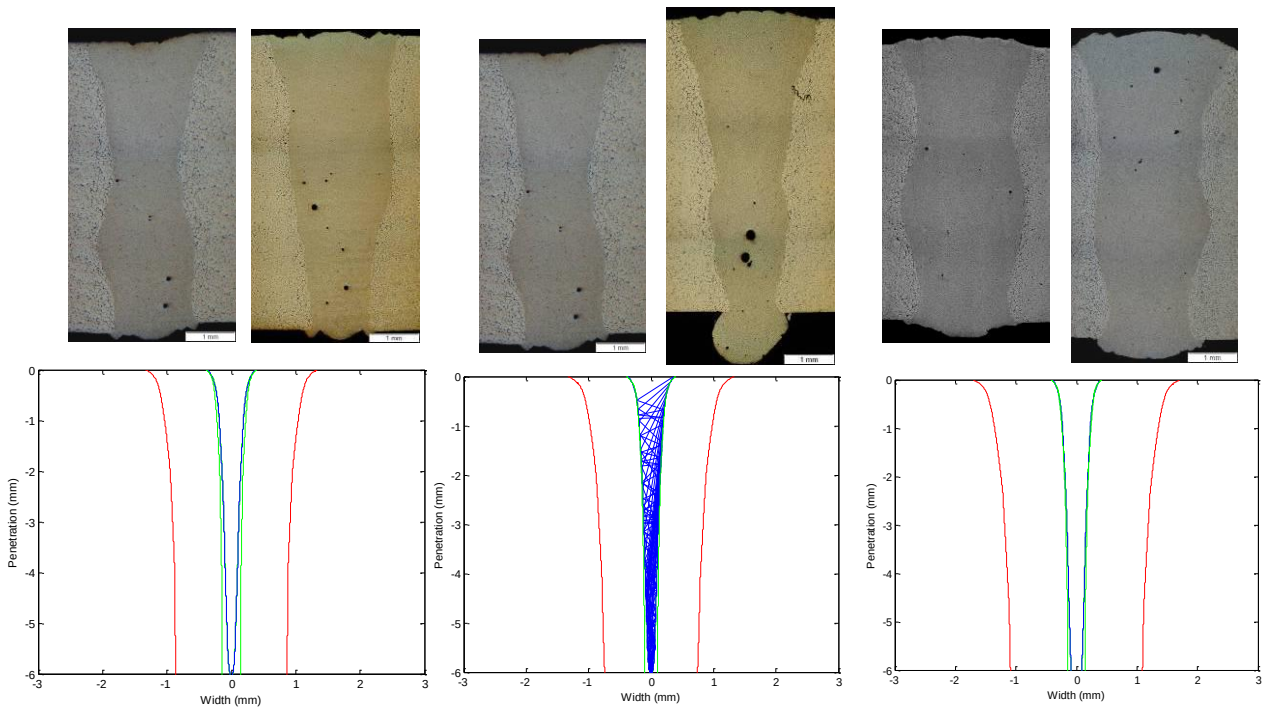

Sample 29 **Sample 30, 32** **Sample 31, 33**

Figure 4.7.10 –Comparison between Experimental and Calculated Weld Geometry for the 6 mm Laser Welded Plates

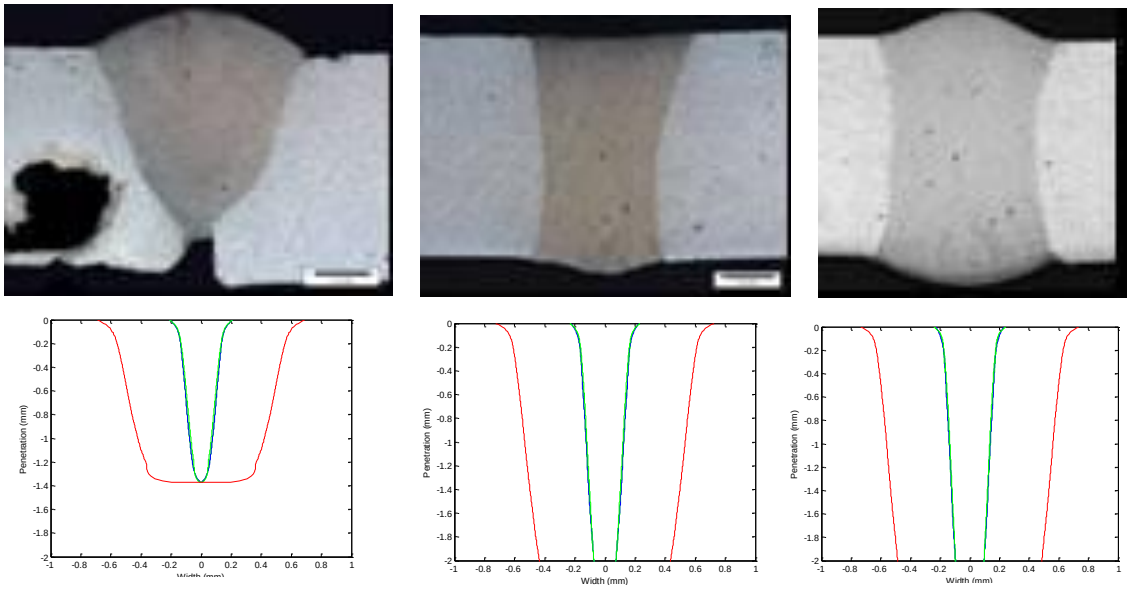

Sample 11 **Sample 14** **Sample 16**

Figure 4.7.11 –Comparison between Experimental and Calculated Weld Geometry Showing the Effect of Laser Power on Laser Welding of the 2 mm Plates

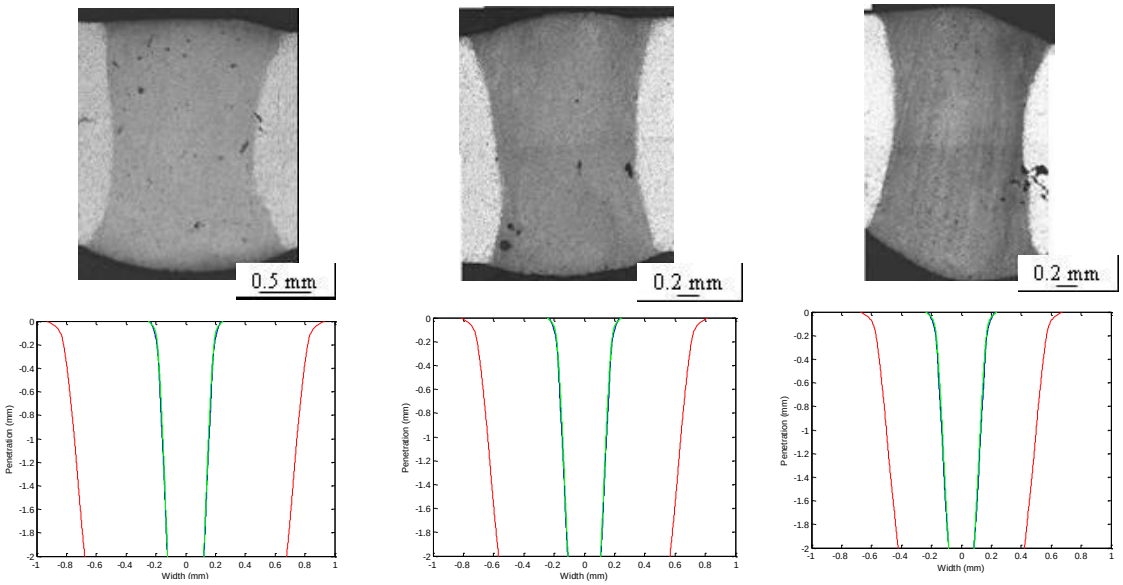

Sample 1 **Sample 2** **Sample 4**

Figure 4.7.12 - Comparison between Experimental and Calculated Weld Geometry the Model Showing the Effect of Welding Speed on Laser Welding of the 2 mm Plates

Chapter 5

5.1 Summary and Concluding Remarks

The laser weldability of ZE41A-T5 Mg sand castings using 1.6 mm filler wire EZ33A-T5 was studied for 2 and 6-mm butt joint plates. The weldability of an alloy is defined as the ability to produce sound and acceptable weld joints using certain sets of process laser parameters. This study was carried out through analyzing the weld geometry, microstructure, defects and mechanical properties. The repeatability of laser welding process was also examined.

5.1.1 Laser Welding of 2-mm Thin Plates

The plates were laser welded using the following process parameters: laser power (2.5 – 4 kW), welding speed (4 – 7 m/min), surface defocusing, and gap size (0.1 – 0.6 mm). The following conclusions can be drawn:

- The optimized parameters were: laser power of 4 kW, welding speed of 6 m/min, and gap size of 0.4 mm
- The penetration depth, average weld width and weld area decreased with increasing welding speed.
- Increasing welding speed reduces porosity area percentage and the solidification cracks.
- A significant grain refinement is observed in the FZ due to high cooling rate. No grain coarsening occurred in the HAZ

- Gap size smaller than 0.3 mm leads to irregular weld geometry with defects at crown and root. Gap size larger than 0.4 mm leads to sag and drop through defects.
- There is no significant effect of the gap size on the grain size or the FZ hardness.
- Increasing the laser power results in changing the FZ geometry from partial to full penetration welding also the keyhole changes from the blind to the open mode. This variation in keyhole mode from the blind to the open may result in changing the cooling rate and thus the grain size and hardness in the FZ.
- Porosity area percentage can be reduced if the open keyhole mode with suitable heat input is achieved. The transition fluctuation mode between open and close keyhole may lead to increase in porosity %.
- The optimized parameters for 2-mm plates resulted in a joint efficiency between 91 to 93 %.
- The hardness in the FZ is similar to that in the BM after a natural aging of around one year. The hardness dropped within the HAZ whose typical width was between 1.5 and 2 mm.

5.1.2 Reliability of Laser Welding Process

The optimized parameters for 2 mm laser welded plates were used to verify the reliability and repeatability of laser welding process by welding 8 joints using better casting quality. The data were analyzed using Weibull distribution method. The following conclusions can be drawn:

- Weld bead width (top width) and FZ hardness show high repeatability (m value from 39.2 to 67.7). Tensile strength and FZ total area show medium repeatability

(m value from 16.6 to 31.1). Whereas the defects and fracture elongation show low repeatability (m value from 1.9 to 3.4).

- Post – weld heat treatment (artificial aging heat treatment - T5) has little influence on the improvement of the mechanical properties of the joints. This heat treatment causes a slight increase in the FZ hardness and higher repeatability than the as – welded condition but still lower than the hardness in the BM.

5.1.3 Effect of Casting Quality on Weldability

Two casting qualities were used in this study. The better quality was used for testing the reliability of laser welding process and for the study of laser welding of 6 mm plates.

- Better casting quality can significantly reduce the defects (porosity and crack) in the FZ.
- The HAZ – PMZ interface for the good casting laser welded plates showed a liquation of some grain boundaries near the PMZ which was not found in the castings used in the first round of experiments.
- Most of the joints fractured in the HAZ – PMZ interface during the tensile tests.

5.1.4 Laser Welding of 6 mm Plates

The plates were laser welded using a laser power of 4 kW, welding speed (2 – 5 m/min), defocusing distance (0, -2, -4 mm), gap size (0, 0.2, 0.4 mm). The following conclusions can be drawn:

- Successful butt joints were obtained at 0, 0.2 and 0.4 mm gap sizes. For autogenous welding the welding speed was 3 m/min. For 0.2 and 0.4 mm the

welding speed was 2 m/min. The optimized defocusing was – 4 mm at which good surface quality was obtained.

- Open keyhole mode resulted in more uniform temperature and cooling rate inside the weld pool and hence similar grain size across the plate thickness.
- The blind – open mixed keyhole mode may increase the porosity in the FZ.
- Conduction mode welding may cause an increase in solidification cracks due to the wide temperature gradient inside the FZ.
- Laser welding with filler wire increases the losses of the reflected laser beam outside the keyhole compared with the autogenous laser welding.
- Excessive increase in defocusing distance leads to a surface power density to near or less than the threshold value required to form the keyhole.
- In general, a joint efficiency between 85 and 95 % was obtained using the optimized parameters for welding with and without filler wire. Applying filler wire caused an increase in joint efficiency by 3 to 5%.

5.1.5 Coupling and Melting Efficiencies

Different concepts were used to calculate coupling, thermal and melting efficiencies using the experimental results. The following can be concluded:

- Laser process efficiencies for the successful joints for the 2 and 6 mm plates were around 13 and 20 – 25 %, respectively. The corresponding coupling efficiency for 6 mm plates was significantly higher than the coupling efficiency for the 2 mm plates due to the increase in multiple reflections inside the keyhole.
- Increasing the welding speed leads to lower melting efficiency as long as the welding keyhole is not fluctuating between open and blind modes.

- There was no significant effect of increasing the filler feed rate on the coupling and melting efficiencies.
- Applying filler wire leads to increase in the laser power losses by 12 %.
- Coupling and melting efficiencies decrease as the keyhole changes from the blind to the open mode.

5.1.6 Simulation of Laser Welding Process

MATLAB program was developed to simulate the laser welding process with the physical properties and laser process parameters as inputs. This enabled the calculation of the keyhole and the weld geometries. The calculated weld bead width and penetration depth were compared with the pertinent experimental results and found in good agreement.

5.2 Contributions to Knowledge

- The present work provides thorough investigation for laser weldability of aerospace grade Mg alloy ZE41A-T5 using filler wire EZ33A-T5.
- The reliability of laser welding process has been studied using Weibull distributions.
- A new method was introduced to calculate the process, thermal and coupling efficiencies from the experimental weld geometry data.
- A MATLAB program using graphical user interface (GUI) application was developed to simulate the laser welding process (keyhole mode) by combining different models and concepts.

5.3 Recommendations for Future Work

- More study and work is needed to understand the mechanisms of crack formation.
- Dual leaser beam welding can be investigated to minimize weld defects in the FZ.
- To increase the welding speed above 7 m/min, it is recommended to improve the feeding mechanism and the control system.
- Laser welding of curved and complicated geometries needs to be investigated because it is important application for the aerospace industry. For this purpose, it is essential to improve the feed-back controller to in-situ adjust the focusing parameters and the movement of the laser head.
- Development of smaller diameter filler wire will help to improve the positioning tolerance for the joint and hence provide more stable process.
- It is recommended to compare the weldability and the operational costs between laser welding at high speed – high power and low speed – low power for thin plates for practical purposes.
- Laser welding of thick plates can also be investigated using multiple pass technique.
- Further investigations are required to optimize the heat treatment for laser welded ZE41A-T5 plates.
- To improve the laser welding model, it is required to verify the absorptivity of this alloy in the liquid state at different incident angles for Nd:YAG short wavelength. Also, it is necessary to acquire some of the physical properties used in the model such as thermal conductivity, specific heat and density of the molten alloy experimentally.

References:

1. M. Dhahri, J. Masse, J. Mathieu, G. Barreau, and M. Autric: Laser Welding of AZ91 and WE43 Magnesium Alloys for Automotive and Aerospace Industries. J. Advanced Engineering Materials, Vol. 3, 2001, 2001, pp. 504 – 507.

2. K. G. Watkins: Laser welding of magnesium alloys. Magnesium Technology 2003, Proceedings of the Symposium held during the 2003 TMS Annual Meeting, San Diego, CA, United States, 2003, pp. 153-156.

3. S. Lathabai, K.J. Barton, D. Harris, P.G. Lloyd, D.M. Viano and A. McLean: Welding and Weldability of AZ31B by Gas Tungsten Arc and Laser Beam Welding Process. Magnesium Technology 2003, Proceedings of the Symposium held during the 2003 TMS Annual Meeting, San Diego, CA, United States, 2003, pp. 157-162.

4. H. Friedrich, S. Schumann: Research for a "New Age of Magnesium" in the Automotive Industry. J. Materials Processing Technology, Vol. 117, 2001, pp. 276 – 281.

5. Z. Sun, D. Pan, and J. Wei: Comparative Evaluation of Tungsten Inert Gas and Laser Welding of AZ31 Magnesium Alloy. J. Science and Technology of Welding and Joining, Vol. 7, No. 6, 2002, pp. 343 – 351.

6. H. Haferkamp, M. Goede, A. Bormann, P. Cordini: Laser Beam Welding of Magnesium Alloys-New Possibilities Using Filler Wire and Arc Welding. Laser Zentrum Hannover e.V laser Assisted Net Shape Engineering 3, Proceeding of the Lane 2001, pp. 333-338.

7. H. Hiraga and Tinoue: Effects of the Shielding Gas and Laser Wavelength in Laser Welding Magnesium Alloy Sheets. J. Welding International, Vol. 16, No. 6, 2002, pp. 442 – 450.

8. H. Haferkamp, F. von Alvensleben , I. Burmester and M. Niemeyer: The Characteristics of Laser Beam Welded Magnesium Alloys. Laser Zentrum Hannover e.V, Proceeding of the Laser Material Processing Conference, ICALEO' 97, 1997, pp. G/140-G/149.

9. M. Dhahri, J.E. Masse, J.F. Mathieu, G. Barreau and M. Autric: CO_2 Laser Welding of Magnesium Alloys. Proceeding of Spie – The International Society For Optical Engineering, 2000, pp. 725-732.

10. M. Pastor, H. Zhao, and T. Debroy: Continuous wave – Nd: Yttrium – Aluminum – Garnet Laser Welding of AM60B Magnesium Alloy. Journal of Laser Applications, Vol. 12, No. 3, 2000, pp. 91 – 100.

11. R. Gradinger, P. Stolfig: Magnesium Wrought Alloys for Automotive Applications. Magnesium Technology 2003, Proceedings of the Symposium held during the 2003 TMS Annual Meeting, San Diego, CA, United States, 2003, pp. 231 – 236.

12. Lehner, G. Reinhart and L. Schaller: Welding of Die Casted Magnesium Alloys on Production Machines. Proceeding of the Laser Material Processing Conference, ICALEO' 98.C, pp. F18-F27.

13. R. Galun, A. Weisheit, B. L. Mordike and C. Zellerfeld: Welding of Magnesium Alloys with a CO_2 Laser. J. Welding & Cutting, Vol. 10, 1997, pp. E146 – E148.

14. A. Weisheit, R. Galun and B. L. Mordike: CO_2 Laser Beam Welding of magnesium – Based Alloys. Welding Journal, Vol. 77, No. 4, 1998, pp. 149-s – 154-s.

15. Z. Sun, M. Kuo: Bridging the Joint with Wire Feed Laser Welding. Journal of Materials Processing Technology, Vol. 87, No 1-3, 1999, pp. 213 – 222.

16. T. Jokinen, V. Kujanpaa: High power Nd: YAG Laser Welding in Manufacturing of Vacuum Vessel of Fusion Reactor. J. Fusion Engineering and Design, Vol. 69, No 1-4, 2003, pp. 349-353.

17. H. Zhao and T. Debroy: Pore Formation During Laser Beam Welding of Die – Cast Magnesium alloy AM60B – Mechanism and Remedy. Welding Journal, Vol. 80, N0. 8, 2001, pp. 204-s – 210-s.

18. S.A. Tsirkas, P. Papanikos, Th. Kermanidis: Numerical Simulation of the Laser Welding Process in Butt-Joint Specimens. Journal of Materials Processing Technology, Vol. 134, 2003, pp. 59 – 69.

19. C. Dawes and C Eng: Laser Welding, McGraw-Hill, Inc. USA, 1992.

20. W. W. Duley: Laser Welding, John Wiley & Sons, Inc. USA, 1998

21. A. Punkari, D.C. Weckman and H.W. Kerr: Effects of Magnesium Content on Dual Beam Nd:YAG Laser Welding of Al-Mg Alloys. J. Science and Technology of Welding and Joining, Vol. 8, No. 4, 2003, pp. 269 – 281.

22. P.G. Sanders, J.S. Keske, K. H. Leong and G. Kornecki: High Power Nd:YAG and CO_2 Laser Welding of Magnesium. Journal of Laser Applications, Vol. 11, No. 2, 1999, pp. 96 – 103.

23. K.H. Leuong, G. Karnecki, P.G. Sanders and J.S. Keske: laser welding of AZ31B-H24 magnesium alloy. Proceeding of the laser materials processing conference ICALEO 98/PT.2, 1998, pp. F28 – F36.

24. B. A. Mickucki and J. D. Shearhouse: Proceeding of Magnesium and Magnesium Properties and Applications for Automobiles Conference, Detroit, SAE INC, 1993, pp. 107 – 115.

25. W. A. Baeslack, S. J. Savnge, and F.H. Froes: Laser Weld Heat Affected Zone Liquation and Cracking in a High Strength Mg Based Alloy. Journal of Material Science, Vol. 5, No. 9, 1986, pp. 935 939.

26. X. Cao, M. Xiao, M. Jahazi, and Y. L. Lin: Continuous Wave Nd: YAG Laser Welding of Sand-Cast ZE41A-T5 Magnesium Sand Casting: Conduction or Keyhole Mode. Proceedings of the International Symposium on Aerospace Materials and Manufacturing: Development, Testing and Life Cycle Issues--Honoring William Wallace, 2nd, Aerospace Materials and Manufacturing: Development, Hamilton, ON, Canada, 2004, 187-197.

27. American Welding Society, American National Standard, B1.11, 2000.

28. Cao, X. Xiao, M. Jahazi, M. Immarigeon, J.-P. Continuous Wave ND:YAG Laser Welding of Sand-Cast ZE41A-T5 Magnesium Alloys. Materials and Manufacturing Processes, Vol. 20, No. 6, 2005, pp. 987-1004.

29. L. G. Reinhart, and L. Schaller: Welding of Die Casted Magnesium Alloys on Production Machines," Pt. 2, Proceedings of the Laser Materials Processing Conference, ICALEO'98, Laser Institute of America, 1998, pp. F18-F27.

30. European Standard: Welding – Electron and Laser Beam Welded Joints – Guided on Quality Levels for Imperfections – Part 2, "Aluminum and Its Weldable Alloys," EN ISO 13919 – 2:2001, 2001.

31. J.C. Borland: Generalized Theory of Super-Solidus Cracking in Welds (and Castings). Brit. Welding Research Assocn, Vol. 7, No. 8, 1960, 508 – 512.

32. J.C. Borland: Suggested Explanation of Hot Cracking in Mild and Low Alloy Steel Welds. Brit. Welding Research Assocn., Vol. 8, No. 11, 1960, 526 – 540.

33. M. Marya, G. Edwards, S. Marya, and D.L. Olson: Fundamental in the Fusion Welding of Magnesium and Its Alloys. Proceedings of the 7th JWS Int. Symp., Kobe, 2001, pp. 597-602.

34. A. S. Salminen: Effect of Welding Parameters on the Efficiency and Energy Distribution during Laser Welding with Filler Wire. Proceeding of Laser

Materials Processing Conference and Laser Microfabrication Conference 92 / 93, 2001, pp. 409 – 418.

35. H. Haferkamp, Fr.-W Bach, I Burmester, K Kreutzburg, M Niemeyer: Nd:YAG Laser Beam Welding of Magnesium Constructions. Proceedings of the International Magnesium Conference, 3rd, Manchester, UK, Apr. 10-12, 1996, pp. 89-98.

36. L. Abbaschian, M. Lima: Cracking Susceptibility of Aluminum Alloys During laser Welding. Journal of Material Research, Vol. 6, No. 2, 2003, pp. 273 – 278.

37. X. Cao, M. Xiao, M. Jahazi, YL Lin: Nd:YAG Laser Welding of Magnesium Alloy Castings. Magnesium Technology 2005, Proceedings of the Symposium held during the TMS Annual Meeting, San Francisco, CA, United States, 2005, pp. 441-443.

38. M. Y. Krasnoperov, R. R. G. M. Pieters, and I. M. Richardson: Weld Pool Geometry during Keyhole Laser Welding of Thin Steel Sheets. Science and Technology of Welding and Joining, Vol. 9, No. 6, 2004, pp. 501-506.

39. F. Dausinger, J. Rapp, M. Beck, F. Faisst, R. Hack, and Helmut Hugel: Welding of Aluminum: a Challenging Opportunity for Laser Technology. Journal of Laser Applications, Vol. 8, No. 6, 1996, pp. 285 – 290.

40. C. Lampa, A. F H Kaplan, J. Powell, and C. Magnusson: An Analytical Thermodynamic Model of Laser Welding. Journal of Physics D: Applied Physics, Vol. 30, No. 9, 1997, pp. 1293 -1299.

41. Z.-T. Fan and S. Ji: Low Pressure Lost Foam Pressure for Casting Magnesium Alloys. Journal of Material Science and Technology, Vol. 21, No. 6, 2005, pp. 727 – 734.

42. R. Taghiabadi, M. Mahmoudi, M. E. Ghomy, and J. Campbell: Effect of Casting Techniques on Tensile Properties of Cast Aluminum Alloy (Al-Si-Mg) and TiB_2 Containing Metal Matrix Composite. Journal of Materials Science and Technology, Vol. 19, No. 4, 2003, pp. 497-502.

43. H. Hugel: Strahlwerkzeug Laser, Eine Einfuhrung, Stuttgart, Teubner, 1992

44. M. Marya and G. R. Edward: Factors Controlling the Magnesium Weld Morphology in Deep Penetration Welding by CO_2 Laser. Journal of Materials Engineering and Performance, Vol. 10, No. 4, 2001, pp. 435 – 443.

45. J. Xie: Dual Beam Laser Welding. Welding Research Journal, October, 2002, pp. 223/S-230/S.

46. D. T. Swift-Hook and A. E. F. Gick: Penetration Welding with Lasers. Welding Journal, Vol. 52, No. 11, 1973, pp. 492s – 499s.

47. D. Rosenthal: The Theory of Moving Sources of Heat and its Application to Metal Treatments. Transactions of the ASME, Vol. 68, 1946, pp. 848 – 866.

48. A. Kaplan: A Model of Deep Penetration Laser Welding Based on Calculation of the Keyhole Profile. Journal of Physics D: Applied Physics, Vol. 27, 1994, pp. 1805 – 1814.

49. P. Solana and G. Negro: A Study of the Effect of Multiple Reflections on the Shape of the Keyhole of the Keyhole in the Laser Processing of Materials. Journal of Physics D: Applied Physics, Vol. 30 1997, pp. 3216 – 3222.

50. X. Jin, L. Li and Y. Zhang: A Study on Fresnel Absorption and Reflections in the Keyhole in Deep Penetration Laser Welding. Journal of Physics D: Applied Physics, Vol. 35, 2002, pp. 2304 – 2310.

51. R. Ducharme, K. Williams, P. Kapadia, J. Dowden, B. Steen and M. Glowacki: The Laser Welding of Thin Metal Sheets: an Integrated Keyhole and Weld Pool Model with Supporting Experiments. Journal of Physics D: Applied Physics, Vol. 27, 1994, pp. 1619 – 1627.

52. J. Y Lee, S. H Ko, D. F Farson and C. D Yoo: Mechanism of Keyhole Formation and Stability in Stationary Laser Welding. Journal of Physics D: Applied Physics, Vol. 35, 2002, pp. 1570 – 1576.

53. Y. Zhang, L. Li and G, Zhang: Spectroscopic Measurements of Plasma inside the Keyhole in Deep Penetration Laser Welding. Journal of Physics D: Applied Physics, Vol. 38, 2005, pp. 703 – 710.

54. L. M. Leemis: Reliability – Probabilistic Models and Statistical Methods, Prentice-Hall, Inc, USA, 1995.

55. R. D. Leitch: Reliability Analysis for Engineers, Oxford University Press Inc., USA, 1995.

56. X. Cao and J. Campbell: Effect of Precipitation of Primary Intermetallic Compounds on Tensile Properties of Cast Al-11.5Si-0.4Mg Alloy. Transactions of the American Foundrymen's Society, 2000, pp. 391 – 400.

57. X. Cao, M. Jahazi, J.P. Immarigeon and W. Wallace: A review of laser welding techniques for magnesium alloys. Journal of Materials Processing Technology, Vol. 171, No. 2, 2006, pp. 188 – 204.

58. Magnesium Elektron: http://www.magnesium-elektron.com/. (March – 05 – 2006).

Appendix

A.1 Summary of Literature Survey

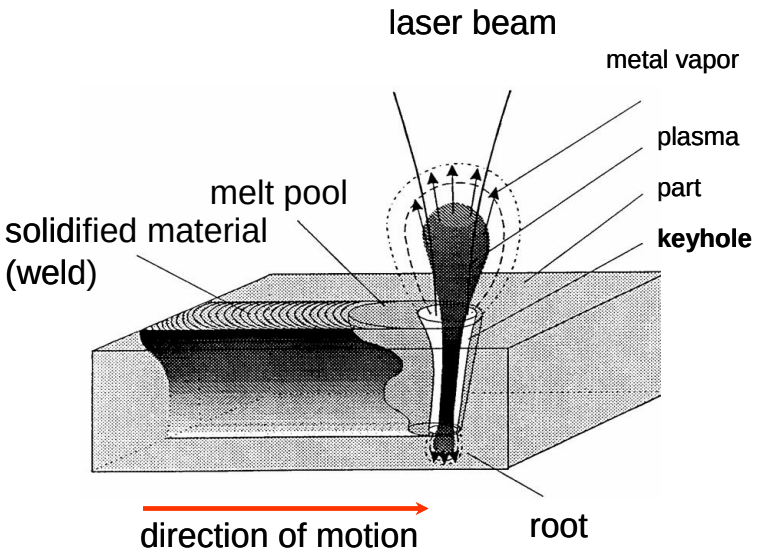

Laser Welding at the keyhole mode

Laser Welding Modes

Laser welding modes	Condition	Effects
conduction mode	laser power density < threshold value	Larger HAZ
keyhole mode	laser power density >> threshold value	small HAZ and higher welding speed
Mixed mode	Laser power density ≈ the threshold value	causing instability in the keyhole and weld geometry. But this type of welding was not obtained when welding Mg alloys

Effect s of laser power and welding speed on the weldability of Mg alloy

+ (increase) - (decrease)		Penetration depth and weld area	Grain size	Porosity	losses in alloy elements	Hardness	residual stresses	Cracking
Laser power	+	+	+	+	+	-	+	+
Welding speed	+	-	-	-	-	+	-	-

Effects of f-number on the focusing parameters and process criticalness

+ (increase) - (decrease)		focal spot diameter	laser power density	depth of focus	process criticalness
f - number	+	+	-	+	-

Microstructure in FZ and HAZ of Mg alloys.

	Fusion Zone		HAZ	
Mg alloy	**Grain shape**	**Grain size**	**Grain shape**	**Grain size**
most of Mg alloys	cellular structure	fine grains	liquation of grain boundaries	small
WE54	globular	fine grains	no liquation	small
AZ61, AZ91	dendritic	fine grains	liquation of grain boundaries	small
AZ31	coarse	large grains	liquation of grain boundaries	large grains

Porosity formation during laser welding of Mg

Mg Alloy	Porosity
sand cast & extruded	low
high content of Al or Zn	few large pores
non vacuum producible alloy	extremely high

Mechanism of porosity formation of Mg alloys.

Ref.	Mechanism of Porosity formation	Solution
10, 17	Coalescence and expansion of preexisting pores	reducing laser heat energy
10, 17	keyhole instability may lead to porosity formation	not found in Mg alloy
12	Coalescence and expansion of preexisting pores	reducing laser power and welding speed
24	depend on the amount of dissolved hydrogen	------

Cracks formation during laser welding of Mg alloys.

Ref.	alloys sensitive to crack formation	Crack type
13, 14	QE22	Solidification cracking
25	WE54	HAZ liquation cracking
13, 14	WE54	no cracks observed
5	AZ31	Solidification cracking
3	AZ31	not sensitive to solidification cracking
8	alloys that have high Al or Zn content	sensitive to micro cracking

Hardness in FZ and HAZ of Mg Alloys

Ref.	Alloy type	Hardness in FZ and HAZ	reasons
13, 14, 10	as - cast	FZ > base metal	grains refinement
		HAZ = Base metal	no change in microstructure
13, 14	wrought	FZ = base metal	balance between loss in work
		HAZ = Base metal	hardening and grain refinement
13, 14	age - hardened	FZ <= base metal	----------
		HAZ <= base metal	----------
8	as - cast	FZ > base metal at higher speed welding	grains refinement
		FZ = base metal at low speed welding	no change in microstructure
9	WE43, ZE41	FZ = base metal	----------
7, 9	AZ31	FZ < base metal	grain growth effect
		HAZ < base metal	grain growth effect

A.2 Weibull Distribution

This distribution is very convenient as a model for various physical phenomena, applied mechanical problems; it is highly adaptable and is used widely in engineering reliability since it is two parametrical. This model also most accurately described the distribution of tensile strength. A normal distribution is symmetrical about the mean strength, whereas a Weibull distribution is skewed, showing a longer trail of low strengths and a sharper cut – off at high strengths.

The two – parameter for of Weibull's equation can be expressed as:

$$P_f = 1 - e^{(-\frac{\sigma}{\sigma_o})^m} \tag{A-1}$$

Where P_f is the fraction of specimens that fail at a given stress or lower. The stress σ_o is that value at which approximately 63.2% of the population of specimens have failed, and m is a constant for that particular population known as the Weibull modulus, which is an assessment of reliability (i.e., the degree of scatter).

The value of m can be obtained by taking the logarithm of equation (A-1) twice over:

$$Ln\{Ln[\frac{1}{(1-P_f)}]\} = m\,Ln(\sigma) - m\,Ln(\sigma_o) \tag{A-2}$$

The linear equation is a a straight line and can be plotted $Ln\{Ln[\frac{1}{(1-P_f)}]\}$ versus Ln(σ) giving slop m and intercept $-m\,Ln(\sigma_o)$. This is often referred as a Weibull plot. Linear regression analysis is widely employed to evaluate m. The σ values (tensile strength) are arranged in ascending order:

$$\sigma_1 \le \sigma_2 \le \sigma_3 \le \sigma_j \le \sigma_n$$

A probability of failure will be assigned to each σ such that:

$$P_{f,1} \le P_{f,2} \le P_{f,3} \le P_{f,j} \le P_{f,n}$$

Where $0 \le P_f \le 1$, and P_f can be estimated as follows:

$$P_f = \frac{(j-0.5)}{N} \qquad \text{(A-3)}$$

Where N is number of specimens, j is the rank number of the specimen as arranged in the ascending order. [54, 55, 56]

A.3 Solidification Cracks for 6 mm Laser Welded Plates

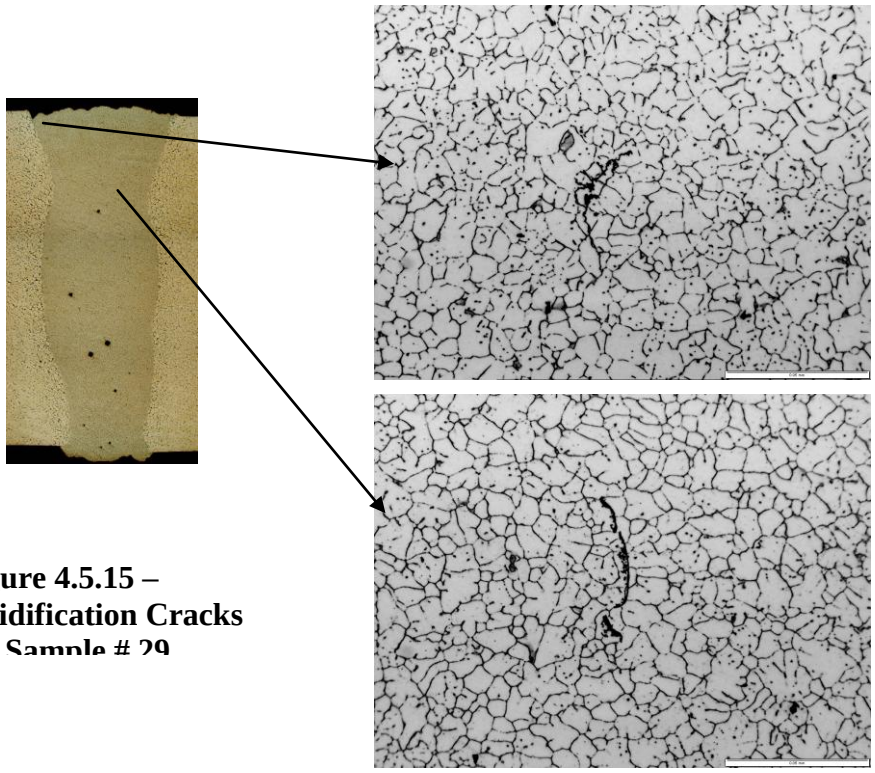

Figure 4.5.15 – Solidification Cracks for Sample # 29

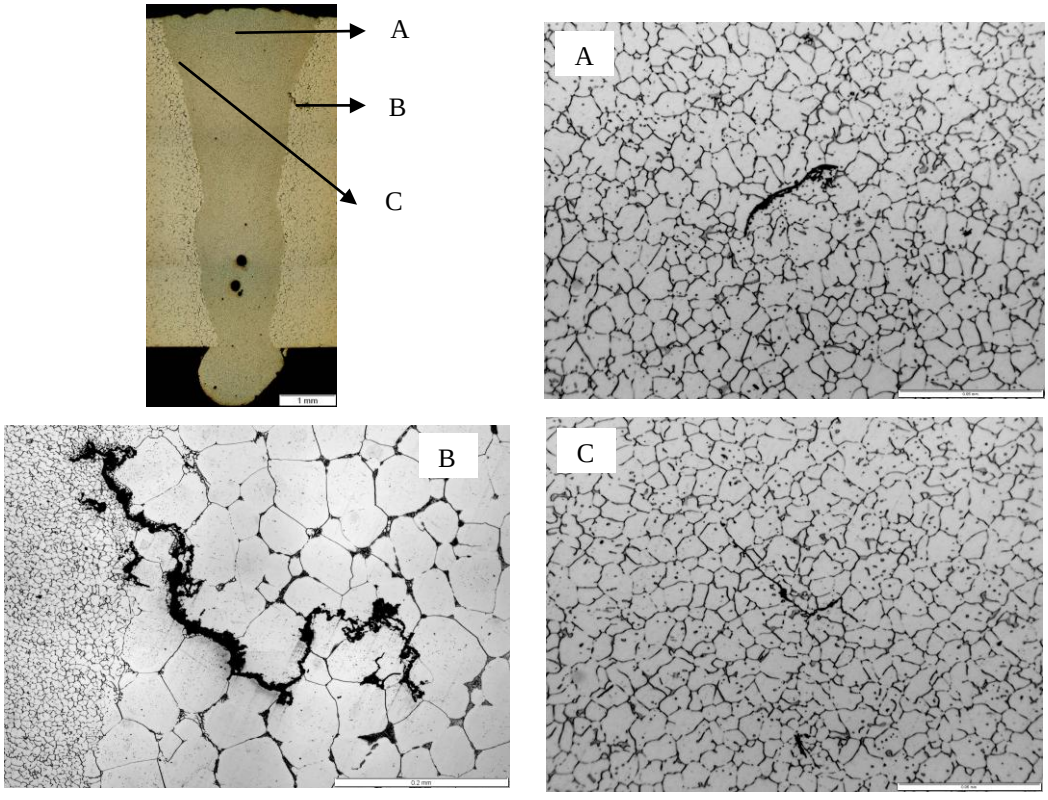

Figure 4.5.16 – Solidification and Liquation Cracks for Sample 30

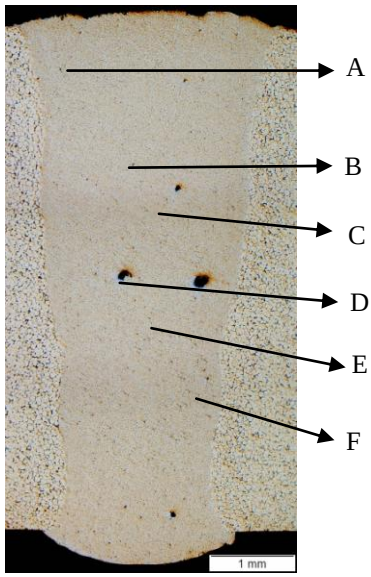

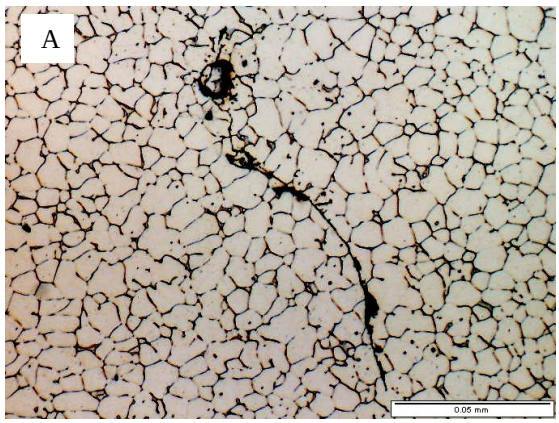

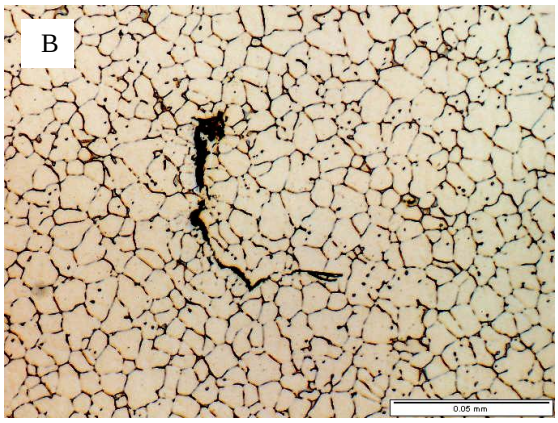

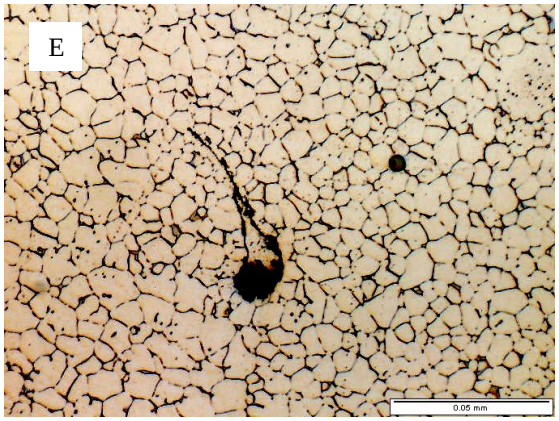

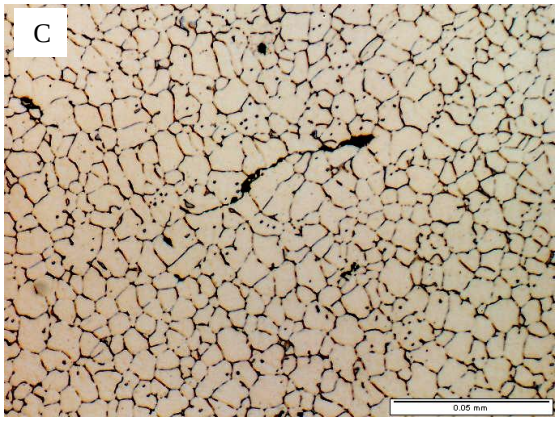

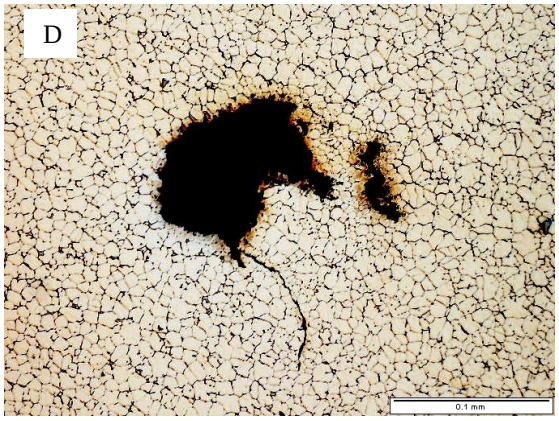

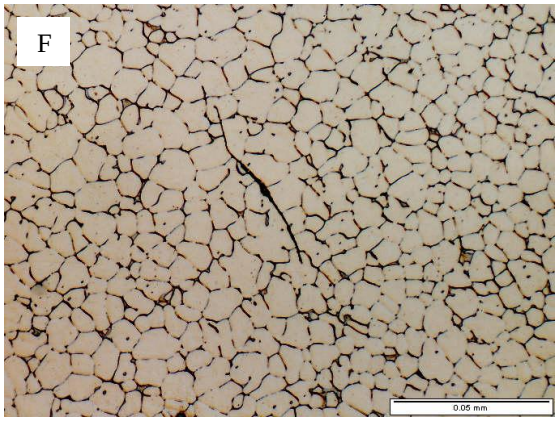

Figure 4.5.17 – Solidification Cracks for Sample 31

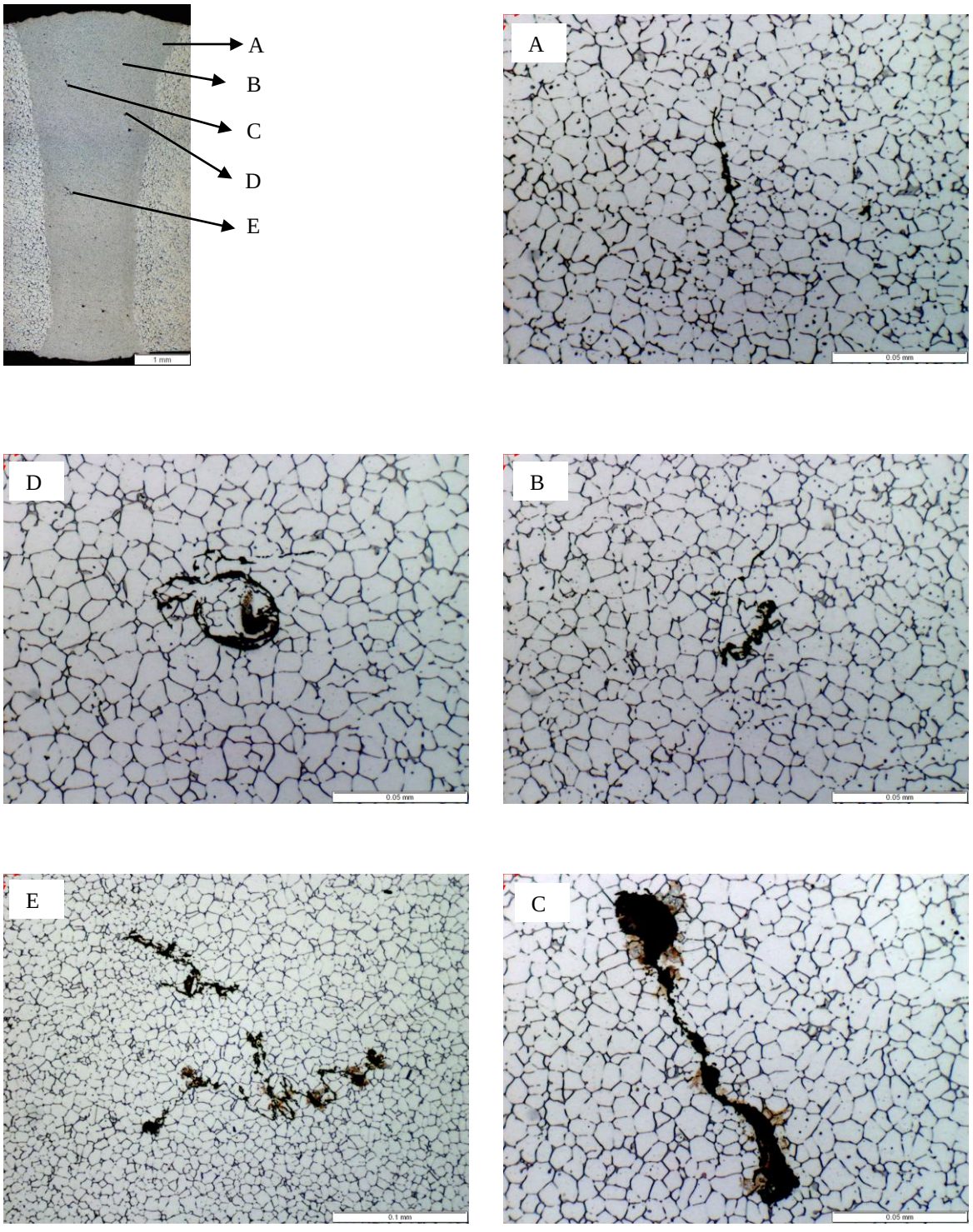

Figure 4.5.18 – Solidification Cracks for Sample 33

A.4: Physical Properties for pure Mg, ZE41A and pure Al

Properties	Pure Mg	ZE41	Pure Al
Melting Point (^{o}C)	650 [57]	530 - 640 [58]	660 [57]
Thermal Conductivity (W M^{-1} K^{-1})	$78_{melting}$ [57]	$109_{room\ T.}$ [58]	$94_{melting}$ [57]
Specific Heat (J Kg^{-1} K^{-1})	$1360_{melting}$ [57]	$960_{room\ T.}$ [58]	$1080_{melting}$ [57]
Density (Kg M^{-3})	$1590_{melting}$ [57]	$1840_{room\ T.}$ [58]	$2385_{melting}$ [57]
Boiling Point (^{o}C)	1110 [2]	-----	2520 [57]
Heat of Fusion (J Kg^{-1})	3.7×10^{5} [57]	-----	4×10^{5} [57]

A.5: Simulation of Laser Welding Process Using MATLAB Programming

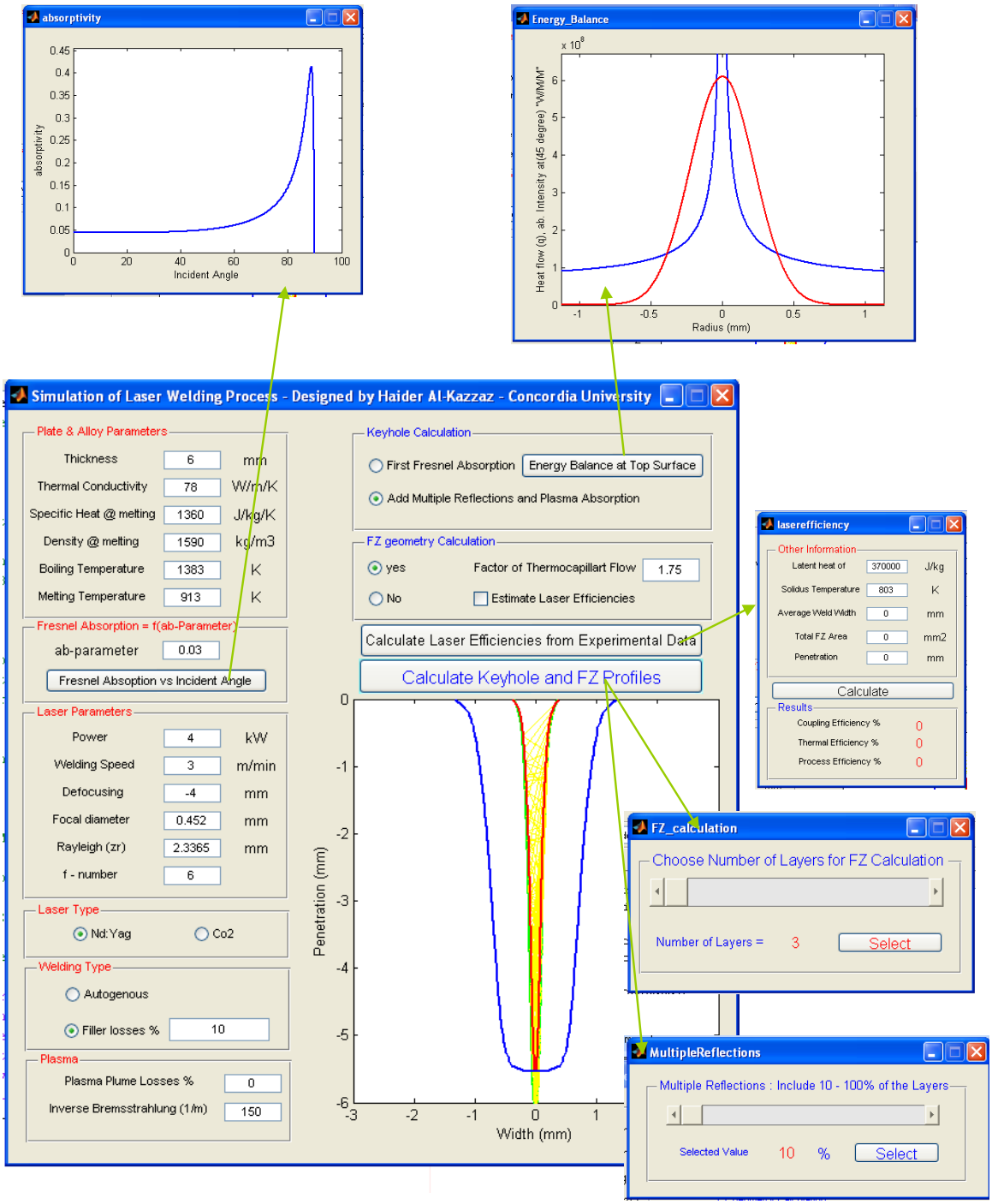

Figure A.5.1 – Graphical User Interface for the Program

A.5.1: programming of the main window

```
function varargout = hklaser(varargin)
gui_Singleton = 1;
gui_State = struct('gui_Name',       mfilename, ...
                   'gui_Singleton',  gui_Singleton, ...
                   'gui_OpeningFcn', @hklaser_OpeningFcn,
...
                   'gui_OutputFcn',  @hklaser_OutputFcn,
...
                   'gui_LayoutFcn',  [] , ...
                   'gui_Callback',   []);
if nargin && ischar(varargin{1})
    gui_State.gui_Callback = str2func(varargin{1});
end

if nargout
    [varargout{1:nargout}] = gui_mainfcn(gui_State,
varargin{:});
else
   gui_mainfcn(gui_State, varargin{:});
end
% End initialization code - DO NOT EDIT


% --- Executes just before hklaser is made visible.
function hklaser_OpeningFcn(hObject, eventdata, handles,
varargin)
handles.output = hObject;
guidata(hObject, handles);

global yagplasma
global qw
global qw2
global filler
global filler2
global thickness
global k
global troom
global cp
global den
global tboil
global tmelt
global p
global v
```

```
global dfo
global zr
global zo
global ab
global Alib
global plume
global cap
global fillercheck
global f
global hh
global efffrom
fillercheck = 1;
filler2 = 10;
yagplasma = 100;
filler = filler2;
qw = 0;
qw2 = 1;
hh = 0;
thickness = str2double(get(handles.th, 'String'));
k = str2double(get(handles.k, 'String'));
troom = str2double(get(handles.troom, 'String'));
cp = str2double(get(handles.cp, 'String'));
den = str2double(get(handles.den, 'String'));
f =  str2double(get(handles.f, 'String'));
tboil = str2double(get(handles.tboil, 'String'));
tmelt = str2double(get(handles.tmelt, 'String'));
p = str2double(get(handles.p, 'String'));
v = str2double(get(handles.v, 'String'));
dfo = (str2double(get(handles.dfo, 'String')));
zr = str2double(get(handles.zr, 'String'));
zo = str2double(get(handles.de, 'String'));
ab = str2double(get(handles.ab, 'String'));
Alib = str2double(get(handles.alib, 'String'));
plume = str2double(get(handles.plume, 'String'));
cap = str2double(get(handles.cap, 'String'));
% --- Outputs from this function are returned to the
command line.
function varargout = hklaser_OutputFcn(hObject, eventdata,
handles)
varargout{1} = handles.output;
function den_Callback(hObject, eventdata, handles)
global den
if isnan(str2double(get(hObject, 'String')))
    set(hObject, 'String', den);
    errordlg('Input must be a number','Error');
else
% Save the new den value
```

```
den = str2double(get(hObject, 'String'));
end
function den_CreateFcn(hObject, eventdata, handles)
if ispc && isequal(get(hObject,'BackgroundColor'),
get(0,'defaultUicontrolBackgroundColor'))
    set(hObject,'BackgroundColor','white');
end
function tboil_Callback(hObject, eventdata, handles)
global tboil
if isnan(str2double(get(hObject, 'String')))
    set(hObject, 'String', tboil);
    errordlg('Input must be a number','Error');
else
tboil = str2double(get(hObject, 'String'));

end
function tboil_CreateFcn(hObject, eventdata, handles)
if ispc && isequal(get(hObject,'BackgroundColor'),
get(0,'defaultUicontrolBackgroundColor'))
    set(hObject,'BackgroundColor','white');
end
function tmelt_Callback(hObject, eventdata, handles)
global tmelt
if isnan(str2double(get(hObject, 'String')))
    set(hObject, 'String', tmelt);
    errordlg('Input must be a number','Error');
else
% Save the new tmelt value
tmelt = str2double(get(hObject, 'String'));
end
% --- Executes during object creation, after setting all
properties.
function tmelt_CreateFcn(hObject, eventdata, handles)
.
if ispc && isequal(get(hObject,'BackgroundColor'),
get(0,'defaultUicontrolBackgroundColor'))
    set(hObject,'BackgroundColor','white');
end


function th_Callback(hObject, eventdata, handles)
global thickness
if isnan(str2double(get(hObject, 'String')))
    set(hObject, 'String', thickness);
    errordlg('Input must be a number','Error');
else
% Save the new thickness value
```

```
thickness = str2double(get(hObject, 'String'));
end
% --- Executes during object creation, after setting all
properties.
function th_CreateFcn(hObject, eventdata, handles)
if ispc && isequal(get(hObject,'BackgroundColor'),
get(0,'defaultUicontrolBackgroundColor'))
    set(hObject,'BackgroundColor','white');
end
function k_Callback(hObject, eventdata, handles)
global k
if isnan(str2double(get(hObject, 'String')))
    set(hObject, 'String', k);
    errordlg('Input must be a number','Error');
else
% Save the new k value
k = str2double(get(hObject, 'String'));
end
function k_CreateFcn(hObject, eventdata, handles)
if ispc && isequal(get(hObject,'BackgroundColor'),
get(0,'defaultUicontrolBackgroundColor'))
    set(hObject,'BackgroundColor','white');
end
function cp_Callback(hObject, eventdata, handles)
global cp
if isnan(str2double(get(hObject, 'String')))
    set(hObject, 'String', cp);
    errordlg('Input must be a number','Error');
else
% Save the new cp value
cp = str2double(get(hObject, 'String'));

end
% --- Executes during object creation, after setting all
properties.
function cp_CreateFcn(hObject, eventdata, handles)
if ispc && isequal(get(hObject,'BackgroundColor'),
get(0,'defaultUicontrolBackgroundColor'))
    set(hObject,'BackgroundColor','white');
end
function ab_Callback(hObject, eventdata, handles)
global ab
if isnan(str2double(get(hObject, 'String')))
    set(hObject, 'String', ab);
    errordlg('Input must be a number','Error');
else
% Save the new ab value
```

```
ab = str2double(get(hObject, 'String'));
end
% --- Executes during object creation, after setting all
properties.
function ab_CreateFcn(hObject, eventdata, handles)
if ispc && isequal(get(hObject,'BackgroundColor'),
get(0,'defaultUicontrolBackgroundColor'))
    set(hObject,'BackgroundColor','white');
end
% --- Executes on button press in fresnel.
function fresnel_Callback(hObject, eventdata, handles)
absorptivity;
function dfo_Callback(hObject, eventdata, handles)
global dfo
if isnan(str2double(get(hObject, 'String')))
    set(hObject, 'String', dfo);
    errordlg('Input must be a number','Error');
else
% Save the new dfo value
dfo = str2double(get(hObject, 'String'));

end
% --- Executes during object creation, after setting all
properties.
function dfo_CreateFcn(hObject, eventdata, handles)
.
if ispc && isequal(get(hObject,'BackgroundColor'),
get(0,'defaultUicontrolBackgroundColor'))
    set(hObject,'BackgroundColor','white');
end
function zr_Callback(hObject, eventdata, handles)
global zr
if isnan(str2double(get(hObject, 'String')))
    set(hObject, 'String', zr);
    errordlg('Input must be a number','Error');
else
% Save the new zr value
zr = str2double(get(hObject, 'String'));

end
% --- Executes during object creation, after setting all
properties.
function zr_CreateFcn(hObject, eventdata, handles)
if ispc && isequal(get(hObject,'BackgroundColor'),
get(0,'defaultUicontrolBackgroundColor'))
    set(hObject,'BackgroundColor','white');
end
```

```
function f_Callback(hObject, eventdata, handles)
global f
if isnan(str2double(get(hObject, 'String')))
    set(hObject, 'String', f);
    errordlg('Input must be a number','Error');
else
% Save the new f value
f = str2double(get(hObject, 'String'));
end

% --- Executes during object creation, after setting all
properties.
function f_CreateFcn(hObject, eventdata, handles)
if ispc && isequal(get(hObject,'BackgroundColor'),
get(0,'defaultUicontrolBackgroundColor'))
    set(hObject,'BackgroundColor','white');
end
function p_Callback(hObject, eventdata, handles)
global p
if isnan(str2double(get(hObject, 'String')))
    set(hObject, 'String', p);
    errordlg('Input must be a number','Error');
else
% Save the new p value
p = str2double(get(hObject, 'String'));
end
% --- Executes during object creation, after setting all
properties.
function p_CreateFcn(hObject, eventdata, handles)
if ispc && isequal(get(hObject,'BackgroundColor'),
get(0,'defaultUicontrolBackgroundColor'))
    set(hObject,'BackgroundColor','white');
end
 function v_Callback(hObject, eventdata, handles)
global v
 if isnan(str2double(get(hObject, 'String')))
    set(hObject, 'String', v);
    errordlg('Input must be a number','Error');
else
% Save the new v value
v = str2double(get(hObject, 'String'));
guidata(hObject,handles)
end
% --- Executes during object creation, after setting all
properties.
function v_CreateFcn(hObject, eventdata, handles)
```

```
if ispc && isequal(get(hObject,'BackgroundColor'),
get(0,'defaultUicontrolBackgroundColor'))
    set(hObject,'BackgroundColor','white');
end
 function de_Callback(hObject, eventdata, handles)
global zo
 if isnan(str2double(get(hObject, 'String')))
    set(hObject, 'String', zo );
    errordlg('Input must be a number','Error');
else
 % Save the new zo value
zo = str2double(get(hObject, 'String'));
 end
 % --- Executes during object creation, after setting all
properties.
function de_CreateFcn(hObject, eventdata, handles)
if ispc && isequal(get(hObject,'BackgroundColor'),
get(0,'defaultUicontrolBackgroundColor'))
    set(hObject,'BackgroundColor','white');
end
 function fillerlosses_Callback(hObject, eventdata,
handles)
global filler2
 if isnan(str2double(get(hObject, 'String')))
    set(hObject, 'String', filler2);
    errordlg('Input must be a number','Error');
else
 % Save the new fillerlosses value
filler2 = str2double(get(hObject, 'String'));
 end
 % --- Executes during object creation, after setting all
properties.
function fillerlosses_CreateFcn(hObject, eventdata,
handles)
if ispc && isequal(get(hObject,'BackgroundColor'),
get(0,'defaultUicontrolBackgroundColor'))
    set(hObject,'BackgroundColor','white');
end
 function plume_Callback(hObject, eventdata, handles)
global plume
if isnan(str2double(get(hObject, 'String')))
    set(hObject, 'String', plume);
    errordlg('Input must be a number','Error');
else
% Save the new plume value
plume = str2double(get(hObject, 'String'));
end
```

```
% --- Executes during object creation, after setting all
properties.
function plume_CreateFcn(hObject, eventdata, handles)
%
if ispc && isequal(get(hObject,'BackgroundColor'),
get(0,'defaultUicontrolBackgroundColor'))
    set(hObject,'BackgroundColor','white');
end



function alib_Callback(hObject, eventdata, handles)
global Alib

if isnan(str2double(get(hObject, 'String')))
    set(hObject, 'String', Alib);
    errordlg('Input must be a number','Error');
else
% Save the new Alib value
Alib = str2double(get(hObject, 'String'));
end
% --- Executes during object creation, after setting all
properties.
function alib_CreateFcn(hObject, eventdata, handles)
if ispc && isequal(get(hObject,'BackgroundColor'),
get(0,'defaultUicontrolBackgroundColor'))
    set(hObject,'BackgroundColor','white');
end
function troom_Callback(hObject, eventdata, handles)
global troom
if isnan(str2double(get(hObject, 'String')))
    set(hObject, 'String', troom);
    errordlg('Input must be a number','Error');
else
% Save the new troom value
troom = str2double(get(hObject, 'String'));
end
% --- Executes during object creation, after setting all
properties.
function troom_CreateFcn(hObject, eventdata, handles)
if ispc && isequal(get(hObject,'BackgroundColor'),
get(0,'defaultUicontrolBackgroundColor'))
    set(hObject,'BackgroundColor','white');
end
function cap_Callback(hObject, eventdata, handles)
global cap
if isnan(str2double(get(hObject, 'String')))
```

```
    set(hObject, 'String', cap);
    errordlg('Input must be a number','Error');
else
% Save the new cap value
cap = str2double(get(hObject, 'String'));
end

% --- Executes during object creation, after setting all
properties.
function cap_CreateFcn(hObject, eventdata, handles)
if ispc && isequal(get(hObject,'BackgroundColor'),
get(0,'defaultUicontrolBackgroundColor'))
    set(hObject,'BackgroundColor','white');
end
% ------------------------------------------------------------
-----------
function lasertype_SelectionChangeFcn(hObject, eventdata,
handles)

global yagplasma
if (hObject == handles.yag)
    yagplasma = 100;
else
    yagplasma = 1;
     err_dlg =warndlg('Future Work','Keyhole Calculation')
;
    end
 % ------------------------------------------------------------
------------
function weldingtype_SelectionChangeFcn(hObject, eventdata,
handles)
% hObject    handle to weldingtype (see GCBO)
% eventdata  reserved - to be defined in a future version
of MATLAB
% handles    structure with handles and user data (see
GUIDATA)
global fillercheck
%handles = guihandles(hklaser);
if (hObject == handles.yesfiller)
    fillercheck = 1;

else
    fillercheck = 0;
end
% ------------------------------------------------------------
-----------
```

```
function keyholecal_SelectionChangeFcn(hObject, eventdata,
handles)
% hObject    handle to keyholecal (see GCBO)
% eventdata  reserved - to be defined in a future version
of MATLAB
% handles    structure with handles and user data (see
GUIDATA)
global qw2
if (hObject == handles.firstfresnel)
    qw2 = 0;
else
    qw2 = 1;
end
% ------------------------------------------------------------
-----------
function fzcal_SelectionChangeFcn(hObject, eventdata,
handles)
% hObject    handle to fzcal (see GCBO)
% eventdata  reserved - to be defined in a future version
of MATLAB
% handles    structure with handles and user data (see
GUIDATA)
global qw
if (hObject == handles.yesfz)
    qw = 1;
else
    qw = 0;

end
% --- Executes during object creation, after setting all
properties.
function laser_CreateFcn(hObject, eventdata, handles)
% hObject    handle to laser (see GCBO)
% eventdata  reserved - to be defined in a future version
of MATLAB
% handles    empty - handles not created until after all
CreateFcns called
% --- Executes on button press in energy.
function energy_Callback(hObject, eventdata, handles)
% hObject    handle to energy (see GCBO)
% eventdata  reserved - to be defined in a future version
of MATLAB
% handles    structure with handles and user data (see
GUIDATA)
Energy_Balance;
% --- Executes on button press in effcal.
function effcal_Callback(hObject, eventdata, handles)
```

```
% hObject    handle to effcal (see GCBO)
% eventdata  reserved - to be defined in a future version
of MATLAB
% handles    structure with handles and user data (see
GUIDATA)
global efffrom
efffrom = 0;
laserefficiency;
% --- Executes on button press in estimateeff.
function estimateeff_Callback(hObject, eventdata, handles)
% hObject    handle to estimateeff (see GCBO)
% eventdata  reserved - to be defined in a future version
of MATLAB
% handles    structure with handles and user data (see
GUIDATA)
% Hint: get(hObject,'Value') returns toggle state of
estimateeff
global hh
if (get(hObject,'Value') == get(hObject,'Max'))
  hh = 1
else
   hh = 0
end
% --- Executes on button press in calculate.
function calculate_Callback(hObject, eventdata, handles)
% hObject    handle to calculate (see GCBO)
% eventdata  reserved - to be defined in a future version
of MATLAB
% handles    structure with handles and user data (see
GUIDATA)
set(handles.laser, 'name', 'Simulation of Laser Welding
Process - Designed by Haider Al-Kazzaz - Concordia
University(busy)')

 err_dlg =warndlg('Calculating : Please Wait','Keyhole
Calculation') ;
waitfor(err_dlg); % code execution is stopped till err_dlg
is dismissed.
hold off
global yagplasma
global qw
global qw2
global filler
global thickness
global k
global troom
global cp
```

```
global den
global tboil
global tmelt
global p
global v
global dfo
global zr
global zo
global ab
global Alib
global plume
global cap
global filler2
global fillercheck
global f
if fillercheck == 0
    filler = 0;
else
    filler = filler2;
end
kd = k/(cp*den);
 rfo = dfo/2 ;
z = 0;
r = 0;
filler = filler + plume;
%%%%%%%%%%%%%%%%%%%%%%%%%%%%%%%%%%%% Calculate keyhole top
radius
%%%%%%%%%%%%%%%%%%%%%%%%%%%%%%%%%%%%
%%%%%%%%%%%%%%%%%%%%%%%%%%%%%%%%%%%%
% first keyhole angle
angle1 = pi/4;
% angle between ray and normal to keyhole wall
anglep = pi/2-angle1;
% fresnel average energy trasmision
ta = fresnelcof2(ab,anglep);
ee = 0;
for xx = 0.0001:0.001:(rfo*15)
% cal peclet number
pe = (xx/1000)*(v/60)/(2*kd);
% bessel function of second kind and zero order
    k0 = besselk(0,pe);
% bessel functon of second kind and first order
    k1 = besselk(1,pe);
        % heat q
        q = (1000/xx)*(tboil-troom)*k*pe*(0+k1/k0);
    % inten(kw,mm,mm,mm,mm)
    intensity = inten(p,rfo,z,zo,zr,xx);
```

```
        check = q/(intensity*ta*tan(pi/4));
    if abs(check-1) <= 0.02
        ee = ee+1;
        rrk(ee)=xx;
        chch(ee)=check;
    end;
end
checko = isequal(ee,0);
if checko == 0
    rk = max(rrk);
end
if checko ==1
    rk = 0;
            set(handles.laser, 'name', 'Simulation of
Laser Welding Process - Designed by Haider Al-Kazzaz -
Concordia University');
    return;
end
 %%%%%%%%%%%%%%%%%%%%%%%%%%%%%Calculate keyhole profile from
fisrt fresnel
%%%%%%%%%%%%%%%%%%%%%%%%%%%%absorption
%%%%%%%%%%%%%%%%%%%%%
zz = 0.01;
an = angle1;
keyholeangle(1) = an;
pent(1) = 0;
xx(1) = rk;
uu = 1;
% cal source strength at the rk, z = 0
pe = (rk/1000)*(v/60)/(2*kd);
k0 = besselk(0,pe);
source(1) = (tboil-troom)*2*pi*k*(1/k0)*1;
while (xx(uu) >= 0.001)
uu = uu+1;
    xx(uu) = xx(uu-1)- zz*tan(an);

    if xx(uu)< 0
        uu = uu-1;
        break;
    end
    pent(uu) = - zz * (uu-1);


% cal peclet number
pe = (xx(uu)/1000)*(v/60)/(2*kd);
% bessel function of second kind and zero order
    k0 = besselk(0,pe);
```

```
     % bessel functon of second kind and first order
    k1 = besselk(1,pe);
        % heat q
        q = (1000/xx(uu))*(tboil-troom)*k*pe*(0+k1/k0);
     % inten(kw,mm,mm,mm,mm)
    intensity = inten(p,rfo,pent(uu),zo,zr,xx(uu));
 anglep = pi/2-an;
 % fresnel average energy trasmision
 ta = fresnelcof2(ab,anglep);
tanan = (q / (intensity*ta));
an = atan(tanan);
 keyholeangle(uu) = an;
 % cal source strength at the rk, z = 0
source(uu) = (tboil-troom)*2*pi*k*(1/k0)*1;
 end
 %%%%%%%%%% the keyhole was divided into numbers of layers
(uu)
 %%%%%%%%%%%%%%%%
mirror%%%%%%%%%%%%%%%%%%%%%%%%%%%%%%%%%%%%%%%%%%%%%%%%%%%%
tt = uu;
for pp = uu+1:uu*2
        xx(pp) = -xx(tt);
    pent(pp)=pent(tt);
    tt = tt-1;
end
 profile1xx = xx;
profile1pent=pent;
 disp('keyhole radius (mm)=');disp(rk);
disp('penetration depth (mm)=');disp(pent(uu));
 %%%%%%%%%%%%%%%%%%%%%%%%%%%%%%%%%%%%%%%%%%%%%%%%%%%%%curve
fitting%%%%%%%%%%%%%%%%%%%%%%
for pp = 1 : uu
   pentm(pp,1) = pent(pp);
   xxcurve(pp,1)=xx(pp);
end
 degree = 7;
op = 0;
kpk = polyfit(pentm,xxcurve,degree);
 for pp = 1 : uu

    xxfit(pp) = 0;
end

%%%% calculate x value from a given z value ((poly. eg.))
for pp = 1 : uu
op = 0;
    for orr = degree :-1: 0
```

```
        op = op+1;
        xxfit(pp)=xxfit(pp)+kpk(op)*pentm(pp)^orr;
    end
end
%%%%%%
mirror%%%%%%
```

```
    zzz = .001;
    flip = 0;
    % start x comp. from eq-1 right curve
    xxv = fz(startz,eqrx,degree);
    solz = startz;
    % slop of keyhole angle
    slop = dfz(startz,eqrx,degree);
    % keyhole angle
    angleave = atan(slop);
    %incedence angle
    anglep = pi/2-angleave;
    %reflected angle with hoizontal
    refanh = anglep - angleave;
    %reflected angle with vertical
    refan = pi/2-refanh;
    raydepth=startz;
    % intensity of the coming ray without any reduction
    intensity = inten(p,rfo,pent(layer),zo,zr,xx(layer));
    % intensity left after filler above the surface
    %intensity = intensity * exp(-Alib*hp);
   intensity = intensity * (1-filler/100);
    % wall
    plasma(layer) = plasma(layer) + intensity*(1-exp(-
Alib*abs(pent(layer)/1000)))/yagplasma;
    % intensity left after plasma inside the keyhole before
hitting the keyhole
    intensity = intensity - intensity*(1-exp(-
Alib*abs(pent(layer)/1000)))/yagplasma;
    %intensity after first Fresnel absorption
    ta = fresnelcof2(ab,anglep);
    intensity = intensity * (1-ta);

    if angleave <= anglep
        % pp is number of reflection after the first
reflection
        for pp = 1: 20
                flip = flip+1;
                % current location of the ray
                    x1 = xxv;
                z1 = startz;
               sol = 0;
                % check current penetration with the total
pent.
                if solz<pent(uu)
                    break;
                end
                while (sol == 0)
```

```
                    solz = solz-zzz;
                   solxray = rayeq(x1,solz,z1,refanh,flip);
                       %
                    solxpoly = ((-
1)^flip)*fz(solz,eqrx,degree);
                            % tttt = solxray-solxpoly;
                    if abs(1-solxray/solxpoly) <= 0.05
                              solution = solz;
                              if layer >= (draw)
                                  pointx = [x1 solxpoly];
                                  pointz = [z1 solz];

line(pointx,pointz,'LineStyle','-
','Color','y','LineWidth',0.1);
                                   % mirror lines
                                     %line(-pointx,pointz);
                                     sos = 1;
                         end
                         break;
                    end
                    if abs(solxray) >= abs(solxpoly)
                        break;
                    end
                    if solz<pent(uu)

                        break;
                        end
                 end % while
                     if solz<pent(uu)
                       break;
                   end
                 % finding the corresponding layer number
for solz
                 for jj = 1: 1 : uu
                       if abs(1-pent(jj)/solz) <= 0.09
                                layernumber = jj;

                        break;
                       end
                 end

                solx = ((-1)^flip)*fz(solz,eqrx,degree);
                    slop =  dfz(solz,eqrx,degree);
                        angleave = atan(slop);
     raylength = ((solx-x1)^2+(solz-z1)^2)^.5;
                anglep = (refanh - angleave);
```

```
                plasma(layernumber) = plasma(layernumber)
+ intensity * (1-exp(-Alib*raylength/1000))/yagplasma;

               % intensity left after plasma absorption
between two reflections
                intensity = intensity - intensity * (1-
exp(-Alib*raylength/1000))/yagplasma;
                % save the absorbed intensity by plasma
and layer location in the array
                % intensity absorbed by multiple
reflection
                ta = fresnelcof2(ab,anglep);
                intensity = intensity * ta;
                % save the m. reflection with the location
of the layer in array of m.refl
                mfresnel(layernumber,1) =
mfresnel(layernumber,1)+ intensity;
                          % save the horizontale angle for
the array in the same matrix
                mfresnel(layernumber,2) = refanh;
                % intensity after the reflection
                intensity = intensity * (1-ta);
                if refanh <= anglep
                    break;
                end
                if anglep <= 0
                     break;
                end
                %new refanh
                refanh = (anglep - angleave);
                     % cal fresnel abs
                xxv = solx;
                startz=solz;
          end % for # reflection
     end %if
    if sos == 1
              draw = draw+10;
    end
    sos = 0;
    end % for layer =
 groupn = 3;
uu3 = round(uu/groupn);
startuu3 = 1;
enduu3 = uu3;
 uugroup1plasma =0;
 for mm = 1:groupn
       for jj = startuu3: enduu3
```

```
            uugroup1plasma = uugroup1plasma + plasma(jj);
     end
    uugroup1plasma =  uugroup1plasma/(enduu3-startuu3+1);
     for jj = startuu3: enduu3
                 plasma(jj)= uugroup1plasma;
 %
  end
  startuu3 = enduu3+1;
enduu3 = startuu3+uu3;
  if enduu3 > uu
       enduu3 = uu;
  end
 end
 %%%%%%%%%%%%%%%%%%%%%%%%recalculate the keyhole
profile%%%%%%%%%%%%%%%%%%%%%
  checkuu = uu;
 clear xx;
clear keyholeangle;
clear ee;
clear source;
clear pent;
 an = angle1;
keyholeangle(1) = an;
pent(1) = 0;
xx(1) = rk;
uu = 1;
 % cal source strength at the rk, z = 0
pe = (rk/1000)*(v/60)/(2*kd);
k0 = besselk(0,pe);
source(1) = (tboil-troom)*2*pi*k*(1/k0)*1;
 while (xx(uu) >= 0.001)
     uu = uu+1;
    xx(uu) = xx(uu-1)- zz*tan(an);
         if xx(uu)< 0
            uu = uu-1;
                break;
        end
    pent(uu) = - zz * (uu-1);
     % cal peclet number
     pe = (xx(uu)/1000)*(v/60)/(2*kd);
        % bessel function of second kind and zero order
    k0 = besselk(0,pe);
     % bessel functon of second kind and first order
    k1 = besselk(1,pe);
        % heat q
        q = (1000/xx(uu))*(tboil-troom)*k*pe*(0+k1/k0);
     % inten(kw,mm,mm,mm,mm), without any reduction
```

```
    intensity = inten(p,rfo,pent(uu),zo,zr,xx(uu));
     % intensity left after filler above the surface
     %intensity = intensity * exp(-Alib*hp);
    intensity = intensity * (1-filler/100);
     % intensity left after plasma inside the keyhole
before hitting the keyhole
     % wall
      intensity = intensity - intensity*(1-exp(-
Alib*abs(pent(uu)/1000)))/yagplasma;
         anglep = pi/2-an;
     if uu>checkuu
            mfresnel(uu,1)=0;
        mfresnel(uu,2)=0;
        plasma(uu)=0;
        end
    ta = fresnelcof2(ab,anglep);
         tanan = ((q-plasma(uu)) /
(abs(intensity*ta+mfresnel(uu,1))));
    an = atan(tanan);
     keyholeangle(uu) = an;
     % cal source strength at the rk, z = 0
     source(uu) = (tboil-troom)*2*pi*k*(1/k0)*1;
 end
 %%%%%%%%%%%%%%%%%%%%%%%%%%%%%%%%%%%%%%%%%%%%%%generate
mirror keyhole side
%%%%%%%%%%%%%%%%%%%%%%%%%%%%%%%%%%%%%%%%%%%%%%%%%%%%%%%%%%%%
%%%%%%%%%%%%%%%
 tt = uu;
for pp = uu+1:uu*2
    xx(pp) = -xx(tt);
    pent(pp)=pent(tt);
    tt = tt-1;
end
hold all
plot(xx,pent,'r-','LineWidth',2)
ylim([-thickness 0]);
xlabel('Width (mm)');
     ylabel('Penetration (mm)');

end % qw2



 set(handles.laser, 'name', 'Simulation of Laser Welding
Process - Designed by Haider Al-Kazzaz - Concordia
University');
 %%%%%%%%%%%%%%%%%%%%%%%%%%%%%%%%%%%%%Calculate FZ
```

```
%%%%%%%%%%%%%%%%%%%%%%%%%%%%%%%%%%%%geometry%%%%%%%%%%%%%%%
%%%%%%%%%
 if qw == 1
    global layervalue
   global maxuu
    maxuu = uu;
    set(handles.laser, 'name', 'Simulation of Laser Welding
Process - Designed by Haider Al-Kazzaz - Concordia
University');
  FZ_calculation;
 handlesFZ = guihandles(FZ_calculation);
  %err_dlg =warndlg('Calculating : Please Wait','Keyhole
Calculation')
waitfor(handlesFZ.FZ_calculation, 'Visible', 'off' );
 global layervalue
 endradius = 2;
    ee =0;
    tt = 0;
 step = round(uu/layervalue);
 pp = 1;
     while (pp <= uu)
        ee = 0;
             if (uu-pp)<step
            step = round((uu-pp)/2);
        end
        for radius = 4: -0.001:xx(pp)
                       % cal peclet number
                   pe = (radius/1000)*(v/60)/(2*kd);
                 % bessel function of second kind and zero
order
                 k0 = besselk(0,pe);
                  source2 = (tmelt-troom)*2*pi*k*(1/k0)*1;
check2 = source2/(source(pp)*cap);
if abs(check2-1) <= 0.01
ee = ee+1;
rmelt(pp,ee) = radius;
end % if
end % radius
pp = pp+step;
if step ==0
            break;
        end
    end % pp
    ppp = max(rmelt,[],2);
    endradius = ppp(1);
    ee = 0;
    [m,n] = size(rmelt);
```

```
    ppp = max(rmelt,[],2);
    %%%%%%%%%%%%%%%%%%%%%%%%%%%%%%% generate FZ
mirror%%%%%%%%%%%%%%%%%%%%%%
    tt = uu;
    %for pp = uu+1:uu*2
     %   ppp(pp)=-ppp(tt);
      %  tt = tt-1;
    %end % profile pp
    ee = 0;
    for pp = 1:uu
        if ppp(pp)~= 0
            ee = ee+ 1;
            xxfz(ee)=ppp(pp);
        pentfz(ee) = pent(pp);
        end
    end
    baselinex = [xxfz(ee) -xxfz(ee)];
    baseliney = [pentfz(ee) pentfz(ee)];
hold all
    plot(xxfz,pentfz,'b-',-xxfz,pentfz,'b-','LineWidth',2);
    line(baselinex,baseliney,'Color','b','LineWidth',2);

    xlim([-thickness/2 thickness/2]);

    ylim([-thickness 0]);
    xlabel('Width (mm)');
     ylabel('Penetration (mm)');
end % if meltpool
set(handles.laser, 'name', 'Simulation of Laser Welding
Process - Designed by Haider Al-Kazzaz - Concordia
University');
global efffrom
global averagewidth
global totalFZarea
global penetrationdepth
global hh
if qw == 1
if hh ==1
    efffrom = 1;
    if abs(pent(uu))>thickness
    for pp = 1 : uu
        if abs(pent(pp))>thickness
            thicknesslayer = pp;
            break;
        end
    end
    else
```

```
          thicknesslayer = uu;
    end
penetrationdepth = abs(pent(thicknesslayer));
ee = 0;
    for pp = 1:thicknesslayer
         if ppp(pp)~= 0
            ee = ee+ 1;
            xxfzav(ee)=ppp(pp);

        end
    end
averagewidth = mean(xxfzav)*2;
totalFZarea = averagewidth*penetrationdepth;
laserefficiency;
end
end
```

A.5.2: programming of the absoptivity window

```
function varargout = absorptivity(varargin)
gui_Singleton = 1;
gui_State = struct('gui_Name',       mfilename, ...
                   'gui_Singleton',  gui_Singleton, ...
                   'gui_OpeningFcn',
@absorptivity_OpeningFcn, ...
                   'gui_OutputFcn',
@absorptivity_OutputFcn, ...
                   'gui_LayoutFcn',  [] , ...
                   'gui_Callback',   []);
if nargin && ischar(varargin{1})
    gui_State.gui_Callback = str2func(varargin{1});
end
if nargout
    [varargout{1:nargout}] = gui_mainfcn(gui_State,
varargin{:});
else
    gui_mainfcn(gui_State, varargin{:});
end
% End initialization code - DO NOT EDIT
% --- Executes just before absorptivity is made visible.
function absorptivity_OpeningFcn(hObject, eventdata,
handles, varargin)
handles.output = hObject;
% Update handles structure
guidata(hObject, handles);
```

```
% UIWAIT makes absorptivity wait for user response (see
UIRESUME)
% uiwait(handles.figure1);
%handlesa = guihandles(hklaser);
%ab2 = str2double(get(handlesa.ab, 'String'))
global ab
hold off
cont = 0;
for an = 0.1:.01:90.01
    cont = cont + 1;
    angle(cont) = an;
    anglep = an*pi/180;
    ave(cont) =  fresnelcof2(ab,anglep);
end
axes(handles.axes2)
plot(angle,ave,'b-','LineWidth',2);
xlim([0 100]);
    ylim([0 max(ave)*1.1]);
    xlabel('Incident Angle');
     ylabel('absorptivity');
% --- Outputs from this function are returned to the
command line.
function varargout = absorptivity_OutputFcn(hObject,
eventdata, handles)
varargout{1} = handles.output;
```

A.5.3: programming of the energy balance window

```
function varargout = Energy_Balance(varargin)
gui_Singleton = 1;
gui_State = struct('gui_Name',       mfilename, ...
                   'gui_Singleton',  gui_Singleton, ...
                   'gui_OpeningFcn',
@Energy_Balance_OpeningFcn, ...
                   'gui_OutputFcn',
@Energy_Balance_OutputFcn, ...
                   'gui_LayoutFcn',  [] , ...
                   'gui_Callback',   []);
if nargin && ischar(varargin{1})
    gui_State.gui_Callback = str2func(varargin{1});
end
if nargout
    [varargout{1:nargout}] = gui_mainfcn(gui_State,
varargin{:});
else
```

```
    gui_mainfcn(gui_State, varargin{:});
end
% End initialization code - DO NOT EDIT


% --- Executes just before Energy_Balance is made visible.
function Energy_Balance_OpeningFcn(hObject, eventdata,
handles, varargin)

handles.output = hObject;
 % Update handles structure
guidata(hObject, handles);
function varargout = Energy_Balance_OutputFcn(hObject,
eventdata, handles)
% varargout  cell array for returning output args (see
VARARGOUT);
% hObject    handle to figure
% eventdata  reserved - to be defined in a future version
of MATLAB
% handles    structure with handles and user data (see
GUIDATA)

% Get default command line output from handles structure
varargout{1} = handles.output;
 hold off
global k
global troom
global cp
global den
global tboil
global tmelt
global p
global v
global dfo
global zr
global zo
global ab
global f
kd = k/(cp*den)
rfo = dfo/2
z = 0
r = 0
axes(handles.axes3)
angle1 = pi/4;
% angle between ray and normal to keyhole wall
anglep = pi/2-angle1;
% fresnel average energy trasmision
```

```
ta = fresnelcof2(ab,anglep);
ee = 0;

for xx = 0.0001:0.001:(rfo*15)
ee = ee+1;
radiusxx(ee)=xx;
% cal peclet number
pe = (xx/1000)*(v/60)/(2*kd);
% bessel function of second kind and zero order
    k0 = besselk(0,pe);
% bessel functon of second kind and first order
    k1 = besselk(1,pe);
    % heat q
    heatloss(ee) = (1000/xx)*(tboil-troom)*k*pe*(0+k1/k0);
    % inten(kw,mm,mm,mm,mm)
    laserintensity(ee) =
inten(p,rfo,z,zo,zr,xx)*ta*tan(pi/4);
end
plot(radiusxx,heatloss,'b-',-radiusxx,heatloss,'b-
',radiusxx,laserintensity,'r-',-radiusxx,laserintensity,'r-
','LineWidth',2 );
%plot(radiusxx,laserintensity,'r-','LineWidth',2 );
ylim([0 max(laserintensity)*1.1]);
xlim([-rfo*5 rfo*5]);
xlabel('Radius (mm)');
ylabel('Heat flow (q), ab. Intensity at(45 degree)
"W/M/M"');
```

A.5.4: programming of the FZ_calculation window

```
function varargout = FZ_calculation(varargin)
gui_Singleton = 1;
gui_State = struct('gui_Name',       mfilename, ...
                   'gui_Singleton',  gui_Singleton, ...
                   'gui_OpeningFcn',
@FZ_calculation_OpeningFcn, ...
                   'gui_OutputFcn',
@FZ_calculation_OutputFcn, ...
                   'gui_LayoutFcn',  [] , ...
                   'gui_Callback',   []);
if nargin && ischar(varargin{1})
    gui_State.gui_Callback = str2func(varargin{1});
end

if nargout
```

```
    [varargout{1:nargout}] = gui_mainfcn(gui_State,
varargin{:});
else
    gui_mainfcn(gui_State, varargin{:});
end
function FZ_calculation_OpeningFcn(hObject, eventdata,
handles, varargin)
handles.output = hObject;
guidata(hObject, handles);
set(handles.FZlayers,'min',0);
set(handles.FZlayers,'max',1);
global gogo
gogo = 0;
global layervalue
layervalue = 3;
% --- Outputs from this function are returned to the
command line.
function varargout = FZ_calculation_OutputFcn(hObject,
eventdata, handles)
varargout{1} = handles.output;
% --- Executes on slider movement.
function FZlayers_Callback(hObject, eventdata, handles)

% Hints: get(hObject,'Value') returns position of slider
%        get(hObject,'Min') and get(hObject,'Max') to
determine range of slider
global maxuu

global layervalue
layervalue = round((maxuu-
3)*(get(handles.FZlayers,'Value'))+3);


set(handles.Numberoflayers,'String',num2str(layervalue));

% --- Executes during object creation, after setting all
properties.
function FZlayers_CreateFcn(hObject, eventdata, handles)
if isequal(get(hObject,'BackgroundColor'),
get(0,'defaultUicontrolBackgroundColor'))
    set(hObject,'BackgroundColor',[.9 .9 .9]);
end
% --- Executes on button press in Select.
function Select_Callback(hObject, eventdata, handles)
% hObject    handle to Select (see GCBO)
% eventdata  reserved - to be defined in a future version
of MATLAB
```

```
% handles    structure with handles and user data (see
GUIDATA)

delete(handles.FZ_calculation);
global layervalue
global gogo
gogo = 1;
% --- Executes during object creation, after setting all
properties.
function Numberoflayers_CreateFcn(hObject, eventdata,
handles)
% hObject    handle to Numberoflayers (see GCBO)
% eventdata  reserved - to be defined in a future version
of MATLAB
% handles    empty - handles not created until after all
CreateFcns called
```

A.5.4: programming of the `MultipleReflections` window

```
function varargout = MultipleReflections(varargin)
gui_Singleton = 1;
gui_State = struct('gui_Name',       mfilename, ...
                   'gui_Singleton',  gui_Singleton, ...
                   'gui_OpeningFcn',
@MultipleReflections_OpeningFcn, ...
                   'gui_OutputFcn',
@MultipleReflections_OutputFcn, ...
                   'gui_LayoutFcn',  [] , ...
                   'gui_Callback',   []);
if nargin && ischar(varargin{1})
    gui_State.gui_Callback = str2func(varargin{1});
end

if nargout
    [varargout{1:nargout}] = gui_mainfcn(gui_State,
varargin{:});
else
    gui_mainfcn(gui_State, varargin{:});
end
function MultipleReflections_OpeningFcn(hObject, eventdata,
handles, varargin)
handles.output = hObject;
guidata(hObject, handles);
set(handles.mrslide,'min',0);
set(handles.mrslide,'max',1);
```

```
global mrstep
mrstep = 10;

% --- Outputs from this function are returned to the
command line.
function varargout = MultipleReflections_OutputFcn(hObject,
eventdata, handles)
varargout{1} = handles.output;
% --- Executes on slider movement.
function mrslide_Callback(hObject, eventdata, handles)
maxmr = 100;

global mrstep
mrstep = round((100-10)*(get(handles.mrslide,'Value'))+10);
set(handles.mrvalue,'String',num2str(mrstep));
function mrslide_CreateFcn(hObject, eventdata, handles)
if isequal(get(hObject,'BackgroundColor'),
get(0,'defaultUicontrolBackgroundColor'))
    set(hObject,'BackgroundColor',[.9 .9 .9]);
end
% --- Executes on button press in mrselect.
function mrselect_Callback(hObject, eventdata, handles)
delete(handles.MultipleReflections);
global mrstep
```

A.5.5: programming of the `laserefficiency` window

```
function varargout = laserefficiency(varargin)
gui_Singleton = 1;
gui_State = struct('gui_Name',       mfilename, ...
                   'gui_Singleton',  gui_Singleton, ...
                   'gui_OpeningFcn',
@laserefficiency_OpeningFcn, ...
                   'gui_OutputFcn',
@laserefficiency_OutputFcn, ...
                   'gui_LayoutFcn',  [] , ...
                   'gui_Callback',   []);
if nargin && ischar(varargin{1})
    gui_State.gui_Callback = str2func(varargin{1});
end

if nargout
    [varargout{1:nargout}] = gui_mainfcn(gui_State,
varargin{:});
else
```

```
    gui_mainfcn(gui_State, varargin{:});
end
% End initialization code - DO NOT EDIT


% --- Executes just before laserefficiency is made visible.
function laserefficiency_OpeningFcn(hObject, eventdata,
handles, varargin)
handles.output = hObject;
guidata(hObject, handles);
global penetration
global widthav
global FZarea
global hf
global tsolidus
global efffrom
global averagewidth
global totalFZarea
global penetrationdepth
tsolidus = str2double(get(handles.tsolidus, 'String'))
hf = str2double(get(handles.hfg, 'String'))
if efffrom ==0
 set(handles.w_ave,'Enable','on');
  set(handles.FZarea,'Enable','on');
      set(handles.penet,'Enable','on');
widthav = str2double(get(handles.w_ave, 'String'));
FZarea = str2double(get(handles.FZarea, 'String'));
penetration = str2double(get(handles.penet, 'String'));

else
    set(handles.w_ave,'Enable','off');
  set(handles.FZarea,'Enable','off');
      set(handles.penet,'Enable','off');
widthav = averagewidth;
FZarea = totalFZarea;
penetration = penetrationdepth;
set(handles.w_ave,'string',widthav);
  set(handles.FZarea,'string',FZarea);
      set(handles.penet,'string',penetration);
end
function varargout = laserefficiency_OutputFcn(hObject,
eventdata, handles)
varargout{1} = handles.output;
function tsolidus_Callback(hObject, eventdata, handles)
global tsolidus
 if isnan(str2double(get(hObject, 'String')))
    set(hObject, 'String', tsolidus);
```

```
    errordlg('Input must be a number','Error');
else
tsolidus = str2double(get(hObject, 'String'))

end
function tsolidus_CreateFcn(hObject, eventdata, handles)
if ispc && isequal(get(hObject,'BackgroundColor'),
get(0,'defaultUicontrolBackgroundColor'))
    set(hObject,'BackgroundColor','white');
end
function w_ave_Callback(hObject, eventdata, handles)
global widthav
global efffrom
if efffrom ==0
if isnan(str2double(get(hObject, 'String')))
    set(hObject, 'String',  widthav);
    errordlg('Input must be a number','Error');
else
widthav = str2double(get(hObject, 'String'));
end
end
function w_ave_CreateFcn(hObject, eventdata, handles)
if ispc && isequal(get(hObject,'BackgroundColor'),
get(0,'defaultUicontrolBackgroundColor'))
    set(hObject,'BackgroundColor','white');
end
function FZarea_Callback(hObject, eventdata, handles)
global FZarea
global efffrom
if efffrom ==0
if isnan(str2double(get(hObject, 'String')))
    set(hObject, 'String', FZarea);
    errordlg('Input must be a number','Error');
else
FZarea = str2double(get(hObject, 'String'));
end
end
function FZarea_CreateFcn(hObject, eventdata, handles)
if ispc && isequal(get(hObject,'BackgroundColor'),
get(0,'defaultUicontrolBackgroundColor'))
    set(hObject,'BackgroundColor','white');
end
function hfg_Callback(hObject, eventdata, handles)
global hf
if isnan(str2double(get(hObject, 'String')))
    set(hObject, 'String', hf);
    errordlg('Input must be a number','Error');
```

```
else


% Save the new dfo value
hf = str2double(get(hObject, 'String'));
end
function hfg_CreateFcn(hObject, eventdata, handles)
if ispc && isequal(get(hObject,'BackgroundColor'),
get(0,'defaultUicontrolBackgroundColor'))
    set(hObject,'BackgroundColor','white');
end
function penet_Callback(hObject, eventdata, handles)
global penetration
global efffrom
if efffrom ==0
if isnan(str2double(get(hObject, 'String')))
    set(hObject, 'String', penetration);
    errordlg('Input must be a number','Error');
else
penetration = str2double(get(hObject, 'String'));
end
end
function penet_CreateFcn(hObject, eventdata, handles)
if ispc && isequal(get(hObject,'BackgroundColor'),
get(0,'defaultUicontrolBackgroundColor'))
    set(hObject,'BackgroundColor','white');
end

% --- Executes on button press in eff_cal.
function eff_cal_Callback(hObject, eventdata, handles)
global k
global troom
global cp
global den
global tboil
global tmelt
global p
global v
global penetration
global widthav
global FZarea
global hf
global tsolidus
% thermal diffusivity is the ratio of thermal conductivity
to heat capacity m^2/s.
kd = k/(cp*den);
% input average radius of melting (mm)
```

```
rm1 = widthav/2;
% cal. source strength at melting radius

% cal peclet number
pe = (rm1/1000)*(v/60)/(2*kd);
% bessel function of second kind and zero order
    k0 = besselk(0,pe);
% bessel functon of second kind and first order
    k1 = besselk(1,pe);
% cal. source strength at melting radius
source(1) = (tmelt-troom)*2*pi*k*(1/k0)*1;
% coupling efficiency Method -1 %
ceff1 = source(1)/1000*penetration/1000/p*100
% thermal efficiency
thermaleff = ((v/60*FZarea/1000000)*den*(cp*(tsolidus -
troom)+ hf))/(source(1)*penetration/1000)*100
% Process efficiency
MR = ((FZarea/1000000)*den*(cp*(tsolidus - troom)+
hf))/(p*1000/(v/60))*100
set(handles.coupling, 'String', ceff1);
set(handles.thermal, 'String',thermaleff );
set(handles.process, 'String', MR);
```

A.5.6: other functions

```
function xray = rayeq(x1,zu,z1,refanh, flip)

xray = ((-1)^(flip))*abs((zu-z1)/tan(refanh))+x1;
%%%%%%%%%%%%%%%%%%%%%%%%%%%%%%%%%%%%%%%%%%%%%%%%%%%%%%%%%%%%%%%%%%%%%%%
function dxdz = dfz(z,eqrx,degree)
dxdz=0;
op =0;
for orr = degree :-1: 0
    op = op+1;
     dxdz=dxdz+orr*eqrx(op)*(z^(degree-op));
end
%%%%%%%%%%%%%%%%%%%%%%%%%%%%%%%%%%%%%%%%%%%%%%%%%%%%%%%%%%%%%%%%%%%%%%%
% cal energy fresnel trasmision coe
function ta = fresnelcof2(ab,anglep)
ta = 1 - 0.5*((1+(1-
ab*cos(anglep)^2))/(1+(1+ab*cos(anglep)^2))+(ab^2-
2*ab*cos(anglep)+2*cos(anglep)^2)/(ab^2+2*ab*cos(anglep)+2*
cos(anglep)^2));
end
%%%%%%%%%%%%%%%%%%%%%%%%%%%%%%%%%%%%%%%%%%%%%%%%%%%%%%%%%%%%%%%%%%%%%%%
function xpoint = fz(z,kpk,degree)
```

Table 11: Hardness in FZ and HAZ of

```
xpoint = 0;
op =0;

for orr = degree :-1: 0
    op = op+1;
     xpoint=xpoint+(kpk(op))*(z^orr);
end
%%%%%%%%%%%%%%%%%%%%%%%%%%%%%%%%%%%%%%%%%%%%%%%%%%%%%%%%%%%%%%%%%%%%%%%%%%%%
function intensity = inten(p,rfo,z,zo,zr,r)
p = p*1000;
rfo = rfo / 1000;
z = z / 1000;
zo = zo/1000;
zr = zr/1000;
r = r / 1000;
io = 2*p/((rfo)^2*pi);
rf = rfo*((1+((z-zo)/zr)^2)^0.5);
intensity = io*((rfo/rf)^2)*(exp(-2*(r^2)/(rf^2)));
end
%%%%%%%%%%%%%%%%%%%%%%%%%%%%%%%%%%%%%%%%%%%%%%%%%%%%%%%%%%%%%%%%%%%%%%%%%%%%
```